# Investigation of membrane reactors based on dense mixed-conducting ceramics for separation and catalysis process

Von der Naturwissenschaftlichen Fakultät

der Gottfried Wilhelm Leibniz Universität Hannover

zur Erlangung des Grades

**Doktor der Naturwissenschaften**

**Dr. rer. nat.**

genehmigte Dissertation

von

**Jian Xue, Master (China)**

geboren am 16.07.1988 in Shanxi, China

2016

Referent: Prof. Dr. Armin Feldhoff

Korreferent: Prof. Dr. Jürgen Caro

Korreferent: Prof. Dr. Georg Garnweitner

Korreferent: Prof. Dr. Haihui Wang

Tag der Promotion: 21.07.2016

# Preface

The results given in this thesis were achieved in the period of my Ph.D. study, since Oct. 2013, at the Institute of Physical Chemistry and Electrochemistry at the Gottfried Wilhelm Leibniz Universität Hannover, under the supervision of Prof. Dr. Armin Feldhoff. In this time, I have been a scientific co-worker with subject on dense ceramic oxygen- as well as hydrogen-separating membranes. Seven research papers, in which I am the first author or second author, are included in this thesis. The following statement will clarify my contribution to the seven articles collected in this thesis. For all these articles, I would like to thank the valuable discussions and suggestions from the co-authors and the referees. Special thanks for their kind help and instructions are to Prof. Dr. Jürgen Caro, Prof. Dr. Haihui Wang, Prof. Dr. Henny J. M. Bouwmeester and Prof. Dr. Yanying Wei.

Four articles, studying the dense ceramic oxygen-permeable membranes, form chapter 2 of this thesis. The first article, *The phase stability of the Ruddlesden-Popper type oxide $(Pr_{0.9}La_{0.1})_{2.0}Ni_{0.74}Cu_{0.21}Ga_{0.05}O_{4+\delta}$ in an oxidizing environment*, published in the ***Journal of Membrane Science***, was written by me and modified by all the co-authors, especially Prof. Dr. Haihui Wang and Prof. Dr. Armin Feldhoff. The materials synthesis and permeation test were done by myself. And I obtained technical support on *in-situ* XRD characterizations by Alexander Wollbrink. The second paper, *A new $CO_2$-resistant Ruddlesden-Popper oxide with superior oxygen transport: A-site deficient $(Pr_{0.9}La_{0.1})_{1.9}(Ni_{0.74}Cu_{0.21}Ga_{0.05})O_{4+\delta}$*, published in the ***Journal of Materials Chemistry A,*** was written by me. The materials were prepared by myself and the oxygen permeation measurements were complete by Dr. Liao and me. Moreover, I got support from Dr. Wei Chen and Prof. Dr. Henny J.M. Bouwmeester for oxygen content test and the theoretical explanation for the influence of A-site deficiency on the oxygen transport. I wrote the first draft, the co-authors helped in correcting and improving the manuscript. The third article, *Improvement of the oxygen permeation and stability of Ruddlesden-Popper-type membrane by surface modification*, which has been submitted to the ***Journal of Membrane Science***, was written by me. The materials were synthesized by myself, and the oxygen permeation measurements were done by Yanpeng Suo and me. I obtained support on the thermogravimetry tests by Li Chen. The fourth paper, *Ambient air partial internal reduction of NiO in a mixed ionic-electronic conducting ceramic*, published in the ***Journal of the European Ceramic Society***, was written by me. I got technical and theoretical support from Prof. Armin Feldhoff.

Three articles, about dense ceramic hydrogen-permeable membrane reactors, are collected in Chapter 3. The first two articles, *Enhanced stability of Zr-doped $Ba(CeTb)O_{3-\delta}$-Ni cermet membrane for hydrogen separation*, which has been published in the ***Chemical Communications***, and *Hydrogen permeability and stability of $BaCe_{0.85}Tb_{0.05}Zr_{0.1}O_{3-\delta}$ asymmetric membranes*, which has been published in the ***Journal of Membrane Science***, with my colleague Prof. Dr. Yanying Wei being the principal author. My contribution was to carry out hydrogen permeation measurements and to share experimental knowledge. The third paper, *Gas to liquids: Natural gas conversion to aromatic fuels and chemicals in a hydrogen-permeable ceramic hollow-fiber membrane reactor*, which has been published in ***ACS Catalysis***, was written by me. The catalysis measurements and characterizations were conducted by me. And I got help from Prof. Dr. Yanying Wei and Prof. Dr. Jürgen Caro on correcting and improving the manuscript. The hollow-fiber membrane employed in this work was prepared by Dr. Yan Chen.

# Acknowledgement

# Abstract

Dense ceramic membranes with mixed conductivity for oxygen ions and electrons or protons and electrons enable the separation of oxygen or hydrogen, respectively, from gas mixtures with unrivalled selectivity when a chemical potential gradient of oxygen or hydrogen is applied at high temperature. These membranes have attracted increasing interest due to their potential applications in gas sensors, oxygen or hydrogen pumps, gas separation units and catalytic membrane reactors. For industrial applications, the dense ceramic membranes should possess a high permeation flux, good phase stability and good chemical stability under the practice conditions. Based on these requirements, this thesis presents seven original research articles, in which oxygen-permeable membranes and hydrogen-permeable membranes were investigated, respectively. A general fundamental overview on the separation process, materials, preparation and applications of dense ceramic membranes is depicted in Chapter 1.

Chapter 2 focuses on the development of oxygen-permeable membranes with good separation performance. The Ruddlesden-Popper oxide $(Pr_{0.9}La_{0.1})_{2.0}Ni_{0.74}Cu_{0.21}Ga_{0.05}O_{4+\delta}$ possesses good chemical stability under $CO_2$-containing atmosphere, while its permeation flux is low and it demonstrates a reversible phase decomposition at intermediate temperature. As proven by *in-situ* X-ray diffraction, the phase decomposition conditions as function of temperature and oxygen partial pressure were examined. The influence of calcination temperature and A-site deficiency on the material's phase stability are discussed to guide the development of Ruddlesden-Popper type materials with improved phase stability. The A-site deficient Ruddlesden-Popper oxide $(Pr_{0.9}La_{0.1})_{1.9}Ni_{0.74}Cu_{0.21}Ga_{0.05}O_{4+\delta}$, which was developed in this work, exhibits stable and twice higher oxygen transport rate compared to its cation-stoichiometric parent phase. The high oxygen transport rate is attributed to highly mobile oxygen vacancies, which compensate the A-site deficiency. To further improve the oxygen permeation flux and the phase stability of the A-site deficient Ruddlesden-Popper membrane, a catalytic layer was coated on the membrane surfaces. The modified membranes show both enhanced permeability and phase stability under practice-relevant conditions. In course of membrane preparation, during the cooling process in ambient air, partial internal reduction of NiO precipitates was firstly observed in a mixed ionic-electronic conducting oxide. No highly reducing atmosphere is needed. Instead the mixed ionic-electronic conducting oxide acts as local oxygen sink.

Chapter 3 includes the development of stable hydrogen-separating membranes and the application of hydrogen membrane reactor in nonoxidative dehydroaromatization of methane. Among the reported hydrogen-permeable membranes, Ni-$BaCe_{0.95}Tb_{0.05}O_{3-\delta}$ is a state of the art material due to its good hydrogen permeability, while it bears a phase segregation, which results in a sharp decline to half the hydrogen permeation flux after a few days of operation. Remarkably enhanced phase stability and good hydrogen permeation flux could be achieved through a Ni-$BaCe_{0.85}Tb_{0.05}Zr_{0.1}O_{3-\delta}$ cermet membrane, which was developed by partial substitution of Ce with Zr. Moreover, the Zr-doped $BaCe_{0.85}Tb_{0.05}Zr_{0.1}O_{3-\delta}$ hydrogen-permeable membrane was firstly reported, which can be steadily operated for hydrogen separation for more than two weeks. To overcome the thermodynamic constraints, a hydrogen-permeable ceramic hollow-fiber membrane was combined with the nonoxidative methane dehydroaromatization reaction, which could *in-situ* remove the produced hydrogen so that the methane conversion and aromatics yield were improved.

**Keywords**: dense ceramic membrane, oxygen separation, hydrogen separation, catalytic membrane reactor.

# Zusammenfassung

Gasdichte keramische Membranen mit gemischter Leitfähigkeit für Sauerstoffionen und Elektronen oder Protonen und Elektronen ermöglichen die Abtrennung von Sauerstoff oder Wasserstoff aus Gasgemischen mit unerreichter Selektivität, wenn bei hoher Temperatur ein chemischer Potentialgradient des Sauerstoffs oder Wasserstoffs angelegt wird. Wegen ihrer Anwendungsmöglichkeiten in Gassensorik, Sauerstoff- oder Wasserstoffpumpen, Gastrennvorrichtungen und katalytischen Membranreaktoren, erfahren diese Membranen ein wachsendes Interesse. Für industrielle Anwendungen müssen die gasdichten keramischen Membranen einen hohen Permeationsfluss (von Sauerstoff bzw. Wasserstoff), eine gute Phasenstabilität sowie eine gute chemische Stabilität unter praxisrelevanten Bedingungen aufweisen. Die vorliegende Schrift bündelt sieben Forschungsartikel, in denen sauerstoffdurchlässige und wasserstoffdurchlässige Membranen im Lichte der zuvor geschilderten Erfordernisse behandelt werden. Kapitel 1 gibt einen grundlegenden Überblick über Gastrennprozesse sowie keramische Membranmaterialien, Membranherstellung und Membrananwendungen.

Kapitel 2 ist auf die Entwicklung sauerstoffpermeabler Membranen mit guten Trenneigenschaften fokusiert. Das Ruddlesden-Popper-artige Oxid $(Pr_{0.9}La_{0.1})_{2.0}Ni_{0.74}Cu_{0.21}Ga_{0.05}O_{4+\delta}$ hat eine gute chemische Stabilität in $CO_2$-haltiger Atmosphäre, wohingegen sein Sauerstoffpermationsfluss mäßig ist und im mittleren Temperaturbereich eine reversible Phasenzersetzung auftreten kann. Mittels *in-situ* Röntgenbeugung bei Variation der Temperatur und des Sauerstoffpartialdrucks wurden Stabilitätsfenster bestimmt. Untersuchungen zum Einfluss der Kalzinierungstemperatur und der A-Gitterplatz-Kationenunterstöchiometrie führten zur Entwicklung des A-Platz-unterstöchiometrischen Ruddlesden-Popper-Oxids $(Pr_{0.9}La_{0.1})_{1.9}Ni_{0.74}Cu_{0.21}Ga_{0.05}O_{4+\delta}$, welches eine stabile und doppelt so hohe Sauerstofftransportrate aufweist wie die kationenstöchiometrische Ausgangsphase. Die hohe Sauerstofftransportrate konnte auf die hohe Mobilität von Sauerstoffleerstellen zurückgeführt werden, die die A-Platz-Unterstöchiometrie kompensieren. Durch eine Modifizierung der Membranoberflächen mit einer porösen katalytischen Schicht konnten eine nochmals verbesserte Sauerstoffpermeation sowie Phasenstabilität unter praxisrelevanten Bedingungen erreicht werden. Im Zuge der Membranherstellung konnte während des Abkühlprozesses in Umgebungsluft erstmals eine partielle innere Reduzierung von NiO-Ausscheidungen in einer sauerstoffionisch-elektronisch gemischtleitenden Oxidmatrix, die als lokale Sauerstoffsenke wirkt, beobachtet werden. Hierbei ist keine stark reduzierende Atmosphäre erforderlich.

Kapitel 3 behandelt die Entwicklung stabiler Wasserstofftrennmembranen und deren Anwendung in einem Membranreaktor zur nicht-oxidativen Dehydroaromatisierung von Methan. Unter den wasserstoffpermeablen Membranen stellt $Ni-BaCe_{0.95}Tb_{0.05}O_{3-\delta}$ den Stand der Technik dar. Es hat eine gute Wasserstoffpermeabilität aber ist anfällig für eine Phasensegregation, die zu einem Abfall des Wasserstoffpermeationsflusses auf die Hälfte innerhalb weniger Tage des Betriebs führt. Durch die partielle Substitution von Ce durch Zr, hin zu einer $Ni-BaCe_{0.85}Tb_{0.05}Zr_{0.1}O_{3-\delta}$ Kompositmembran, konnte eine verbesserte Phasenstabilität bei gutem Wasserstoffpermeationsfluss erreicht werden. Zudem ermöglichte die erstmals berichtete Zr-dotierte $BaCe_{0.85}Tb_{0.05}Zr_{0.1}O_{3-\delta}$-Membran einen stabilen Betrieb von mehr als zwei Wochen. In einem Membranreaktor konnte mit einer wasserstoffpermeablen Hohlfasermembran die nicht-oxidative Dehydroaromatisierung von Methan demonstriert werden, welche auf der in-situ-Entfernung des erzeugten Wasserstoffs beruht und die Aromatenausbeute in der Methanumsetzung deutlich erhöht.

**Schlagwörter**: gasdichte keramische Membran, Sauerstoffabtrennung, Wasserstoffabtrennung, katalytischer Membranreaktor.

# Abbreviations

## Acronyms

| | |
|---|---|
| BCT | $BaCe_{0.85}Tb_{0.05}O_{3-\delta}$ |
| BCTZ | $BaCe_{0.85}Tb_{0.05}Zr_{0.1}O_{3-\delta}$ |
| EDTA | Ethylenediaminetetraacetic acid |
| GC | Gas chromatograph |
| MDA | Nonoxidative methane dehydroaromatization |
| MFC | Mass flow controller |
| MIEC | Mixed oxygen-ionic and electronic conducting |
| MPEC | Mixed protonic and electronic conducting |
| Ni-BCT | $Ni\text{-}BaCe_{0.95}Tb_{0.05}O_{3-\delta}$ |
| Ni-BCTZ | $Ni\text{-}BaCe_{0.85}Tb_{0.05}Zr_{0.1}O_{3-\delta}$ |
| NMP | 1-methyl-2-pyrrolidinone |
| OCM | Oxidative coupling of methane |
| PESf | Polyethersulfone |
| $(PL)_{2.0}NCG$ | $(Pr_{0.9}La_{0.1})_{2.0}Ni_{0.74}Cu_{0.21}Ga_{0.05}O_{4+\delta}$ |
| $(PL)_{1.9}NCG$ | $(Pr_{0.9}La_{0.1})_{1.9}Ni_{0.74}Cu_{0.21}Ga_{0.05}O_{4+\delta}$ |
| POM | Partial oxidation of methane |
| PVP | Polyvinyl pyrrolidone |
| RP | Ruddlesden-Popper oxide |

## Formula signs

| | |
|---|---|
| $\mu$ | Gas chemical potential |
| $T$ | Temperature |
| $p^{o}$ | Reference gas partial pressure |
| $p''$ | Gas partial pressure in the feed side |
| $p'$ | Gas partial pressure in the sweep side |
| $j$ | Gas permeation flux |
| R | Gas constant, |
| F | Faraday constant |

| | |
|---|---|
| L | Membrane thickness |
| $\sigma_e$ | Electronic conductivity |
| $\sigma_i$ | Ionic conductivity |
| $V_m$ | Molar volume |
| C | Concentration of the oxygen-ionic or protonic carriers |
| D | Diffusion coefficient |
| $L_C$ | Characteristic thickness |
| k | Surface exchange coefficient |
| $O_2(g)$ | Gaseous oxygen |
| $V_O^{\cdot\cdot}$ | Oxygen vacancy |
| $O^\times$ | Lattice oxygen |
| $O_i''$ | Interstitial oxygen |
| $e'$ | Electron |
| $h^\cdot$ | Electron hole |
| $H_2(g)$ | Gaseous hydrogen |
| $H^\cdot$ | Proton |
| $C_{O_2}$ | Oxygen concentration |
| $C_{N_2}$ | Nitrogen concentration |
| S | Membrane active area |
| $C_{H_2}$ | Hydrogen concentration |
| $C_{He}$ | Helium concentration |
| $C_{H_2{}_{feed}}$ | Concentration of hydrogen in the feed gas |
| $C_{He_{feed}}$ | Concentration of helium in the feed gas |

X

# Content

# Chapter 1

# Introduction

## 1.1 Motivation

A membrane is a selective barrier that allows some components in a mixture to pass through but stops others. This makes membranes a suitable mean to separate a mixture of components. Gas separation membrane science and technologies are recognized as powerful tools in solving some important global problems [1-3]. Based on the separation mechanism, gas separation membranes can be classified as porous membranes and dense membranes [4, 5]. Porous membranes contain voids, which allow small molecules to move through the membrane while the big molecules are left. Selectivity of the porous membranes is determined primarily by the relative molecular sizes of the gases being separated, so that the selectivity is low [4-6]. In dense membranes, the permeated molecule is adsorbed on one side of the membrane, dissolves in the membrane material, diffuses through the membrane and desorbs on the other side of the membrane [7, 8]. So that dense membranes possess much higher selectivity as compared to the porous membranes.

Dependent on the composition, dense membranes can be divided into polymer membranes, metallic membranes and ceramic membranes [2, 5, 8]. The selectivity and flux of dense polymer membranes are competitive while these membranes are unstable when the temperature is higher than 100 $^\circ$C [5]. Dense metallic membranes (Pd, Pd alloys) can be applied at intermediate temperature (300-600 $^\circ$C) and exhibit good selectivity and high flux, however, their chemical stability is poor and the cost is often too high for practical applications [7]. Recently, dense ceramic membranes have attracted a lot of attentions as they possess unrivaled selectivity and can be operated at 600-1000 $^\circ$C and, moreover, be coupled with several reactions for process intensification [7, 9, 10].

Dense gas separation ceramic membranes are oxygen-ionic or protonic conducting materials and have been applied in oxygen separation from air and hydrogen separation from hydrogen containing gases in the past 30 years [9, 10]. These membranes could be integrated with some reactions to overcome the thermodynamic limit and simplify the reaction system and saving energy [11]. For practical applications, dense gas separation ceramic membranes should possess high flux, good phase stability, and good chemical stability under practical conditions such as $CO_2$-containing gas [10, 11].

The main aim of this thesis is to develop dense ceramic oxygen-permeable membranes and hydrogen-separating membranes with high flux and good chemical and phase stability, and integrate the separation and catalysis process for a practical reaction.

## 1.2 Concepts of dense ceramic separation membranes

### 1.2.1 General separation process in dense ceramic separation membranes

Dense ceramic membranes can separate gas from a gas mixture at elevated temperatures under a chemical potential gradient [9-12]. The gas molecules pass the membranes through mobile point defects in the crystal lattice, which results in an unrivalled selectivity. Therefore, the dense ceramic membranes are the ideal separation units for practical applications [10, 11, 13].

In the dense ceramic membranes, the gas separation process includes three major progressive steps (gas insertion on the feed side, bulk diffusion and gas release on the sweep side), as described in detail below as shown in **Figure 1** [9, 10, 14].
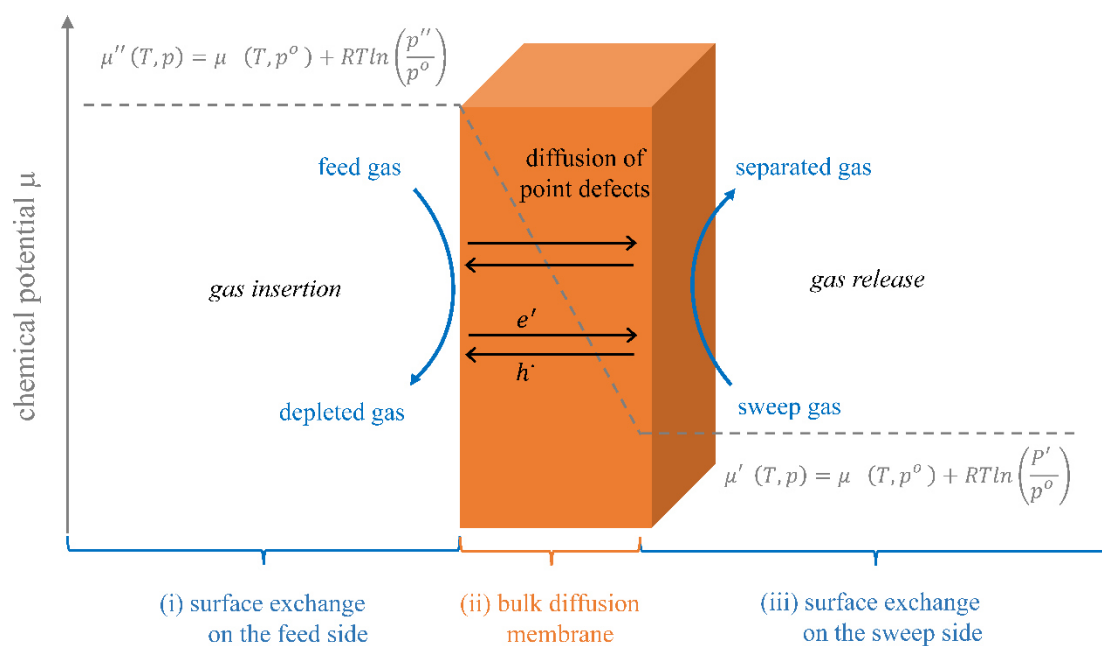


**Figure 1**. Schematic diagram of the different sections involved in the dense ceramic separation membranes during separation process. In this figure, $\mu$, $T$, $p^o$, $p''$, $p'$ are chemical potential, temperature, reference gas partial pressure, gas partial pressure in the feed side and gas partial pressure in the sweep side.

Firstly, the gaseous molecules adsorb, disassociate, ionize and combine with the crystal lattice defects on the feed side. Then the charged species of the gas diffuse from the feed side surface to the sweep side surface under the gas chemical potential gradient. The overall charge neutrality is maintained by the transport of electrons or electron holes simultaneously. Finally, charged species of the gas associate and desorb to a

gaseous molecules on the sweep side surface.

The overall permeation process is limited by the slowest step among abovementioned three (gas insertion, bulk diffusion, gas release) [10, 14, 15]. For a relatively thick membrane, the bulk diffusion process plays a dominant role in the separation process, which can be expressed by the Wagner equation [10, 14, 16, 17]:

$$j = -\frac{RT}{4^2 F^2 L} \int_{lnp'}^{lnp''} \frac{\sigma_e \sigma_i}{\sigma_e + \sigma_i} dlnp \qquad (1)$$

where $j$ is the gas permeation flux, R is gas constant,, F is Faraday constant, T is temperature, L is the membrane thickness, $\sigma_e$ is the electronic conductivity, respectively. $p''$ is the gas partial pressure maintained at the feed side, while $p'$ is the gas partial pressure at the sweep side. The ionic conductivity $\sigma_i$ can be described by the Nernst-Einstein equation [10, 14]:

$$\sigma_i = \frac{4F^2}{RTV_m} CD \qquad (2)$$

where $V_m$ is the molar volume, C is the concentration and D is the diffusivity of the charged carriers, respectively.

In this case, as shown in **Eq. 1**, the gas permeation flux $j$ is proportional to the reciprocal of the membrane thickness 1/L, so that reducing the membrane thickness could result in increased gas permeation flux. In the meantime, the relative limiting effect of surface exchange also increased, as shown in **Figure 2** [10, 15].
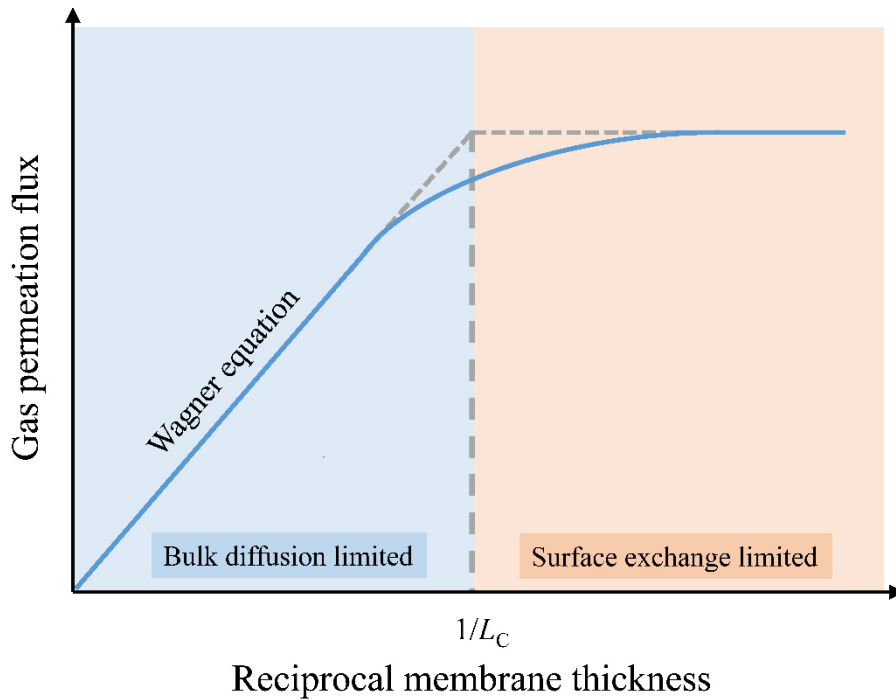


**Figure 2**. Dependence of gas permeation flux on the inverse membrane thickness as described in **Eq. 1**.

If the thickness is reduced below a critical value $L_C$, the surface exchange process becomes the rate-controlling step [10, 15]. The characteristic thickness $L_C$ which is defined as a theoretical thickness at which the gas separation process is equally affected by both the surface-exchange kinetics and the bulk diffusion, as described by following equation [15]:

$$L_C = \frac{D}{k} \qquad (3)$$

D is the diffusion coefficient and k is the surface exchange coefficient, respectively. $L_C$ is a theoretical value which depends on the materials and test conditions, and can be used to distinguish the rate controlling step during the gas permeation process. The gas permeation process is determined by bulk diffusion when $L > L_C$, and by surface-exchange when $L < L_C$. To obtain higher gas permeation flux, both surfaces of the membrane should have good catalytic effects for the gas insertion and release, and the membrane should be as thin as possible to decrease the transfer resistance in the bulk.

## 1.2.2 Oxygen-permeable membrane

Oxygen is one of the most widely used commodity chemicals in the world as its numerous applications in modern society such as the production cycle of steel, plastics and textiles, brazing, welding and cutting of steels and other metals, rocket propellant, in oxygen therapy and life support systems in aircraft, submarines, spaceflight and diving. Nearly 100 million tons of oxygen are produced every year so that the separation of oxygen from air is a big business [12]. Nowadays, there are three fundamental approaches for air separation, which are cryogenic distillation, electrolysis of water and pressure swing adsorption using molecular sieve adsorbents [18, 19]. The first two methods are energy-consuming as the cryogenic distillation requires ultra-low temperature and electrolysis of water needs larger amount of electricity, while the last approach cannot produce high purity oxygen [18, 19].

Recently, a new advanced category for oxygen separation has emerged, which is based on specialized dense ceramic mixed oxygen-ionic and electronic conducting (MIEC) oxides. The MIEC membrane can separate oxygen from air or oxygen-containing atmosphere at elevated temperatures under an oxygen partial pressure gradient (oxygen chemical potential gradient) with unrivalled selectivity [9-12]. Therefore, the dense ceramic oxygen-permeable membranes are the ideal oxygen supply for some high-temperature reactions like partial oxidation of methane, oxidative coupling of methane, oxidative dehydroaromatization and oxyfuel combustion [10, 11, 13].

In the dense ceramic MIEC oxygen-permeable membranes, the oxygen separation process includes three major progressive steps, as described in detail below as shown in **Figure 1** [10, 15, 20]:

1) **Surface exchange on the feed side** (high oxygen chemical potential): Firstly gaseous oxygen adsorbs, disassociates, ionizes and then combines with crystal lattice

defects. This is an oxygen insertion period, which can be described by using Kröger-Vink defect notation as follows [21]:

$$O_2(g) + 2V_O^{\cdot\cdot} + 4e' \rightarrow 2O_O^x \qquad (4)$$
$$O_2(g) + 2V_O^{\cdot\cdot} \rightarrow 2O_O^x + 4h^{\cdot} \qquad (5)$$
$$O_2(g) + 4e' \rightarrow 2O_i'' \qquad (6)$$
$$O_2(g) \rightarrow 2O_i'' + 4h^{\cdot} \qquad (7)$$
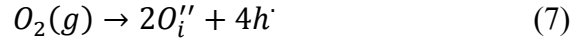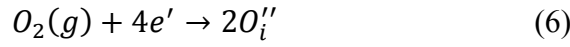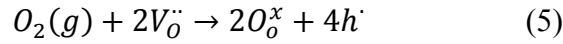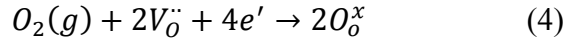
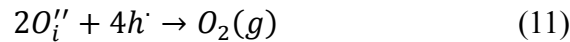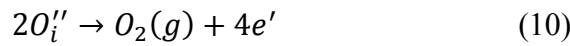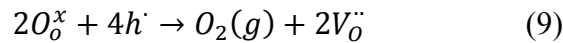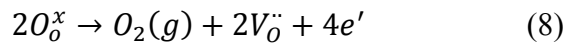Where $O_2(g)$, $V_O^{\cdot\cdot}$, $O^{\times}$, $O_i''$, $e'$ and $h^{\cdot}$ are gaseous oxygen, oxygen vacancy, lattice oxygen, interstitial oxygen, electron and electron hole in the respective oxides. Here, different equations are used for different materials with various oxygen-ionic and electronic carriers. The oxygen source in the feed side can be not only air, but also some oxygen-containing gases like NO, $N_2O$, $H_2O$, $CO_2$ [22-30]. These oxygen-containing gases could decompose at high temperature, and the produced oxygen can be selectively removed by the dense ceramic oxygen-separating membrane, which results in improved conversion [22-30].

2) **Bulk diffusion of charged oxygen species** (oxygen vacancies or interstitial oxygen) and electrons or electron holes simultaneously. During this period, oxygen-ionic carriers will be transported from the high oxygen chemical potential side to the low oxygen chemical potential side, whilst the overall charge neutrality is maintained by a counterbalancing flux of electrons or electron holes [10, 15].

3) **Surface exchange on the sweep side** (low oxygen chemical potential): Charged oxygen species associate and desorb to a gaseous oxygen. This is an oxygen release process as described below:

$$2O_O^x \rightarrow O_2(g) + 2V_O^{\cdot\cdot} + 4e' \qquad (8)$$
$$2O_O^x + 4h^{\cdot} \rightarrow O_2(g) + 2V_O^{\cdot\cdot} \qquad (9)$$
$$2O_i'' \rightarrow O_2(g) + 4e' \qquad (10)$$
$$2O_i'' + 4h^{\cdot} \rightarrow O_2(g) \qquad (11)$$

Oxygen release is a reverse process compared with the reaction in the feed side. The sweep gases can be inert gases (e.g. He, Ar) or some reducing gases (e.g. $CH_4$, $C_2H_6$) [11, 23, 28, 31, 32]. Some oxygen-consuming reactions like partial oxidation of methane (POM), oxidative coupling of methane (OCM), oxidative dehydroaromatization and oxyfuel combustion can be coupled with the oxygen separation process in this side [11, 23, 28, 31-35].

## 1.2.3 Hydrogen-permeable membrane

Hydrogen is not only a sustainable eco-friendly energy carrier with high energy density, high conversion efficiency and recyclability but also an important raw material for modern industry, large amounts of hydrogen are used in the petroleum and chemical industries like production of ammonia [36, 37]. Currently, most commercial hydrogen

is produced by the steam reforming of natural gas, and the product mixture is synthesis gas ($CO + H_2$) rather than pure hydrogen [38, 39]. Therefore, hydrogen separation and purification from the mixtures are necessary.

Traditionally metal alloy films possess good hydrogen selectivity and permeability, while its brittle property, poor mechanical strength, bad chemical stability in practical conditions and high costs limit their applications [40-44]. Recently, mixed protonic and electronic ceramic conductors (MPEC) have attracted increasing attention due to their potential applications in hydrogen separation and relative catalytic membrane reactors [45-47]. The mixed protonic and electronic ceramic can be applied as a hydrogen-permeable membrane with unrivaled selectivity, high flux and good chemical stability. The dense ceramic hydrogen-permeable membranes can selectively separate hydrogen rather than other gases from a $H_2$-containing atmosphere under the driving force of a hydrogen chemical potential gradient across the membrane, so that these membranes could be coupled with some high-temperature reactions such as steam reforming of natural gas or nonoxidative methane dehydroaromatization [48-54].

The hydrogen separation process through a dense proton-electron conducting ceramic membrane under a hydrogen chemical potential gradient is schematically illustrated in **Figure 1**. In this membrane, hydrogen moves from the high partial pressure side (feed side with $H_2$-rich gas), to the low partial pressure side (sweep side). Overall, there are three steps are involved in this process [14]:

1) **Surface exchange on the feed side** (high hydrogen chemical potential): Hydrogen absorbes on the surface of the membrane, then dissociates with electrons or electron holes into protons. This is a hydrogen insertion period, which can be described by using Kröger-Vink defect notation as follows [21]:

$$H_2(g) + 2h^{\cdot} \rightarrow 2H^{\cdot} \qquad (12)$$
$$H_2(g) \rightarrow 2e' + 2H^{\cdot} \qquad (13)$$
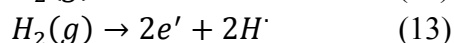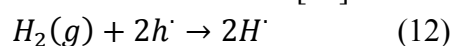
Here, $H_2(g)$, $H^{\cdot}$, $e'$ and $h^{\cdot}$ are gaseous hydrogen, proton, electron and electron hole respectively. The feed gas could not only be hydrogen-containing gases, but also be coupled with some hydrogen producing reactions such as steam reforming of natural gas to syngas or nonoxidative methane dehydroaromatization (MDA) [38, 40, 55, 56]. In the hydrogen-permeable membrane reactor, the produced hydrogen is removed continuously, so that the equilibrium limitation of the reactions could be broken to get high product yield and pure hydrogen is obtained [56].

2) **Bulk diffusion of protons and electrons or electron holes** at the same time under the hydrogen chemical potential gradient. During this period, protons will be transported from the high hydrogen chemical potential side to the low hydrogen chemical potential side, whilst the overall charge neutrality is maintained by a counterbalancing flux of electrons or electron holes.

3) **Surface exchange on the sweep side** (low hydrogen chemical potential): Protons associate with electrons or electron holes to hydrogen. This is a hydrogen release process as described below:

$$2H^{\cdot} \rightarrow H_2(g) + 2h^{\cdot} \qquad (14)$$
$$2e' + 2H^{\cdot} \rightarrow H_2(g) \qquad (15)$$
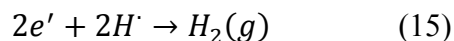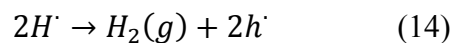
Normally, inert gas (Ar) is used as sweep gas, while it could not provide low enough hydrogen chemical potential. Some hydrogen-consuming reactions could be combined with the hydrogen-permeable membrane in this side, such as reduction emission of some oxidative greenhouse gases like NO, $NO_2$, and $N_2O$ which are combusted with hydrogen to eco-friendly nitrogen and water.

# 1.3 Materials of dense ceramic separation membranes

## 1.3.1 Mixed oxygen-ionic and electronic conducting materials

### 1.3.1.1 Perovskite oxides

Perovskites take their name from a mineral oxide of $CaTiO_3$, which was first discovered in 1839 [57]. Since Teraoka et al. reported the oxygen permeation properties of $La_{1-x}Sr_xCo_{1-y}Fe_yO_{3-\delta}$ membrane, perovskite oxides ($ABO_3$) became the mostly studied MIEC materials due to their high oxygen permeation flux [58]. The performance of the MIEC membranes is dependent on their composition and structure, which are discussed in detail below.
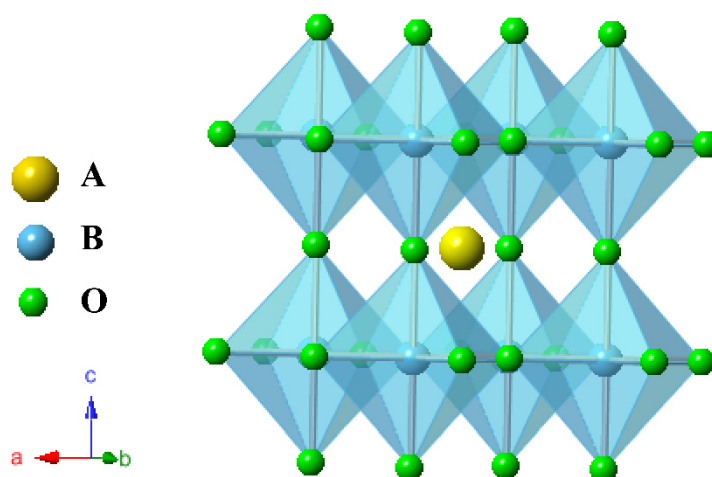


**Figure 3**. Structure of the cubic perovskite oxides (space group $Pm\overline{3}m$). Atomic positions are calculated from ICSD 109462 ($Ba_{0.5}Sr_{0.5}Co_{0.8}Fe_{0.2}O_{3-\delta}$) [59]. The atomic radius are not drawn to scale.

Perovskite oxides with a general formula of $ABO_3$ are easily formed with different

valence A or B-site cations such as $A^{1+}B^{5+}O_3$, $A^{2+}B^{4+}O_3$, $A^{3+}B^{3+}O_3$ [10]. In the perovskites structure as shown in **Figure 3**, the B-site atoms are located at the corners and the A-site atoms at the center of the cube, while the oxygen atoms are placed in the centers of the cube edges leading to the formation of $BO_6$ octahedral extended three dimensionally. Normally, the A-site cations (can be alkaline-earth metals or lanthanide series metals like Ba, Sr, La) are larger than B-site cations (can be 3d, 4d, and 5d transition metals like Co, Fe) as the requirement of the different coordination environment [10]. In 1926, Goldschmidt first described perovskites with tolerance factors t which can be used to define the formation possibility of different combination of A- or B-site cations, as shown below [60, 61]:

$$t = \frac{r_A + r_O}{\sqrt{2}(r_B + r_O)} \qquad (16)$$

where $r_A$, $r_B$, $r_O$ are the ionic radius of the A-site cation, B-site cation and oxygen ion. Therefore, perovskites have the capability to adjust the A- or B-site elements in the lattice with the constraints that t is in the range of 0.75 - 1.0.

In MIEC perovskite oxides, oxygen ions transport through the oxygen vacancies which can be adjust by introduction of low valence A-site or B-site metals [10, 58, 62]. To easily understand the transport path of the oxygen ions, the model reported by Zhou et al. is used here [63]. In the ideal cubic perovskite structure, oxygen occupies octahedral sites and is coordinated with four co-planar A-site cations and two apical B-site cations, as shown in **Figure 4a** [10, 63].
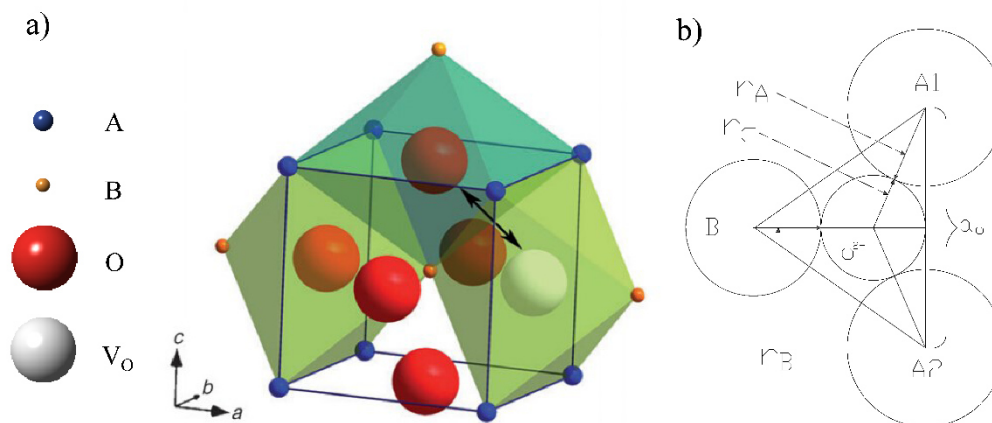


**Figure 4. a)** Transport path of oxygen ions in ideal cubic perovskite materials as described by Zhou et al. [63]. The oxygen or oxygen vacancies are coordinated by four co-planar A-site cations and two apical B-site cations, which form octahedral edges. Oxygen movement from an occupied octahedron to a vacant octahedron, as indicated by a black arrow. The atomic radius are not drawn to scale; **b)** oxygen transport in ideal cubic perovskite structure is related to the passing of the octahedron face, which is spanned by two A-site and one B-site cations, the narrowest space along the oxygen octahedral edge is defined as the critical radius $r_c$ [64].

During oxygen-ion migration, an oxygen ion jumps from one occupied octahedral site

to an adjacent octahedral vacant, as indicated by the black arrow in **Figure 4a** [62, 63, 65]. The oxygen ions have to pass through the octahedron face which consists of two A-site cations and one B-site cation. As described in **Figure 4b**, the narrowest space along the oxygen octahedral edge (called the saddle point) can be estimated by the critical radius $r_c$, which is defined as [62, 64, 65]:

$$r_c = \frac{r_A^2 + \frac{3}{4}a_O^2 - \sqrt{2}a_O r_B + r_B^2}{2(r_A - r_B) + \sqrt{2}a_O} \qquad (17)$$

Where $r_A$ and $r_B$ are the A-site and B-site cation radius, respectively and $a_O$ is the lattice parameter. Therefore, larger $r_c$ can be obtained by reducing $r_A$ or increasing $r_B$, which might enhance the oxygen-ionic diffusivity to increase the oxygen-ionic conductivity. As described by **Eq. 2**, higher oxygen vacancies concentrations will also result in higher oxygen-ionic conductivity. Up to 1/4 of the oxygen sites can be vacancies, while too many oxygen vacancies will lead to the order of oxygen vacancies which largely decrease the oxygen-ionic conductivity [66, 67]. Among the perovskite MIEC materials, $Ba_{0.5}Sr_{0.5}Co_{0.8}Fe_{0.2}O_{3-\delta}$ exhibits excellent oxygen permeability of 1.4 mL/(min·cm$^2$) with 1.8 mm thickness at 950 °C [67]. However, most peroskite MIEC membranes are alkaline-earth-containing so that their chemical stability in $CO_2$-containing atmosphere is very poor which limits their practical applications [67-69].

### 1.3.1.2 K$_2$NiF$_4$-type oxides

K$_2$NiF$_4$-type oxides with a common formula $A_2BO_4$ are the first members of the Ruddlesden-Popper (RP) $A_{n+1}B_nO_{3n+1}$ materials with $n = 1$ [10, 70-72]. Usually, the A-site metals are lanthanide series metals such as La, Pr, and the B-site metals are transition metals such as Ni, Cu [10, 73, 74]. The K$_2$NiF$_4$ structure, as shown in **Figure 5a**, is composed of an alternating perovskite-like layer and rock-salt layer along the crystallographic c-axis [75-77]. To release the structural stress, overstoichiometric oxygen is inserted in the rock-salt layer.

As described in **Figure 5b**, there are three possible transport paths for oxygen ions: 1. interstitial mechanism; 2. interstitialcy mechanism; 3. vacancy mechanism [75-77]. However, as proven by molecular dynamics simulations, the oxygen transport in the K$_2$NiF$_4$-type materials proceeds mainly via a migration of interstitial oxygen (O3) in the rock-salt layers by the interstitialcy diffusion mechanism, which refers to the "knock-on" or "push-pull" mechanism. It involves an interstitial oxygen, which replaces an apical oxygen (O2) in the perovskite layer and then moves to an adjacent interstitial oxygen site [72, 76, 78, 79]. The contribution of the oxygen vacancy mechanism should be considered when there are some oxygen vacancies formed in the structure as Cleave et al. predicted the lower activation energy of vacancy mechanisms compared to the interstitialcy process [75]. In conclusion, the migration of oxygen ions in the K$_2$NiF$_4$-type oxides is anisotropic and takes place mainly in the a-b plane, which results in the relatively low oxygen permeability compared to perovskites [77, 80].

However, most $K_2NiF_4$-type oxygen-permeable membranes have good chemical stability against carbonation as they are alkaline-earth-metals free in contrast to perovskites [76, 81].
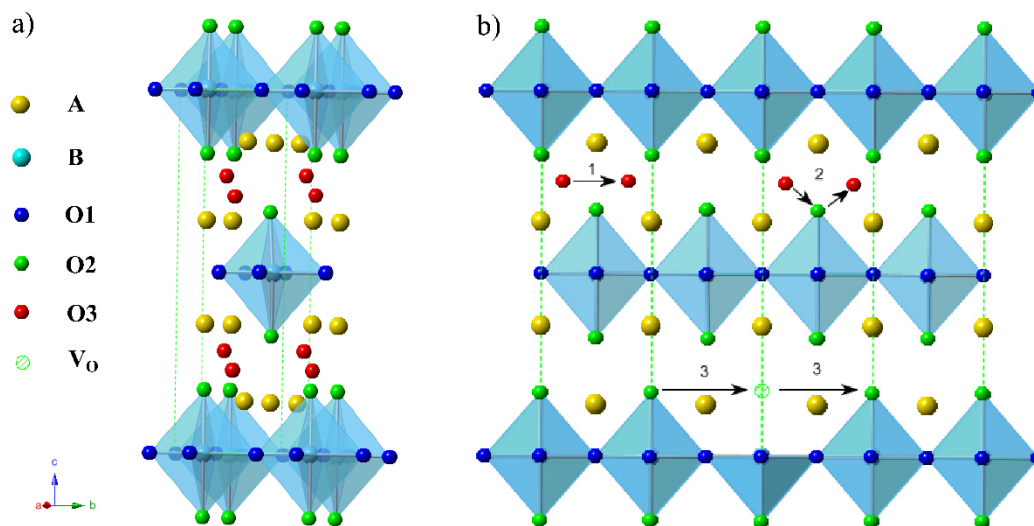


**Figure 5. a)** Structure of the tetragonal $K_2NiF_4$-type oxides (space group I4/mmm, from ICSD 173422, $(Pr_{0.9}La_{0.1})_{2.0}Ni_{0.74}Cu_{0.21}Ga_{0.05}O_{4+\delta}$) [72]; **b)** transport paths for different oxygen ions diffusion mechanism: 1, interstitial mechanism; 2, interstitialcy mechanism; 3, vacancy mechanism. The atomic radius are not drawn to scale.

## 1.3.2 Mixed protonic and electronic conducting materials

### 1.3.2.1 Perovskite oxides

Perovskite oxide $SrCe_{0.95}Yb_{0.05}O_{3-\delta}$ was the first reported protonic conducting materials by Iwahara in the 1980s [82, 83]. Afterwards, the mixed protonic and electronic conducting ceramics have attracted a lot of attentions. Several perovskite oxides possess protonic conductivity, such as oxides based on $ACeO_3$ or $AZrO_3$ (the A-site element can be Ba, Sr) [84-92]. The cerate-based oxides show relative high proton conductivity, and zirconate-based oxides show good mechanical strength and good chemical stability against $CO_2$ [90, 93-95].

It is observed that doping low valance cations in the A/B site can create more oxygen vacancies, which results in higher proton conductivity [14]. Therefore, oxygen vacancies in perovskite oxides play an important role in the formation and transport of protons. However, the proton transfer mechanisms in ceramic materials are not clear, and two possibilities have been proposed as shown in **Figure 6**, one is the vehicle mechanism, and the other is the Grotthuss mechanism (hopping mechanism) [96-99]. According to the vehicle mechanism, proton is transported by the migration of OH$^-$, and the oxygen in the hydroxyl ion is the vehicle [96, 97, 99]. For the Grotthuss

mechanism, proton transport occurs by hopping between adjacent oxygen ions that proton combines with an oxygen ion and forms a weak O-H bond, then the bonded proton hops with another neighboring oxygen ion [98, 100, 101].
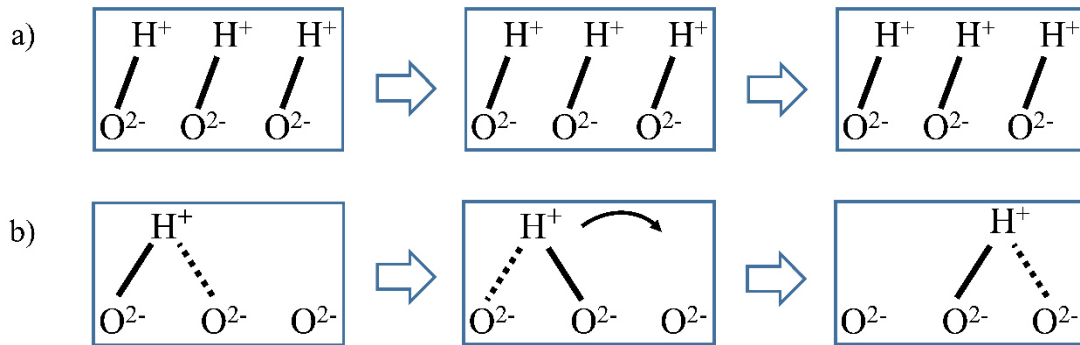


**Figure 6.** The proton transfer mechanisms in ceramic materials: **a)** vehicle mechanism; **b)** Grotthuss mechanism.

The difference between these two mechanisms is whether the oxygen ions diffuse during the proton conducting process: in the vehicle mechanism, oxygen ions carry proton diffuse through the oxides; while in the Grotthuss mechanism, oxygen ions are fixed medium, protons hop between different oxygen ions [14].

### 1.3.2.2 Tungstate-based oxides

Tungstate-based compounds with a formula of $La_{28-x}W_{4+x}O_{54+\delta}$ have attracted attention due to their high protonic conductivity [46, 47, 102-104]. Here, x is the amount of tungsten siting on the lanthanum site. Until now, the structure of these materials is still unclear, the first structure model was reported by Magraso et al., who identified these materials as a cubic structure with space group $F\overline{4}3m$ as shown in **Figure 7** [104]. In this case, some lanthanum ions and tungstate ions are coordinated with eight oxygen in distorted cubes. W sites are fully occupied and they and some lanthanum sites are empty. Later, with the DFT simulation, they reported that the centered tetragonal structure with the I4/mmm space group is better to describe these materials [105]. However, the tetragonal structure could not improve the agreement factor of XRD refinements. Combining the *in-situ* high temperature powder neutron diffraction data, their following study recognized that the structure of lanthanum tungstate oxides could be well described by both $F\overline{4}3m$ and $Fm\overline{3}m$ space group with minor differences [46, 47].

Moreover, the materials with a lanthanum tungstate ratio (La/W) equal to 6 are not single phase, and only the La-deficient oxides (5.3 < La/W < 5.7, 1.08 > x > 0.74) was found as a pure phase [104-108]. Segregation of $La_2O_3$, when the ratio La/W > 5.7 (x < 0.74), and $La_6W_2O_{15}$, when the ratio La/W < 5.3 (x > 1.08), were found respectively [104-108]. Normally, the La-site is La or Nd and the W-site could be partially

substituted by Mo or Re, therefore, these materials show remarkable chemical stability in $CO_2$ environment [109]. The tungstate-based materials could be appealing membranes for practical applications in catalytic membrane reactor due to their remarkable protonic conductivity and good stability under $CO_2$ atmosphere [56, 109].
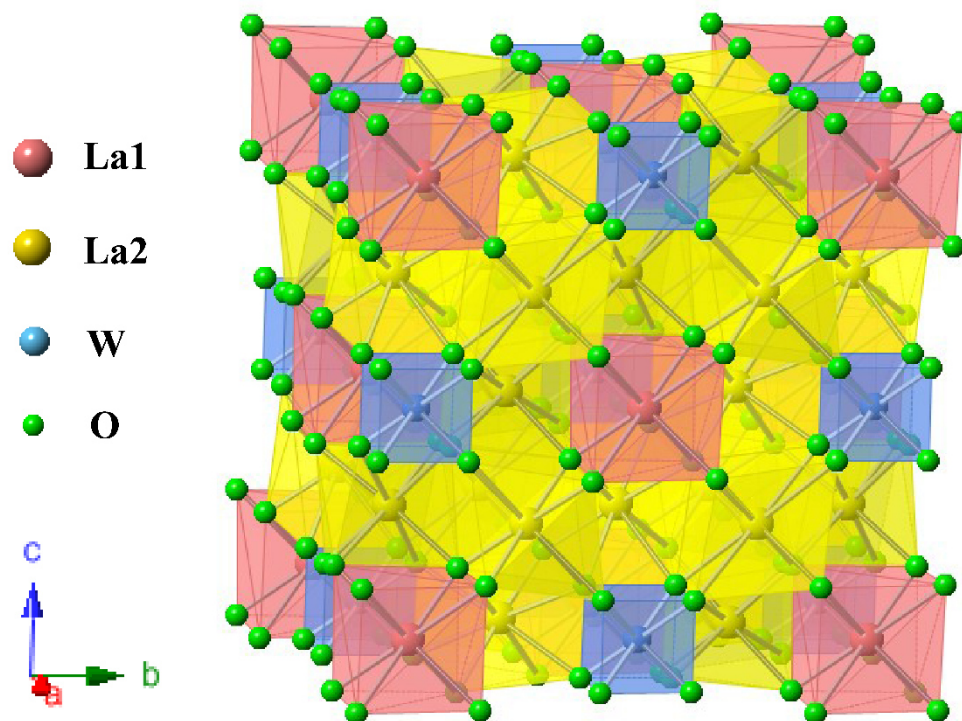


**Figure 7**. Structure of the cubic lanthanum tungstate oxides (space group $F\bar{4}3m$). Atomic positions are calculated from ICSD 250503 ($La_{6.56}W_{1.16}O_{13.13}$) [104]. The atomic radius are not drawn to scale.

# 1.4 Preparation of dense ceramic separation membranes

## 1.4.1 Powder

The first step to process a dense ceramic membrane is the preparation of the powder. Several methods can be applied for the synthesis of the ceramic powders such as conventional solid state methods, co-precipitation methods, hydrothermal methods and sol-gel methods [10, 14]. The sol-gel methods are liquid methods, which involve the dehydration at low temperature and formation of amorphous gel [110]. The powders in this thesis are prepared by the sol-gel method due to this method delivers high purity and good homogeneity. In this method, ethylenediaminetetraacetic acid (EDTA) and citric acid are used as chelating agents to complex the metal cations. The steps of sol-gel route in detail are shown in **Figure 8** as below [111, 112]. The appropriate stoichiometric metal nitrates in aqueous solutions are mixed in a beaker, followed by the addition of proper amount of citric acid and EDTA, and the pH value is adjusted to ~7 by aqueous ammonia. The molar ratio of total metal ions: citric acid: EDTA was

1:2:1. Then the solutions are stirred and heated to 150 ºC, until the water and ammonia evaporate and a gel is formed. Afterward, the gel is ignited to flame to get the precursor. The precursor is ground and calcined at 950 ºC for 10 h with a heating/cooling rate of 2 ºC/min.
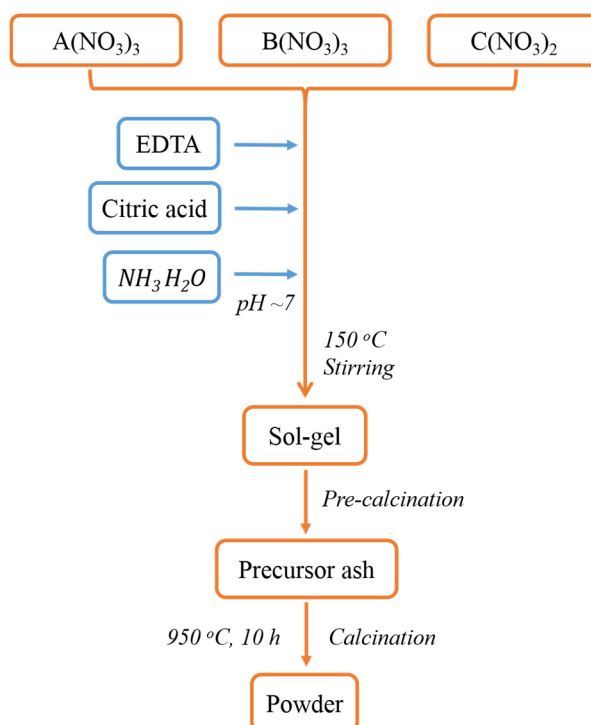


**Figure 8**. Schematic flow chart of the sol-gel method.

## 1.4.2 Disk

The dense disk membranes used in this thesis are prepared by uniaxial pressing process following by sintering at high temperature. The obtained powder after sol-gel process is put into a mold with 18 mm diameter, then pressed with around 30 kN for ten minutes. Then the green pellets are sintered in air at sintering temperature for 10 h with 2 ºC/min heating/cooling rate. The diameter of the final ceramic pellets are reduced during the sintering process. The density and microstructure are controlled by the sintering temperature and holding time and the sintering temperature is largely different for different composition materials. The density of the sintered disks are measured by the Archimedes method using distilled water. Sintered ceramics with a relative density higher than 95% could be selected as membranes for the gas separation tests. The disk membranes are polished to the desired thickness using sandpaper and then washed with ethanol to remove the dust.

## 1.4.3 Hollow-fiber membranes

Compared with the disk membranes which are fabricated by a simple conventional pressing method, hollow-fiber membranes possess high effective area to volume ratio,

relatively thin thickness, and they are easy to assemble with a reactor module [14, 113]. Therefore, the dense ceramic membranes in hollow-fiber geometry exhibit large gas separation flux. The ceramic hollow-fiber membranes used in this thesis are fabricated by wet-spinning/sintering method [109, 114]. To spin the hollow-fiber membranes, the prepared powders are ball-milled for 24 h and then dried using a spray dryer with a nozzle of 1 μm. At the same time, spinning solutions which are composed of polyethersulfone (PESf, A-300) with the additive polyvinyl pyrrolidone (PVP, K30) and 1-methyl-2-pyrrolidinone (NMP) solvent are prepared in 250-ml wide-neck bottles. Then the obtained powders are gradually added to the organic solution and the mixtures are stirred for 48 h to ensure that the powders are dispersed uniformly in the polymer solution. The hollow-fiber precursors are spined by a spinneret (orifice diameter and inner diameter of 1.5 and 1.0 mm, respectively) in deionized water bath at room temperature and stored for 24 h to complete the solidification process. Afterward, the hollow-fiber precursors are sintered at high temperature for several hours at an air flow rate of 60 mL/min to remove the polymers and obtain gastight membranes.

## 1.5 Measurements of dense ceramic separation membranes

### 1.5.1 Oxygen permeation test

Oxygen permeation flux and long-term stability are the two key factors for industrial applications for dense oxygen-permeable membranes. The oxygen permeation fluxes through the membranes are investigated using a home-made high-temperature oxygen permeation cell, as described in **Figure 9** [109, 114, 115]. This test apparatus consisted of a gas supply system with gas mass flow controllers (MFCs), the membrane reactor module with high-temperature furnace, and online gas chromatograph (GC) coupled with a soap-bubble flow meter. The disk membranes are sealed in a corundum tube with a commercial ceramic sealant. Air or a mixture of nitrogen and oxygen or $CO_2$-containing gas is fed to the feed side of the membrane reactor whereas helium is applied as sweep gas to collect the permeated oxygen. Gases flow rates are calibrated by a soap bubble flow meter. The composition of the effluent gas is measured by an online GC with a thermal conductivity detector. The leakage of the oxygen due to the imperfect sealing is subtracted in the calculation of oxygen permeation flux which are less than 5% during all the experiments. Assuming that leakage of nitrogen and oxygen are in accordance with Knudsen diffusion, the fluxes of leaked $N_2$ and $O_2$ are related by

$$J_{N_2}^{Leak} : J_{O_2}^{Leak} = \sqrt{\frac{32}{28} \times \frac{0.8}{0.2}} = 4.28$$

$$J_{O_2} = \left[ C_{O_2} - \frac{C_{N_2}}{4.28} \right] \frac{F}{S}$$

where $C_{O_2}$ and $C_{N_2}$ are the oxygen and nitrogen concentrations calculated from the GC results, F is the flow rate of the effluent, and S is the membrane active area.
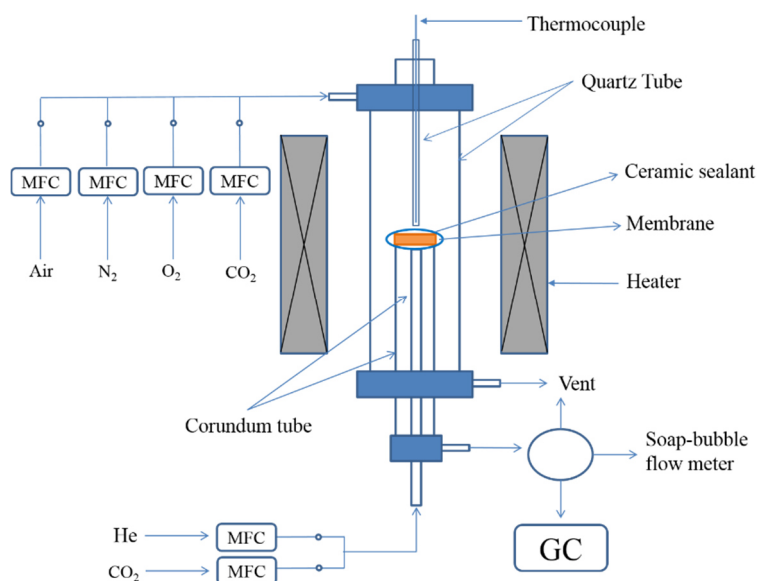
**Figure 9**. Schematic diagram of the oxygen permeation test apparatus.

## 1.5.2 Hydrogen permeation test

The hydrogen permeation performance of the dense ceramic hydrogen-separating membranes are measured in a home-made apparatus, as shown in **Figure 10** [109]. A mixture of hydrogen and helium is fed into the feed side and different hydrogen concentration gases can be obtained by adjusting the flow rates of the hydrogen and helium. Argon is applied as sweep gas. The composition of the permeated gas is detected by an online-coupled GC (argon is used as reference gas). The leakage from imperfect sealing is less than 5% during all measurements.
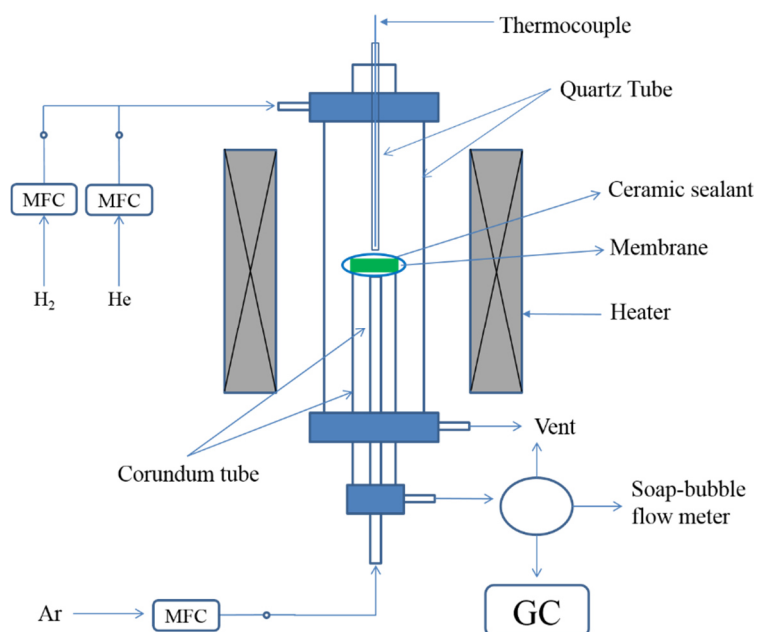


**Figure 10**. The hydrogen permeation apparatus for the disk dense ceramic membranes.

Assuming that leakage of hydrogen and helium are in accordance with Knudsen diffusion, the fluxes of leaked hydrogen and helium are related by $J_{He}^{Leak}:J_{H_2}^{Leak} = \sqrt{\frac{2}{2}} \times \frac{C_{He_{feed}}}{C_{H_2{_{feed}}}}$,

$$J_{H_2} = \left[ C_{H_2} - \frac{C_{He}}{\frac{C_{He_{feed}}}{C_{H_2{_{feed}}}}} \right] \frac{F}{S}$$

where $C_{H_2}$ and $C_{He}$ are the hydrogen and helium concentrations calculated from the GC results, $C_{H_2{_{feed}}}$ and $C_{He_{feed}}$ are the concentrations of hydrogen and helium in the feed gas, F is the flow rate of the effluent, and S is the membrane active area.

## 1.5.3 Catalysis in ceramic membrane reactor

Membrane reactors are one of the promising approaches to intensify the industrial chemical process [11, 23]. A dense ceramic separation membrane could combine a chemical reaction with an *in-situ* separation unit. In the coupled membrane reactors, the chemical reaction performance will be improved, as the continuously selectively removed product ($H_2$ or $O_2$) could break the limitation of thermodynamic equilibrium and the reaction rate can be maintained with a high conversion of reactant. The dense ceramic membrane reactors can be classified by their function into extractor and distributor, respectively, as shown in **Figure 11** [11].
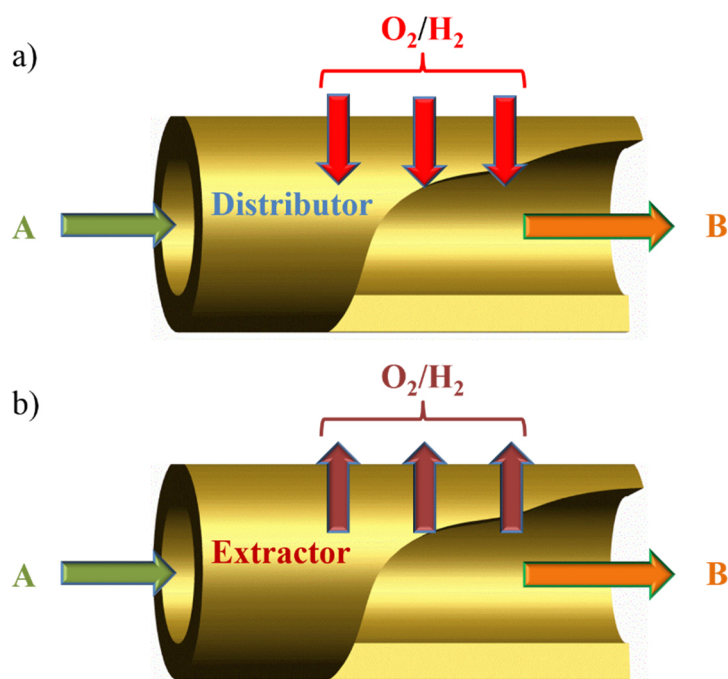


**Figure 11**. Different function dense ceramic membrane reactors, a) distributor; b) extractor.

In a distributor membrane reactor, as shown in **Figure 11a**, oxygen or hydrogen is supplied by the dense ceramic membrane to the reaction system, such as partial oxidation of methane (POM) and oxidative couple of methane (OCM) [24, 33]. Compared with the direct oxygen supplying of air or pure oxygen, this method could provide unrivaled purity and high activity oxygen or hydrogen in an economic, environmental friendly way. Moreover, the dense ceramic membranes can also be applied as an extractor to selectively remove the produced oxygen or hydrogen to overcome the thermodynamic limitation as shown in **Figure 11b**. In the thermal water splitting, $N_xO$ decomposition reactions, and nonoxidative methane dehydroaromatization (MDA), oxygen- or hydrogen-permeable membranes play an important role to increase the reactant's (e.g. $H_2O/ N_xO$) conversion and products yield [26, 28, 29, 56].

# 1.6 Bibliography

[1] R.W. Baker, Future directions of membrane gas separation technology, *Industrial and Engineering Chemistry Research*, 41 (2002) 1393-1411.

[2] R.W. Baker, Membrane Technology and Applications, Wiley, 2012.

[3] T. Harlacher, M. Wessling, Gas-gas separation by membranes, in: Progress in Filtration and Separation, Elsevier, 2014.

[4] R.D. Noble, S.A. Stern, Membrane separations technology: principles and applications, Elsevier, 1995.

[5] P. Pandey, R.S. Chauhan, Membranes for gas separation, *Progress in Polymer Science*, 26 (2001) 853-893.

[6] A.W. Thornton, J.M. Hill, A.J. Hill, Modelling Gas separation in porous membranes, in: Membrane Gas Separation, Wiley, 2010.

[7] M.L. Fontaine, Y. Larring, T. Norby, T. Grande, R. Bredesen, Dense ceramic membranes based on ion conducting oxides, *Annales de Chimie: Science des Materiaux*, 32 (2007) 197-212.

[8] A. Iulianelli, S. Liguori, T. Longo, A. Basile, Inorganic membrane and membrane reactor technologies for hydrogen production, in:  Hydrogen Production: Prospects and Processes, Nova Science Pub Inc, 2012.

[9] J. Kniep, J.Y.S. Lin, Oxygen-and hydrogen-permeable dense ceramic membranes, in: Solid State Electrochemistry II: Electrodes, Interfaces and Ceramic Membranes, Wiley, 2011.

[10] J. Sunarso, S. Baumann, J.M. Serra, W.A. Meulenberg, S. Liu, Y.S. Lin, J.C. Diniz da Costa, Mixed ionic-electronic conducting (MIEC) ceramic-based membranes for oxygen separation, *Journal of Membrane Science*, 320 (2008) 13-41.

[11] Y. Wei, W. Yang, J. Caro, H. Wang, Dense ceramic oxygen permeable membranes and catalytic membrane reactors, *Chemical Engineering Journal*, 220 (2013) 185-203.

[12] A. Leo, S. Liu, J.C.D. da Costa, Development of mixed conducting membranes for clean coal energy delivery, *International Journal of Greenhouse Gas Control*, 3 (2009) 357-367.

[13] E. Fontananova, E. Drioli, Membrane reactors: advanced systems for intensified chemical processes, *Chemie Ingenieur Technik*, 86 (2014) 2039-2050.

[14] Z. Tao, L. Yan, J. Qiao, B. Wang, L. Zhang, J. Zhang, A review of advanced proton-conducting materials for hydrogen separation, *Progress in Materials Science*, 74 (2015) 1-50.

[15] H.J. Bouwmeester, A.J. Burggraaf, Dense ceramic membranes for oxygen separation, The CRC handbook of solid state electrochemistry, CRC Press, 1997.

[16] F. Akin, J.Y. Lin, Oxygen permeation through oxygen ionic or mixed-conducting ceramic membranes with chemical reactions, *Journal of membrane science*, 231 (2004) 133-146.

[17] C. Wagner, Equations for transport in solid oxides and sulfides of transition metals, *Progress in solid state chemistry*, 10 (1975) 3-16.

[18] D. Hersh, J. Abrardo, Air separation plant design, *Cryogenics*, 17 (1977) 383-390.

[19] R. Thorogood, Developments in air separation, *Gas separation & purification*, 5 (1991) 83-94.

[20] P.-M. Geffroy, M. Reichmann, T. Chartier, J.-M. Bassat, J.-C. Grenier, Evaluating oxygen diffusion, surface exchange and oxygen semi-permeation in $Ln_2NiO_{4+\delta}$ membranes (Ln= La, Pr and Nd), *Journal of Membrane Science*, 451 (2014) 234-242.

[21] F. Kröger, H. Vink, Relations between the concentrations of imperfections in solids, *Journal of Physics and Chemistry of Solids*, 5 (1958) 208-223.

[22] Z. Cao, H. Jiang, H. Luo, S. Baumann, W.A. Meulenberg, H. Voss, J. Caro, Simultaneous overcome of the equilibrium limitations in BSCF oxygen-permeable membrane reactors: Water splitting and methane coupling, *Catalysis Today*, 193 (2012) 2-7.

[23] O. Czuprat, H. Jiang, Catalytic membrane reactors-chemical upgrading and pollution control, *Chemie-Ingenieur-Technik*, 83 (2011) 2219-2228.

[24] H. Jiang, Z. Cao, S. Schirrmeister, T. Schiestel, J. Caro, A coupling strategy to produce hydrogen and ethylene in a membrane reactor, *Angewandte Chemie International Edition*, 49 (2010) 5656-5660.

[25] H. Jiang, F. Liang, O. Czuprat, K. Efimov, A. Feldhoff, S. Schirrmeister, T. Schiestel, H. Wang, J. Caro, Hydrogen production by water dissociation in surface-modified $BaCo_xFe_yZr_{1-x-y}O_{3-\delta}$ hollow-fiber membrane reactor with improved oxygen permeation, *Chemistry - A European Journal*, 16 (2010) 7898-7903.

[26] H. Jiang, H. Wang, F. Liang, S. Werth, S. Schirrmeister, T. Schiestel, J. Caro, Improved water dissociation and nitrous oxide decomposition by in situ oxygen removal in perovskite catalytic membrane reactor, *Catalysis Today*, 156 (2010) 187-190.

[27] H. Jiang, H. Wang, S. Werth, T. Schiestel, J. Caro, Simultaneous production of hydrogen and synthesis gas by combining water splitting with partial oxidation of methane in a hollow-fiber membrane reactor, *Angewandte Chemie International Edition*, 47 (2008) 9341-9344.

[28] H. Jiang, L. Xing, O. Czuprat, H. Wang, S. Schirrnieister, T. Schiestel, J. Caro, Highly effective NO decomposition by in situ removal of inhibitor oxygen using an oxygen transporting membrane, *Chemical Communications*, (2009) 6738-6740.

[29] W. Jin, C. Zhang, X. Chang, Y. Fan, W. Xing, N. Xu, Efficient catalytic decomposition of $CO_2$ to CO and $O_2$ over Pd/mixed-conducting oxide catalyst in an oxygen-permeable membrane reactor, *Environmental Science and Technology*, 42 (2008) 3064-3068.

[30] C. Zhang, W. Jin, C. Yang, N. Xu, Decomposition of $CO_2$ coupled with POM in a thin tubular

oxygen-permeable membrane reactor, *Catalysis Today*, 148 (2009) 298-302.

[31] Z. Cao, H. Jiang, H. Luo, S. Baumann, W.A. Meulenberg, J. Assmann, L. Mleczko, Y. Liu, J. Caro, Natural gas to fuels and chemicals: Improved methane aromatization in an oxygen-permeable membrane reactor, *Angewandte Chemie International Edition*, 52 (2013) 13794-13797.

[32] Z. Cao, H. Jiang, H. Luo, S. Baumann, W.A. Meulenberg, H. Voss, J. Caro, An efficient oxygen activation route for improved ammonia oxidation through an oxygen-permeable catalytic membrane, *ChemCatChem*, 6 (2014) 1190-1194.

[33] Y. Wei, Q. Liao, Z. Li, H. Wang, A. Feldhoff, J. Caro, Partial oxidation of methane in hollow-fiber membrane reactors based on alkaline-earth metal-free $CO_2$-tolerant oxide, *AIChE Journal*, 60 (2014) 3587-3595.

[34] Y. Wei, Y. Wang, J. Tang, Z. Li, H. Wang, Oxy-fuel combustion for $CO_2$ capture using a $CO_2$-tolerant oxygen transporting membrane, *AIChE Journal*, 59 (2013) 3856-3862.

[35] Y.Y. Wei, L. Huang, J. Tang, L.Y. Zhou, Z. Li, H.H. Wang, Syngas production in a novel perovskite membrane reactor with co-feed of $CO_2$, *Chinese Chemical Letters*, 22 (2011) 1492-1496.

[36] V.A. Goltsov, T.N. Veziroglu, From hydrogen economy to hydrogen civilization, *International Journal of Hydrogen Energy*, 26 (2001) 909-915.

[37] K. McHugh, Hydrogen production methods, Hydrogen Production Methods, MPR Associates Inc., 2005.

[38] R.D. Cortright, R.R. Davda, J.A. Dumesic, Hydrogen from catalytic reforming of biomass-derived hydrocarbons in liquid water, *Nature*, 418 (2002) 964-967.

[39] R.W. Spillman, Economics of gas separation membranes, *Chemical engineering progress*, 85 (1989) 41-62.

[40] F. Gallucci, E. Fernandez, P. Corengia, M. van Sint Annaland, Recent advances on membranes and membrane reactors for hydrogen production, *Chemical Engineering Science*, 92 (2013) 40-66.

[41] P. Kamakoti, B.D. Morreale, M.V. Ciocco, B.H. Howard, R.P. Killmeyer, A.V. Cugini, D.S. Sholl, Prediction of hydrogen flux through sulfur-tolerant binary alloy membranes, *Science*, 307 (2005) 569-573.

[42] P.P. Mardilovich, Y. She, Y.H. Ma, M.H. Rei, Defect-free palladium membranes on porous stainless-steel support, *AIChE Journal*, 44 (1998) 310-322.

[43] C.Y. Park, T.H. Lee, S.E. Dorris, U.B. Balachandran, Palladium based film-type cermet membranes for hydrogen separation, *Journal of Materials Chemistry*, 22 (2012) 4904-4909.

[44] S. Uemiya, State-of-the-art of supported metal membranes for gas separation, *Separation and Purification Methods*, 28 (1999) 51-85.

[45] C.M. Gore, J.O. White, E.D. Wachsman, V. Thangadurai, Effect of composition and microstructure on electrical properties and $CO_2$ stability of donor-doped, proton conducting $BaCe_{1-(x+y)}Zr_xNb_yO_3$, *Journal of Materials Chemistry A*, 2 (2014) 2363-2373.

[46] A. Magrasó, R. Haugsrud, Effects of the La/W ratio and doping on the structure, defect structure, stability and functional properties of proton-conducting lanthanum tungstate $La_{28-x}W_{4+x}O_{54+\delta}$. A review, *Journal of Materials Chemistry A*, 2 (2014) 12630-12641.

[47] A. Magrasó, C.H. Hervoches, I. Ahmed, S. Hull, J. Nordström, A.W.B. Skilbred, R. Haugsrud, In situ high temperature powder neutron diffraction study of undoped and Ca-doped $La_{28-x}W_{4+x}O_{54+3x/2}$ (x = 0.85), *Journal of Materials Chemistry A*, 1 (2013) 3774-3782.

[48] M. Amsif, A. Magrasó, D. Marrero-López, J.C. Ruiz-Morales, J. Canales-Vázquez, P. Núñez, Mo-Substituted lanthanum tungstate $La_{28-y}W_{4+y}O_{54+\delta}$: A competitive mixed electron-proton conductor for gas separation membrane applications, *Chemistry of Materials*, 24 (2012) 3868-3877.

[49] S. Escolastico, J. Seeger, S. Roitsch, M. Ivanova, W.A. Meulenberg, J.M. Serra, Enhanced $H_2$ separation through mixed proton-electron conducting membranes based on $La_{5.5}W_{0.8}M_{0.2}O_{11.25-\delta}$, *ChemSusChem*, 6 (2013) 1523-1532.

[50] S. Escolástico, C. Solís, C. Kjølseth, J.M. Serra, Outstanding hydrogen permeation through $CO_2$-stable dual-phase ceramic membranes, *Energy and Environmental Science*, 7 (2014) 3736-3746.

[51] S. Escolástico, S. Somacescu, J.M. Serra, Solid state transport and hydrogen permeation in the system $Nd_{5.5}W_{1-x}Re_xO_{11.25-\delta}$, *Chemistry of Materials*, 26 (2014) 982-992.

[52] G. Marnellos, M. Stoukides, Ammonia synthesis at atmospheric pressure, *Science*, 282 (1998) 98-100.

[53] J. Seeger, M.E. Ivanova, W.A. Meulenberg, D. Sebold, D. Stöver, T. Scherb, G. Schumacher, S. Escolástico, C. Solís, J.M. Serra, Synthesis and characterization of nonsubstituted and substituted proton-conducting $La_{6-x}WO_{12-y}$, *Inorganic Chemistry*, 52 (2013) 10375-10386.

[54] D. van Holt, E. Forster, M.E. Ivanova, W.A. Meulenberg, M. Müller, S. Baumann, R. Vaßen, Ceramic materials for $H_2$ transport membranes applicable for gas separation under coal-gasification-related conditions, *Journal of the European Ceramic Society*, 34 (2014) 2381-2389.

[55] J.R. Rostrup-Nielsen, Conversion of hydrocarbons and alcohols for fuel cells, *Physical Chemistry Chemical Physics*, 3 (2001) 283-288.

[56] J. Xue, Y. Chen, Y. Wei, A. Feldhoff, H. Wang, J. Caro, Gas to liquids: natural gas conversion to aromatic fuels and chemicals in a hydrogen-permeable ceramic hollow-fiber membrane reactor, *ACS Catalysis*, 6 (2016) 2448-2451.

[57] G. Rose, Mineralogisch-geognostische Reise nach dem Ural, dem Altai und dem Kaspischen Meere, Рипол Классик, 2012.

[58] Y. Teraoka, H.-M. Zhang, S. Furukawa, N. Yamazoe, Oxygen permeation through perovskite-type oxides, *Chemistry Letters*, 14 (1985) 1743-1746.

[59] H. Koster, Powder diffraction of the cubic perovskite $Ba_{0.5}Sr_{0.5}Co_{0.8}Fe_{0.2}O_{3-\delta}$, *Powder Diffraction*, 18 (2003) 56-59.

[60] V. Goldschmidt, Krystallbau und chemische Zusammensetzung, *Berichte der deutschen chemischen Gesellschaft*, 60 (1927) 1263-1296.

[61] V. Goldschmidt, Geochemische Verteilungsgesetze und kosmische Häufigkeit der Elemente, *Naturwissenschaften*, 18 (1930) 999-1013.

[62] K. Zhang, J. Sunarso, Z. Shao, W. Zhou, C. Sun, S. Wang, S. Liu, Research progress and materials selection guidelines on mixed conducting perovskite-type ceramic membranes for oxygen production, *RSC Advances*, 1 (2011) 1661-1676.

[63] W. Zhou, J. Sunarso, M. Zhao, F. Liang, T. Klande, A. Feldhoff, A highly active perovskite electrode for the oxygen reduction reaction below 600 ºC, *Angewandte Chemie International Edition*, 52 (2013) 14036-14040.

[64] A.F. Sammells, R.L. Cook, J.H. White, J.J. Osborne, R.C. MacDuff, Rational selection of advanced solid electrolytes for intermediate temperature fuel cells, *Solid State Ionics*, 52 (1992) 111-123.

[65] J. Richter, P. Holtappels, T. Graule, T. Nakamura, L.J. Gauckler, Materials design for perovskite

SOFC cathodes, *Monatshefte für Chemie-Chemical Monthly*, 140 (2009) 985-999.

[66] L. Qiu, T.H. Lee, L.M. Liu, Y.L. Yang, A.J. Jacobson, Oxygen permeation studies of $SrCo_{0.8}Fe_{0.2}O_{3-\delta}$, *Solid State Ionics*, 76 (1995) 321-329.

[67] Z. Shao, W. Yang, Y. Cong, H. Dong, J. Tong, G. Xiong, Investigation of the permeation behavior and stability of a $Ba_{0.5}Sr_{0.5}Co_{0.8}Fe_{0.2}O_{(3-\delta)}$ oxygen membrane, *Journal of Membrane Science*, 172 (2000) 177-188.

[68] M. Arnold, H. Wang, A. Feldhoff, Influence of $CO_2$ on the oxygen permeation performance and the microstructure of perovskite-type $(Ba_{0.5}Sr_{0.5})(Co_{0.8}Fe_{0.2})O_{3-\delta}$ membranes, *Journal of Membrane Science*, 293 (2007) 44-52.

[69] J. Yi, M. Schroeder, T. Weirich, J. Mayer, Behavior of $Ba(Co, Fe, Nb)O_{3-\delta}$ perovskite in $CO_2$-containing atmospheres: Degradation mechanism and materials design, *Chemistry of Materials*, 22 (2010) 6246-6253.

[70] E. Boehm, J.M. Bassat, M.C. Steil, P. Dordor, F. Mauvy, J.C. Grenier, Oxygen transport properties of $La_2Ni_{1-x}Cu_xO_{4+\delta}$ mixed conducting oxides, *Solid State Sciences*, 5 (2003) 973-981.

[71] A.A. Yaremchenko, V.V. Kharton, M.V. Patrakeev, J.R. Frade, p-Type electronic conductivity, oxygen permeability and stability of $La_2Ni_{0.9}Co_{0.1}O_{4+\delta}$, *Journal of Materials Chemistry*, 13 (2003) 1136-1144.

[72] M. Yashima, M. Enoki, T. Wakita, R. Ali, Y. Matsushita, F. Izumi, T. Ishihara, Structural disorder and diffusional pathway of oxide ions in a doped $Pr_2NiO_4$-based mixed conductor, *Journal of the American Chemical Society*, 130 (2008) 2762-2763.

[73] V. Kharton, A. Viskup, E. Naumovich, F.B. Marques, Oxygen ion transport in $La_2NiO_4$-based ceramics, *Journal of Materials Chemistry*, 9 (1999) 2623-2629.

[74] V.V. Kharton, A.A. Yaremchenko, A.L. Shaula, M.V. Patrakeev, E.N. Naumovich, D.I. Logvinovich, J.R. Frade, F.M.B. Marques, Transport properties and stability of Ni-containing mixed conductors with perovskite- and $K_2NiF_4$-type structure, *Journal of Solid State Chemistry*, 177 (2004) 26-37.

[75] A.R. Cleave, J.A. Kilner, S.J. Skinner, S.T. Murphy, R.W. Grimes, Atomistic computer simulation of oxygen ion conduction mechanisms in $La_2NiO_4$, *Solid State Ionics*, 179 (2008) 823-826.

[76] J. Xue, Q. Liao, W. Chen, H.J. Bouwmeester, H. Wang, A. Feldhoff, A new $CO_2$-resistant Ruddlesden-Popper oxide with superior oxygen transport: A-site deficient $(Pr_{0.9}La_{0.1})_{1.9}(Ni_{0.74}Cu_{0.21}Ga_{0.05})O_{4+\delta}$, *Journal of Materials Chemistry A*, 3 (2015) 19107-19114.

[77] M. Yashima, H. Yamada, S. Nuansaeng, T. Ishihara, Role of $Ga^{3+}$ and $Cu^{2+}$ in the high interstitial oxide-ion diffusivity of $Pr_2NiO_4$-based oxides: design concept of interstitial ion conductors through the higher-valence $d^{10}$ dopant and Jahn-Teller effect, *Chemistry of Materials*, 24 (2012) 4100-4113.

[78] J.M. Bassat, P. Odier, A. Villesuzanne, C. Marin, M. Pouchard, Anisotropic ionic transport properties in $La_2NiO_{4+\delta}$ single crystals, *Solid State Ionics*, 167 (2004) 341-347.

[79] L. Minervini, R.W. Grimes, J.A. Kilner, K.E. Sickafus, Oxygen migration in $La_2NiO_{4+\delta}$, *Journal of Materials Chemistry*, 10 (2000) 2349-2354.

[80] A. Chroneos, D. Parfitt, J.A. Kilner, R.W. Grimes, Anisotropic oxygen diffusion in tetragonal $La_2NiO_{4+\delta}$: molecular dynamics calculations, *Journal of Materials Chemistry*, 20 (2010) 266.

[81] J. Tang, Y. Wei, L. Zhou, Z. Li, H. Wang, Oxygen permeation through a $CO_2$-tolerant mixed conducting oxide $(Pr_{0.9}La_{0.1})_2(Ni_{0.74}Cu_{0.21}Ga_{0.05})O_{4+\delta}$, *AIChE Journal*, 58 (2012) 2473-2478.

[82] H. Iwahara, T. Esaka, H. Uchida, N. Maeda, Proton conduction in sintered oxides and its application

to steam electrolysis for hydrogen production, *Solid State Ionics*, 3-4 (1981) 359-363.

[83] H. Uchida, N. Maeda, H. Iwahara, Relation between proton and hole conduction in SrCeO$_3$-based solid electrolytes under water-containing atmospheres at high temperatures, *Solid State Ionics*, 11 (1983) 117-124.

[84] I. Kosacki, H.U. Anderson, The structure and electrical properties of SrCe$_{0.95}$Yb$_{0.05}$O$_3$ thin film protonic conductors, *Solid State Ionics*, 97 (1997) 429-436.

[85] K.D. Kreuer, Aspects of the formation and mobility of protonic charge carriers and the stability of perovskite-type oxides, *Solid State Ionics*, 125 (1999) 285-302.

[86] Y. Liu, K. Li, Preparation of SrCe$_{0.95}$Yb$_{0.05}$O$_{3-\alpha}$ hollow fibre membranes: Study on sintering processes, *Journal of Membrane Science*, 259 (2005) 47-54.

[87] T. Schober, H.G. Bohn, Water vapor solubility and electrochemical characterization of the high temperature proton conductor BaZr$_{0.9}$Y$_{0.1}$O$_{2.95}$, *Solid State Ionics*, 127 (2000) 351-360.

[88] H. Uchida, H. Yoshikawa, H. Iwahara, Dissolution of water vapor (or hydrogen) and proton conduction in SrCeO3-based oxides at high temperature, *Solid State Ionics*, 35 (1989) 229-234.

[89] T. Yajima, H. Iwahara, H. Uchida, Protonic and oxide ionic conduction in BaCeO$_3$-based ceramics - effect of partial substitution for Ba in BaCe$_{0.9}$O$_{3-\alpha}$ with Ca, *Solid State Ionics*, 47 (1991) 117-124.

[90] T. Yajima, H. Kazeoka, T. Yogo, H. Iwahara, Proton conduction in sintered oxides based on CaZrO$_3$, *Solid State Ionics*, 47 (1991) 271-275.

[91] T. Yajima, H. Suzuki, T. Yogo, H. Iwahara, Protonic conduction in SrZrO$_3$-based oxides, *Solid State Ionics*, 51 (1992) 101-107.

[92] H. Yugami, S. Matsuo, M. Ishigame, Persistent spectral hole-burning of Eu$^{3+}$ and Pr$^{3+}$ in SrZr$_{1-x}$Y$_x$O$_3$ crystals, *Solid State Ionics*, 77 (1995) 195-200.

[93] S. Shin, H.H. Huang, M. Ishigame, H. Iwahara, Protonic conduction in the single crystals of SrZrO$_3$ and SrCeO$_3$ doped with Y$_2$O$_3$, *Solid State Ionics*, 40-41 (1990) 910-913.

[94] Y. Wei, J. Xue, W. Fang, Y. Chen, H. Wang, J. Caro, Enhanced stability of Zr-doped Ba(CeTb)O$_{3-\delta}$-Ni cermet membrane for hydrogen separation, *Chemical Communications*, 51 (2015) 11619-11621.

[95] Y. Wei, J. Xue, H. Wang, J. Caro, Hydrogen permeability and stability of BaCe$_{0.85}$Tb$_{0.05}$Zr$_{0.1}$O$_{3-\delta}$ asymmetric membranes, *Journal of Membrane Science*, 488 (2015) 173-181.

[96] E. Fabbri, D. Pergolesi, E. Traversa, Materials challenges toward proton-conducting oxide fuel cells: a critical review, *Chemical Society Reviews*, 39 (2010) 4355-4369.

[97] H. Maekawa, Y. Ukei, K. Morota, N. Kashii, J. Kawamura, T. Yamamura, High temperature proton NMR study of yttrium doped barium cerates, *Solid State Communications*, 130 (2004) 73-77.

[98] B. Merinov, W. Goddard III, Proton diffusion pathways and rates in Y-doped BaZrO$_3$ solid oxide electrolyte from quantum mechanics, *The Journal of Chemical Physics*, 130 (2009) 194707.

[99] M. Saito, K. Hayamizu, T. Okada, Temperature dependence of ion and water transport in perfluorinated ionomer membranes for fuel cells, *The Journal of Physical Chemistry B*, 109 (2005) 3112-3119.

[100] N. Bonanos, Transport properties and conduction mechanism in high-temperature protonic conductors, *Solid State Ionics*, 53 (1992) 967-974.

[101] E.C.C.d. Souza, R. Muccillo, Properties and applications of perovskite proton conductors, *Materials Research*, 13 (2010) 385-394.

[102] S. Escolástico, V.B. Vert, J.M. Serra, Preparation and characterization of nanocrystalline mixed

proton-electronic conducting materials based on the system $Ln_6WO_{12}$, *Chemistry of Materials*, 21 (2009) 3079-3089.

[103] R. Haugsrud, Defects and transport properties in $Ln_6WO_{12}$ (Ln= La, Nd, Gd, Er), *Solid State Ionics*, 178 (2007) 555-560.

[104] A. Magrasó, C. Frontera, D. Marrero-López, P. Núñez, New crystal structure and characterization of lanthanum tungstate "$La_6WO_{12}$" prepared by freeze-drying synthesis, *Dalton Transactions*, (2009) 10273-10283.

[105] A. Magrasó, J.M. Polfus, C. Frontera, J. Canales-Vázquez, L.-E. Kalland, C.H. Hervoches, S. Erdal, R. Hancke, M.S. Islam, T. Norby, Complete structural model for lanthanum tungstate: A chemically stable high temperature proton conductor by means of intrinsic defects, *Journal of Materials Chemistry*, 22 (2012) 1762-1764.

[106] T. Shimura, S. Fujimoto, H. Iwahara, Proton conduction in non-perovskite-type oxides at elevated temperatures, *Solid State Ionics*, 143 (2001) 117-123.

[107] C. Solís, S. Escolastico, R. Haugsrud, J.M. Serra, $La_{5.5}WO_{12-\delta}$ characterization of transport properties under oxidizing conditions: A conductivity relaxation study, *Journal of Physical Chemistry C*, 115 (2011) 11124-11131.

[108] M. Yoshimura, A. Rouanet, F. Sibieude, Chacterization and high-temperature phase relations of $3La_2O_3 \cdot WO_3$ and $5La_2O_3 \cdot 2WO_3$, *High Temperatures-High Pressures*, 7 (1975) 227-234.

[109] Y. Chen, Q. Liao, Z. Li, H. Wang, Y. Wei, A. Feldhoff, J. Caro, A $CO_2$-stable hollow-fiber membrane with high hydrogen permeation flux, *AIChE Journal*, 61 (2015) 1997-2007.

[110] A. Feldhoff, M. Arnold, J. Martynczuk, T.M. Gesing, H. Wang, The sol-gel synthesis of perovskites by an EDTA/citrate complexing method involves nanoscale solid state reactions, *Solid State Sciences*, 10 (2008) 689-701.

[111] J. Xue, Q. Liao, Y. Wei, Z. Li, H. Wang, A $CO_2$-tolerance oxygen permeable $60Ce_{0.9}Gd_{0.1}O_{2-\delta}$-$40Ba_{0.5}Sr_{0.5}Co_{0.8}Fe_{0.2}O_{3-\delta}$ dual phase membrane, *Journal of Membrane Science*, 443 (2013) 124-130.

[112] J. Xue, A. Schulz, H. Wang, A. Feldhoff, The phase stability of the Ruddlesden-Popper type oxide $(Pr_{0.9}La_{0.1})_{2.0}Ni_{0.74}Cu_{0.21}Ga_{0.05}O_{4+\delta}$ in an oxidizing environment, *Journal of Membrane Science*, 497 (2016) 357-364.

[113] Y. Wei, H. Liu, J. Xue, Z. Li, H. Wang, Preparation and oxygen permeation of U-shaped perovskite hollow-fiber membranes, *AIChE Journal*, 57 (2011) 975-984.

[114] Y. Wei, J. Tang, L. Zhou, Z. Li, H. Wang, Oxygen permeation through U-shaped $K_2NiF_4$-type oxide hollow-fiber membranes, *Industrial & Engineering Chemistry Research*, 50 (2011) 12727-12734.

[115] H. Luo, Y. Wei, H. Jiang, W. Yuan, Y. Lv, J. Caro, H. Wang, Performance of a ceramic membrane reactor with high oxygen flux Ta-containing perovskite for the partial oxidation of methane to syngas, *Journal of Membrane Science*, 350 (2010) 154-160.

# Chapter 2
# Dense ceramic oxygen-separating membranes
## 2.1 Summary

The dense ceramic oxygen-separating membranes used in practical applications should not only possess good oxygen permeability, but also good chemical stability especially under the $CO_2$-containing atmosphere and oxidizing environment. However, the competitive perovskite materials contain alkaline-earth metals so that their chemical stability is poor especially in $CO_2$-containing atmosphere. The alkaline-earth free Ruddlesden-Popper-type oxide $(Pr_{0.9}La_{0.1})_{2.0}Ni_{0.74}Cu_{0.21}Ga_{0.05}O_{4+\delta}$ $((PL)_{2.0}NCG)$ possesses good chemical stability under $CO_2$-containing atmosphere, while its permeation flux is low and it demonstrates a reversible phase decomposition at intermediate temperature.

In section 2.2, *in-situ* X-ray powder diffraction was used to estimate the boundary conditions for the oxidative decomposition of Ruddlesden-Popper-type $(PL)_{2.0}NCG$ oxide. The observations help to construct an Ellingham diagram, which shows in a simple plot the oxygen chemical potential over temperature above a mixture of oxides as well as for the atmosphere. This kind of diagram is expected to have great impact as it easily allows estimate the conditions for the realistic operation of the Ruddlesden-Popper-type oxide as an oxygen-transporting membrane or in any other applications. Moreover, two methods are proposed to improve the oxidative stability of RP oxide.

Section 2.3 describes the development of the A-site deficient Ruddlesden-Popper oxide $(Pr_{0.9}La_{0.1})_{1.9}Ni_{0.74}Cu_{0.21}Ga_{0.05}O_{4+\delta}$ $((PL)_{1.9}NCG)$. This material possesses good chemical stability under $CO_2$-containing atmosphere and its oxygen permeation flux is twice higher than that of the cation-stoichiometric parent compound, and it can compete with the perovskites. The remarkable improvement of oxygen permeability is governed by different crystallographic oxygen sublattices being highly involved into the oxygen diffusion mechanism. With this in mind, a new strategy to develop the Ruddlesden-Popper-type oxides for membrane applications is proposes.

In section 2.4, to further improve the oxygen permeability and phase stability of thin Ruddlesden-Popper-type membrane, a catalytic layer was coated on the A-site deficient $(PL)_{1.9}NCG$ membrane surfaces. The sweep-side coated membrane exhibits largely enhanced permeation fluxes and feed-side coated membrane possess better phase stability under the same practice-relevant conditions. The remarkable improvements of permeability and phase stability by surface modification are discussed based on the oxygen surface exchange properties and the oxygen transporting mechanism in detail.

In section 2.5, a metallic Ni interlayer between NiO precipitate and mixed ionic-electronic conducting ceramic oxide after sintering in ambient atmosphere was observed for the first time. No highly reducing atmosphere was needed. Instead the mixed ionic-electronic conducting oxide acted as local oxygen sink. The formation mechanism and the diffusion processes during the internal reduction have been discussed in detail. The phenomenological description of the diffusion processes that take place during the internal reduction process is useful to materials scientists as well as to ceramic membranes engineers as a model for the interpretation of similar morphologies occurring in metal/oxide or oxide/oxide composite systems.

## 2.2 The phase stability of the Ruddlesden-Popper type oxide $(Pr_{0.9}La_{0.1})_{2.0}Ni_{0.74}Cu_{0.21}Ga_{0.05}O_{4+\delta}$ in an oxidizing environment

Jian Xue, Alexander Schulz, Haihui Wang and Armin Feldhoff

# The phase stability of the Ruddlesden-Popper type oxide (Pr$_{0.9}$La$_{0.1}$)$_{2.0}$Ni$_{0.74}$Cu$_{0.21}$Ga$_{0.05}$O$_{4+\delta}$ in an oxidizing environment

CrossMark

Jian Xue [a], Alexander Schulz [a], Haihui Wang [b,c], Armin Feldhoff [a,*]

[a] *Institute of Physical Chemistry and Electrochemistry, Leibniz University Hannover, Callinstrasse 3A, D-30167 Hannover, Germany*
[b] *School of Chemistry & Chemical Engineering, South China University of Technology, No. 381 Wushan Road, Guangzhou 510640, China*
[c] *School of Chemical Engineering, The University of Adelaide, Adelaide, SA 5005, Australia*

ABSTRACT

The Ruddlesden-Popper type oxide (Pr$_{0.9}$La$_{0.1}$)$_{2.0}$Ni$_{0.74}$Cu$_{0.21}$Ga$_{0.05}$O$_{4+\delta}$ ((PL)$_{2.0}$NCG) is important for oxygen separating membranes and intermediate temperature solid-oxide fuel cell (SOFC) cathodes if the high chemical stability of CO$_2$ is required. This oxide exhibits good phase stability in the air at high temperatures, whereas at intermediate temperatures it demonstrates a reversible decomposition into Pr$_4$Ni$_3$O$_{10-\delta}$ (a higher member of the Ruddlesden-Popper series) and praseodymium oxide phases, which are barriers to the oxygen transport. The phase decomposition conditions of (PL)$_{2.0}$NCG, as a function of temperature and oxygen pressure, have been examined. The defined phase stability window of temperature and oxygen partial pressure for (PL)$_{2.0}$NCG can be the instruction for practical applications. The influence of calcination temperature and A-site deficiency on the material's phase stability are discussed to guide the development of Ruddlesden-Popper type materials with improved stability.

© 2015 Elsevier B.V. All rights reserved.

## 1. Introduction

Mixed ionic and electronic conductors (MIECs) are critical for gas separation membranes, oxygen sensors and intermediate temperature solid-oxide fuel cell (SOFC) cathodes [1,2]. Previous studies of MIECs in these applications have examined perovskite-type materials such as SrCo$_{0.8}$Fe$_{0.2}$O$_{3-\delta}$ and Ba$_{0.5}$Sr$_{0.5}$Co$_{0.8}$Fe$_{0.2}$O$_{3-\delta}$. These materials demonstrate excellent oxygen transport properties [3,4]. Although these oxides display high transport performance, these materials exhibit high thermal expansion coefficients and low chemical stability especially in a CO$_2$-containing atmosphere [5,6].

These limitations have fueled a search for alternative materials within the perovskite-related Ruddlesden-Popper (RP) A$_{n+1}$B$_n$O$_{3n+1}$ materials, and in particular, those with the A$_2$BO$_4$ structure (the first member of the RP oxides with $n=1$) [7,8]. The A$_2$BO$_4$ structure consists of offset perovskite layers interspersed with AO rock-salt layers. Oxygen ionic conduction in these compounds may occur through an interstitialcy mechanism [9,10]. Among the A$_2$BO$_{4+\delta}$ series (A=La, Pr, Nd, B=Ni), Pr$_2$NiO$_{4+\delta}$ exhibited the highest oxygen tracer diffusion coefficients, and the Pr$_2$NiO$_4$-based oxides possess a higher oxygen permeability than La$_2$NiO$_4$-based oxides [7,11–13]. Doping of Cu in Pr$_2$NiO$_{4+\delta}$ stabilizes the high-temperature interstitial oxygen disordered

tetragonal structure. The addition of Ga into Pr$_2$(Ni$_{0.75}$Cu$_{0.25}$)O$_{4+\delta}$ increases the oxygen permeability [14]. The doping of La atoms at the Pr site could improve their phase stability at high temperatures and prevent decomposition into Pr$_4$Ni$_3$O$_{10}$- and Pr$_2$O$_3$-based phases [15,16]. Yashima et al. developed the A$_2$BO$_4$-type (Pr$_{0.9}$La$_{0.1}$)$_{2.0}$Ni$_{0.74}$Cu$_{0.21}$Ga$_{0.05}$O$_{4-\delta}$ ((PL)$_{2.0}$NCG), which demonstrated moderate thermal expansion coefficients, good oxygen transport properties and chemical stability in CO$_2$ [17–19].

Despite the advantages of the A$_2$BO$_4$-type (PL)$_{2.0}$NCG, improvements are still required for practical application. It is reported that, in oxidizing atmospheres, the A$_2$BO$_4$-type praseodymium nickelate phase decomposes into the multilayered perovskite Pr$_4$Ni$_3$O$_{10+\delta}$ (a higher member of the RP oxides with $n=3$) and PrO$_{2+\delta'}$ [13,15]. It is necessary to clarify this behavior under various conditions because the decomposition influences the stability and transport properties. This work investigates the phase stability of (PL)$_{2.0}$NCG at the border of stability by using *in-situ* X-ray powder diffraction (XRPD) analysis. The A-site deficient (Pr$_{0.9}$La$_{0.1}$)$_{1.9}$Ni$_{0.74}$Cu$_{0.21}$Ga$_{0.05}$O$_{4+\delta}$ ((PL)$_{1.9}$NCG) material was also studied to determine the influence of A-site deficiency on the stability.

## 2. Experimental

### 2.1. Preparation

Powders of (PL)$_{1.9}$NCG and (PL)$_{2.0}$NCG were prepared by a

* Corresponding author. Fax: ┤ 49 511 762 19121.
*E-mail address:* armin.feldhoff@pci.uni-hannover.de (A. Feldhoff).

combined citrate and ethylene-diamine-tetraacetic-acid (EDTA) method as described previously [20,21]. The powders were uniaxially pressed at 20 MPa to obtain green pellets followed by sintering in air at 1503 K for 10 h. The density of the sintered disks was measured by the Archimedes method using distilled water. Sintered ceramics with a relative density higher than 95% were selected as membranes for the oxygen permeation experiments. The membranes were polished to the desired thickness using 1200 grit-sandpaper and then washed with ethanol.

### 2.2. Phase characterization

The *in-situ* X-ray powder diffraction (XRPD) measurements were performed on a Bruker D8 Advance diffractometer (Bruker AXS GmbH) with a Bragg-Brentano geometry using Cu K$\alpha_{1,2}$ radiation, a secondary Ni-filter and a 1-dimensional LynxEye detector (silicon strip). Temperature depending measurements were performed with a HTK-1200N high-temperature oven chamber (Anton-Paar) under different oxygen partial pressure atmospheres (mixtures of hydrocarbon free synthetic air and $N_2$). The *in-situ* XRPD measurements were performed between 10° and 110° (2$\theta$), with a step size of 0.01°, a time per step of 0.75 s, a total number of 9511 steps, without rotation and in the temperature range of 303–1373 K. The temperature was increased step-wise, with a dwell time of 30 min at each step before data collection. After each treatment, the atmosphere was changed from the oxidizing condition (oxygen-containing gas) to reducing conditions ($N_2$ only) to obtain a pure phase before next test. The microstructure of the disk membrane was examined by secondary electron contrast in a field-emission scanning electron microscope (FE-SEM) (JEOL JSM-6700F) that was operated at 2 kV.

### 2.3. Oxygen permeation experiments

The oxygen flux was investigated in the temperature range of 1073–1173 K with a 0.6 mm thick membrane using a home-made high-temperature oxygen permeation cell, which was described in detail elsewhere [22,23]. A commercial ceramic sealant (Huitian, Hubei, China) was used to seal the disk-shaped membrane onto an alumina tube. Synthetic air was fed (150 ml min$^{-1}$) to the feed side of the membrane, and He gas (30 ml min$^{-1}$) was fed to the sweep side. Gas flow rates were controlled using a mass flow controller (Bronkhorst GmbH) and calibrated with a soap bubble counter. The composition of the effluent was analyzed by on-line coupled gas chromatography (GC, Agilent Technologies, 7890A). The leakage of oxygen, because of imperfect sealing, was subtracted in the calculation of the oxygen flux [22,24]. The contribution of leakage to the apparent oxygen flux was below 5% in all cases. Assuming that leakage of nitrogen and oxygen follows Knudsen diffusion, the fluxes of leaked $N_2$ and $O_2$ are related by

$$J_{N_2}^{Leak} : J_{O_2}^{Leak} = \sqrt{\frac{32}{28}} \times \frac{0.8}{0.2} = 4.28$$

$$J_{O_2} = [C_{O_2} - \frac{C_{N_2}}{4.28}]\frac{F}{S} \tag{1}$$

in which $C_{O_2}$ and $C_{N_2}$ are the oxygen and nitrogen concentrations calculated from the GC measurements, $F$ is the flow rate of the sweep stream, which can be measured by the soap flow meter, and $S$ is the membrane active area.

## 3. Results and discussion

### 3.1. Long-term oxygen permeation test

The long-term oxygen permeation behavior of (PL)$_{2.0}$NCG and

(PL)$_{1.9}$NCG ceramic membranes at 1173, 1123 and 1073 K under an air/He gradient are reported in Fig. 1. The permeation flux of the A-site deficient (PL)$_{1.9}$NCG membrane was slightly fluctuating ca. 1% at 1173 K, whereas the flux of the stoichiometric (PL)$_{2.0}$NCG membrane decreased to ca. 89% of the initial permeation flux during an 100 h operation under identical conditions. The decline of the oxygen permeation flux increased at temperatures lower than 1173 K. For example, the permeation fluxes of the (PL)$_{2.0}$NCG membrane decreased to ca. 19% at 1123 K and ca. 46% at 1073 K of the initial permeation flux over a period of 100 h. The decline of the oxygen permeation flux of the A-site deficient (PL)$_{1.9}$NCG membrane is slower than that of (PL)$_{2.0}$NCG under the same conditions, for example, its oxygen permeation flux decreased ca. 13% at 1123 K and ca. 43% at 1073 K. The enhanced stability by the introduction of an A-site deficiency will be discussed in detail. The high oxygen transport rates of A-site deficient (PL)$_{1.9}$NCG were attributed to the highly mobile oxygen vacancies and the charge compensating cationic vacancies. These findings have been previously discussed [7,25].

The (PL)$_{1.9}$NCG and (PL)$_{2.0}$NCG ceramic disks were annealed in air or Ar at 1073 K for 80 h to simulate the oxygen permeation conditions and to explain the declined oxygen permeability. Fig. 2 depicts the XRPD pattern of the as-sintered and treated (PL)$_{1.9}$NCG and (PL)$_{2.0}$NCG ceramics. Both as-sintered materials can be assigned to the tetragonal structure without the detection of other impurity phases (cf. Fig. 2a and b). After treatment at 1073 K in Ar for 80 h, the structure remained tetragonal (cf. Fig. 2c and d) while they decomposed into multilayered perovskite Pr$_4$Ni$_3$O$_{10+\delta'}$ (higher member of the RP oxides with $n=3$) and PrO$_{2+\delta'}$ during treatment in air at 1073 K (cf. Fig. 2e and f). The decomposition results in the decreased oxygen permeation flux. This decomposition behavior is a widespread phenomenon in Pr$_2$NiO$_4$-based materials and other researchers have reported similar results [13,15]. This behavior was attributed to the phase decomposition in an oxidative atmosphere at low temperatures according to the following reaction:

$$3Pr_2NiO_{4+\delta} + bO_2 \leftrightarrow Pr_4Ni_3O_{10+\delta'} + 2PrO_{2+\delta''} \tag{2}$$
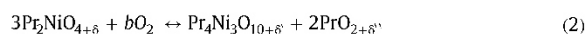
Here $b = 1 - 1.5\ \delta + 0.5\ \delta' + \delta''$, denotes the required oxygen amount for the decomposition; $\delta$, $\delta'$, $\delta''$ denote the oxygen non-stoichiometry of Pr$_2$NiO$_{4+\delta}$ ($n=1$), Pr$_4$Ni$_3$O$_{10+\delta'}$ ($n=3$), and the binary oxide PrO$_{2+\delta''}$ respectively [11,26]. The A-site occupancy is related to the oxygen content of (PL)$_{2.0}$NCG and may influence the
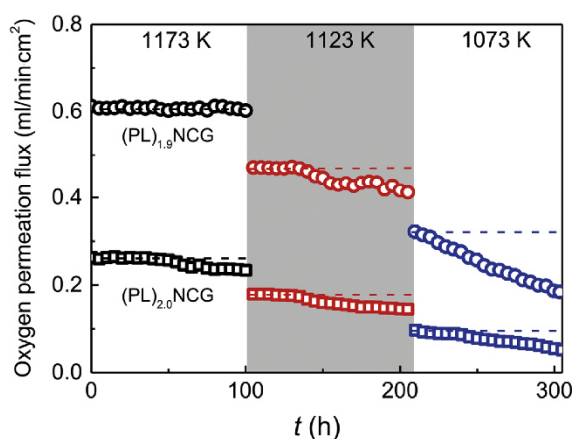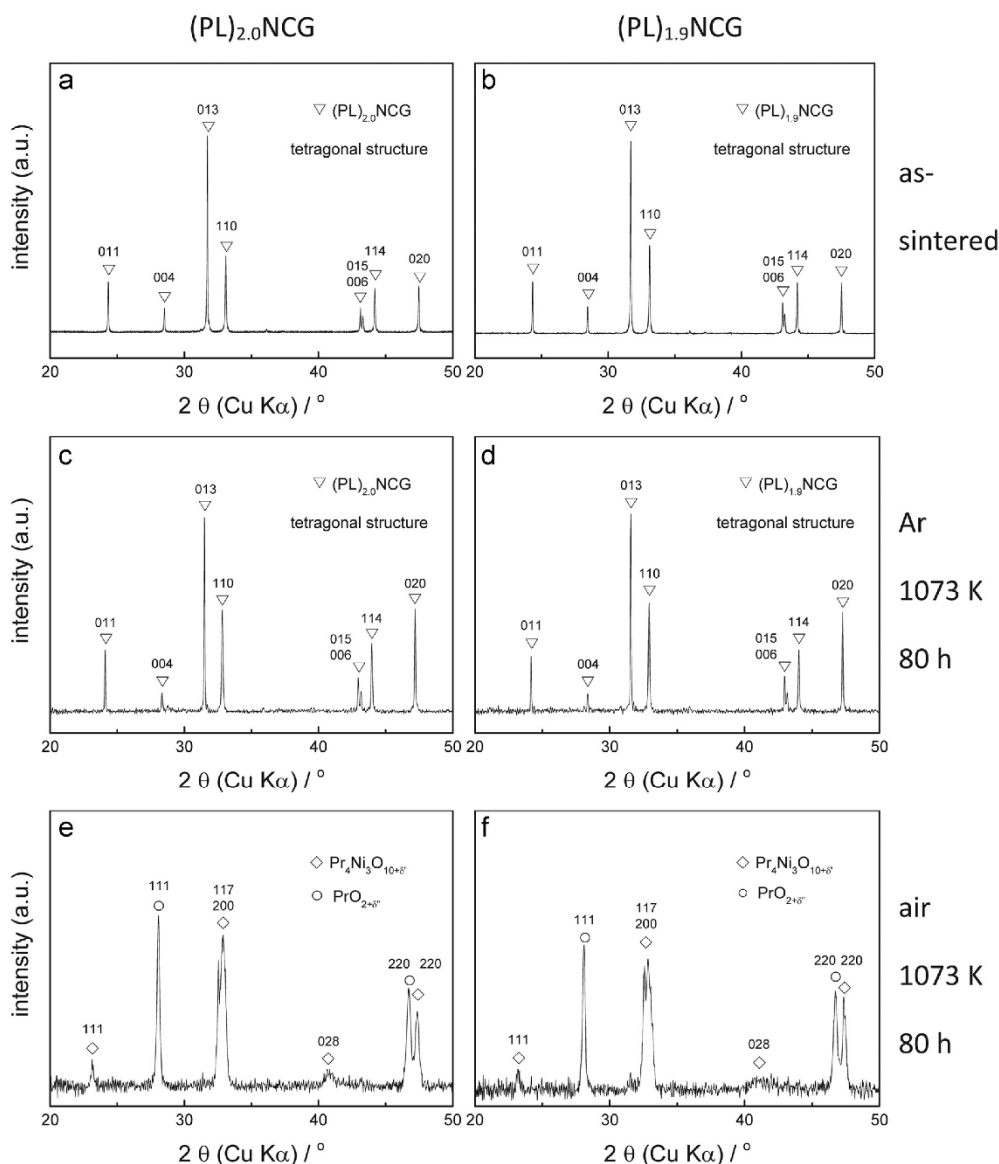


**Fig. 1.** Long-term oxygen permeation fluxes of the (PL)$_{2.0}$NCG and (PL)$_{1.9}$NCG membranes at different temperatures. The initial values are marked by horizontal dashed lines. Conditions: The air flow rates in the feed side are 150 mL/min. The flow rates at the sweep side are 30 mL/min. The thicknesses are 0.6 mm each.

28

**Fig. 2.** X-ray powder diffraction patterns of (PL)$_{2.0}$NCG and (PL)$_{1.9}$NCG ceramic surfaces in as-sintered state (1503 K for 10 h in air) and after additionally treated at 1073 K for 80 h under air or Ar atmosphere.

phase stability [7].

### 3.2. The phase decomposition conditions of (PL)$_{2.0}$NCG

We characterized the $pO_2$-$T$ dependence of the phase stability of cation stoichiometric (PL)$_{2.0}$NCG to assess the decomposition conditions of (PL)$_{2.0}$NCG series materials. The (PL)$_{2.0}$NCG powder was pretreated at 1373 K for 10 h and then tested with *in-situ* XRPD techniques. The reflections in the range of 26–35 ° are magnified and compared in Fig. 3a, b and c, and the full data are reported in Figs. S1–S3. As shown in Fig. 3a, the (PL)$_{2.0}$NCG powder was stable in synthetic air (20 vol.% O$_2$) after 8 h in the range of 1373–1223 K, whereas the 117 reflection of the Pr$_4$Ni$_3$O$_{10+\delta'}$ phase

(higher member of the RP oxides with $n=3$) appeared at 1173 K. The amount of Pr$_4$Ni$_3$O$_{10+\delta'}$ increased with time as the 117 reflection area increased (Fig. 3a). The sample that annealed at 1123 K in a 15 vol.% oxygen-containing atmosphere also decomposed after several hours, as shown in Fig. 3b. Similar results were found at 1073 K under a 10 vol.% oxygen-containing atmosphere shown in Fig. 3c, which indicate the approximate oxidation conditions.

The stability of the A$_2$BO$_4$-type oxides (the first member of the RP oxides with $n=1$) in the oxygen-containing atmospheres can be estimated using the Ellingham diagram in Fig. 4. This illustration predicts the thermodynamic stability of the materials at given temperatures and oxygen partial pressures. The dashed lines give
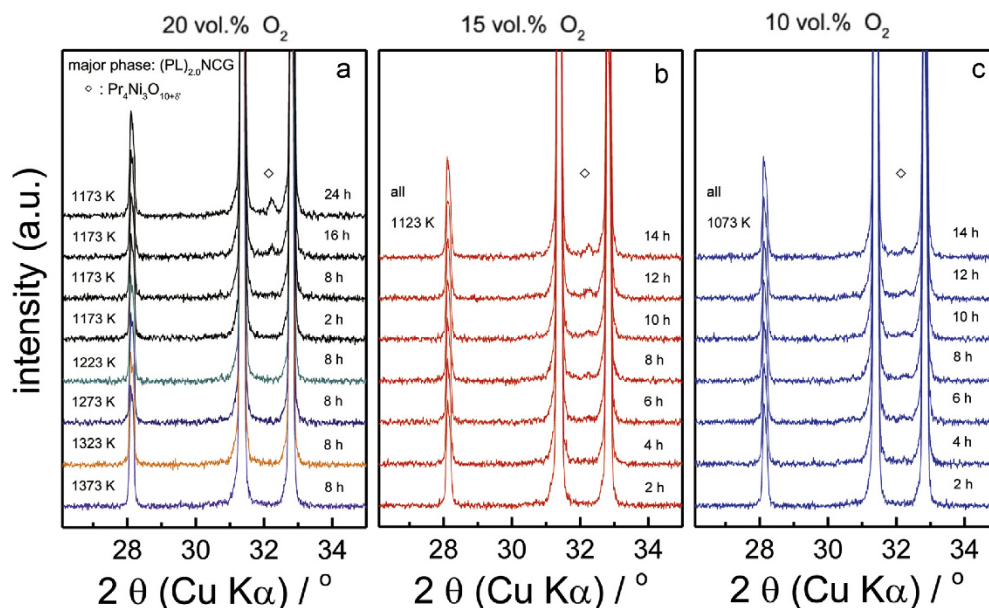
**Fig. 3.** Close-ups of selected regions of in-situ XRPD patterns of $(PL)_{2.0}NCG$ powder during annealing for different times: (a) under synthetic air (20 vol.% $O_2$) in the range of 1373–1173 K; (b) under 15 vol.% $O_2$ atmosphere at 1123 K; (c) under 10 vol.% $O_2$ atmosphere at 1073 K. The reflections of $(PL)_{2.0}NCG$ ($n=1$) are 004 (~28.4 °), 013 (~31.6 °), 110 (~33.0 °) from low angle to high angle in sequence and the reflection of $Pr_4Ni_3O_{10+\delta}$ ($n=3$) is 117 (~32.6 °). The $(PL)_{2.0}NCG$ powder was pre-treated in air at 1373 K for 10 h. The spent powder was refreshed by $N_2$ at the identical temperature (Fig. 5). The order of the experiments is Figs. 3a, 5a, 3b, 5b, 3c and 5c. The data were obtained by in-situ XRPD and are presented in full in the Supporting Information Figs. S1–S3.
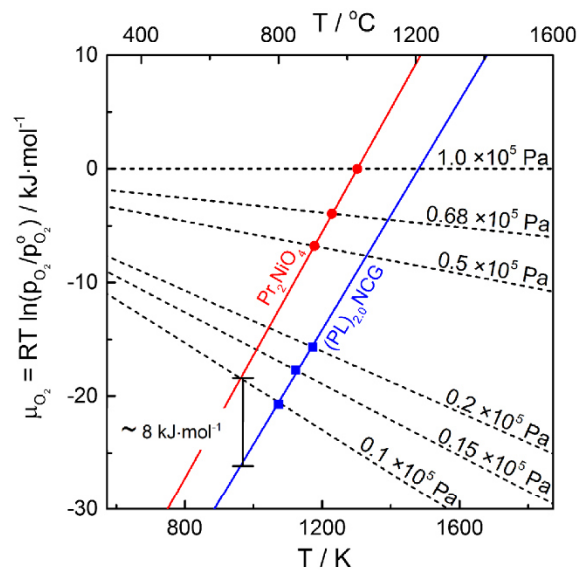


**Fig. 4.** Oxygen chemical potential versus temperature plots for different oxygen partial pressures including equilibrium values above $Pr_2NiO_4$ and $(PL)_{2.0}NCG$ according to Eq. (1). Experimental data are added as bullets (from Sullivan et al.) and squares (Figs. 3 and 5) [26]. The solid lines are the results of least square fits. A reference to standard conditions is given by $p_{O_2}^0 = 1.013 \times 10^5$ Pa.

$Pr_2NiO_4$ data were obtained from the work of Sullivan et al. [26]. The relative stability of the $A_2BO_4$-type oxides ($n=1$) were evaluated using a comparison of the oxygen chemical potential at a given temperature. From the thermodynamic point of view, The $A_2BO_4$-type oxides ($n=1$) are stable until the oxygen chemical potential of the environment is lower than the corresponding partial pressure of the decomposition reaction, or the temperature is higher than that of the critical condition. Therefore, these oxides are stable only in the region below the solid lines. For example, $(PL)_{2.0}NCG$ was stable to 1223 K in a $0.2 \times 10^5$ Pa oxygen partial pressure atmosphere. At approximately 1173 K, the oxidative decomposition will occur with decreasing temperature (Fig. 3a). The decomposition of $(PL)_{2.0}NCG$ also occurred at 1173 K when increasing the oxygen partial pressure from $0.1 \times 10^5$ Pa to $0.2 \times 10^5$ Pa.

The $(PL)_{2.0}NCG$ material should be stable under synthetic air (oxygen partial pressure is $0.2 \times 10^5$ Pa) above 1173 K, or at a lower oxygen partial pressure ( $< 0.2 \times 10^5$ Pa) at 1173 K. The two solid lines for the equilibrium oxygen chemical potential over oxide mixture are almost parallel while the line for $(PL)_{2.0}NCG$ is 8 kJ/mol lower than the line for $Pr_2NiO_4$. This difference indicates that the $(PL)_{2.0}NCG$ is slightly less stable forwards oxidation than $Pr_2NiO_4$. The Ellingham diagram of Fig. 4 predicts the thermodynamic stability of the $A_2BO_4$-type oxides under different conditions. However, the Ellingham diagram provides only an outline, the kinetics of the decomposition may also play an important role in the stability of the material, which are not considered here by principle.

### 3.3. Reversibility of the oxidative decomposition of $(PL)_{2.0}NCG$

As predicted by the Ellingham diagram shown in Fig. 4, the decomposition of the $A_2BO_4$-type materials under oxidizing conditions at low temperature should be reversible with by reducing the oxygen partial pressure or increasing the temperature. Similar
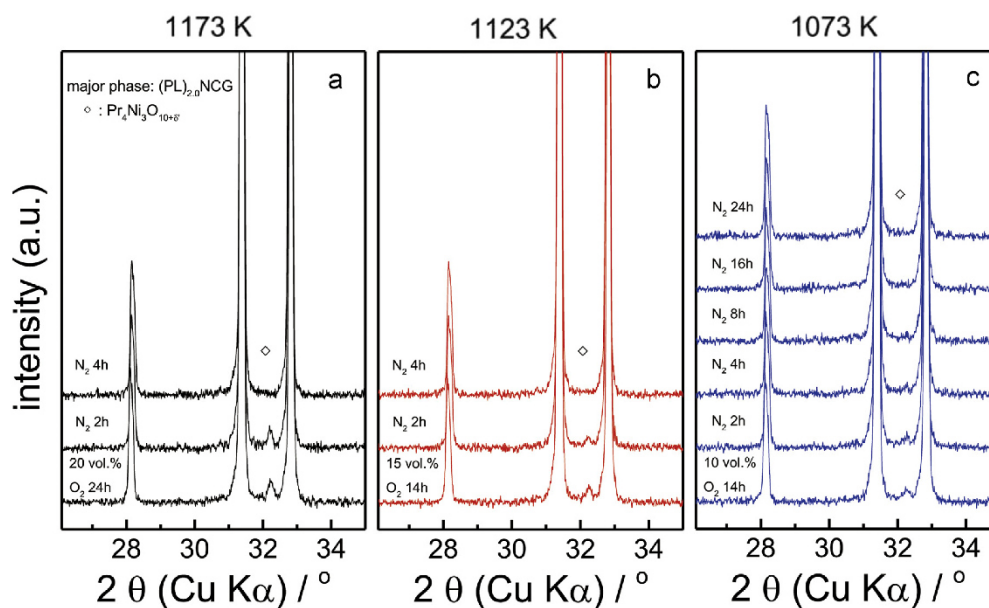
the oxygen chemical potential at various oxygen partial pressures [27]. The solid lines represent the equilibrium oxygen chemical potential over a mixture of oxides corresponding to those occurring in Eq. 2. The data points and the linear regression of $(PL)_{2.0}NCG$ were obtained from the XRPD experiments, and the

**Fig. 5.** Phase reversibility investigation of (PL)$_{2.0}$NCG by changing from an oxidizing atmosphere to an inert atmosphere: (a) annealing at 1173 K under N$_2$ after treatment in synthetic air (20 vol.%O$_2$) for 24 h; (b) annealing at 1123 K under N$_2$ after treatment in 15 vol.%O$_2$ for 14 h; (c) annealing at 1073 K under N$_2$ after treatment in 10 vol.%O$_2$ for 14 h.



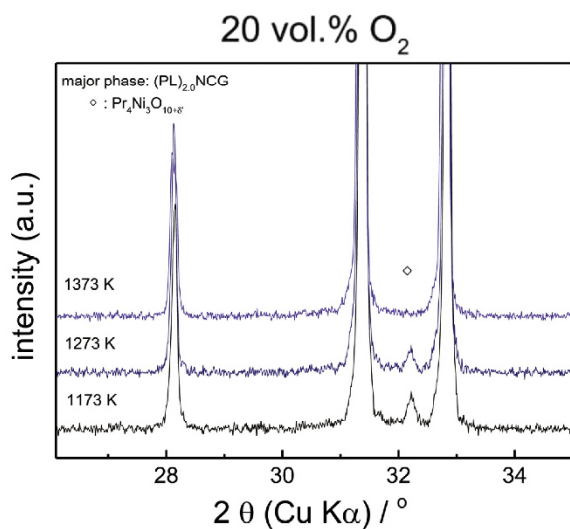**Fig. 6.** Phase reversibility investigation of (PL)$_{2.0}$NCG with increased temperature under synthetic air (20 vol.%O$_2$) for 8 h. The (PL)$_{2.0}$NCG powder was pre-treated in air at 1223 K for 10 h. The data were obtained using in-situ XRPD and presented in full in the Supporting Information Fig. S7.

results were found by Frade et al. who reported that the decomposition of Pr$_2$NiO$_4$ was reversible with increasing temperature [11,15]. The oxygen partial pressure in N$_2$ is approximately 10$^{-4}$ atm (10 Pa). The (PL)$_{2.0}$NCG powder was pre-treated in air at 1373 K for 10 h. The data were obtained by *in-situ* XRPD and presented in full in the Supporting Information Figs. S4–S6.

However, Odier et al. reported conflicting results for Pr$_2$NiO$_4$ oxide in which they suggest Pr$_2$NiO$_4$ oxide underwent an irreversible decomposition under pure oxygen at ambient pressure during thermogravimetric testing [13]. They reported that the

Pr$_2$NiO$_4$ oxide uptakes oxygen from 1123 K and loses oxygen above 1293 K. Up until 1423 K, the oxygen content reached the value identical to the one extrapolated from 1123 K. They selected a temperature 10 K greater (1303 K) than the initial point (1293 K) of the oxygen loss to investigate the reversibility. The structure of Pr$_2$NiO$_4$ oxide was still decomposed after quenching at 1303 K from the thermochemical investigation with 5 K/min heating and cooling under pure oxygen (without waiting). In pure oxygen, the Pr$_2$NiO$_4$ oxide was stable above 1303 K (Sullivan et al.) and is shown in the Ellingham diagram in Fig. 4 [26]. The Ellingham diagram of Fig. 4 demonstrates that at 1303 K and $pO_2 = 1 \times 10^5$ Pa, there is no driving force to rebuild the Pr$_2$NiO$_4$ according to Eq. (2). The oxygen chemical potential above the mixture of oxides was lower than that of the atmosphere for the conditions applied by Odier et al. [13]. Therefore, their experimental conditions were oxidative such that they did not observe the reversible process. It is important to investigate the reversibility of the decomposition of (PL)$_{2.0}$NCG with time and under different conditions. We reduced the oxygen partial pressure at different temperatures. As shown in Fig. 5, the (PL)$_{2.0}$NCG (pretreated at 1373 K for 10 h) demonstrated reversibility when the oxidized condition were changed to an oxygen-free atmosphere in the range of 1073–1173 K. The transformation was slow at low temperatures, requiring more time at 1073 K than 1173 K.

We then investigated the reversibility by increasing the temperature. Similar reversibility of (PL)$_{2.0}$NCG was observed when increasing the temperature from 1173 K to 1373 K as depicted in Fig. 6. At 1173 K and 1273 K, the phases of (PL)$_{2.0}$NCG (pretreated at 1223 K for 10 h) are mixed with Pr$_4$Ni$_3$O$_{10+\delta}$ phases. After annealing at 1373 K, the Pr$_4$Ni$_3$O$_{10+\delta}$ phase disappeared and the pure A$_2$BO$_4$-type structure reformed. Similar results were reported by Frade et al. [11,15]. The results reported in Figs. 5 and 6 are similar to the Ellingham diagram of Fig. 4. The diagram can be used to predict such results.
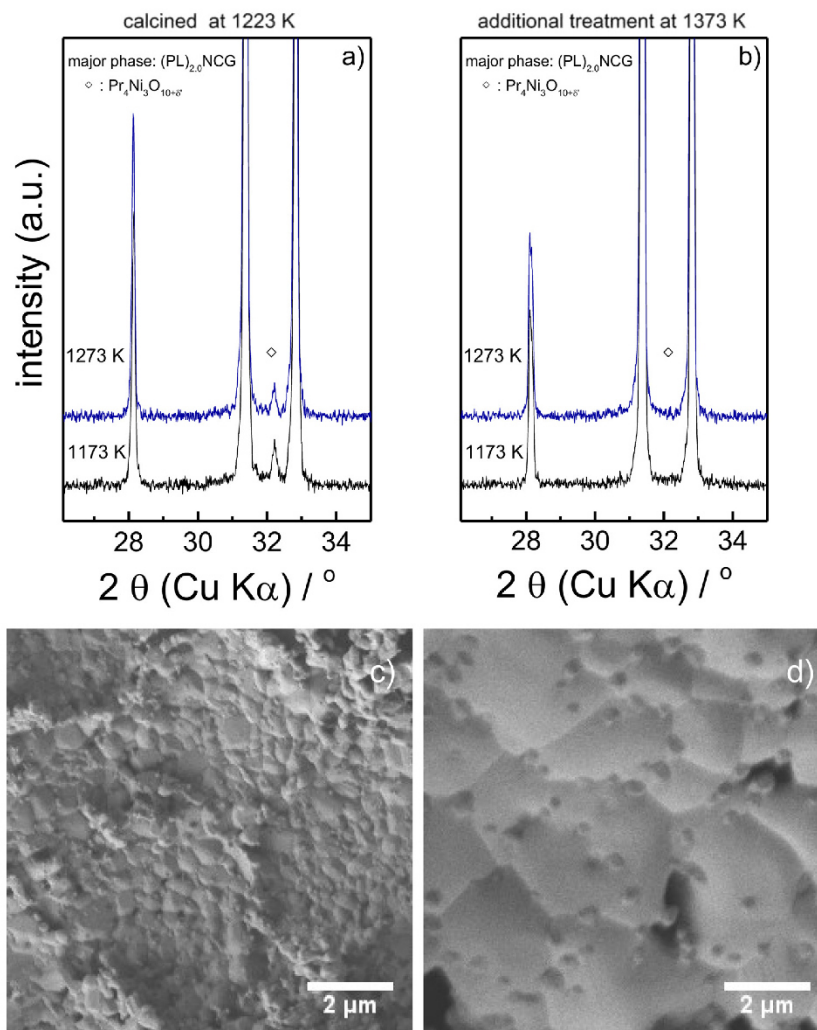
**Fig. 7.** The influence of calcination temperature on the phase stability (top) and grain size (bottom) of $(PL)_{2.0}NCG$: (a, c) calcination at 1223 K for 10 h; (b, d) additional treatment at 1373 K for 10 h. The data were obtained using in-situ XRPD and presented in full in the Supporting Information Figs. S8 and S9.

### 3.4. Various methods to enhance oxidation stability

Not only the ambient $O_2$ partial pressure and temperature have influence on the stability of $A_2BO_4$-type oxides, but also the properties of its own. We observed that the calcination temperature of powder influences the stability of the $A_2BO_4$ structure using *in-situ* XRPD measurements. The $(PL)_{2.0}NCG$ precursor, after sol–gel process, was calcined at 1223 K for 10 h. Some of the calcined powder was then treated at 1373 K for 10 h. Fig. 7 depicts the *in-situ* XRPD patterns and the micrograph of $(PL)_{2.0}NCG$ powder after annealing at 1223 K and 1373 K, respectively. After calcination at 1223 K for 10 h, the $(PL)_{2.0}NCG$ powder contained $Pr_4Ni_3O_{10-\delta}$ by-phase at 1173 K and 1273 K under synthetic air as shown in Fig. 7a. However, the amount of $Pr_4Ni_3O_{10+\delta}$ by-phase was low at 1173 K and the by-phase disappeared at 1273 K under the identical conditions after the $(PL)_{2.0}NCG$ powder was additionally treated at 1373 K for 10 h as shown in Fig. 7b. This behavior may be because of the increased grain size during the calcination process. The decomposition may have originated at the

grain surface and was active at the grain boundary, where the kinetic diffusion is fast [28–30]. The grain size increased from 0.3 μm to 3 μm with increased calcination temperature from 1223 K to 1373 K. Therefore, the increased calcination temperature may improve the oxidation stability of $A_2BO_4$-type oxides. This finding is important for porous SOFC cathodes.

The introduction of A-site deficiency may also improve the stability of $(PL)_{2.0}NCG$ as indicated by the oxygen permeation test as shown in Fig. 1. This conclusion was confirmed by the XRPD analysis as illustrated in Fig. 8a and b. $(PL)_{2.0}NCG$ underwent an oxidative decomposition to $Pr_4Ni_3O_{10+\delta}$, 5 h after annealing the as-prepared samples at 1173 K for different times and quenching, as shown in Fig. 8a. However, the amount of $Pr_4Ni_3O_{10+\delta}$ by-phase in the $(PL)_{1.9}NCG$ powder was less than the amount observed under the identical conditions with $(PL)_{2.0}NCG$ as shown in Fig. 8b. The incorporation of A-site deficiency decreased the oxygen content. This finding has been validated previously [7,25]. $(PL)_{2.0}NCG$ is hyperstoichiometric with $4+\delta=4.25$ at 900 °C in air (20 vol.% $O_2$), but $(PL)_{1.9}NCG$ is almost oxygen stoichiometric,
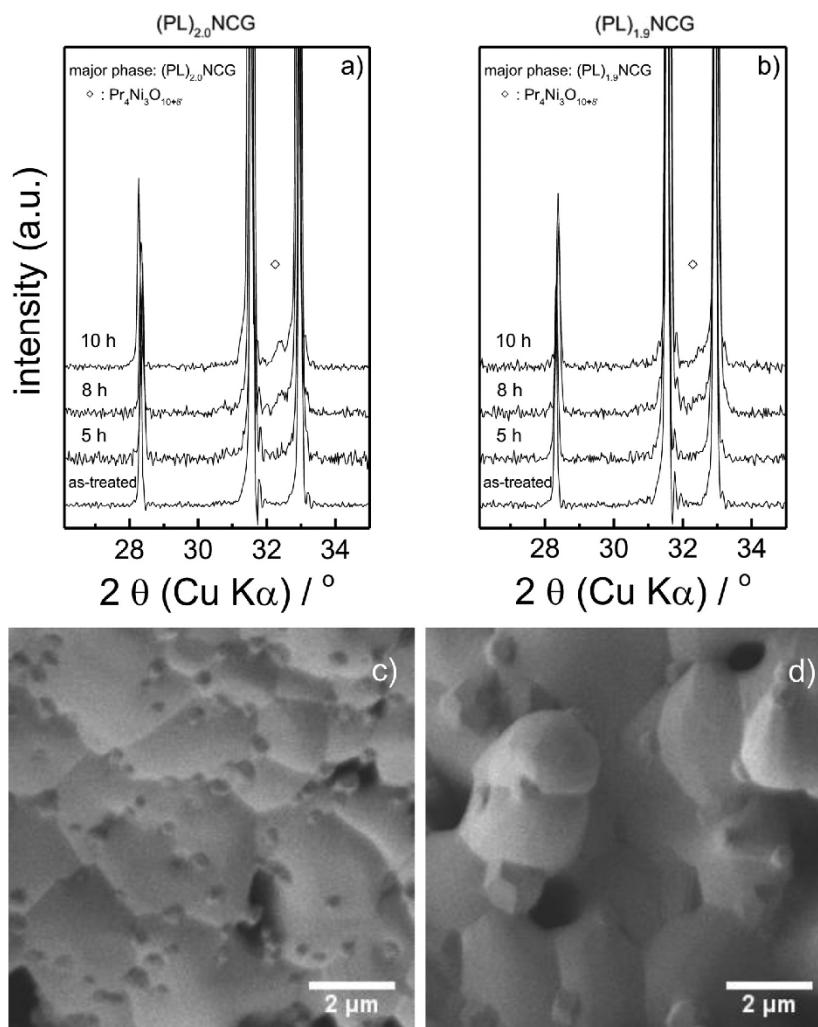
**Fig. 8.** The influence of A-site deficiency on the phase stability (top) and grain size (bottom): (a, c) (PL)$_{2.0}$NCG; (b, d) (PL)$_{1.9}$NCG. The (PL)$_{2.0}$NCG and (PL)$_{1.9}$NCG powders were annealing at 1373 K for 10 h in air and then treated at 1173 K in air for different times. The data were obtained by ex-situ XRPD and presented in full in the Supporting Information Figs. S10 and S11.

$4+\delta=3.98$ [25].

The improved oxidation stability may be the result of the decreased oxygen non-stoichiometry in A$_2$BO$_4$-type oxides, and such behavior could be predicted with Eq. (2). The prolonged transient process is accompanied by extensive oxygen uptake. The required oxygen amount is $b=1-1.5\delta+0.5\delta'+\delta''$ [15,26]. If we assume that $\delta'$ and $\delta''$ are negligible, then b is only dependent on the oxygen content of the A$_2$BO$_4$-type ($n=1$) materials. The A$_2$BO$_4$-type oxides with lower oxygen content (low $\delta$) should be more stable because they require more oxygen to decompose under identical conditions. A similar phenomenon was also observed by Frade et al. The incorporation of a Cu cation into Pr$_2$NiO$_4$ (A$_2$BO$_4$-type oxide) decreased the oxygen content and expanded the stability domain of the A$_2$BO$_4$-type solid solution towards lower temperatures. And Fe doping had the opposite effect [15]. Therefore, the decomposition temperature of A$_2$BO$_4$-type oxides is determined by the oxygen content. Moreover, A-site deficiency could enhance the sintering process [25,31]. The grain size of (PL)$_{1.9}$NCG was larger than that of (PL)$_{2.0}$NCG as shown in Fig. 8c and d, which might also be the

reason for the improved stability by the introduction of A-site deficiency.

Both the cation-stoichiometric (PL)$_{2.0}$NCG and A-site deficient (PL)$_{1.9}$NCG oxides were decomposed under air (20 vol.% O$_2$) at 900 °C (Fig. 8). However, only the cation-stoichiometric (PL)$_{2.0}$NCG exhibited unstable oxygen permeation flux at 900 °C. The situation is complex when the powder was prepared as the oxygen permeable membrane (Fig. 1). The decomposition occurred on the feed side (high O$_2$ partial pressure side) (Fig. 2). The oxygen was partly transported from the feed side (high O$_2$ concentration side) to the sweep side (low O$_2$ concentration side) during the oxygen permeation process.

Therefore, the oxygen partial pressure near the membrane surface would be lower than that of the feed gas because of the polarized concentration [32,33]. Although oxygen permeation was a steady-state process, the oxygen permeation fluxes of (PL)$_{1.9}$NCG were much higher, which made the O$_2$ concentration near the feed side surface of (PL)$_{1.9}$NCG membrane much lower than that of (PL)$_{2.0}$NCG under the same condition. Therefore, the A-site

deficient $(PL)_{1.9}NCG$ membrane exhibited improved stability during the oxygen permeation test as shown in Fig. 1.

## 4. Conclusions

This research investigated the phase stability against the oxidation decomposition of a Ruddlesden-Popper type oxide $(PL)_{2.0}NCG$ ($A_2BO_4$-structure, the first member of the RP oxides with $n=1$) under an oxidizing atmosphere at intermediate temperatures. We observed that an $A_2BO_4$-structure $(PL)_{2.0}NCG$ decomposed into $Pr_4Ni_3O_{10+\delta}$ (higher member of the RP oxides with $n=3$) and praseodymium oxide phases, which are barriers to oxygen transport. We have constructed an Ellingham diagram, which can be used to guide further applications. We observed that the oxidative decomposition was reversible and related to the temperature and the oxygen partial pressure as predicted by the Ellingham diagram. The stability of the $A_2BO_4$-type oxides was dependent on their oxygen content and grain size. Phase stabilization was achieved by high-temperature calcination and by introducing an A-site deficiency. Our method could be used to understand the phase stability of other $A_2BO_4$-type oxides, and two effective methods to improve the stability of Ruddlesden-Popper type materials were proposed.

## Acknowledgments

## Appendix A. Supplementary material

Supplementary data associated with this article can be found in the online version at http://dx.doi.org/10.1016/j.memsci.2015.09.026.

## References

[1] Z. Shao, S.M. Halle, A high-performance cathode for the next generation of solid-oxide fuel cells, Nature 431 (2004) 170–173.
[2] J. Sunarso, S. Baumann, J.M. Serra, W.A. Meulenberg, S. Liu, Y.S. Lin, J.C. Diniz da Costa, Mixed ionic-electronic conducting (MIEC) ceramic-based membranes for oxygen separation, J. Membr. Sci. 320 (2008) 13–41.
[3] L. Qiu, T.H. Lee, L.M. Liu, Y.L. Yang, A.J. Jacobson, Oxygen permeation studies of $SrCo_{0.8}Fe_{0.2}O_{3-\delta}$, Solid State Ion. 76 (1995) 321–329.
[4] Z. Shao, W. Yang, Y. Cong, H. Dong, J. Tong, G. Xiong, Investigation of the permeation behavior and stability of a $Ba_{0.5}Sr_{0.5}Co_{0.8}Fe_{0.2}O_{3-\delta}$ oxygen membrane, J. Membr. Sci. 172 (2000) 177–188.
[5] M. Arnold, H. Wang, A. Feldhoff, Influence of $CO_2$ on the oxygen permeation performance and the microstructure of perovskite-type $(Ba_{0.5}Sr_{0.5})(Co_{0.8}Fe_{0.2})O_{3-\delta}$ membranes, J. Membr. Sci. 293 (2007) 44–52.
[6] J. Yi, M. Schroeder, T. Weirich, J. Mayer, Behavior of $Ba(Co, Fe, Nb)O_{3-\delta}$ perovskite in $CO_2$-containing atmospheres: Degradation mechanism and materials design, Chem. Mater. 22 (2010) 6246–6253.
[7] E. Boehm, J. Bassat, P. Dordor, F. Mauvy, J. Grenier, P. Stevens, Oxygen diffusion and transport properties in non-stoichiometric LnNiO oxides, Solid State Ion. 176 (2005) 2717–2725.
[8] M. Yashima, Diffusion pathway of mobile ions and crystal structure of ionic and mixed conductors-A brief review, J. Ceram. Soc. Jpn. 117 (2009) 1055–1059.
[9] A. Chroneos, D. Parfitt, J.A. Kilner, R.W. Grimes, Anisotropic oxygen diffusion in tetragonal $La_2NiO_{4+\delta}$: molecular dynamics calculations, J. Mater. Chem. 20 (2010) 266.
[10] A.R. Cleave, J.A. Kilner, S.J. Skinner, S.T. Murphy, R.W. Grimes, Atomistic computer simulation of oxygen ion conduction mechanisms in $La_2NiO_4$, Solid State Ion. 179 (2008) 823–826.
[11] A.V. Kovalevsky, V.V. Kharton, A.A. Yaremchenko, Y.V. Pivak, E.N. Naumovich, J. R. Frade, Stability and oxygen transport properties of $Pr_2NiO_{4-\delta}$ ceramics, J. Eur. Ceram. Soc. 27 (2007) 4269–4272.
[12] S. Miyoshi, T. Furuno, O. Sangoanruang, H. Matsumoto, T. Ishihara, Mixed conductivity and oxygen permeability of doped $Pr_2NiO_4$-based oxides, J. Electrochem. Soc. 154 (2007) B57–B62.
[13] P. Odier, C. Allançon, J.M. Bassat, Oxygen exchange in $Pr_2NiO_{4+\delta}$ at high temperature and direct formation of $Pr_4Ni_3O_{(10-x)}$, J. Solid State Chem. 153 (2000) 381–385.
[14] T. Ishihara, K. Nakashima, S. Okada, M. Enoki, H. Matsumoto, Defect chemistry and oxygen permeation property of $Pr_2Ni_{0.75}Cu_{0.25}O_4$ oxide doped with Ga, Solid State Ion. 179 (2008) 1367–1371.
[15] A.V. Kovalevsky, V.V. Kharton, A.A. Yaremchenko, Y.V. Pivak, E.V. Tsipis, S. O. Yakovlev, A.A. Markov, E.N. Naumovich, J.R. Frade, Oxygen permeability, stability and electrochemical behavior of $Pr_2NiO_{4+\delta}$-based materials, J. Electroceram. 18 (2007) 205–218.
[16] M. Yashima, N. Sirikanda, T. Ishihara, Crystal structure, diffusion path, and oxygen permeability of a $Pr_2NiO_4$-based mixed conductor $(Pr_{0.9}La_{0.1})_2(Ni_{0.74}Cu_{0.21}Ga_{0.05})O_{4+\delta}$, J. Am. Chem. Soc. 132 (2010) 2385–2392.
[17] J. Tang, Y. Wei, L. Zhou, Z. Li, H. Wang, Oxygen permeation through a $CO_2$-tolerant mixed conducting oxide $(Pr_{0.9}La_{0.1})_2(Ni_{0.74}Cu_{0.21}Ga_{0.05})O_{4+\delta}$, AIChE J. 58 (2012) 2473–2478.
[18] Y. Wei, O. Ravkina, T. Klande, H. Wang, A. Feldhoff, Effect of $CO_2$ and $SO_2$ on oxygen permeation and microstructure of $(Pr_{0.9}La_{0.1})_2(Ni_{0.74}Cu_{0.21}Ga_{0.05})O_{4+\delta}$ membranes, J. Membr. Sci. 429 (2013) 147–154.
[19] M. Yashima, M. Enoki, T. Wakita, R. Ali, Y. Matsushita, F. Izumi, T. Ishihara, Structural disorder and diffusional pathway of oxide ions in a doped $Pr_2NiO_4$-based mixed conductor, J. Am. Chem. Soc. 130 (2008) 2762–2763.
[20] A. Feldhoff, M. Arnold, J. Martynczuk, T.M. Gesing, H. Wang, The sol–gel synthesis of perovskites by an EDTA/citrate complexing method involves nanoscale solid state reactions, Solid State Sci. 10 (2008) 689–701.
[21] J. Xue, Q. Liao, Y. Wei, Z. Li, H. Wang, A $CO_2$-tolerance oxygen permeable $60Ce_{0.9}Gd_{0.1}O_2-\delta$-$40Ba_{0.5}Sr_{0.5}Co_{0.8}Fe_{0.2}O_3-\delta$ dual phase membrane, J. Membr. Sci. 443 (2013) 124–130.
[22] H. Luo, B. Tian, Y. Wei, H. Wang, H. Jiang, J. Caro, Oxygen permeability and structural stability of a novel tantalum-doped perovskite $BaCo_{0.7}Fe_{0.2}Ta_{0.1}O_{3-\delta}$, AIChE J. 56 (2010) 604–610.
[23] J. Xue, Q. Zheng, Y. Wei, K. Yuan, Z. Li, H. Wang, Dual phase composite oxide of $Ce_{0.9}Gd_{0.1}O_2-\delta$-$Ba_{0.5}Sr_{0.5}Co_{0.8}Fe_{0.2}O_3-\delta$ with excellent oxygen permeation, Ind. Eng. Chem. Res. 51 (2012) 4703–4709.
[24] H. Wang, R. Wang, D.T. Liang, W. Yang, Experimental and modeling studies on $Ba_{0.5}Sr_{0.5}Co_{0.8}Fe_{0.2}O_3-\delta$ (BSCF) tubular membranes for air separation, J. Membr. Sci. 243 (2004) 405–415.
[25] J. Xue, Q. Liao, W. Chen, H.J. Bouwmeester, H. Wang, A. Feldhoff, A new $CO_2$-resistant Ruddlesden-Popper oxide with superior oxygen transport: A-site deficient $(Pr_{0.9}La_{0.1})_{1.9}(Ni_{0.74}Cu_{0.21}Ga_{0.05})O_{4+\delta}$, J. Mater. Chem. 3 (2015) 19107–19114.
[26] J.D. Sullivan, D.J. Buttrey, D.E. Cox, J. Hriljac, A conventional and high-resolution synchrotron X-ray diffraction study of phase separations in $Pr_2NiO_{4+\delta}$, J. Solid State Chem. 94 (1991) 337–351.
[27] H.U. Fuchs, The Dynamics of Heat, Springer, New York, 1996.
[28] E. Navickas, T.M. Huber, Y. Chen, W. Hetaba, G. Holzlechner, G. Rupp, M. Stöger-Pollach, G. Friedbacher, H. Hutter, B. Yildiz, Fast oxygen exchange and diffusion kinetics of grain boundaries in Sr-doped $LaMnO_3$ thin films, Phys. Chem. Chem. Phys. 17 (2015) 7659–7669.
[29] T. Surholt, Y.M. Mishin, C. Herzig, Grain-boundary diffusion and segregation of gold in copper: Investigation in the type-B and type-C kinetic regimes, Phys. Rev. B 50 (1994) 3577.
[30] S. Tsai, A. Huntz, C. Dolin, Growth mechanism of $Cr_2O_3$ scales: oxygen and chromium diffusion, oxidation kinetics and effect of yttrium, Mater. Sci. Eng. A 212 (1996) 6–13.
[31] K. Shan, X.-M. Guo, Electrical conduction behavior of A-site deficient (Y, Fe) co-doped $SrTiO_3$ mixed ionic-electronic conductor, Mater. Lett. 113 (2013) 126–129.
[32] S. Baumann, J. Serra, M. Lobera, S. Escolástico, F. Schulze-Küppers, W. Meulenberg, Ultrahigh oxygen permeation flux through supported $Ba_{0.5}Sr_{0.5}Co_{0.8}Fe_{0.2}O_3-\delta$ membranes, J. Membr. Sci. 377 (2011) 198–205.
[33] P.-M. Geffroy, M. Reichmann, T. Chartier, J.-M. Bassat, J.-C. Grenier, Evaluating oxygen diffusion, surface exchange and oxygen semi-permeation in $Ln_2NiO_{4+\delta}$ membranes (Ln= La, Pr and Nd), J. Membr. Sci. 451 (2014) 234–242.

***Supporting information to***

# The phase stability of the Ruddlesden-Popper type oxide $(Pr_{0.9}La_{0.1})_{2.0}Ni_{0.74}Cu_{0.21}Ga_{0.05}O_{4+\delta}$ in an oxidizing environment by Jian Xue, Alexander Schulz, Haihui Wang, and Armin Feldhoff

**Oxidation decomposition conditions of (PL)2.0NCG**

As shown in Fig. S1, the $(PL)_{2.0}NCG$ powder was stable in synthetic air (20 vol.% $O_2$) in the range of 1373-1223 K, while the $Pr_4Ni_3O_{10+\delta'}$ phase (another member of the RP oxides with $n = 3$) appeared at 1173 K. And the amount of $Pr_4Ni_3O_{10+\delta'}$ increased with time of treatment.
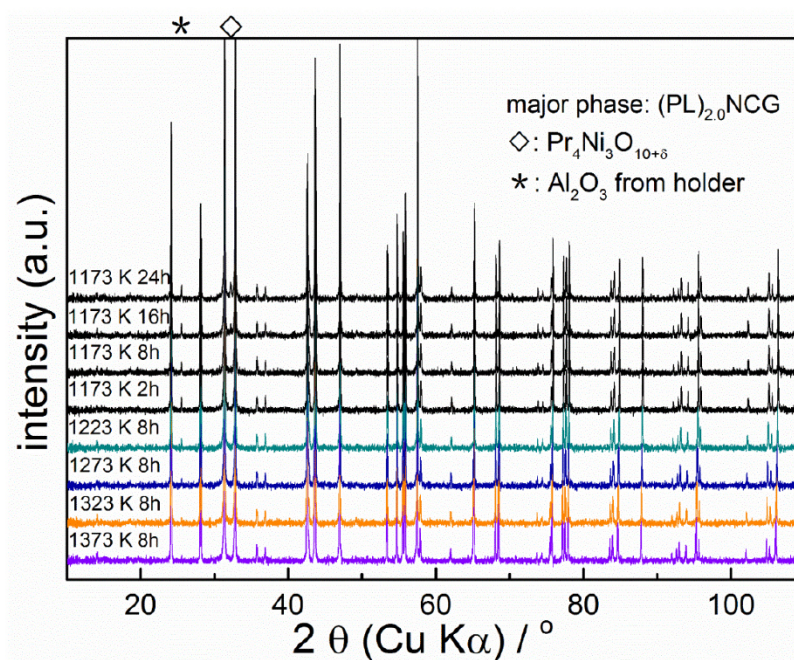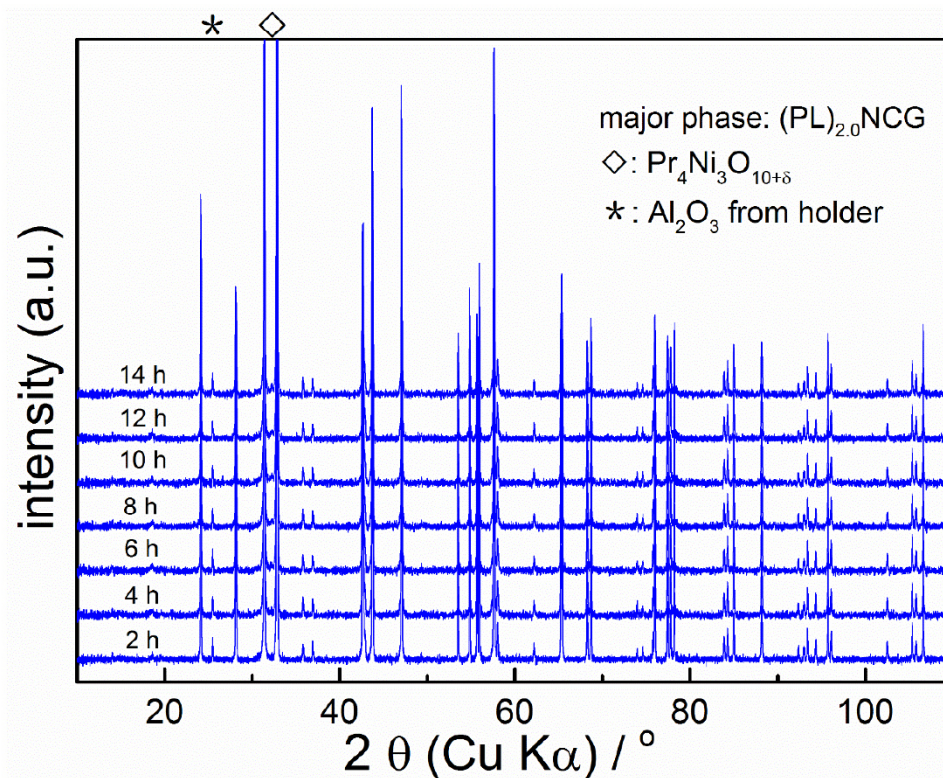


**Fig. S1.** In-situ XRPD patterns of $(PL)_{2.0}NCG$ powder during annealing for different time under synthetic air (20 vol.% $O_2$) in the range of 1373-1173 K. Note, the $(PL)_{2.0}NCG$ powder was pre-treated in air at 1373 K for 10 h. $\diamond$ marks 117 reflection (~32.6°) of $Pr_4Ni_3O_{10+\delta'}$ (n=3). $*$ marks 012 reflection (~25.6°) of $Al_2O_3$ from the holder.

The $(PL)_{2.0}NCG$ powder annealed at 1123 K in 15 vol.% oxygen-containing atmosphere also decomposed after several hours, as shown in Fig. S2.
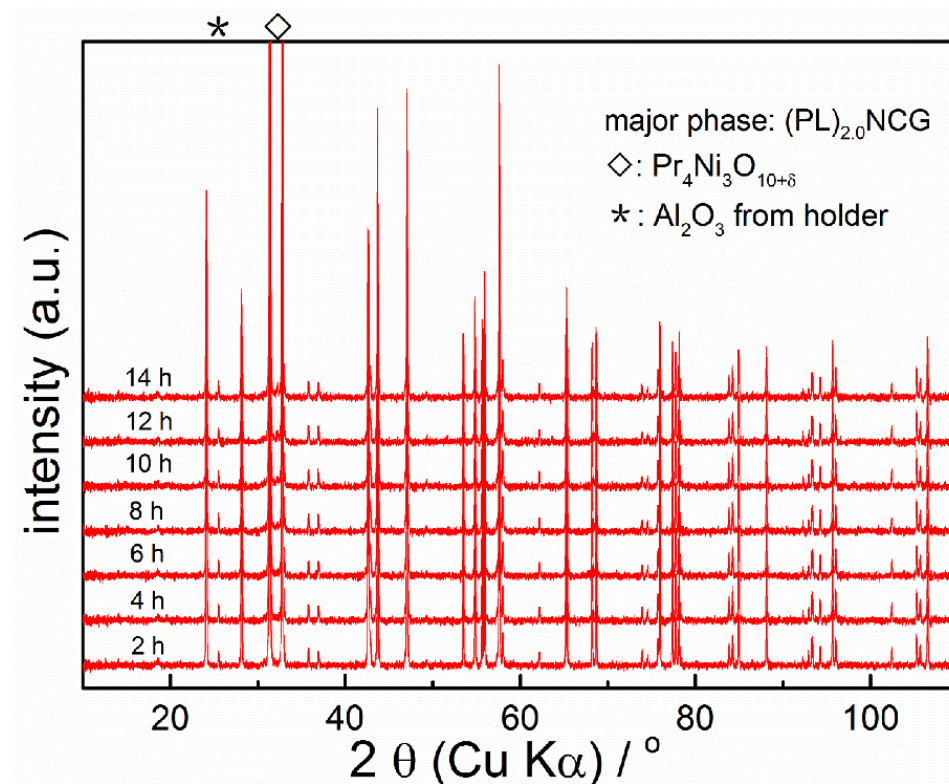


**Fig. S2.** In-situ XRPD patterns of $(PL)_{2.0}NCG$ powder during annealing for different time under 15 vol.% $O_2$ atmosphere at 1123 K. Note, the $(PL)_{2.0}NCG$ powder was pre-treated in air at 1373 K for 10 h. $\diamond$ marks 117 reflection (~32.6°) of $Pr_4Ni_3O_{10+\delta}$ (n=3). $*$ marks 012 reflection (~25.6°) of $Al_2O_3$ from the holder.

Similar results as shown in Fig. S1 and S2 were also found at 1073 K under 10 vol.% oxygen-containing atmosphere shown in Fig. S3, which indicating the immediate proximity of the oxidation conditions.



**Fig. S3.** In-situ XRPD patterns of (PL)$_{2.0}$NCG powder during annealing for different time under 10 vol.% O$_2$ atmosphere at 1073 K. Note, the (PL)$_{2.0}$NCG powder was pre-treated in air at 1373 K for 10 h. $\diamond$ marks 117 reflection (~32.6°) of Pr$_4$Ni$_3$O$_{10+\delta}$ (n=3). $*$ marks 012 reflection (~25.6°) of Al$_2$O$_3$ from the holder.

**Reversibility of the oxidative decomposition of (PL)$_{2.0}$NCG**

After 14 h decomposition in 20 vol.% oxygen containing atmosphere, the spent (PL)$_{2.0}$NCG powder was placed in inert atmosphere. The impurity phase disappeared after 4 h, which indicates that the decomposition was reversible at 1173 K.
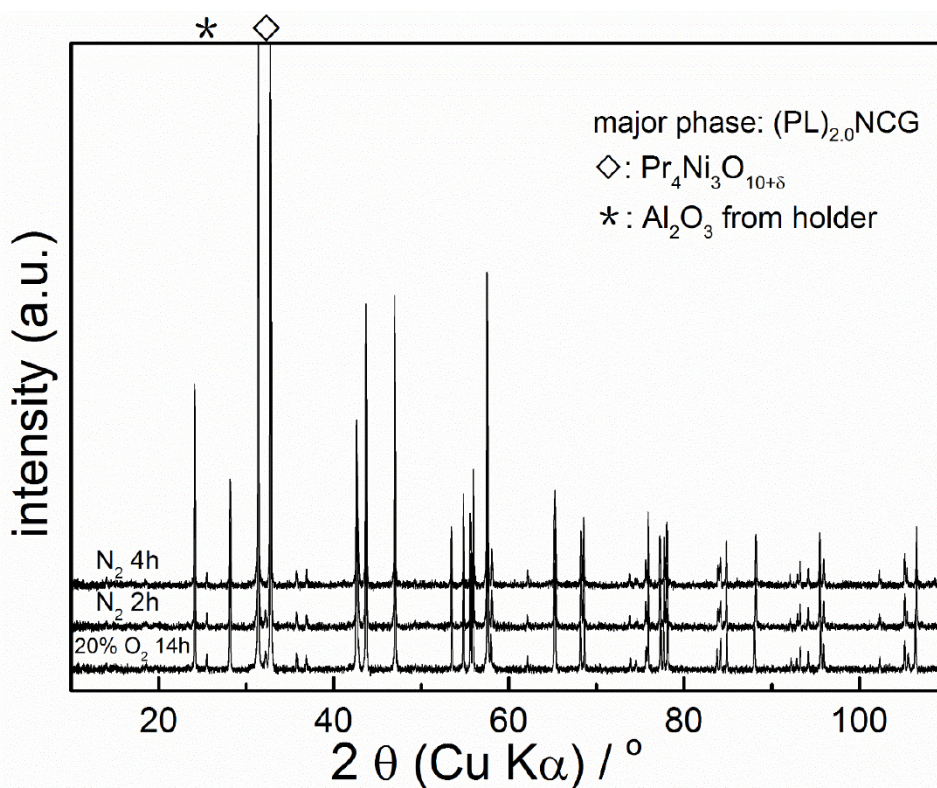


**Fig. S4.** Phase reversibility investigation on (PL)$_{2.0}$NCG when changing the 20 vol.% O$_2$-containing atmosphere to inert atmosphere at 1173 K. Note, the (PL)$_{2.0}$NCG powder was pre-treated in air at 1373 K for 10 h. $\Diamond$ marks 117 reflection (~32.6°) of Pr$_4$Ni$_3$O$_{10+\delta}$ (n=3).

$*$ marks 012 reflection (~25.6°) of Al$_2$O$_3$ from the holder.

After the (PL)$_{2.0}$NCG powder treated for 14 h in 15 vol.% oxygen containing atmosphere at 1123 K, the spent materials was placed in inert atmosphere. The impurity phase also disappeared after 4 h, which indicates that the decomposition was reversible at 1123 K.
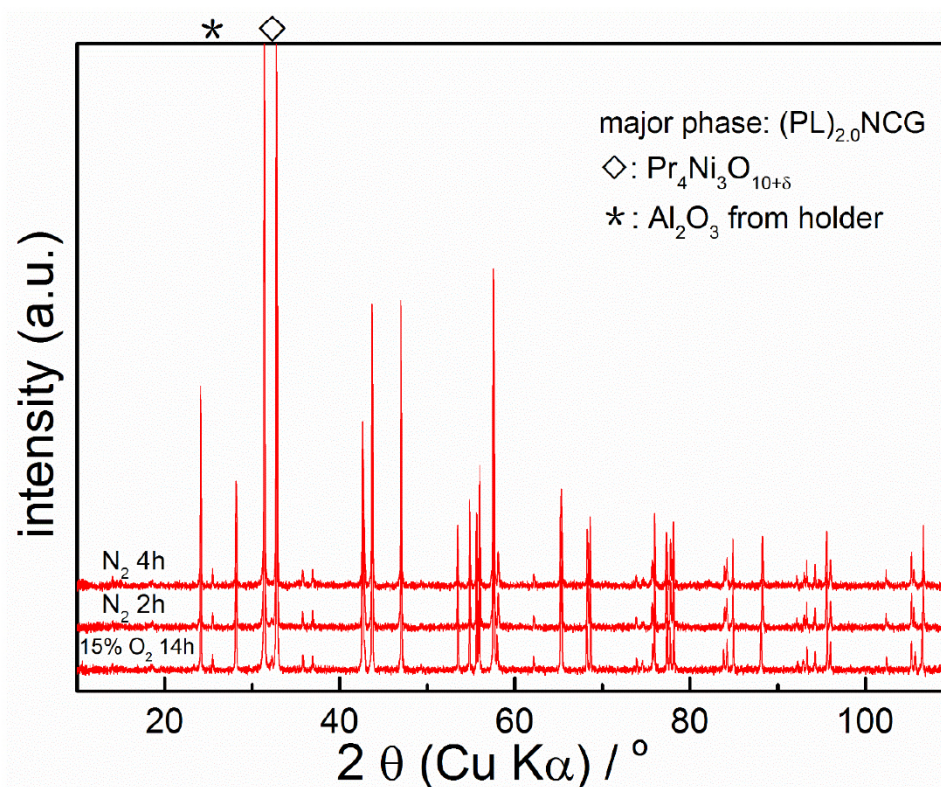


**Fig. S5.** Phase reversibility investigation on (PL)$_{2.0}$NCG when changing the 15 vol.% O$_2$-containing atmosphere to inert atmosphere at 1123 K. Note, the (PL)$_{2.0}$NCG powder was pre-treated in air at 1373 K for 10 h. $\diamond$ marks 117 reflection (~32.6°) of Pr$_4$Ni$_3$O$_{10+\delta}$ (n=3). $*$ marks 012 reflection (~25.6°) of Al$_2$O$_3$ from the holder.

When changing the 10 vol.% oxygen containing atmosphere to inert atmosphere at 1073 K, the impurity phase slowly disappeared with treated time, which indicates that the decomposition was reversible at 1073 K.



**Fig. S6.** Phase reversibility investigation on $(PL)_{2.0}NCG$ when changing the 10 vol.% $O_2$-containing atmosphere to inert atmosphere at 1073 K. Note, the $(PL)_{2.0}NCG$ powder was pre-treated in air at 1373 K for 10 h. $\diamond$ marks 11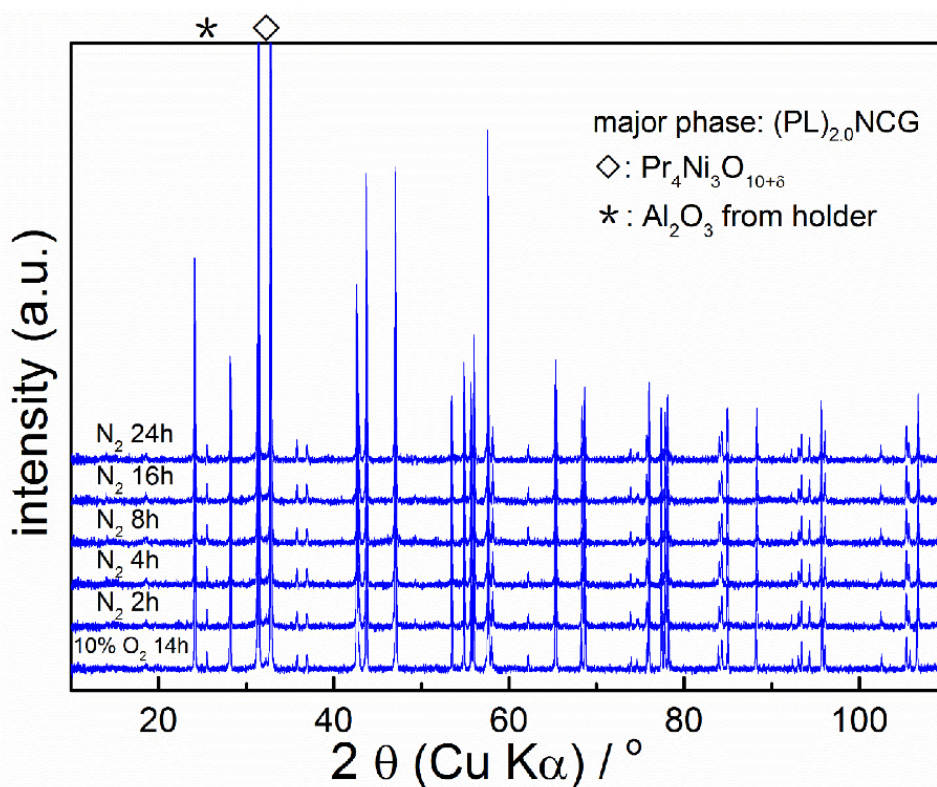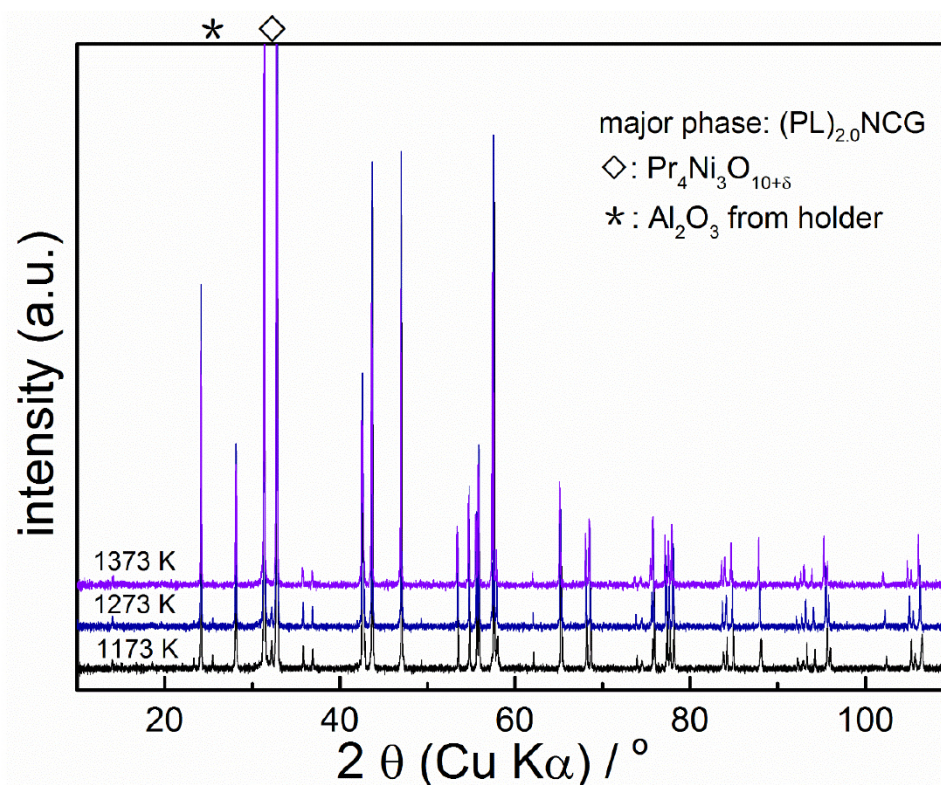7 reflection ($\sim32.6°$) of $Pr_4Ni_3O_{10+\delta}$ (n=3). $*$ marks 012 reflection ($\sim25.6°$) of $Al_2O_3$ from the holder.

Not only does the oxygen partial pressure influence the stability of the $A_2BO_4$-type oxides, but the temperature of the environment does also. As shown in Fig. S7, at 1173 K and 1273 K, the phases of $(PL)_{2.0}NCG$ (pretreated at 1223 K for 10 h) are mixed with $Pr_4Ni_3O_{10+\delta'}$ phases, while after annealing at 1373 K, the $Pr_4Ni_3O_{10+\delta'}$ phase disappeared and the pure $K_2NiF_4$-type structure formed again.



**Fig. S7.** Phase reversibility investigation on $(PL)_{2.0}NCG$ with increased temperature under synthetic air (20 vol.% $O_2$) for 8 h. Note, the $(PL)_{2.0}NCG$ powder was pre-treated in air at 1223 K for 10 h. $\Diamond$ marks 117 reflection (~32.6°) of $Pr_4Ni_3O_{10+\delta'}$ (n=3). $*$ marks 012 reflection (~25.6°) of $Al_2O_3$ from the holder.

**Enhanced oxidation stability by high temperature calcination**

After calcination at 1223 K for 10 h, the $(PL)_{2.0}NCG$ powder contained $Pr_4Ni_3O_{10\ \delta'}$ phase at 1173 K and 1273 K under synthetic air as shown in Fig. S8.
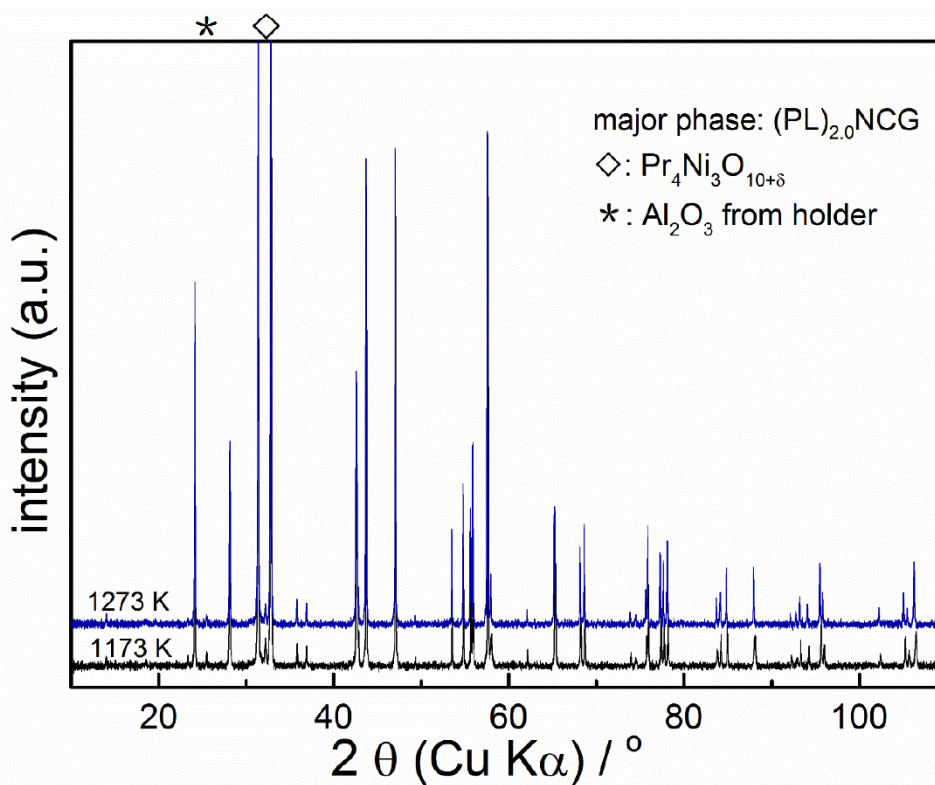


**Fig. S8.** The in-situ XRPD patterns of $(PL)_{2.0}NCG$ powder during annealing at 1173 K and 1273 K for 8 h. Note, the $(PL)_{2.0}NCG$ powder was pre-treated in air at 1223 K for 10 h. $\diamond$ marks 117 reflection (~32.6°) of $Pr_4Ni_3O_{10+\delta'}$ (n=3). $*$ marks 012 reflection (~25.6°) of $Al_2O_3$ from the holder.

The amount of Pr$_4$Ni$_3$O$_{10-\delta'}$ phase was very low at 1173 K and disappeared at 1273 K after the

(PL)$_{2.0}$NCG powder was annealed at 1373 K for 10 h as shown in Fig. 7b. Compared to the

powder calcination at 1223 K for 10 h, the (PL)$_{2.0}$NCG possessed enhanced stability after

annealing at 1373 K for 10 h.
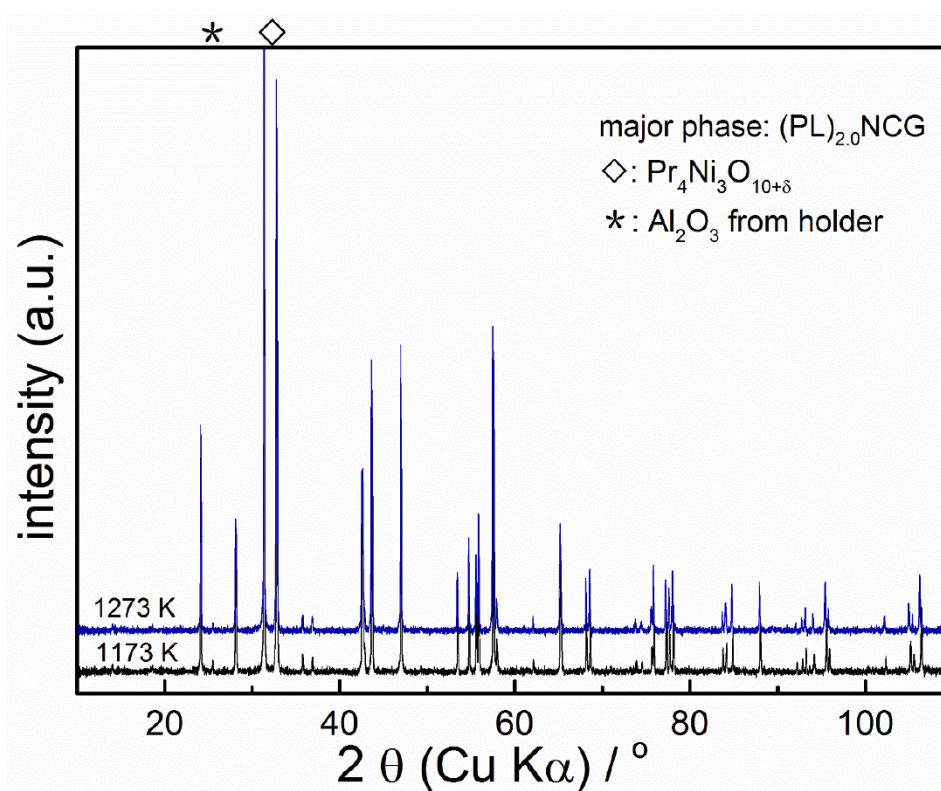


**Fig. S9.** The in-situ XRPD patterns of (PL)$_{2.0}$NCG powder during annealing at 1173 K and

1273 K for 8 h. Note, the (PL)$_{2.0}$NCG powder was pre-treated in air at 1373 K for 10 h. $\diamond$

marks 117 reflection (~32.6°) of Pr$_4$Ni$_3$O$_{10+\delta'}$ (n=3). $\star$ marks 012 reflection (~25.6°) of

Al$_2$O$_3$ from the holder.

**Enhanced oxidation stability by introduction of A-site dificiency**

After annealing of the as-prepared samples at 1173 K for different time and quenching, $(PL)_{2.0}NCG$ underwent an oxidation decomposition to $Pr_4Ni_3O_{10+\delta}$ after 5 hours, as shown in Fig. S10.
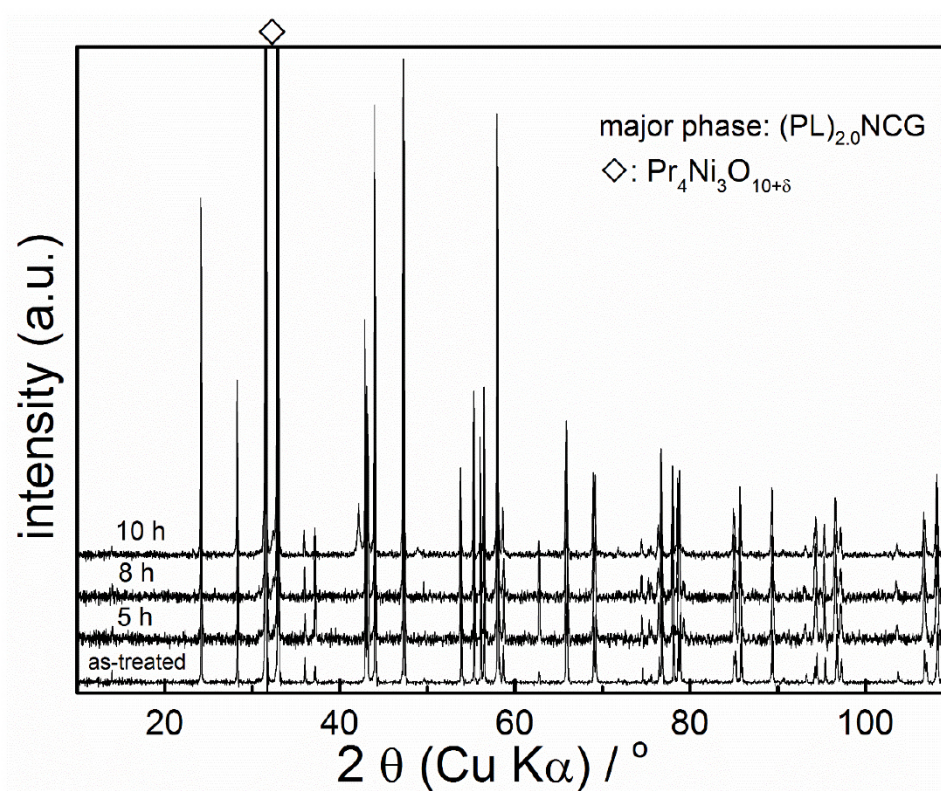


**Fig. S10.** The ex-situ XRPD patterns of $(PL)_{2.0}NCG$ powder during annealing at 1173 K for different time. Note, the $(PL)_{2.0}NCG$ powder was pre-treated in air at 1373 K for 10 h. $\diamond$ marks 117 reflection ($\sim32.6°$) of $Pr_4Ni_3O_{10+\delta}$ (n=3).

There is also some $Pr_4Ni_3O_{10+\delta'}$ impurity phase in the (PL)$_{1.9}$NCG powder after annealing of

the as-prepared samples at 1173 K for 5 h. However, the amount of the impurity phase was

much smaller than that in (PL)$_{2.0}$NCG under the same condition as shown in Fig. S11.

Abovementioned results indicate that the introduction of A-site deficiency could also improve

the stability of (PL)$_{2.0}$NCG.
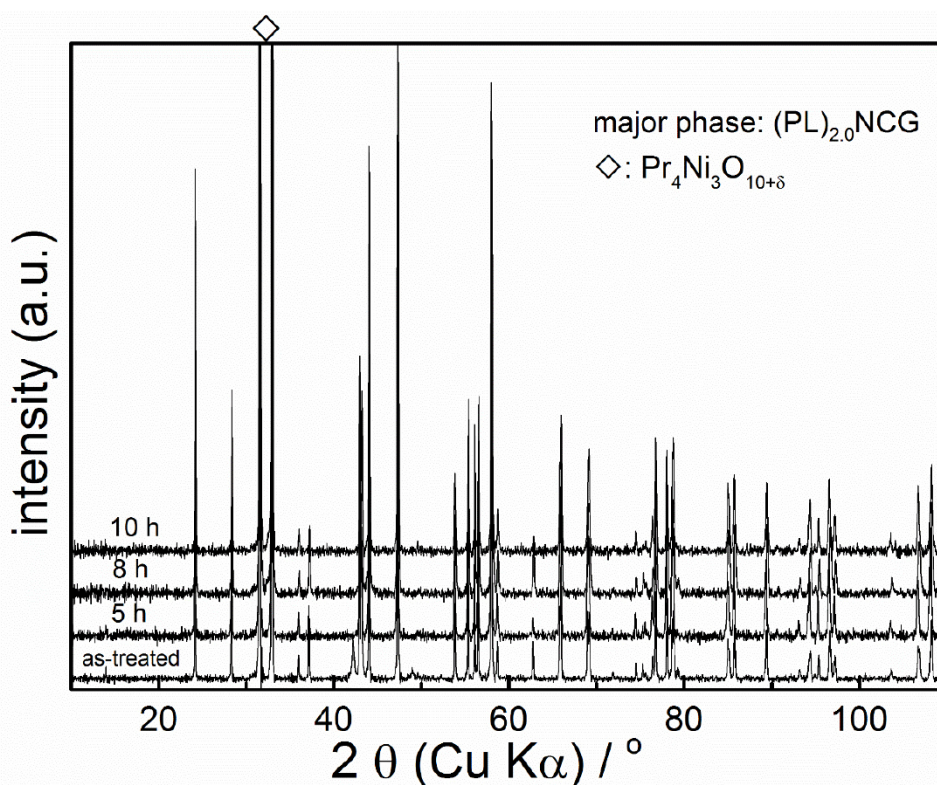


**Fig. S11.** The ex-situ XRPD patterns of (PL)$_{1.9}$NCG powder during annealing at 1173 K for

different time. Note, the (PL)$_{1.9}$NCG powder was pre-treated in air at 1373 K for 10 h. ◇

marks 117 reflection (~32.6°) of $Pr_4Ni_3O_{10+\delta'}$ (n=3).

## 2.3 A new $CO_2$-resistant Ruddlesden-Popper oxide with superior oxygen transport: A-site deficient $(Pr_{0.9}La_{0.1})_{1.9}(Ni_{0.74}Cu_{0.21}Ga_{0.05})O_{4+\delta}$

Jian Xue, Qing Liao, Wei Chen, Henny J.M. Bouwmeester, Haihui Wang, and Armin Feldhoff

**PAPER**

## A new CO₂-resistant Ruddlesden–Popper oxide with superior oxygen transport: A-site deficient (Pr$_{0.9}$La$_{0.1}$)$_{1.9}$(Ni$_{0.74}$Cu$_{0.21}$Ga$_{0.05}$)O$_{4+\delta}$

Jian Xue,[a] Qing Liao,[c] Wei Chen,[b] Henny J. M. Bouwmeester,*[b] Haihui Wang*[cd] and Armin Feldhoff*[a]

A-site deficient (Pr$_{0.9}$La$_{0.1}$)$_{1.9}$Ni$_{0.74}$Cu$_{0.21}$Ga$_{0.05}$O$_{4+\delta}$ ((PL)$_{1.9}$NCG), with the K$_2$NiF$_4$ structure, is found to exhibit higher oxygen transport rates compared with its cation-stoichiometric parent phase. A stable oxygen permeation flux of 4.6 × 10$^{-7}$ mol cm$^{-2}$ s$^{-1}$ at 900 °C at a membrane thickness of 0.6 mm is measured, using either helium or pure CO$_2$ as sweep gas at a flow rate of 30 mL min$^{-1}$. The oxygen flux is more than two times higher than that observed through A-site stoichiometric (PL)$_{2.0}$NCG membranes operated under similar conditions. The high oxygen transport rates found for (PL)$_{1.9}$NCG are attributed to highly mobile oxygen vacancies, compensating A-site deficiency. The high stability against carbonation gives (PL)$_{1.9}$NCG potential for use, *e.g.*, as a membrane in oxy-fuel combustion processes with CO$_2$ capture.

## 1 Introduction

Clean energy delivery technologies are imperatively required for the purpose of reducing the emission of CO$_2$ to avert global climate change. Oxygen-transport membranes (OTMs) based on mixed electronic and ionic conductors have gained increasing attention due to their economical, efficient, and environmentally friendly production of oxygen from air and their potential integration in oxy-fuel technologies with CO$_2$ capture.[1,2] In the oxy-fuel process, a part of the flue gas, which contains CO$_2$, is recycled and used as sweep gas. Therefore, oxygen-transport membranes should not only exhibit a high oxygen flux, but also show good stability under CO$_2$-containing atmospheres.[3,4]

Acceptor-doped perovskite-type oxides A$_{1-x}$A$_x$'B$_{1-y}$B'$_y$O$_{3-\delta}$ (A, A' = La, Sr, Ba; B, B' = Fe, Co, Nb, *etc.*) have been investigated extensively as OTMs over the past two decades.[5,6] The ionic charge carriers created by acceptor-doping are mobile oxygen vacancies. Indeed, high oxygen fluxes are measured for materials with high concentrations of oxygen vacancies. Up to 1/4 of the oxygen sites can be vacant like, for example, SrCo$_{0.8}$Fe$_{0.2}$O$_{3-\delta}$ and Ba$_{0.5}$Sr$_{0.5}$Co$_{0.8}$Fe$_{0.2}$O$_{3-\delta}$.[7,8] A drawback is that these materials are prone to carbonation. An oxygen-impermeable

*aInstitute of Physical Chemistry and Electrochemistry, Leibniz University Hannover, Callinstrasse 3A, D-30167 Hannover, Germany. E-mail: armin.feldhoff@pci.uni-hannover.de*

*bDepartment of Science and Technology, MESA+ Institute for Nanotechnology, University of Twente, 7500 AE Enschede, The Netherlands. E-mail: h.j.m.bouwmeester@utwente.nl*

*cSchool of Chemistry & Chemical Engineering, South China University of Technology, No. 381 Wushan Road, Guangzhou 510640, China. E-mail: hhwang@scut.edu.cn*

*dSchool of Chemical Engineering, The University of Adelaide, Adelaide, SA 5005, Australia*

alkaline-earth carbonate layer will be formed on the membrane surface exposed to the CO$_2$-containing sweep gas, resulting in a decline of the oxygen permeation flux with time.[9,10] A-site deficiency is commonly adopted in an attempt to lower the basicity, thereby increasing the resistance of the membrane material towards carbonation.[11]

Alternatively, problems with limited CO$_2$ stability could be avoided by the development of alkaline-earth-free membrane materials. In this regard, perovskite-related Ruddlesden–Popper (RP) A$_{n-1}$B$_n$O$_{3n+1}$ materials, in particular those with the K$_2$NiF$_4$ structure (the first member of the RP oxides with n = 1), are attracting increasing attention.[12,13] The latter structure consists of alternate AO rock-salt and ABO$_3$ perovskite-like layers along the crystallographic *c*-axis, as shown in Fig. 1. Oxygen transport proceeds *via* migration of oxygen interstitials (O3) in the rock-salt layers.[14,15] Molecular dynamics (MD) simulations predict an interstitialcy diffusion mechanism, also referred to as a 'knock-on' or 'push–pull' mechanism, involving concerted jumps between interstitial oxygen (O3) and apical oxygen (O2) sites, rather than a direct jump between two interstitial sites.[16] A contribution of vacancy-mediated transport may be considered, but this necessitates the formation of oxygen vacancies. Using atomistic computer simulation, Cleave *et al.* predicted that all of the vacancy mechanisms studied in La$_2$NiO$_4$ exhibit lower activation energies than the interstitial process.[17] Most reported oxides with the K$_2$NiF$_4$ structure are, however, oxygen hyperstoichiometric so that in most of these cases the role of mobile interstitials is predominant.[12,18]

Using *in situ* high-temperature neutron powder diffraction, Yashima *et al.* provided evidence that indeed the ionic charge carriers in (Pr$_{0.9}$La$_{0.1}$)$_{2.0}$Ni$_{0.74}$Cu$_{0.21}$Ga$_{0.05}$O$_{4+\delta}$ ((PL)$_{2.0}$NCG) are oxygen interstitials.[18,19] It was determined that (PL)$_{2.0}$NCG
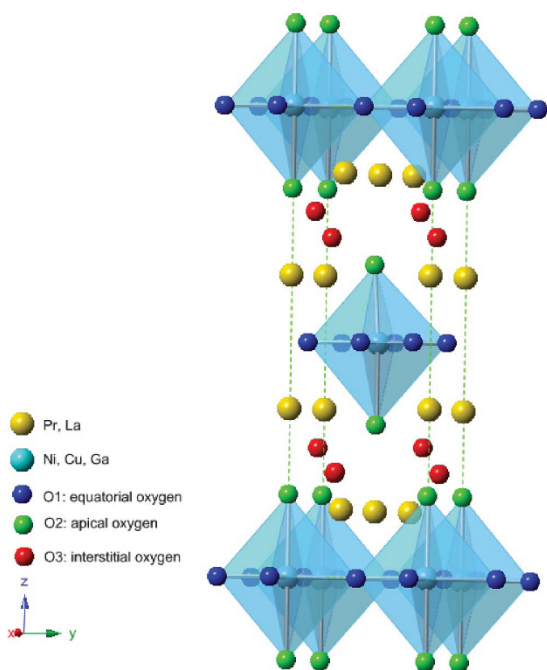
Fig. 1 Oxide with the tetragonal $K_2NiF_4$-type structure (space group *I4/mmm*). Atomic positions were calculated from ICSD 173422. For clarity only a subset of the interstitial oxygen ions (O3) is shown.

Legend:
- Pr, La
- Ni, Cu, Ga
- O1: equatorial oxygen
- O2: apical oxygen
- O3: interstitial oxygen

exhibits specific thermal anisotropic temperature factors expected for migration *via* the interstitialcy mechanism. Interestingly, Ishihara and colleagues found that A-site deficient oxides $Nd_{1.9}(Ni_{0.75}Cu_{0.25})_{0.95}Ga_{0.05}O_4$ and $Pr_{1.9}Ni_{0.75}Cu_{0.25}Ga_{0.05}O_4$ exhibit higher oxygen fluxes than their cation-stoichiometric parent phases.[20,21] The authors, however, refrained from giving a clear explanation of the role of A-site deficiency in oxygen transport. In this work, we have investigated the influence of A-site deficiency of $(PL)_{2.0}NCG$ on structural parameters, oxygen transport, and stability in $CO_2$ atmospheres.

## 2 Experimental

### 2.1. Preparation

Powders of $(Pr_{0.9}La_{0.1})_{1.9}Ni_{0.74}Cu_{0.21}Ga_{0.05}O_{4+\delta}$ ($(PL)_{1.9}NCG$) and $(PL)_{2.0}NCG$ were prepared by a combined citrate and ethylene-diamine-tetraacetic-acid (EDTA) method as described previously.[22,23] The as-prepared powders were uniaxially pressed at 20 MPa to obtain green pellets followed by their sintering in air at 1230 °C for 10 h in a bed of the corresponding powder. The density of the sintered disk membranes obtained was measured by the Archimedes method using distilled water. Only membranes with a relative density higher than 95% were selected for permeation experiments. The membranes were polished to the desired thickness using 1200 grit-sandpaper and then washed with ethanol.

### 2.2. Structural characterization

The crystal structure of the sintered disks was studied by using an *in situ* X-ray diffractometer (XRD, D8 Advance, Bruker-AXS, with Cu Kα radiation) equipped with a HTK-1200N high-temperature oven chamber (Anton-Paar). Measurements were conducted under a $CO_2$ atmosphere from 30 to 1000 °C. The temperature was step-wise increased, with a dwell time at each step of 50 min before actual data collection. The oxygen content of $(PL)_{1.9}NCG$ and $(PL)_{2.0}NCG$ in air at 900 °C was evaluated by hydrogen reduction in a thermogravimetric (TGA) apparatus (Netzsch TG 449 F3), assuming that the products of hydrogen reduction were $Pr_2O_3$, $La_2O_3$, Ni, Cu and Ga.[12,24] The microstructure of the disk membrane was examined by scanning electron microscopy (SEM) using a JEOL JSM-6700F field-emission instrument operating at an excitation voltage of 2 kV. The elemental composition of the membrane was determined by energy dispersive X-ray spectroscopy (EDXS), using an Oxford Instruments INCA-300 EDX spectrometer with an ultrathin window and at an excitation voltage of 20 kV.

### 2.3. Oxygen permeation experiments

The oxygen flux through the membranes with different thicknesses was investigated in the range of 800–975 °C using a home-made high-temperature oxygen permeation cell, which is described in detail elsewhere.[25,26] A commercial ceramic sealant (Huitian, Hubei, China) was used to seal the disk-shaped membrane onto an alumina tube. Synthetic air was fed (150 mL min$^{-1}$) to the feed side of the membrane, while He or $CO_2$ gas was fed to the sweep side. Unless specified otherwise a sweep gas flow rate of 30 mL min$^{-1}$ was maintained. Gas flow rates were calibrated with a soap bubble flow meter. The composition of the effluent was analyzed by on-line gas chromatography (GC, Agilent Technologies, 7890A). The leakage of oxygen was subtracted in the calculation of the oxygen flux.[25,27] The contribution of leakage to the apparent oxygen flux was below 0.5% in all cases.

## 3 Results and discussion

### 3.1. Phase analysis and microstructure

Fig. 2 shows the XRD patterns of $(PL)_{1.9}NCG$ and $(PL)_{2.0}NCG$ ceramics after sintering at 1230 °C for 10 h in air. Analysis of the patterns confirms that both materials adopt the tetragonal $K_2NiF_4$ structure (ICDD PDF number: 01-087-1679). No impurity phases are detected.[28,29] For a more precise evaluation of the influence of A-site deficiency on the XRD pattern, the reflections at 31.6°, 69° and 79° are magnified and compared in Fig. 2b–d, respectively. The 113 reflection of $(PL)_{1.9}NCG$ at 31.6° is slightly shifted to higher $2\theta$ values compared to that of $(PL)_{2.0}NCG$ as shown in Fig. 2b. The 324 and 400 reflections are shifted to a higher angle and merge with the 208 reflection, which is shifted to a lower angle, as shown in Fig. 2c. A similar phenomenon is found around 79° as shown in Fig. 2d, where the 414 and 420 reflections are found to be merged with the 228 reflection. These observations are consistent with the different lattice parameters of $(PL)_{1.9}NCG$ and $(PL)_{2.0}NCG$, which are reported in Table 1.

**19108** | *J. Mater. Chem. A*, 2015, **3**, 19107–19114

This journal is © The Royal Society of Chemistry 2015

*In situ* XRD measurements were performed on $(PL)_{1.9}NCG$ under a pure $CO_2$ atmosphere from room temperature to 1000 °C. As seen from Fig. 3, no additional reflections are found that would indicate the presence or formation of other phases, *e.g.*, carbonates. The results are consistent with those from our previous study, in which it was found that $(PL)_{2.0}NCG$ also possesses excellent chemical stability under $CO_2$ atmospheres.[29,30]

SEM micrographs of the $(PL)_{1.9}NCG$ and $(PL)_{2.0}NCG$ membranes, which were sintered at 1230 °C for 10 h in air, are presented in Fig. 4. As seen from this figure, both membranes show high density. The average grain area estimated from the micrographs is about 51 μm² for $(PL)_{1.9}NCG$, which is slightly higher than the value of 42 μm² found for $(PL)_{2.0}NCG$. Some fine-grained furnace dust particles are seen in both SEM micrographs. These could be successfully removed by polishing the membranes prior to permeation measurements as was revealed from SEM micrographs recorded after the polishing procedure.

Table 1 lists various properties of $(PL)_{1.9}NCG$ and $(PL)_{2.0}NCG$. The unit cell parameters of both materials are close. Compared to $(PL)_{2.0}NCG$, the lattice of $(PL)_{1.9}NCG$ has shrunk slightly in the *c*-axis direction and has expanded slightly in the *a–b* plane.[31,32] Furthermore, $(PL)_{1.9}NCG$ shows a higher relative

density, which might indicate that A-site deficiency enhances the sintering process.[33] The average thermal expansion coefficient of $(PL)_{1.9}NCG$ under a $CO_2$ atmosphere is $15.9 \times 10^{-6}$ K⁻¹, which is slightly higher than the value of $15.1 \times 10^{-6}$ K⁻¹ observed for $(PL)_{2.0}NCG$ under the same conditions.[30] Note further that the oxygen content of A-site deficient $(PL)_{1.9}NCG$, at 900 °C in air, is significantly less than that observed for A-site stoichiometric $(PL)_{2.0}NCG$. The latter suggests that A-site deficiency is mainly compensated by the removal of oxygen from the lattice.

### 3.2. Oxygen flux

An Arrhenius plot of the oxygen flux through a $(PL)_{1.9}NCG$ membrane with a thickness of 0.6 mm is shown in Fig. 5. Also included are data of oxygen permeation for $(PL)_{2.0}NCG$ from our previous study.[29] Similar oxygen fluxes are found whether using He or $CO_2$ as sweep gas, albeit at the lowest temperatures the measured oxygen flux using $CO_2$ as sweep gas tends to be slightly lower. The latter may be attributed to the adsorption of $CO_2$ molecules at the surface, thereby blocking the surface exchange reaction.[29,34] Compared to $(PL)_{2.0}NCG$, slightly lower activation energies are found for A-site deficient $(PL)_{1.9}NCG$. Apparent activation energies in the temperature range of 800–975 °C, using He as sweep gas, are 25 and 27 kJ mol⁻¹ for $(PL)_{1.9}NCG$ and $(PL)_{2.0}NCG$, respectively. At 900 °C, the oxygen flux through $(PL)_{1.9}NCG$ is $4.6 \times 10^{-7}$ mol cm⁻² s⁻¹ irrespective of the use of $CO_2$ or He as sweep gas. The observed oxygen flux is more than two times higher than the value of $1.9 \times 10^{-7}$ mol cm⁻² s⁻¹ observed for $(PL)_{2.0}NCG$ under the same conditions.[29] A-site cation deficiency thus has a large influence on the oxygen permeability.

The oxygen flux was further investigated as a function of membrane thickness. Oxygen permeation through dense mixed-conducting oxide membranes is governed by bulk diffusion and surface exchange. If bulk diffusion is the rate limiting step, the flux can be described by the Wagner equation,[5,35]

$$jO_2 = -\frac{RT}{4^2F^2L}\frac{\sigma_e\sigma_i}{\sigma_e + \sigma_i}\ln\frac{pO'_2}{pO''_2} \qquad (1)$$

where $jO_2$, $R$, $F$, $T$, $L$, $\sigma_e$, and $\sigma_i$ denote the oxygen flux, gas constant, Faraday constant, temperature, membrane thickness, and the partial electronic and ionic conductivity, respectively. $pO'_2$ is the oxygen partial pressure maintained at the feed side, while $pO''_2$ is the oxygen partial pressure at the sweep side. Hence, if the oxygen flux is entirely governed by bulk diffusion, the plot of the normalized oxygen flux $jO_2/\ln(pO'_2/pO''_2)$ *versus* reciprocal thickness ($1/L$) should be linear with the line intersecting the origin. Fig. 6 shows that the normalized oxygen fluxes for both $(PL)_{1.9}NCG$ and $(PL)_{2.0}NCG$ increase proportionally with $1/L$ for thicknesses greater than approximately 1.6 mm ($1/L = 0.635$ mm⁻¹), but depart from a linear relationship for smaller thicknesses. These results reveal that the oxygen flux is predominantly limited by bulk diffusion for a membrane thickness greater than ~1.6 mm and by surface exchange for smaller thicknesses.
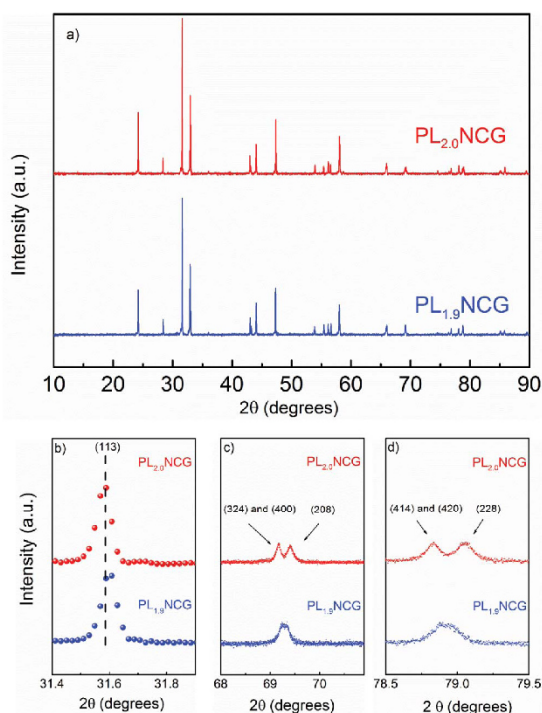


**Fig. 2** (a) XRD patterns of $(PL)_{1.9}NCG$ and $(PL)_{2.0}NCG$ after sintering at 1230 °C for 10 h in air, and (b) magnifications of selected regions of the patterns shown in (a).

**Table 1** Various parameters of $(PL)_{1.9}NCG$ and $(PL)_{2.0}NCG$. Values between parentheses are standard deviations. Experimental data were acquired from sintered ceramics or powder obtained from crushed ceramics

| | $\rho_{exp}$ g cm$^{-3}$ | $\rho_{exp}/\rho_{theo}$ % | Average grain size ($\mu m^2$) | Crystal symmetry (space group) | Cell parameters (Å) | Average thermal expansion coefficients in 30 °C–1000 °C under $CO_2$ ($10^{-6}$ K$^{-1}$) | Oxygen content at 900 °C in air |
|---|---|---|---|---|---|---|---|
| $(PL)_{2.0}NCG$ | 7.51(5) | 96(1) | 42(2) | Tetragonal *I4/mmm* | $a = b = 3.8305(4)$, $c = 12.5600(20)$ | 15.1 (ref. 30) | 4.25(2) |
| $(PL)_{1.9}NCG$ | 7.40(5) | 98(1) | 50(2) | Tetragonal *I4/mmm* | $a = b = 3.8345(4)$, $c = 12.5547(20)$ | 15.9(6) | 3.98(2) |

Since in both $(PL)_{1.9}NCG$ and $(PL)_{2.0}NCG$ the electronic conductivity predominates over the ionic conductivity, eqn (1) can be simplified to

$$jO_2 = -\frac{RT}{4^2F^2L}\sigma_i \ln \frac{pO'_2}{pO''_2} \qquad (2)$$

Using this equation, the ionic conductivity was calculated from the data of oxygen permeation measurements obtained for 2.3 mm thick membranes. At 900 °C, a value of 0.21 S cm$^{-1}$ is found for A-site deficient $(PL)_{1.9}NCG$, to be compared with 0.10 S cm$^{-1}$ found for A-site stoichiometric $(PL)_{2.0}NCG$. Increasing the sweep gas flow rate increases the oxygen partial pressure gradient across the membrane. Fig. 7 shows that the oxygen flux measured through a 0.6 mm thick membrane of $(PL)_{1.9}NCG$ at different temperatures increases upon increasing the flow rate of the He sweep gas.

### 3.3. Stability under $CO_2$

High oxygen flux and good chemical stability are two key factors for industrial application of oxygen transport membranes. Good $CO_2$ resistance was found for the A-site stoichiometric $(PL)_{2.0}NCG$.[29] To assess the stability of A-site deficient $(PL)_{1.9}NCG$ against carbonation, the oxygen permeation performance was studied by periodically changing the sweep gas between He and $CO_2$. As can be seen from Fig. 8, only a marginal, reversible change of the oxygen flux occurs

when the sweep gas is switched back and forth between He and $CO_2$. Fig. 9 shows the long-term oxygen permeation behavior of the $(PL)_{1.9}NCG$ membrane at 900 and 975 °C, using either He or pure $CO_2$ as sweep gas. Stable oxygen fluxes with no sign of deterioration are observed over 200 h. Comparing the XRD patterns of the $(PL)_{1.9}NCG$ membrane before and after the long-term permeation tests revealed no formation of second phases, as shown in Fig. 10. In particular, no evidence of carbonation formation was found. Fig. 11 depicts SEM/EDXS images of a cross-section of the $(PL)_{1.9}NCG$ membrane after the oxygen permeation tests. The results confirm a homogenous distribution of all elements. The observations confirm the excellent stability of $(PL)_{1.9}NCG$ under a $CO_2$ atmosphere. The observed behavior is in marked contrast with many earth-alkaline containing perovskite oxides whose oxygen permeation fluxes are found to decrease sharply upon $CO_2$ exposure.[9,10]

### 3.4. Influence of A-site deficiency on oxygen transport

Data from this study demonstrate that A-site deficient $(PL)_{1.9}NCG$ shows superior oxygen transport properties compared to A-site stoichiometric $(PL)_{2.0}NCG$. As was mentioned in the introduction, similar observations have been reported by Ishihara and colleagues for A-site deficient $Nd_{1.9}(Ni_{0.75}Cu_{0.25})_{0.95}Ga_{0.05}O_4$ and $Pr_{1.9}Ni_{0.75}Cu_{0.25}Ga_{0.05}O_4$ compared to their A-site stoichiometric forms.[20,21] The latter
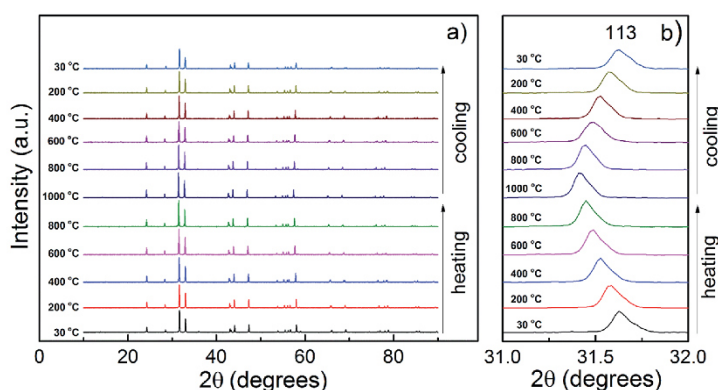


**Fig. 3** (a) *In-situ* high-temperature XRD patterns of calcined $(PL_{1.9})NCG$ powder collected during exposure to pure $CO_2$, and (b) magnified view of the (113) reflection. Diffractograms were recorded in intervals of 100 °C while not all are displayed for clarity reasons.
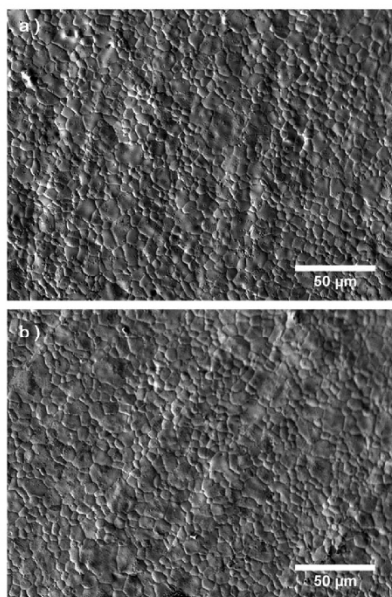
50

**Fig. 4** Surface SEM micrographs of sintered (a) $(PL)_{2.0}NCG$ and (b) $(PL)_{1.9}NCG$ membranes.

authors attributed the phenomenon to grain size effects, increased concentration of interstitial oxygen, or enhanced diffusivity of interstitial oxygen.[20,21,36] It may be noted that the grain sizes found in this study for $(PL)_{1.9}NCG$ and $(PL)_{2.0}NCG$ are similar (see Fig. 4), while the oxygen hyperstoichiometry decreases rather than increases by introducing A-site deficiency
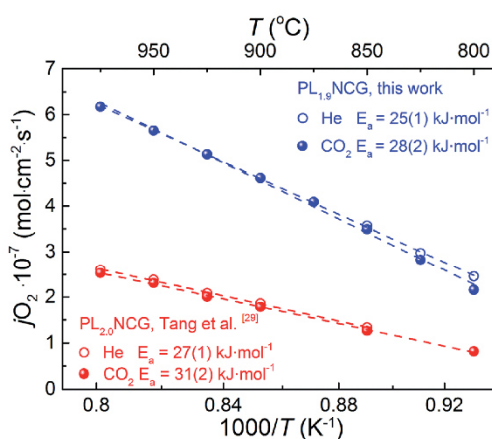
(see Table 1). Clearly other factors must be taken into to account for the observations.

Hydrogen reduction experiments show that, at 900 °C, $(PL)_{2.0}NCG$ is hyperstoichiometric with $4 + \delta = 4.25$, while $(PL)_{1.9}NCG$ is found to be almost oxygen stoichiometric, $4 + \delta = 3.98$ (Table 1). At the same time the oxygen fluxes through $(PL)_{1.9}NCG$ membranes, in the range of 800–975 °C, exceed those through $(PL)_{2.0}NCG$ membranes by a factor of 2–3 (Fig. 5). Interestingly, despite the apparent lowering in the ionic charge carrier concentration by introducing A-site deficiency, oxygen transport has increased. The results are taken as evidence that the ionic charge carriers in $(PL)_{1.9}NCG$ must exhibit a higher diffusivity that overcompensates the loss in the ionic charge carrier concentration compared to those in $(PL)_{2.0}NCG$. As the oxygen content of $(PL)_{1.9}NCG$ is found to be almost stoichiometric, the role of oxygen vacancy diffusion becomes significant. Accordingly, the enhanced oxygen transport observed for $(PL)_{1.9}NCG$ can be accounted for by fast oxygen transport *via* a vacancy mechanism. Such a conclusion would be consistent with the finding by Cleave *et al.* that the most likely pathway for oxygen migration in $La_2NiO_4$, *i.e.*, with the lowest activation energy, is a vacancy mechanism, involving transfer between two apical (O2) sites.[17]



**Fig. 5** Temperature dependence of the oxygen permeation flux for $(PL)_{1.9}NCG$ and $(PL)_{2.0}NCG$, measured using different sweep gases. Data for both materials were collected under similar conditions. The membrane thicknesses are 0.6 mm. Data for $(PL)_{2.0}NCG$ were taken from our previous study.[29] Apparent activation energies are listed in the figure.
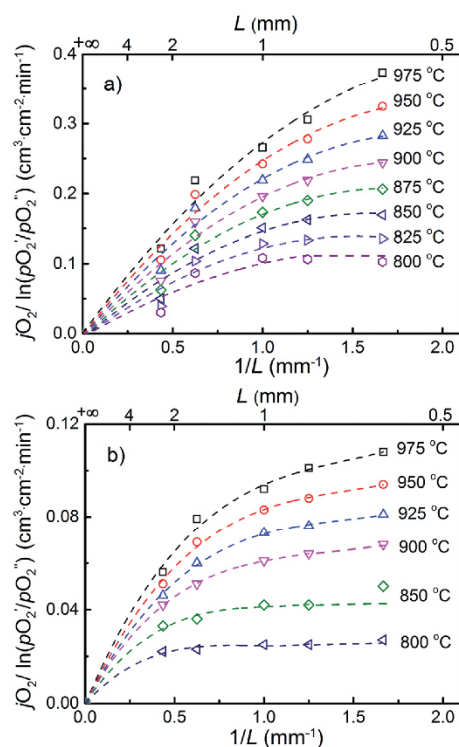


**Fig. 6** Dependence of the normalized oxygen flux on the inverse membrane thickness for (a) $(PL)_{1.9}NCG$ and (b) $(PL)_{2.0}NCG$. Data for the latter were taken from our previous study.[29] Note the different vertical scales.

This journal is © The Royal Society of Chemistry 2015

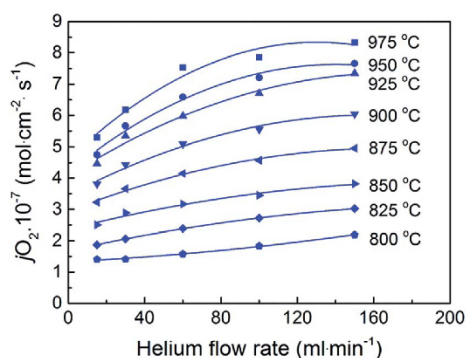*J. Mater. Chem. A*, 2015, **3**, 19107 19114 | **19111**

51

Fig. 7 Dependence of the oxygen flux through a 0.6 mm thick $(PL)_{1.9}NCG$ membrane at different temperatures on the He sweep gas flow rate.
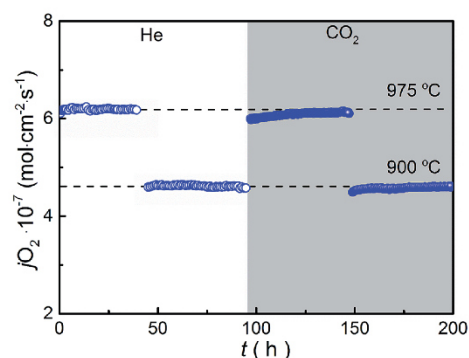


Fig. 9 Long-term stability test of the oxygen permeation flux through a 0.6 mm thick $(PL)_{1.9}NCG$ membrane. Data were collected at two different temperatures, using He and $CO_2$ as sweep gases as indicated in the figure. Horizontal dashed lines are guides to the eye.

The role of a vacancy mechanism in overall oxygen transport in $(PL)_{1.9}NCG$ can be illustrated by simple defect chemical considerations. The concentration of oxygen vacancies is determined by anion Frenkel disorder. Using the standard Kröger–Vink defect notation, this equilibrium can be expressed as

$$O_O^\times + V_i \rightleftarrows O_i'' + V_O^{\cdot\cdot} \qquad (3)$$
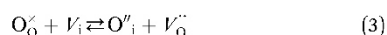
Close to stoichiometric conditions, *i.e.*, in the regime for dilute defect concentrations, and ignoring defect association, the anti-Frenkel equilibrium constant $K_{AF}$ can be presented as

$$K_{AF} \approx [O_i''][V_O^{\cdot\cdot}] \approx \delta_i \cdot \delta_v \qquad (4)$$

where $\delta_i$ and $\delta_v$ are the molar fractions of oxygen interstitials and oxygen vacancies, respectively. The overall non-stoichiometry parameter is given by $\delta = \delta_i - \delta_v$. Eqn (4) can be used to calculate $\delta_i$ and $\delta_v$ provided that $K_{AF}$ is known. Data of such calculation, assuming $K_{AF} = 10^{-2}$, are shown in Fig. 12.

The Nernst–Einstein equation can be used to express the ionic conductivity in terms of the defect concentrations and their diffusivities,

$$\sigma_i = \frac{4F^2}{RTV_m}(\delta_i D_i + \delta_v D_v) \qquad (5)$$

Where $V_m$ is the molar volume, and $D_i$ and $D_v$ are the diffusivities of interstitials and vacancies, respectively. Eqn (5) can be rewritten into,

$$\sigma_i = \frac{4F^2}{RTV_m}D_i(\delta_i + \delta_v\xi) \qquad (6)$$

where we defined the parameter $\xi = D_v/D_i$. The relative magnitudes of the diffusivities affect the overall ionic conductivity, as is illustrated in Fig. 13. If the defect diffusivities are equal ($\xi = 1$), the ionic conductivity is at minimum at the stoichiometric composition ($\delta = 0$). The plot of the ionic conductivity *versus* $\delta$ obtained for $\xi = 1$ is symmetrical about $\delta = 0$. With increasing $\xi$, the minimum shifts to higher $\delta$ values. In this case, a higher ionic conductivity is obtained for hypostoichoimetric ($\delta < 0$) than for hyperstoichiometric ($\delta > 0$) compositions of a similar
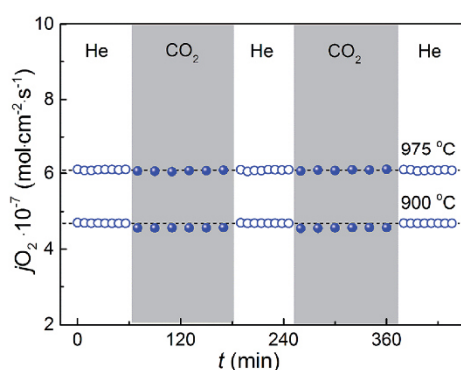


Fig. 8 Oxygen permeation flux through a 0.6 mm thick $PL_{1.9}NCG$ membrane at 900 and 975 °C. Data were collected by periodically changing the sweep gas between He and $CO_2$. Horizontal dashes lines are guides to the eye.
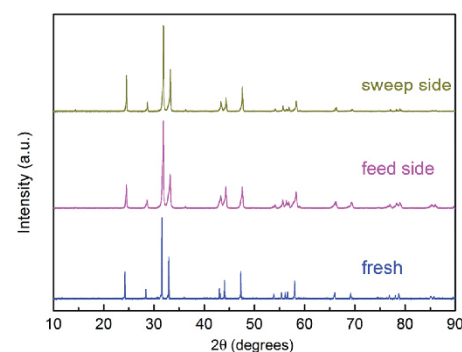


Fig. 10 XRD patterns of fresh and spent $(PL)_{1.9}NCG$ membranes after long-term oxygen permeation tests.
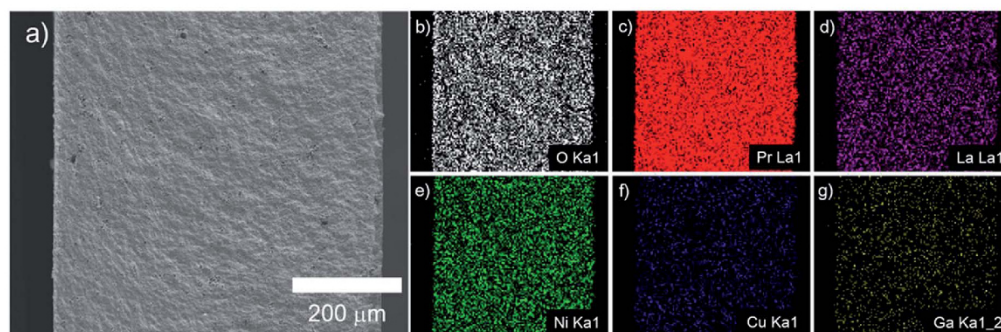
Fig. 11 (a) SEM, and (b–g) EDXS images of a cross-section of the (PL)$_{1.9}$NCG membrane after the long-term permeation tests.

absolute magnitude. It should be emphasized that the value obtained for $\xi$ is determined by the value of $K_{AF}$. It is easily demonstrated by calculation that, at given value of $K_{AF} = 10^{-2}$, $\xi$ must be 10 to yield a two times higher ionic conductivity for (PL)$_{1.9}$NCG, with $\delta = -0.02$, than for (PL)$_{2.0}$NCG, with $\delta = 0.25$, as is experimentally observed (see Table 1).

In the A$_2$BO$_4$ oxides (with the K$_2$NiF$_4$ structure), the interstitial oxygen ions O3 are in a tetrahedral environment of the A-site cations as well as of the apical oxygen O2.[15] MD simulations show only a weak dependence of the diffusivity of oxygen interstitials in Pr$_2$NiO$_{4+\delta}$ with the degree of oxygen hyperstoichiometry.[37] The observations are consistent with MD simulations of oxygen transport in La$_2$NiO$_{4+\delta}$.[16] Several researchers have investigated the effect of acceptor-doping on the oxygen diffusivity in oxides with the K$_2$NiF$_4$ structure. Acceptor doping reduces the concentration of oxygen interstitials. The corresponding results of $^{18}$O tracer diffusion studies by secondary-ion mass spectroscopy (SIMS) show the oxygen diffusivities in La$_{2-x}$Sr$_x$NiO$_{4+\delta}$ and

La$_{2-x}$Sr$_x$CuO$_{4+\delta}$ to be suppressed by several orders of magnitudes below the diffusivities for the undoped materials.[12,38–41] For small Sr addition, the observations are explained by the concomitant decrease in the concentration of oxygen interstitials.[12,41] For the higher Sr addition ($x \leq 0.2$), where charge compensation of the acceptor dopant occurs, in part, by the formation of oxygen vacancies, these are explained by the occurrence of defect associates $V_O^{\cdot\cdot} - Sr'_{La}$, or vacancy ordering, due to the electrostatic interactions between oppositely charged oxygen vacancies and dopant cations. These findings are in apparent contrast with those from the present work. Assuming that, on the introduction of A-site deficiency, A-site cation vacancies ($V'''_{pr}$) and oxygen vacancies are formed, defect associates in (PL)$_{1.9}$NCG are likely on the basis of simple charge considerations. The high oxygen transport rates observed in (PL)$_{1.9}$NCG, however, provide no evidence of their detrimental influence on ionic conductivity. Our results are believed to have general relevance for optimizing
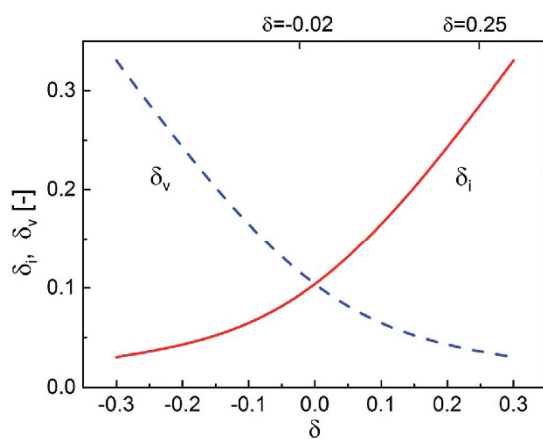


Fig. 12 Concentration of interstitial oxygen ions ($\delta_i$) and oxygen vacancies ($\delta_V$) as a function of the overall nonstoichiometry parameter $\delta = \delta_i - \delta_V$, calculated using eqn (4), assuming $K_{AF} = 10^{-2}$. Values of $\delta$, which are indicated on the top scale, refer to (PL)$_{1.9}$NCG and (PL)$_{2.0}$NCG (see Table 1).
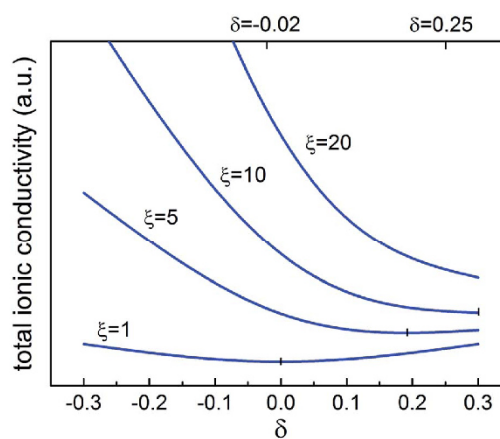


Fig. 13 The influence of oxygen nonstoichiometry on the apparent ionic conductivity calculated for different values of the oxygen vacancy/oxygen interstitial diffusivity ratio $\xi = D_V/D_i$. Values of $\delta$, which are indicated on the top scale, refer to (PL)$_{1.9}$NCG and (PL)$_{2.0}$NCG (see Table 1).

53

the ionic conductivity of $A_2BO_4$ oxides by tuning the A/B-site stoichiometry.

## 4 Conclusion

$(PL)_{1.9}NCG$ has been studied with a view to determine the effects of A-site deficiency on structural parameters, oxygen transport and stability under $CO_2$ atmospheres. $(PL)_{1.9}NCG$ is found to exhibit higher oxygen transport rates compared with its cation stoichiometric parent phase. The high oxygen transport rates are attributed to highly mobile oxygen vacancies and charge compensating cationic vacancies. The high structural stability towards carbonation gives $(PL)_{1.9}NCG$ potential for use as a membrane, e.g., in oxy-fuel combustion processes with $CO_2$ capture. As exemplified in this work, the concept of A-deficiency can be used to optimize oxygen transport in layered $A_2BO_4$ oxides (with the $K_2NiF_4$ structure).

## Acknowledgements

## Notes and references

1 J. D. Figueroa, T. Fout, S. Plasynski, H. McIlvried and R. D. Srivastava, *Int. J. Greenhouse Gas Control*, 2008, **2**, 9–20.
2 C. Gough, *Int. J. Greenhouse Gas Control*, 2008, **2**, 155–168.
3 R. Kneer, D. Toporov, M. Förster, D. Christ, C. Broeckmann, E. Pfaff, M. Zwick, S. Engels and M. Modigell, *Energy Environ. Sci.*, 2010, **3**, 198–207.
4 X. Tan, K. Li, A. Thursfield and I. S. Metcalfe, *Catal. Today*, 2008, **131**, 292–304.
5 J. Sunarso, S. Baumann, J. M. Serra, W. A. Meulenberg, S. Liu, Y. S. Lin and J. C. Diniz da Costa, *J. Membr. Sci.*, 2008, **320**, 13–41.
6 K. Zhang, J. Sunarso, Z. Shao, W. Zhou, C. Sun, S. Wang and S. Liu, *RSC Adv.*, 2011, **1**, 1661–1676.
7 L. Qiu, T. H. Lee, L. M. Liu, Y. L. Yang and A. J. Jacobson, *Solid State Ionics*, 1995, **76**, 321–329.
8 Z. Shao, W. Yang, Y. Cong, H. Dong, J. Tong and G. Xiong, *J. Membr. Sci.*, 2000, **172**, 177–188.
9 M. Arnold, H. Wang and A. Feldhoff, *J. Membr. Sci.*, 2007, **293**, 44–52.
10 J. Yi, M. Schroeder, T. Weirich and J. Mayer, *Chem. Mater.*, 2010, **22**, 6246–6253.
11 V. Kharton, A. Kovalevsky, E. Tsipis, A. Viskup, E. Naumovich, J. Jurado and J. Frade, *J. Solid State Electrochem.*, 2002, **7**, 30–36.
12 E. Bochm, J. Bassat, P. Dordor, F. Mauvy, J. Grenier and P. Stevens, *Solid State Ionics*, 2005, **176**, 2717–2725.
13 M. Yashima, *J. Ceram. Soc. Jpn.*, 2009, **117**, 1055–1059.
14 J. M. Bassat, P. Odier, A. Villesuzanne, C. Marin and M. Pouchard, *Solid State Ionics*, 2004, **167**, 341–347.
15 L. Minervini, R. W. Grimes, J. A. Kilner and K. E. Sickafus, *J. Mater. Chem.*, 2000, **10**, 2349–2354.
16 A. Chroneos, D. Parfitt, J. A. Kilner and R. W. Grimes, *J. Mater. Chem.*, 2010, **20**, 266.
17 A. R. Cleave, J. A. Kilner, S. J. Skinner, S. T. Murphy and R. W. Grimes, *Solid State Ionics*, 2008, **179**, 823–826.
18 M. Yashima, H. Yamada, S. Nuansaeng and T. Ishihara, *Chem. Mater.*, 2012, **24**, 4100–4113.
19 M. Yashima, M. Enoki, T. Wakita, R. Ali, Y. Matsushita, F. Izumi and T. Ishihara, *J. Am. Chem. Soc.*, 2008, **130**, 2762–2763.
20 T. Ishihara, N. Sirikanda, K. Nakashima, S. Miyoshi and H. Matsumoto, *J. Electrochem. Soc.*, 2010, **157**, B141.
21 A. Kawahara and T. Ishihara, *Electrochem. Solid-State Lett.*, 2010, **13**, B76.
22 A. Feldhoff, M. Arnold, J. Martynczuk, T. M. Gesing and H. Wang, *Solid State Sci.*, 2008, **10**, 689–701.
23 J. Xue, Q. Liao, Y. Wei, Z. Li and H. Wang, *J. Membr. Sci.*, 2013, **443**, 124–130.
24 W. Chen, A. Nijmeijer and L. Winnubst, *Solid State Ionics*, 2012, **229**, 54–58.
25 H. Luo, B. Tian, Y. Wei, H. Wang, H. Jiang and J. Caro, *AIChE J.*, 2010, **56**, 604–610.
26 J. Xue, Q. Zheng, Y. Wei, K. Yuan, Z. Li and H. Wang, *Ind. Eng. Chem. Res.*, 2012, **51**, 4703–4709.
27 H. Wang, R. Wang, D. T. Liang and W. Yang, *J. Membr. Sci.*, 2004, **243**, 405–415.
28 C. Tablet, G. Grubert, H. Wang, T. Schiestel, M. Schroeder, B. Langanke and J. Caro, *Catal. Today*, 2005, **104**, 126–130.
29 J. Tang, Y. Wei, L. Zhou, Z. Li and H. Wang, *AIChE J.*, 2012, **58**, 2473–2478.
30 Y. Wei, O. Ravkina, T. Klande, H. Wang and A. Feldhoff, *J. Membr. Sci.*, 2013, **429**, 147–154.
31 W. Cheikh-Rouhou Koubaa, M. Koubaa, A. Cheikh-Rouhou, W. Boujelben and A. M. Haghiri-Gosnet, *J. Alloys Compd.*, 2008, **455**, 67–72.
32 W. Zhou, R. Ran, Z. Shao, W. Jin and N. Xu, *J. Power Sources*, 2008, **182**, 24–31.
33 K. Shan and X.-M. Guo, *Mater. Lett.*, 2013, **113**, 126–129.
34 X. Tan, N. Liu, B. Meng, J. Sunarso, K. Zhang and S. Liu, *J. Membr. Sci.*, 2012, **389**, 216–222.
35 C. Wagner, *Z. Phys. Chem. B*, 1933, **21**, 25–41.
36 S. Miyoshi, T. Furuno, O. Sangoanruang, H. Matsumoto and T. Ishihara, *J. Electrochem. Soc.*, 2007, **154**, B57.
37 D. Parfitt, A. Chroneos, J. A. Kilner and R. W. Grimes, *Phys. Chem. Chem. Phys.*, 2010, **12**, 6834–6836.
38 Z. Li, R. Haugsrud and T. Norby, *Solid State Ionics*, 2011, **184**, 42–46.
39 E. J. Opila, H. L. Tuller, B. J. Wuensch and J. Maier, *J. Am. Ceram. Soc.*, 1993, **76**, 2363–2369.
40 J. Routbort, S. Rothman, B. Flandermeyer, L. Nowicki and J. Baker, *J. Mater. Res.*, 1988, **3**, 116–121.
41 S. J. Skinner and J. A. Kilner, *Solid State Ionics*, 2000, **135**, 709–712.

19114 | *J. Mater. Chem. A*, 2015, **3**, 19107–19114

This journal is © The Royal Society of Chemistry 2015

54

## 2.4 Improvement of the oxygen permeation and stability of Ruddlesden-Popper-type membrane by surface modification

Jian Xue, Li Chen, Yanpeng Suo, Yanying Wei, Haihui Wang and Armin Feldhoff

# Improvement of the oxygen permeation and stability of Ruddlesden-Popper-type membrane by surface modification

Jian Xue,[*,a] Li Chen,[b] Yanpeng Suo,[a] Yanying Wei,[a,b] Haihui Wang,[*,b,c] and Armin Feldhoff,[*,a]

[a] *Institute of Physical Chemistry and Electrochemistry, Leibniz University Hannover, Callinstrasse 3A, D-30167 Hannover, Germany*

[b] *School of Chemistry & Chemical Engineering, South China University of Technology, 381 Wushan Road, 510640 Guangzhou, China*

[c] *School of Chemical Engineering, The University of Adelaide, Adelaide, SA 5005, Australia*

ABSTRACT:

A ceramic membrane, made of A-site deficient $(Pr_{0.9}La_{0.1})_{1.9}Ni_{0.74}Cu_{0.21}Ga_{0.05}O_{4\pm\delta}$ ($(PL)_{1.9}NCG$) possesses considerable oxygen transport rates and good chemical stability in the presence of $CO_2$, while it decomposes under oxygen-containing atmosphere at intermediate temperature during the oxygen separation process. In this work, we propose a feasible approach to improve its oxygen permeability and long-term phase stability by surface coating. A porous layer of $La_{0.6}Sr_{0.4}CoO_3$ perovskite was coated on one surface (sweep side or feed side) or both surfaces of the $(PL)_{1.9}NCG$ membrane with 0.6 mm thickness and the oxygen permeation performance was measured in the temperature range of 800-975 °C. The results reveal that the sweep-side coated membrane exhibits largely enhanced permeation fluxes compared to that through feed-side coated membrane, while the feed-side coated membrane shows better phase stability under the same conditions. The both side modified membrane combines abovementioned advantages, and it shows 57 % enhanced and stable oxygen permeation flux during the long-term test at 800 °C. The observed catalytic effects are discussed based on the oxygen surface exchange properties of $(PL)_{1.9}NCG$ and the mechanism of the oxygen transporting membrane in detail.

*Keywords*: Surface modification, Ruddlesden-Popper oxide, Oxygen permeation membrane, Phase stability

## 1. Introduction

Oxygen is an important raw material for human and widely used in the production cycle of steel, plastics and textiles, brazing, welding and cutting of steels and other metals, rocket propellant, in oxygen therapy and life support systems in aircraft, submarines, spaceflight and diving. Annually, 100 million tonnes of $O_2$ are extracted from air for industrial uses [1]. Oxygen gas can be produced through cryogenic distillation, electrolysis of water or pressure swing adsorption. The first two methods are energy-intensive while the latter cannot produce high purity oxygen [2, 3].

Recently, new advanced technology with mixed oxygen-ionic and electronic conducting (MIEC) membranes have attracted considerable attention due to their applications in oxygen separation with absolute selectivity from an oxygen-containing atmosphere at high temperature under a driving force (an oxygen chemical potential gradient or an electrical potential gradient) [4]. Such membranes systems features high energy-efficiency, clean, simplified operation and can be integrated with some industry processes such as methane coupling, partial oxidation of methane into synthesis gas, methane dehydroaromatization and oxyfuel combustion [5-7].

In a dense MIEC membrane, oxygen could be separated through three progressive steps under an oxygen chemical potential gradient as shown in Fig. 1: (i) the surface-exchange reaction on the feed side, oxygen insertion (oxygen adsorption and dissociation); (ii) the simultaneous bulk diffusion of charged oxygen species (oxygen vacancies or interstitial oxygen) and electrons or electron holes in the bulk phase; (iii) the surface-exchange reaction on the sweep side, oxygen release (oxygen association and desorption) [4, 8, 9].
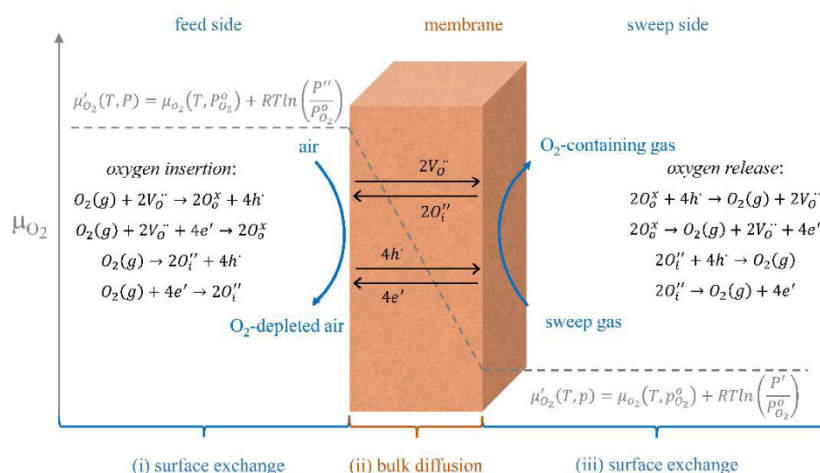


**Fig. 1.** Schematic diagram of the different sections involved in the oxygen transport during oxygen permeation

For a relatively thick membrane, the bulk diffusion process plays a dominant role in the oxygen permeation process, and the permeation flux is proportional to the reciprocal of the membrane thickness, which can be expressed by the Wagner equation [4, 10, 11]:

$$j_{O_2} = -\frac{RT}{4^2 F^2 L} \int_{lnP'_{O_2}}^{lnP''_{O_2}} \frac{\sigma_{el}\sigma_{ion}}{\sigma_{el}+\sigma_{ion}} dlnP_{O_2} \qquad (1)$$

Where $j_{O_2}$, R, F, T, L, $\sigma_{el}$, and $\sigma_{ion}$ denote the oxygen flux, gas constant, Faraday constant, temperature, membrane thickness, and the electronic and ionic conductivity, respectively. $P''_{O_2}$ is the oxygen partial pressure maintained at the feed side, while $P'_{O_2}$ is the oxygen partial pressure at the sweep side. In this case, reducing the membrane thickness could result in increased oxygen permeation flux, while the relative limiting effect of surface exchange also increased. When the thickness is less than a critical value $L_C$ (the characteristic thickness, which is defined as the membrane thickness at which the oxygen permeation is equally determined by the surface-exchange kinetics and bulk-diffusion), the surface exchange process becomes the rate-controlling step [4]. Therefore, further increase of the oxygen permeation flux can be achieved by coating a porous catalytic layer on the membrane surfaces [12-19].In our previous work, it was shown that the A-site deficient $(Pr_{0.9}La_{0.1})_{1.9}Ni_{0.74}Cu_{0.21}Ga_{0.05}O_{4-\delta}$ ((PL)$_{1.9}$NCG), with the K$_2$NiF$_4$ structure (the first member of the Ruddlesden-Popper oxides $A_{n-1}B_nO_{3n-1}$ with n = 1) possesses twice higher oxygen permeation flux than that of A-site stoichiometric one due to its highly mobile oxygen vacancies which compensating the A-site deficiency as described in detail in our previous work [20]. However, the Pr$_2$NiO$_4$-based Ruddlesden-Popper-type materials are not stable in oxidizing atmosphere at intermediate temperature which decompose into the multilayered perovskite $Pr_4Ni_3O_{10+\delta}$ (higher member of the Ruddlesden-Popper oxides with n = 3) and $PrO_{2+\delta}$ [21]. Although their phase stability can be slightly improved by the introduction of A-site deficiency, while it is not enough to stand the practice conditions as discussed in detail previous [21]. Moreover, the oxygen flux through a thick membrane is predominantly limited by bulk diffusion. For thinner membranes, the limitation by the surface oxygen exchange comes into play. Therefore, in this study, we explored the influence of surface modification on the oxygen permeation flux and the phase stability of thin (PL)$_{1.9}$NCG membrane (0.6 mm) in oxygen-containing atmosphere. Perovskite $La_{0.6}Sr_{0.4}CoO_3$ (LSC) was chosen as the coated layer because it has been widely used as a cathode material for intermediate temperature solid oxide fuel cells and an effective coating material for oxygen permeable membrane due to its good oxygen catalytic properties, thus it was chosen as the catalyst here [14, 22, 23].

## 2. Experimental

### 2.1. Materials preparation

The powders of (PL)$_{1.9}$NCG and LSC were prepared by a combined citrate and ethylene-diamine-tetraacetic-acid (EDTA) method as described previously [24, 25]. The powders were uniaxially pressed at 20 MPa to obtain green pellets followed by sintering in air at 1230 °C for 10 h. The density of the sintered disks was measured by the Archimedes method using distilled water. Sintered ceramics with a relative density higher than 95% were selected as membranes for the oxygen permeation experiments. The membranes were polished to the desired thickness using 1200 grit-sandpaper and then washed with ethanol. Then the mixture of LSC and terpilenol was brushed onto the membrane surface. Post treatment was conducted to remove the organic additives at 1000 °C for 2 h.

### 2.2. Sample characterization

Powder X-ray diffraction (PXRD) measurements were performed on a Bruker D8 Advance diffractometer (Bruker AXS GmbH) to characterize the phase evolution of the membranes and the coating materials. The coated membranes were observed by using a field-emission scanning electron microscope (FE-SEM) (JEOL JSM-6700F). Thermogravimetric analyzer (Netzsch 449C) was used to detected the oxygen surface exchange properties of the (PL)$_{1.9}$NCG. About 100 mg powder was put into an alumina pan and heated to 950 °C in air. When the weight of the sample did not change anymore, air was exchanged to nitrogen quickly. After 40 minutes, when the weight did not change remarkably, nitrogen was exchanged with air again. The same procedure were repeated at 900 °C, 850 °C, 800 °C, respectively.

### 2.3. Oxygen permeation measurement

The oxygen flux through the LSC-coated (PL)$_{1.9}$NCG was investigated in the temperature range of 800-975 °C with a 0.6 mm thick membrane using a home-made high-temperature oxygen permeation cell, which was described in detail elsewhere [26, 27]. The coated membrane was sealed on an Al$_2$O$_3$ tube with a ceramic sealant (Huitian, Hubei, China). One side was fed with synthetic air (150 ml min$^{-1}$), and the other side was swept with He gas (30 ml min$^{-1}$). Gas flow rates were controlled using a mass flow controller (Bronkhorst GmbH) and calibrated with a soap bubble counter. The composition of the effluent was analyzed by on-line coupled gas chromatography (GC, Agilent Technologies, 7890A). The leakage of oxygen, because of imperfect sealing, was subtracted in the calculation of the oxygen flux. The contribution of leakage to the apparent oxygen flux was below 5 % in all cases. The calculation of oxygen permeation flux was demonstrated in detail in our previous papers [21, 28].

## 3. Result and discusstion

### 3.1. Characterization of materials

The rate of oxygen permeation in general, is governed by both the bulk diffusion of membrane and surface oxygen-exchange kinetics. When the bulk diffusion is determining the rates, the oxygen flux follows Wagner equation as described in Eq.1 [4, 10, 11]. The relationship between the oxygen flux and the inverse of the membrane thickness should be linear when the oxygen transport through the membrane is controlled by bulk diffusion. Fig. 2a shows however that the relationship for (PL)$_{1.9}$NCG membrane is not linear anymore when the thickness is less than 1.6 mm, indicating that the effect of surface exchange comes into account [20].

When the oxygen permeation flux is limited by both bulk diffusion and surface exchange, the oxygen permeation flux under small oxygen gradient, the Wagner equation is modified to [8, 29],

$$j_{O_2} = -\frac{1}{1+(2L_C/L)} \frac{RT}{4^2 F^2 L} \int_{lnP'_{O_2}}^{lnP''_{O_2}} \frac{\sigma_{el}\sigma_{ion}}{\sigma_{el}+\sigma_{ion}} dlnP_{O_2} \quad (2)$$

Where $L_C$ ($L_C$ = D/k, D is the bulk diffusion coefficient and k is the surface exchange coefficient, respectively) is the characteristic thickness. In Eq. 2, there are two variables ($L_C$ and L) that change the oxygen permeation flux under the fixed oxygen gradient. After simple modification of Eq. 2 by incorporating the thickness-independent parameters into a single constant C, which is the specific permeation flux at a specific oxygen gradient and temperature [16, 30]:

$$j_{O_2} = -\frac{1}{1+\left(\frac{2L_C}{L}\right)} \frac{C}{L} = -\frac{C}{L+2L_C} \qquad (3)$$

Both the C and $L_C$ values could be estimated by using the least-squares fitting method and are varied independently [16, 30],
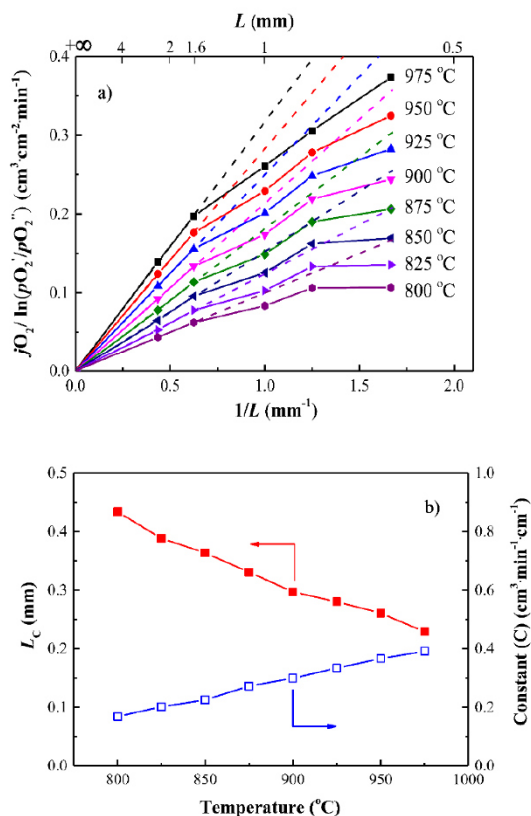
**Fig. 2.** Oxygen permeability of (PL)$_{1.9}$NCG: (a) Dependence of the normalized oxygen flux on the inverse membrane thickness, data were taken from our previous study [20]; (b) the characteristic membrane thickness ($L_C$) and values of the constant (C), which were estimated by fitting the experimental permeability results shown in Fig. 3a. Conditions: The air flow rates in the feed side are 150 mL/min. The flow rates at the sweep side are 30 mL/min.

$$\left(j_{O_2} - \frac{C}{L+2L_C}\right)^2_{sum} = Minimum \qquad (4)$$

The fitting results at different temperatures are shown in Fig. 2b. With increasing temperature from 800 to 975 °C, the $L_C$ values decrease from 0.43 to 0.22 mm and C values increase from 0.17 to 0.39 cm$^3$·min$^{-1}$·cm$^{-1}$. This implies that the surface exchange become more dominate for the oxygen transport through the (PL)$_{1.9}$NCG membrane with decreasing temperature and membrane thickness. Under the premise of membrane mechanical strength, we reduce the (PL)$_{1.9}$NCG membrane thickness to 0.6 mm in which the surface exchange plays a relative significant role in the oxygen permeation process. And enhanced permeation flux could be achieved by surface coating.

Herein, we apply a typical perovskite LSC as the surface exchange catalyst [22, 23]. Fig. 3 depicts the room temperature PXRD patterns of the LSC and (PL)$_{1.9}$NCG samples after calcination at 1000 °C for 10 h. The PXRD patterns of LSC are identified as single perovskite phase and that of (PL)$_{1.9}$NCG is confirmed as K$_2$NiF$_4$ structure phase, no peaks other than abovementioned two phase have been observed on the PXRD patterns [20, 21].
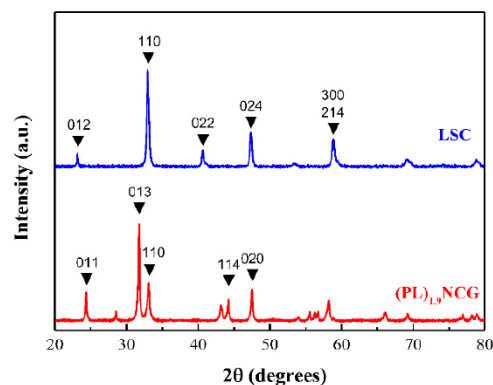


**Fig. 3.** Powder XRD patterns of LSC and (PL)$_{1.9}$NCG powders after calcination at 1000 °C for 10 h. The crystal structures of LSC and (PL)$_{1.9}$NCG are Hexagonal and Tetragonal respectively.
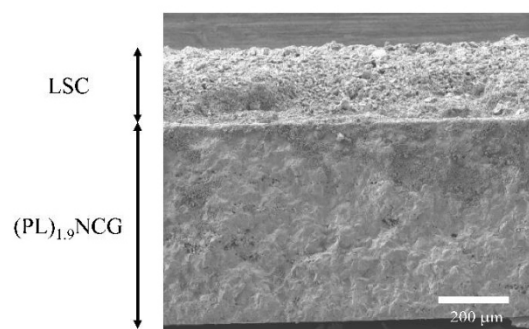


**Fig. 4.** SEM micrographs of the cross-section of the LSC-coated (PL)$_{1.9}$NCG membrane.

The SEM micrographs of the coated membrane are shown in Fig. 4. It could be distinguished that the coated LSC layer is porous with around 200 μm thickness. The LSC layer was porous due to the volatilization of organic solution during the post treatment. This porosity would provide adequate adsorption or desorption sites and increase the effective surface area of the (PL)$_{1.9}$NCG membrane [14, 31, 32].

### 3.2. Oxygen permeability of the membranes

Fig. 5 shows comparison of the oxygen permeation fluxes of (PL)$_{1.9}$NCG membrane with or without LSC catalyst coated. The sweep-side and both sweep- and feed-sides coated (PL)$_{1.9}$NCG membranes show significant enhancement in oxygen permeation fluxes while the feed-side coated one shows modest improvement. The additional porous coating increases the surface exchange kinetics, which results from an increase of the surface exchange between the gas phase and the membrane.

Fig. 6 shows the improvement of the oxygen permeation flux through the LSC modified (PL)$_{1.9}$NCG membranes as a function of temperature. It can be seen that the improvement percentage of both side coated membrane are higher than other two type membranes and decreases from 57% to 36% with increasing temperature as the relative limiting effect of the bulk diffusion gradually becomes more noticeable; similar results are also observed by other researchers [33].
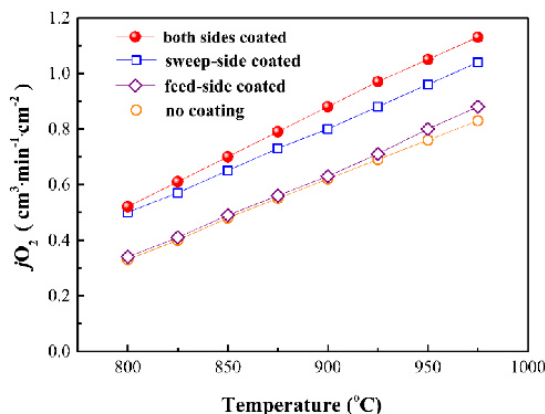
**Fig. 5.** Temperature dependence of oxygen permeation fluxes of the (PL)₁.₉NCG membranes with or without LSC-coated membrane. Conditions: The air flow rates in the feed side are 150 mL/min. The flow rates at the sweep side are 30 mL/min. The thicknesses of (PL)₁.₉NCG membranes are 0.6 mm each.

The enhancement of sweep-side coated membrane are 51% at 800 °C and 25% at 975 °C, that are much higher than that of feed-side coated membrane which are around 5%. Similar results were reported in GdBaCo₂O₅₊δ coated Ba₀.₅Sr₀.₅Co₀.₈Fe₀.₂O₃₋δ membranes, in which the oxygen permeation flux with a single coating layer on the air side can rise by 16%, while a single coating on the helium side will result into a rise of 23%, respectively [31]. Joo et al. also found a modest increase in the oxygen flux with a LSC feed-side coated 80 vol.% Ce₀.₉Gd₀.₁O₂₋δ-20 vol.% La₀.₇Sr₀.₃MnO₃₊δ dual-phase membrane, while improved by about 1 order of magnitude by treating the permeate-side surface [16]. This clearly indicates that the oxygen surface exchange at feed-side (oxygen-rich surface) is not the rate determining step of the oxygen permeation through (PL)₁.₉NCG membranes with the thickness of 0.6 mm and the oxygen flux is indeed governed by oxygen surface exchanges at the sweep-side (oxygen-lean surface).
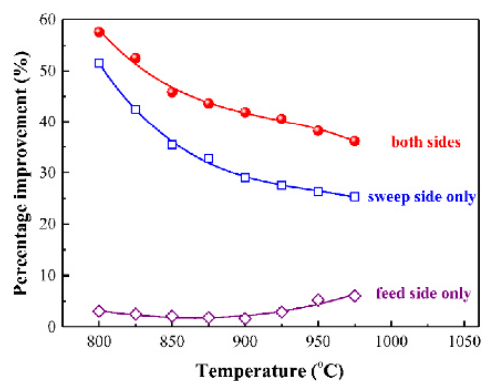


**Fig. 6.** Percentage improvement of oxygen permeation fluxes of LSC-coated compared to the uncoated (PL)₁.₉NCG membrane at different temperatures.

With this in mind, surface exchange properties of (PL)₁.₉NCG are estimated by thermogravimetric (TG) methods. When the atmosphere is changed between air and nitrogen, the sample experiences a weight loss in the oxygen release period and a weight gain in the oxygen insertion process. As shown in Fig. 7, the weight of the

(PL)₁.₉NCG sample decrease (oxygen release) when gas is switched from air to nitrogen and increase (oxygen insertion) when gas is switched back from nitrogen to air at different temperature. At all temperatures, the (PL)₁.₉NCG sample shows a slow weight loss in the oxygen release process (oxygen association and desorption) and a rapid weight gain in the oxygen insertion period (oxygen adsorption and disassociation), similar results are also found in other materials [15, 34-36].
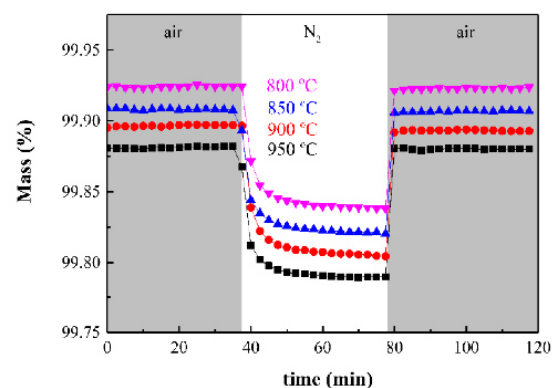


**Fig. 7.** Weight changes of the (PL)₁.₉NCG during air → N₂ → air cycle at different temperatures.

From this TG curves, the oxygen insertion coefficient $k_i$ and the oxygen release coefficient $k_r$ can be calculated by the theoretical model proposed by Lin et al., simplified equation as shown in below [34-36],

$$\frac{w(t)-w(e)}{w(0)-w(e)} = exp(-2\emptyset kt) \qquad (5)$$

Where the w(0) is the weight of the sample at the time of nitrogen switching to air (scale as t = 0) and w(e) is the steady-state weight of the sample after the gas change. The surface exchange rate coefficients $k_i$ and $k_r$ calculated by Eq. 5 are shown in Fig. 8.
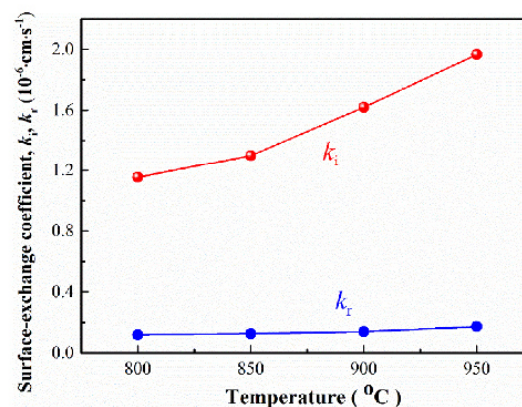


**Fig. 8.** The calculated surface-exchange coefficient $k_i$ and $k_r$ of (PL)₁.₉NCG at different temperatures.

It can be seen that the $k_i$ increases from 1.2 to 2.0 *10⁻⁶ cm·s⁻¹ with increasing temperature from 800 °C to 950 °C, while the $k_r$ is around 0.15 *10⁻⁶ cm·s⁻¹ in the tested temperature range. Most important, the values of $k_i$ are much larger than those of $k_r$ at different temperatures, which clearly indicated that the oxygen release is the limit of the (PL)₁.₉NCG of investigated thickness (0.6 mm), similar

phenomenon are also found in other materials [15, 16, 36]. Therefore, it could be expected that the oxygen release on the sweep side is the rate limiting step in (PL)$_{1.9}$NCG membrane and the modification on the sweep surface (oxygen release side) will result in larger improvement of oxygen permeation flux than that on the feed surface (oxygen insertion side). This is consistent with the oxygen permeation results as shown in Fig. 5 and 6.

Fig. 9 shows the long-term oxygen permeation behavior of the uncoated and LSC coated (PL)$_{1.9}$NCG membrane at 900, 850 and 800 °C. In our previous report, the uncoated (PL)$_{1.9}$NCG membrane (the model is described in Fig. 10a) underwent a phase decomposition under oxygen-containing atmosphere at intermediate temperature, so that its oxygen permeation fluxes decreased with time as also shown in Fig. 9 [21]. For example, the oxygen permeation fluxes of the uncoated (PL)$_{1.9}$NCG membrane decreased 1% at 900 °C, ca. 13% at 850 °C and ca. 43% at 800 °C over a period of 100 h. The oxygen permeation fluxes at low temperatures decreased more than that at high temperature due to the lowering temperature result in more oxidative conditions (higher oxygen chemical potential) [21]. The decline of the oxygen permeation fluxes of the sweep-side coated (PL)$_{1.9}$NCG membrane (the model is described in Fig. 10b) are slower than that of the uncoated one, for example, its oxygen permeation fluxes decrease ca. 1% at 850 °C and 6% at 800 °C of the initial permeation fluxes. The enhanced phase stability by the modification on the sweep surface might result from its higher oxygen permeability. During the oxygen permeation process, the oxygen is partly transported from the feed side (decomposition side with high O$_2$ chemical potential) to the sweep side (low O$_2$ chemical potential). Therefore, higher oxygen permeation fluxes lead to lower O$_2$ chemical potential near the feed-side surface under the same operation condition as show in Fig. 10b [33].
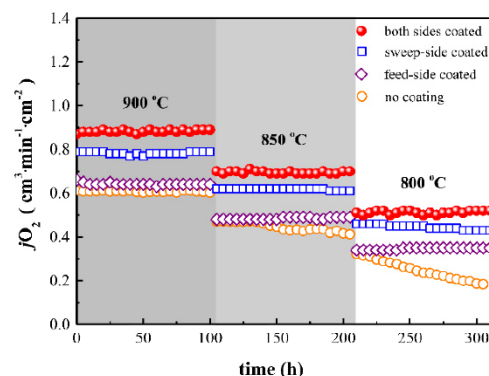


**Fig. 9.** Long-term stability test of the oxygen permeation flux through the unmodified and LSC modified (PL)$_{1.9}$NCG membrane at different temperatures. Conditions: The air flow rates in the feed side are 150 mL/min. The flow rates at the sweep side are 30 mL/min. The thicknesses of (PL)$_{1.9}$NCG membranes are 0.6 mm each.

Therefore, the sweep-side coated (PL)$_{1.9}$NCG membrane exhibits improved phase stability during the oxygen permeation test. Moreover, the feed-side coated membrane shows more stable permeation fluxes even at 800 °C. When the feed side is modified, the catalytic layer on the membrane surface reduces the in-situ oxygen chemical potential on the membrane surface as shown in Fig. 10c. Therefore, the catalytic layer will be a protective layer to prevent the membrane being in direct contact with the high oxygen chemical potential atmosphere, so that the feed-side coated membrane shows better phase stability than the uncoated one.
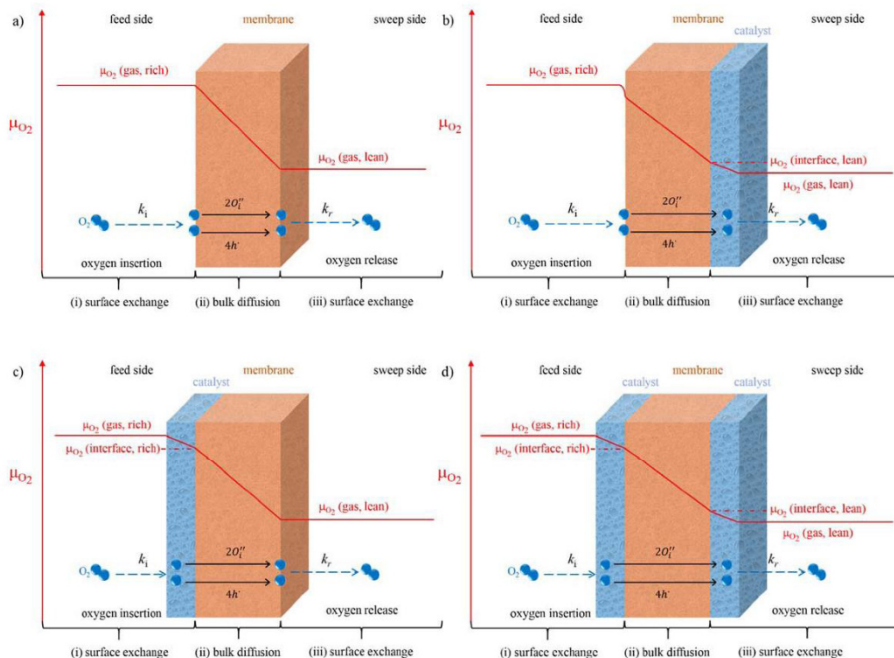


**Fig. 10.** Models of the LSC coated (PL)$_{1.9}$NCG membrane: a) uncoated membrane; b) sweep-side coated membrane; c) feed-side coated membrane; d) both sides coated membrane.

Similar approach was applied to improve the $CO_2$ tolerance of 80 vol.% $Ce_{0.9}Gd_{0.1}O_{2-\delta}$-20 vol.% $La_{0.7}Sr_{0.3}MnO_{3\pm\delta}$ dual-phase membrane, in which the membrane possessed enhanced stability with $Sr_{0.97}Ti_{0.5}Fe_{0.5}O_3$ $_\delta$-$Ce_{0.9}Gd_{0.1}O_{2-\delta}$ composite coated membrane under pure $CO_2$ [16]. When both sides of the membrane are modified with catalytic LSC layer (the model is described in Fig. 10d), the advantages of the feed- and sweep-side coated membrane are combined that it possess not only a higher oxygen permeation, but also good phase stability at intermediate temperature range under oxidative atmosphere, as shown in Fig. 5 and Fig. 9.

## 4. Conclusions

High oxygen permeability and good stability are the two main requirements for the oxygen transporting membranes in practical applications. The Ruddlesden-Popper-type A-site deficient $(PL)_{1.9}NCG$ membrane exhibits considerable oxygen permeation fluxes and good $CO_2$ stability, while decomposes under oxygen-containing atmosphere at intermediate temperature. Herein, the dependence of the oxygen permeability of $(PL)_{1.9}NCG$ on the membrane thickness is investigated in detail, which indicates significant surface exchange limitation to the permeation fluxes with thinner membrane and suggests a possibility to improve the permeation performance by surface coating. A porous layer of LSC was coated on one surface (sweep side or feed side) or both surfaces of the $(PL)_{1.9}NCG$ membrane with 0.6 mm thickness and their oxygen permeation fluxes are measured in the temperature range of 800-975 °C. The enhancement of sweep-side coated membrane are 51% at 800 °C and 25% at 975 °C, which are much higher than that of feed-side coated membrane (around 5%). Concluded from the TG results, the desorption rate of $(PL)_{1.9}NCG$ is much lower than the adsorption rate, which suggests that the surface exchange on the sweep side is the transport limiting process so that the coating on the sweep-side surface shows significant enhancement on the permeation fluxes than that of on the feed-side surface. Moreover, the sweep-side coated membrane also shows slightly improved phase stability compared with the uncoated membrane which might be attributed to the higher oxygen permeation flux of the former. The feed-side coated membrane shows better phase stability not only than the uncoated membrane but also than the sweep-side coated membrane under the same conditions, which are resulted from the reducing in-situ oxygen chemical potential on the membrane surface by the coating layer. Both side modified membrane shows higher permeability and better phase stability as it possesses all the advantages of one side coating.

## Acknowledgments

## References

[1] A. Leo, S. Liu, J.C.D. da Costa, Development of mixed conducting membranes for clean coal energy delivery. Int. J. Greenh. Gas Con. 3 (2009) 357-367.

[2] D. Hersh, J. Abrardo, Air separation plant design. Cryogenics 17 (1977) 383-390.

[3] R. Thorogood, Developments in air separation. Gas Separ. Purif. 5 (1991) 83-94.

[4] J. Sunarso, S. Baumann, J.M. Serra, W.A. Meulenberg, S. Liu, Y.S. Lin, J.C. Diniz da Costa, Mixed ionic-electronic conducting (MIEC) ceramic-based membranes for oxygen separation. J. Membr. Sci. 320 (2008) 13-41.

[5] Z. Cao, H. Jiang, H. Luo, S. Baumann, W.A. Meulenberg, J. Assmann, L. Mleczko, Y. Liu, J. Caro, Natural gas to fuels and chemicals: Improved methane aromatization in an oxygen-permeable membrane reactor, Angew. Chem. Int. Edit. 52 (2013) 13794-13797.

[6] E. Fontananova, E. Drioli, Membrane Reactors: Advanced systems for intensified chemical processes, Chem. Ing. Tech. 86 (2014) 2039-2050.

[7] Y. Wei, W. Yang, J. Caro, H. Wang, Dense ceramic oxygen permeable membranes and catalytic membrane reactors, Chem. Eng. J. 220 (2013) 185-203.

[8] H.J. Bouwmeester, A.J. Burggraaf, Dense ceramic membranes for oxygen separation, The CRC handbook of solid state electrochemistry, (1997) 481.

[9] P.M. Geffroy, M. Reichmann, T. Chartier, J.M. Bassat, J.C. Grenier, Evaluating oxygen diffusion, surface exchange and oxygen semi-permeation in $Ln_2NiO_{4+\delta}$ membranes ($Ln=$ La, Pr and Nd). J. Membr. Sci. 451 (2014) 234-242.

[10] F. Akin, J.Y. Lin, Oxygen permeation through oxygen ionic or mixed-conducting ceramic membranes with chemical reactions, J. Membr. Sci. 231 (2004) 133-146.

[11] C. Wagner, Equations for transport in solid oxides and sulfides of transition metals, Prog. Solid State Chem. 10 (1975) 3-16.

[12] G. Etchegoyen, T. Chartier, P. Del-Gallo, An architectural approach to the oxygen permeability of a $La_{0.6}Sr_{0.4}Fe_{0.9}Ga_{0.1}O_{3-\delta}$ perovskite membrane. J. Eur. Ceram. Soc. 26 (2006) 2807-2815.

[13] V. Kharton, A. Kovalevsky, A. Yaremchenko, F. Figueiredo, E. Naumovich, A. Shaulo, F. Marques, Surface modification of $La_{0.3}Sr_{0.7}CoO_{3-\delta}$ ceramic membranes. J. Membr. Sci. 195 (2002) 277-287.

[14] S. Lee, K.S. Lee, S.K. Woo, J.W. Kim, T. Ishihara, D.K. Kim, Oxygen-permeating property of $LaSrBFeO_3$ (B=Co, Ga) perovskite membrane surface-modified by $LaSrCoO_3$. Solid State Ionics 158 (2003) 287-296.

[15] H. Cheng, J. Liu, X. Lu, W. Ding, Enhancing the Oxygen Permeability of $BaCo_{0.7}Fe_{0.2}Nb_{0.1}O_3$ $_\delta$ Membranes by Coating $GdBaCo_{2-x}Fe_xO_{5+\delta}$ for Partial Oxidation of Coke Oven Gas to Syngas. ACS Appl. Mater. Inter. 3 (2011) 4032-4039.

[16] J.H. Joo, K.S. Yun, J.H. Kim, Y. Lee, C.Y. Yoo, J.H. Yu, Substantial Oxygen Flux in Dual-Phase Membrane of Ceria and Pure Electronic Conductor by Tailoring the Surface, ACS Appl. Mater. Inter. 7 (2015) 14699-14707.

[17] T. Liu, Y. Wang, R. Yuan, J. Gao, C. Chen, H.J. Bouwmeester, Enhancing the oxygen permeation rate of $Zr_{0.84}Y_{0.16}O_{1.92}$-$La0_{.8}Sr_{0.2}Cr_{0.5}Fe_{0.5}O_3$ $_\delta$ dual-phase hollow fiber membrane by coating with $Ce_{0.8}Sm_{0.2}O_{1.9}$ nanoparticles. ACS Appl. Mater.Inter. 5 (2013) 9454-9460.

[18] N. Han, S. Zhang, X. Meng, N. Yang, B. Meng, X. Tan, S. Liu, Effect of enhanced oxygen reduction activity on oxygen permeation of $La_{0.6}Sr_{0.4}Co_{0.2}Fe_{0.8}O_{3-\delta}$ membrane decorated by $K_2NiF_4$-type oxide, J. Alloy. Compd. 654 (2016) 280-289.

[19] K. Zhang, C. Zhang, L. Zhao, B. Meng, J. Liu, S. Liu, Enhanced oxygen permeation behavior of $Ba_{0.5}Sr_{0.5}Co_{0.8}Fe_{0.2}O_{3-\delta}$ membranes in a $CO_2$-containing atmosphere with a $Sm_{0.2}Ce_{0.8}O_{1.9}$ functional shell, Energy Fuel. 30 (2016) 1829-1834.

[20] J. Xue, Q. Liao, W. Chen, H.J. Bouwmeester, H. Wang, A. Feldhoff, A new $CO_2$-resistant Ruddlesden–Popper oxide with superior oxygen transport: A-site deficient $(Pr_{0.9}La_{0.1})_{1.9}Ni_{0.74}Cu_{0.21}Ga_{0.05}O_{4+\delta}$. J. Mater. Chem. A 3 (2015) 19107-19114.

[21] J. Xue, A. Schulz, H. Wang, A. Feldhoff, The phase stability of the Ruddlesden-Popper type oxide $(Pr_{0.9}La_{0.1})_{1.9}Ni_{0.74}Cu_{0.21}Ga_{0.05}O_{4+\delta}$ in an oxidizing environment. J. Membr. Sci. 497 (2016) 357-364.

[22] H. Luo, K. Efimov, H. Jiang, A. Feldhoff, H. Wang, J. Caro, $CO_2$-Stable and Cobalt-Free Dual-Phase Membrane for Oxygen Separation. Angew. Chem. Int. Edit. 50 (2011) 759-763.

[23] R. Ganeshananthan, A.V. Virkar, Measurement of surface exchange coefficient on porous $La_{0.6}Sr_{0.4}CoO_{3-\delta}$ samples by conductivity relaxation. J. Electrochem. Soc. 152 (2005) A1620-A1628.

[24] A. Feldhoff, M. Arnold, J. Martynczuk, T.M. Gesing, H. Wang, The sol-gel synthesis of perovskites by an EDTA/citrate complexing method involves nanoscale solid state reactions. Solid State Sci. 10 (2008) 689-701.

[25] J. Xue, Q. Liao, Y. Wei, Z. Li, H. Wang, A $CO_2$-tolerance oxygen permeable $60Ce_{0.9}Gd_{0.1}O_{2-\delta}$-$40Ba_{0.5}Sr_{0.5}Co_{0.8}Fe_{0.2}O_{3-\delta}$ dual phase membrane. J. Membr. Sci. 443 (2013) 124-130.

[26] H. Luo, Y. Wei, H. Jiang, W. Yuan, Y. Lv, J. Caro, H. Wang, Performance of a ceramic membrane reactor with high oxygen flux Ta-containing perovskite for the partial oxidation of methane to syngas, J. Membr. Sci. 350 (2010) 154-160.

7

[27] J. Xue, Q. Zheng, Y. Wei, K. Yuan, Z. Li, H. Wang, Dual phase composite oxide of Ce$_{0.9}$Gd$_{0.1}$O$_{2-\delta}$-Ba$_{0.5}$Sr$_{0.5}$Co$_{0.8}$Fe$_{0.2}$O$_{3-\delta}$ with excellent oxygen permeation. Ind. Eng. Chem. Res. 51 (2012) 4703-4709.

[28] H. Wang, R. Wang, D.T. Liang, W. Yang, Experimental and modeling studies on Ba$_{0.5}$Sr$_{0.5}$Co$_{0.8}$Fe$_{0.2}$O$_{3-\delta}$ (BSCF) tubular membranes for air separation. J. Membr. Sci. 243 (2004) 405-415.

[29] H. Bouwmeester, H. Kruidhof, A. Burggraaf, Importance of the surface exchange kinetics as rate limiting step in oxygen permeation through mixed-conducting oxides, Solid State Ionics 72 (1994) 185-194.

[30] W.K. Hong, G.M. Choi, Oxygen permeation of BSCF membrane with varying thickness and surface coating. J. Membr. Sci. 346 (2010) 353-360.

[31] Y. Wang, H. Hao. J. Jia, D. Yang, X. Hu, Improving the oxygen permeability of Ba$_{0.5}$Sr$_{0.5}$Co$_{0.8}$Fe$_{0.2}$O$_{3-\delta}$ membranes by a surface-coating layer of GdBaCo$_2$O$_{5+\delta}$. J. Eur. Ceram. Soc. 28 (2008) 3125-3130.

[32] F. Figueiredo, V. Kharton, A. Viskup, J. Frade, Surface enhanced oxygen permeation in CaTi$_{1-x}$Fe$_x$O$_{3-\delta}$ ceramic membranes. J. Membr. Sci. 236 (2004) 73-80.

[33] A. Leo, S. Liu, J.C.D. da Costa, The enhancement of oxygen flux on Ba$_{0.5}$Sr$_{0.5}$Co$_{0.8}$Fe$_{0.2}$O$_{3-\delta}$ (BSCF) hollow fibers using silver surface modification. J. Membr. Sci. 340 (2009) 148-153.

[34] J. Hu, H. Hao, C. Chen, D. Yang, X. Hu, Thermogravimetric study on perovskite-like oxygen permeation ceramic membranes, J. Membr. Sci. 280 (2006) 809-814.

[35] J. Hu, X. Hu, H. Hao, L. Guo, H. Song, D. Yang, A transient thermogravimetric study on the oxygen permeation at high temperature of the superconducting material YBa$_2$Cu$_3$O$_{7-\delta}$. Solid State Ionics 176 (2005) 487-494.

[36] Y. Zeng, Y. Lin, A transient TGA study on oxygen permeation properties of perovskite-type ceramic membrane, Solid State Ionics 110 (1998) 209-221.

## 2.5 Ambient air partial internal reduction of NiO in a mixed ionic-electronic conducting ceramic

Jian Xue and Armin Feldhoff

# ARTICLE IN PRESS

# Ambient air partial internal reduction of NiO in a mixed ionic-electronic conducting ceramic

Jian Xue, Armin Feldhoff*

*Institute of Physical Chemistry and Electrochemistry, Leibniz University Hannover, Callinstrasse 3A, D-30167 Hannover, Germany*

### ARTICLE INFO

### ABSTRACT

Partial internal reduction is observed of NiO precipitates in a matrix of a Ruddlesden-Popper type mixed ionic-electronic conducting ceramic with composition of $(Pr_{0.9}La_{0.1})_{2.0}Ni_{0.74}Cu_{0.21}Ga_{0.05}O_{4+\delta}$ during the cooling from sintering temperature to room temperature in ambient air. A metallic Ni interlayer between NiO and the oxide matrix is demonstrated using scanning transmission electron microscopy combined with electron energy-loss spectroscopy. The possible formation mechanism for the metallic Ni is discussed in light of the partial internal reduction during the cooling process in ambient air. The drop of temperature during cooling process in ambient air causes a drop of the oxygen chemical potential in the Ruddlesden-Popper type oxide ceramic, which acts as an oxygen absorber. Thus, the local oxygen chemical potential at the internal interface between Ruddlesden-Popper type matrix and NiO precipitate can fall below the stability limit of the later. As consequence, NiO is partially reduced to metallic Ni at the interface.

© 2016 Elsevier Ltd. All rights reserved.

## 1. Introduction

Precipitation of metal particles inside a solid oxide matrix could be obtained by internal reduction which has been described by Schmalzried and Backhaus-Ricoult [1–4]. Upon lowering the oxygen partial pressure surrounding the oxide matrix (in e.g. $H_2/CO$ containing atmosphere), one of two oxides being in contact falls beyond its stability limit, which results in the formation of a new metal layer internally. This internal reduction process in an oxygen potential gradient has been extensively studied in different oxide matrices. At the start of these investigations, Schmalzried et al. thoroughly described the internal reduction in reducing atmosphere (in e.g. $H_2/CO$ containing atmosphere, $p_{O_2} < 10^{-8}$ Pa) at high temperature in matrices of low oxygen-ionic conductivity, such as MgO/CuO, MgO/NiO, MgO/Fe₂O₃, Al₂O₃/Fe₂O₃ [1–6]. Later, the internal reduction in matrices of high oxygen-ionic conductivity attracted increasing attentions, especially in ZrO₂/NiO ceramic/metal oxide composite, due to its potential applications in preparation of Ni-containing ferromagnetic materials with enhanced toughness, strength, densification and phase stability [7–10].

Usually, the metal oxides could be reduced to the metal in low oxygen chemical potential environment. Change in the oxygen chemical potential $\mu_{O_2}$ can be made not only by changing the oxygen partial pressure $p_{O_2}$ but also the temperature $T$ [2,11]:

$$\mu_{O_2}\left(T, p_{O_2}\right) = \mu_{O_2}\left(T, p_{O_2}^o\right) + RT \ln\left(\frac{p_{O_2}}{p_{O_2}^o}\right) \tag{1}$$

Here, R is the gas constant, and $p_{O_2}^o$ is the reference oxygen partial pressure, and $p_{O_2}$ is the practical oxygen partial pressure. Inside the ceramic/metal oxide composite, the oxygen potential might change respectively when decreasing or increasing the temperature, which results in a chemical potential gradient between the ceramic matrix and the metal oxide precipitate due to their different thermodynamical properties.

Different to the classic internal reduction (described by Schmalzried et al. [1–6]), which was established in matrices of low oxygen-ionic conductivity under reducing atmosphere, in this study, we firstly report on the partial internal reduction of oxide precipitate in a mixed ionic-electronic conducting (MIEC) ceramic under ambient air during cooling process. The drop of temperature during cooling in air from the sintering temperature causes a drop of the oxygen chemical potential in the ceramic, which locally in the ceramic can fall so deep that partial internal reduction of an oxide precipitate occurs. We observed that small amounts of NiO precipitate exist in a MIEC ceramic with the nominal composition $(Pr_{0.9}La_{0.1})_{2.0}Ni_{0.74}Cu_{0.21}Ga_{0.05}O_{4+\delta}$ ((PL)₂.₀NCG). A metallic

* Corresponding author.
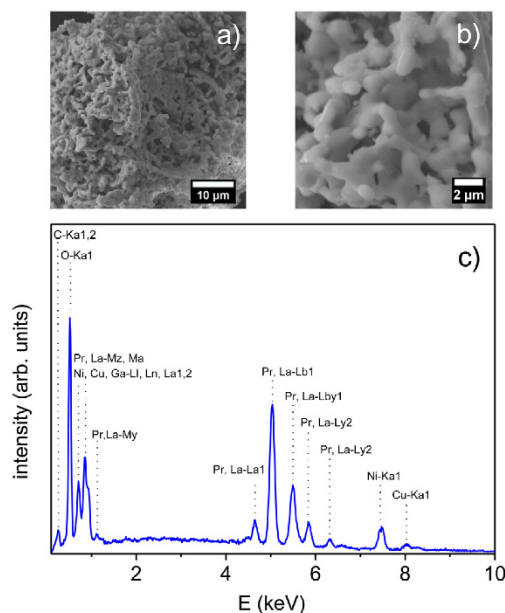  *E-mail address:* armin.feldhoff@pci.uni-hannover.de (A. Feldhoff).

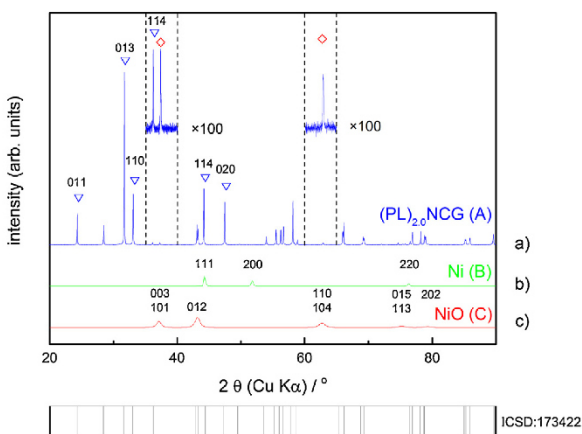**Fig. 1.** (a) SEM micrograph; (b) close up micrograph; and (c) EDX spectrum of calcined $(PL)_{2.0}NCG$ powder.



**Fig. 2.** XRD patterns of three powders: (a) $(PL)_{2.0}NCG$ (**A**) as obtained from crushing of sintered ceramic, commercial (b) Ni (**B**) and c) NiO (**C**). The intensity of $(PL)_{2.0}NCG$ (**A**) was magnified 100 times for comparison. The $(PL)_{2.0}NCG$ (**A**) adopts the tetragonal $K_2NiF_4$ structure (ICSD: 173422) [15]. Blue triangles refer to $(PL)_{2.0}NCG$ (**A**) and red diamonds indicate 003, 101, respectively 110 and 104 reflections of NiO (**C**). (For interpretation of the references to color in this figure legend, the reader is referred to the web version of this article.)

Ni (**B**) interlayer occurs between the NiO (**C**) precipitate and the $(PL)_{2.0}NCG$ (**A**) matrix. These phenomenon and the formation mechanism are discussed in detail.

## 2. Materials and methods

Powder of $(PL)_{2.0}NCG$ was prepared by a combined citrate and ethylene-diamine-tetraacetic-acid (EDTA) method [12,13]. The appropriate stoichiometric metal nitrates $Pr(NO_3)_3$, $La(NO_3)_3$, $Ni(NO_3)_2$, $Cu(NO_3)_2$, $Ga(NO_3)_3$ in aqueous solutions were mixed in a beaker, followed by the addition of proper amount of citric
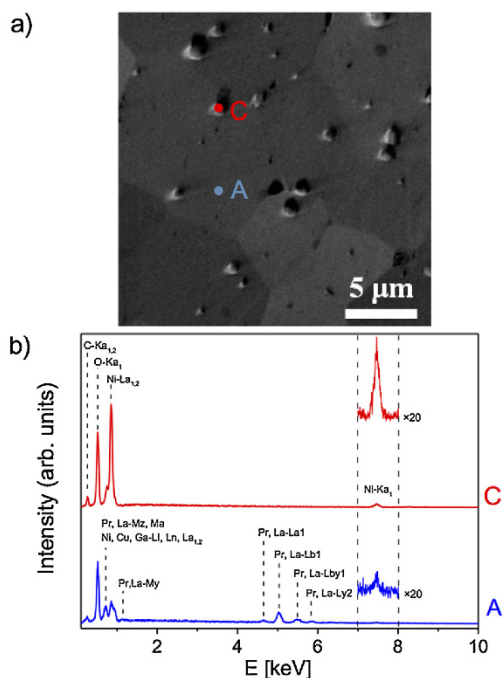


**Fig. 3.** SEM analysis of vibration polished cross-section of as-sintered $(PL)_{2.0}NCG$: (a) micrograph; (b) EDX spectra of areas A and C in (a). In (b), the intensities between 7 and 8 keV were magnified 20 times for comparison.

acid and EDTA, and the pH value was adjusted to ~7 by aqueous ammonia. The molar ratio of total metal ions: citric acid: EDTA was 1:2:1. Then the solution was stirred and heated to 150 °C, until the water evaporated and a gel formed. Afterward, the gel was ignited to flame to get the precursor. The precursor was ground and calcined at 950 °C for 10 h with a heating/cooling rate of 2 °C/min. The particle size of the obtained powder after calcination was around 2 μm as shown in Fig. 1a, b. And the composition of the as-prepared powder was detected by EDXS as shown in Fig. 1c. The powder was uniaxially pressed at 20 MPa to obtain green pellets followed by sintering in air at 1503 K for 10 h with 2 °C/min heating/cooling rate. The diameter and thickness of the final ceramic pellets were around 14 mm and 1 mm, respectively.

The crystal structure of the sintered disk was studied by X-ray diffraction (XRD, D8 Advance, Bruker-AXS, with Cu Kα radiation). The ceramic, which was prepared using a Buehler VibroMet 2 vibratory polisher, was studied by scanning electron microscopy (SEM) using a JEOL JSM-6700F at an excitation voltage of 2 keV. The elemental composition of the membrane was determined by energy dispersive X-ray spectroscopy (EDXS), Oxford Instruments INCA-300 EDX spectrometer with an ultrathin window at an excitation voltage of 20 keV. Transmission electron microscopy (TEM) was performed on a JEOL JEM-2100F that was equipped with a Gatan Imaging Filter (GIF 2001). Scanning transmission electron microscopy (STEM) was performed in annular dark-field contrast. Electron energy-loss spectroscopy (EELS) and selected area electron diffraction (SAED) were performed on the charge-coupled device (CCD) camera of the GIF.

## 3. Results and discussion

Fig. 2 shows the XRD patterns of $(PL)_{2.0}NCG$ (**A**) ceramic after sintering at 1230 °C for 10 h in air with 2 °C/min heating/cooling

ARTICLE IN PRESS

3
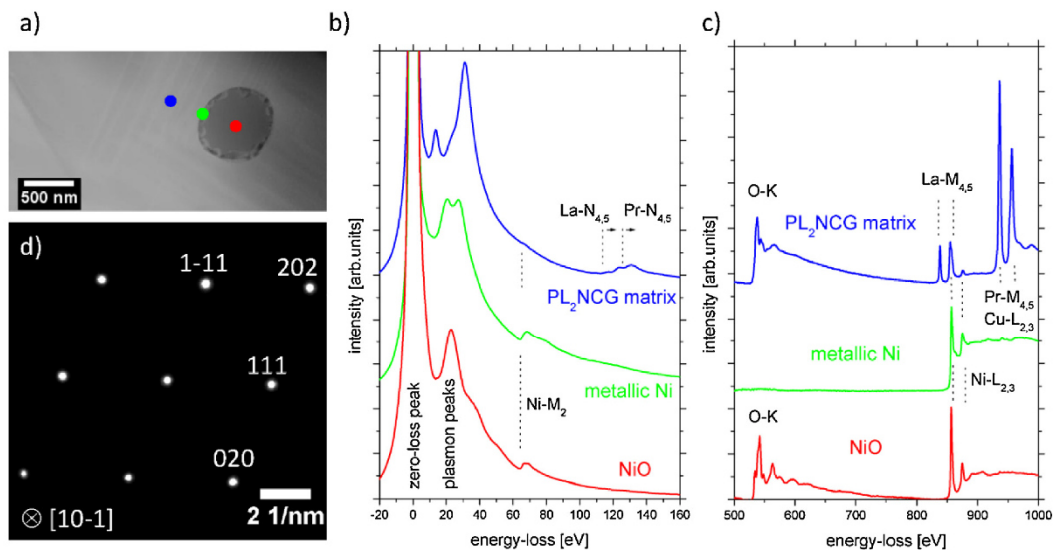


**Fig. 4.** TEM analysis of as-sintered $(PL)_{2.0}NCG$: (a) STEM annular dark-field with indication of analysed spots **A**, **B** and **C** of 1.5 nm in diameter; (b, c) electron energy-loss spectra (EELS) in low-loss (b) and core-loss region (c) exhibit three different phases; (d) selected area electron diffraction pattern of 260 nm circular area at center of precipitate with Laue indices of reflections according to [10-1] zone axis pattern of NiO.

rate. Analysis of the pattern confirms that $(PL)_{2.0}NCG$ (**A**) adopts the tetragonal $K_2NiF_4$ structure (ICSD: 173422) [14,15]. Fig. 2 shows also XRD of Ni (**B**) and NiO (**C**) powders for comparison. Vertically magnifying by a factor of 100, the powder XRD of crushed $(PL)_{2.0}NCG$ (**A**) ceramic in the range of 35–40° and 60–65° reveals 003 and 101, respectively, 110 and 104 reflections of the rocksalt-type NiO (**C**) according to ICSD no. 61324.

Fig. 3 shows the SEM micrographs and the EDXS results of the $(PL)_{2.0}NCG$ (**A**) disk after vibration polishing. As shown in Fig. 3a the grain size of $(PL)_{2.0}NCG$ (**A**) is around 10 μm and some small particles (of approximately 1 μm in diameter) are noted. The small particles are confirmed to be nickel oxide (**C**) precipitates by EDXS as shown in Fig. 3b, which is consistent with the XRD (see Fig. 2).

The existence of NiO (**C**) in the system of $(PL)_{2.0}NCG$ (**A**) is investigated in detail by TEM and EELS, as shown in Fig. 4. The NiO (**C**) particles surrounded by the $(PL)_{2.0}NCG$ (**A**) matrix have a diameter of approximately 1 μm as is shown by the STEM dark-field micrograph in Fig. 4a. The NiO (**C**) precipitate in Fig. 4a shows a ring of dark contrast (80 nm in thickness), which is identified by EELS, in Fig. 4b, c, to be metallic Ni (**B**). The metallic Ni (**B**) exists at the interface of NiO (**C**) and $(PL)_{2.0}NCG$ (**A**). The SAED pattern in Fig. 4d, taken from a 260 nm circular region on center of precipitate, confirms the structure of rock-salt type NiO with cubic lattice parameter a = 417.71 pm according to ICSD no. 61324 as viewed along the [10-1] zone axis.

Similar phenomenon of the internal reduction of NiO had been reported in several systems, such as $Al_2O_3/NiO$, $MgO/NiO$, $ZrO_2/NiO$ [4,16,17]. Compared with other oxides, NiO is easily reduced due to its thermodynamical properties [11,18,19]. The stability limit to reduction of NiO and other oxides can be estimated by Fig. 5. This illustration predicts the thermodynamic stability of the oxides at given temperatures and oxygen partial pressures. The dashed lines give the oxygen chemical potential at various oxygen partial pressures. The solid lines represent the thermodynamic stability limit to reduction of the oxides as a function of temperature and oxygen partial pressure. $MO_2$ and $M'O_2$ represents the $(PL)_{2.0}NCG$ with different copper valence ($MO_2$ with CuO and $M'O_2$ with $Cu_2O$), and the value is from the theoretical calculation based on its composition.
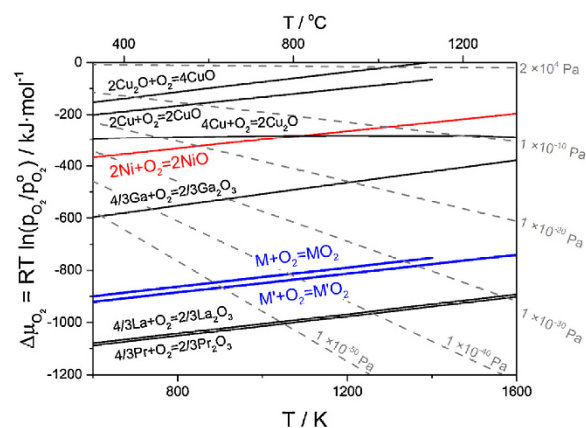


**Fig. 5.** Stability limit to reduction of oxides as a function of temperature and oxygen partial pressure. Original data are from ref. [19]. The vertical axis refers to the oxygen partial pressure difference with respect to standard conditions (cf. Equation 1). $MO_2$ and $M'O_2$ represent the $(PL)_{2.0}NCG$ ($MO_2$ with CuO and $M'O_2$ with $Cu_2O$) to consider different Cu valance in $(PL)_{2.0}NCG$. The values of $(PL)_{2.0}NCG$ $(MO_2/M'O_2)$ are from the theoretical calculation based on its composition as shown in Table 1.

Details are shown in Table 1. For example, CuO is reduced to $Cu_2O$ at 1397 K under $1 \times 10^5$ Pa oxygen partial pressure [20]. This type of graphic representation can be used for evaluating the relative stability of the oxides in contact with metals [18]. The more negative the chemical potential, the more stable the oxides will be. As a result, from Fig. 5, it is noted that NiO is easily reduced compared to the $(PL)_{2.0}NCG$ ($MO_2$ and $M'O_2$). Similar results have been also found by other researchers [21]. Therefore, it is possible to internally reduce the NiO (**C**) in the interface with $(PL)_{2.0}NCG$ (**A**) under chemical potential gradients.

The partial internal reduction of NiO (**C**) in $(PL)_{2.0}NCG$ (**A**) might happen in the cooling process after high-temperature sintering as oxygen chemical potential changes with decreasing temperature (see Eq. (1)). During the cooling procedure, the oxygen content of

**ARTICLE IN PRESS**

4 *J. Xue, A. Feldhoff / Journal of the European Ceramic Society xxx (2016) xxx–xxx*

**Table 1**
Calculation equations for the oxygen chemical potential theoretical value (see M/M' + O$_2$ = MO$_2$/M'O$_2$ in Fig. 5) of (Pr$_{0.9}$La$_{0.1}$)$_{2.0}$Ni$_{0.74}$Cu$_{0.21}$Ga$_{0.05}$O$_{4+\delta}$ ((PL)$_{2.0}$NCG) based on its composition: $M = \dfrac{\sum_i n_i M_i}{\frac{1}{2}(4+\delta)}$.

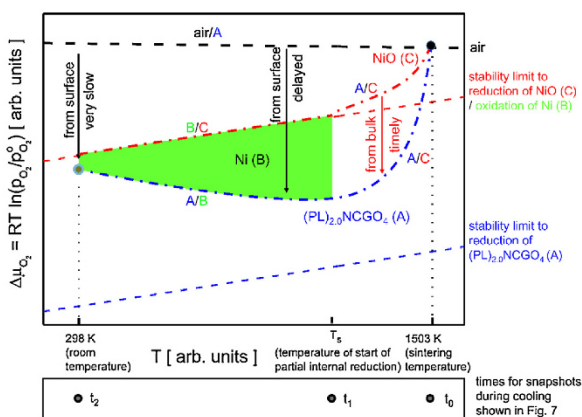| M$_i$ | Real value | Equations for different M$_i$ | n$_i$ |
|---|---|---|---|
| Pr | 1.8 | $\frac{4}{3}Pr + O_2 = \frac{2}{3}Pr_2O_3$ | $\frac{1.8}{4/3}$ |
| La | 0.2 | $\frac{4}{3}La + O_2 = \frac{2}{3}La_2O_3$ | $\frac{0.2}{4/3}$ |
| Ni | 0.74 | $2Ni + O_2 = 2NiO$ | $\frac{0.74}{2}$ |
| Ga | 0.05 | $\frac{4}{3}Ga + O_2 = \frac{2}{3}Ga_2O_3$ | $\frac{0.05}{4/3}$ |
| Cu | 0.21 | $2Cu + O_2 = 2CuO$ (in MO$_2$) | $\frac{0.21}{2}$ |
|  |  | $4Cu + O_2 = 2Cu_2O$ (in M'O$_2$) | $\frac{0.21}{4}$ |
| O | $4 + \delta$ | $O_2$ | MO$_2$: $\frac{4+\delta}{2} = \frac{1.8}{4/3} + \frac{0.2}{4/3} + \frac{0.74}{2} + \frac{0.74}{2} - \frac{0.05}{4/3} = 2.0125$ |
|  |  |  | M'O$_2$: $\frac{4+\delta}{2} = \frac{1.8}{4/3} + \frac{0.2}{4/3} + \frac{0.74}{2} + \frac{0.21}{4} + \frac{0.05}{4/3} = 1.96$ |



**Fig. 6.** Schematic oxygen chemical potential diagram at several interfaces to explain the partial internal reduction of NiO (**C**) to Ni (**B**) in (PL)$_{2.0}$NCG (A) during the cooling process. The external gas-solid interface air/(PL)$_{2.0}$NCG (air/**A**) on the top exhibits the highest oxygen chemical potential of the system. Furthermore, the diagram addresses the following internal solid-solid interfaces: (PL)$_{2.0}$NCG/NiO (**A/C**); Ni/NiO (**B/C**); (PL)$_{2.0}$NCG/Ni (**A/B**). The box at the bottom indicates the times of some specific temperatures during the cooling process. Here, t$_0$ is the starting time of cooling at sintering temperature; t$_1$ is an intermediate time during the cooling process, which refers to the starting of the partial internal reduction at temperature T$_s$; t$_2$ is the final time of cooling to room temperature. Snapshots at these times are shown in Fig. 7.

the oxides will increase and the (PL)$_{2.0}$NCG (**A**) should acquire oxygen from surrounding environment [22,23]. If the material can not obtain oxygen immediately, it will take oxygen from nearby oxides firstly so that the easier reducible NiO (**C**) is deoxidized. In Fig. 6, the oxygen chemical potential is shown over temperature for four interfaces (air/**A**, **A/C**, **A/B**, **B/C**). The relative positions of the oxygen chemical potential of air and the stability limit to reduction of NiO (**C**) and (PL)$_{2.0}$NCG (**A**) are as given by Fig. 5. The box at the bottom indicates the times of some specific temperatures during the cooling process. Here, t$_0$ is the starting time of cooling at sintering temperature, and t$_1$ is an intermediate time during the cooling process, which refers to the starting of the partial internal reduction at temperature T$_s$. At the final time t$_2$, cooling has reached room temperature. Based on the specific time, the partial internal reduction can be classified into five states:

1) At t$_0$, which indicates the end of the sintering process at 1503 K and the start of the cooling process, solid phases NiO (**C**), (PL)$_{2.0}$NCG (**A**) and air are in thermodynamic equilibrium. Therefore, the oxygen chemical potential adopts the same value in all these three phases, and it is constant over the two interfaces (air/**A** and **A/C**).

2) From t$_0$ to t$_1$, the oxygen chemical potential of (PL)$_{2.0}$NCG (**A**) changes largely as it tends to obtain oxygen from surrounding environment, while the oxygen chemical potential of NiO (**C**) changes slowly during the cooling process. As a result, there forms a chemical potential gradient between NiO (**C**) and (PL)$_{2.0}$NCG (**A**). The oxygen chemical potential at the **A/C** interface is higher on the side of NiO (**C**) than on the side of (PL)$_{2.0}$NCG (**A**), and both of them are lower than at the external interface air/**A**. Due to the long transport distance, the oxygen supply from air in the surface to the bulk (PL)$_{2.0}$NCG (**A**) is delayed. Therefore, the bulk (PL)$_{2.0}$NCG (**A**) cannot obtain oxygen immediately from the surface so that it takes oxygen from the adjacent NiO (**C**).

3) At the intermediate time t$_1$, NiO (**C**) has lost a certain amount of oxygen during the cooling process and its oxygen chemical potential at the **A/C** interface drops below the stability limit to reduction, so that the NiO (**C**) will be reduced to metallic Ni (**B**) at the interface to the (PL)$_{2.0}$NCG (**A**). Now, three interfaces are present (air/**A**, **A/B**, **B/C**) as there is no direct contact between (PL)$_{2.0}$NCG (**A**) and NiO (**C**).

4) During further cooling, from t$_1$ to t$_2$, the interfaces between the Ni (**B**) interlayer and the NiO (**C**) precipitate as well as the bulk (PL)$_{2.0}$NCG (**A**) will be in local thermodynamic equilibrium. NiO (**C**) is still an oxygen supplier through the metallic Ni (**B**) interlayer to (PL)$_{2.0}$NCG (**A**), while the oxygen chemical potential at the **B/C** interface will remain at that of the stability limit to reduction of NiO (**C**). The Ni/NiO (**B/C**) interface will be shifted further into the NiO (**C**). The interface **A/B** obtains oxygen simultaneously from air and NiO (**C**), so that its oxygen chemical potential increases during this period.

5) At time t$_2$, after the cooling process has reached room temperature, the oxygen chemical potential of the **A/B** interface increases to a certain value, while it is still below the stability limit to reduction of NiO (**C**). In principle, at room temperature, the **A/B** interface can get oxygen from air in the surface. However, the kinetic rate is very slow at room temperature so that the oxidation of Ni (**B**) between (PL)$_{2.0}$NCG (**A**) and NiO (**C**) layer could not be observed in the specimen under consideration [24,25]. To describe the partial internal reduction in more detail, snapshots at distinct times (t$_0$, t$_1$, t$_2$) are shown in Fig. 7.

As shown in Fig. 7a, at the sintering temperature (t$_0$), the NiO (**C**), (PL)$_{2.0}$NCG (**A**) and air are in thermodynamic equilibrium so that they are at the same oxygen chemical potential. As the (PL)$_{2.0}$NCG (**A**) ceramic tends to obtain more oxygen, during the cooling process (from t$_0$ to t$_1$), its oxygen chemical potential decreases stronger than that of NiO (**C**). Therefore, an oxygen chemical potential gradient not only forms at the outer surface between air and (PL)$_{2.0}$NCG (**A**), but also in the bulk between NiO (**C**) and (PL)$_{2.0}$NCG (**A**), as shown in Fig. 7b. As a result, the (PL)$_{2.0}$NCG (**A**) will take oxygen from both air at the surface and from NiO (**C**) in the bulk. When the oxygen chemical potential of NiO (**C**) is below the stability limit to
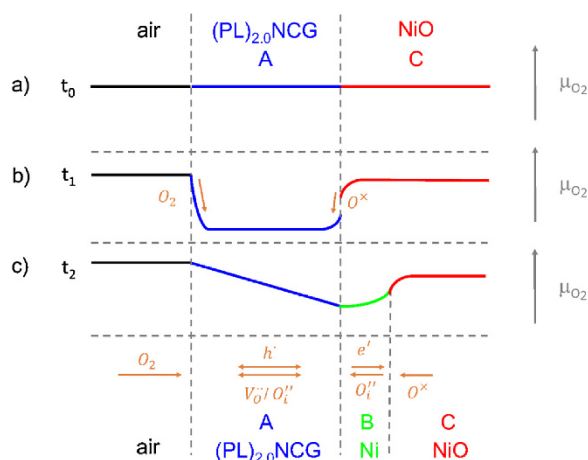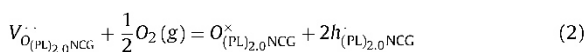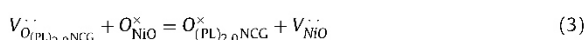
# ARTICLE IN PRESS

**Fig. 7.** The overall changes of the oxygen chemical potential in the air/(PL)$_{2.0}$NCG/Ni/NiO system in different period of time ($t_0$, $t_1$, $t_2$ shown in Fig. 6) during the cooling process and diffusion processes occurring during the partial internal reduction of NiO in the MIEC oxide.

reduction, the NiO (**C**) interface will be reduced to metallic Ni. In the end, at room temperature ($t_2$), local thermodynamic equilibrium is established at each interface (i.e. air/**A**, **A/B**, **B/C**) as shown in Fig. 7c. The oxygen chemical potential of (PL)$_{2.0}$NCG (**A**) at the surface is the same as it is in air and that of the bulk (PL)$_{2.0}$NCG (**A**) is the same as it is in Ni (**B**). In (PL)$_{2.0}$NCG (**A**), an oxygen chemical gradient forms between the surface and the bulk, and it changes slowly due to the kinetic limitation at room temperature [24,25].

In traditional internal reduction research, the ceramic usually is an oxygen-ion conductor (ZrO$_2$) or an oxide of low oxygen-ionic conductivity (e.g. MgO, Al$_2$O$_3$) [5,6,16,26]. Hence, the traditional diffusion mechanism cannot apply for example to our case in (PL)$_{2.0}$NCG/NiO compounds since the (PL)$_{2.0}$NCG is a mixed ionic-electronic conducting (MIEC) oxide [14,27,28]. During the cooling process, the oxygen content of (PL)$_{2.0}$NCG (**A**) increases and that of neighboring NiO (**C**) decreases, resulting in a metallic Ni layer. The diffusion processes occurring during the internal reduction of NiO (**C**) in the (PL)$_{2.0}$NCG (**A**) MIEC oxide are schematically shown in Fig. 7. Both oxygen ions and electrons can transport in (PL)$_{2.0}$NCG (**A**) [14,27,28]. During the cooling process ($t_1$), the oxygen chemical potential difference between the air and (PL)$_{2.0}$NCG (air/**A**), and between (PL)$_{2.0}$NCG and NiO (**A/C**) induce oxygen-ionic flux. The air at the surface of (PL)$_{2.0}$NCG (**A**) and the internal NiO (**C**) precipitates both act as oxygen sources, and the (PL)$_{2.0}$NCG (**A**) acts as sink. The oxygen/oxygen ions exchange in (PL)$_{2.0}$NCG (**A**) shown in Fig. 7b ($t_1$), according to the following equation by using Kröger-Vink defect notation: at the air/(PL)$_{2.0}$NCG (air/**A**) interface:
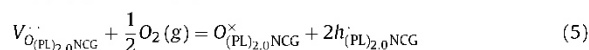
$$V_{O_{(PL)_{2.0}NCG}}^{\cdot\cdot} + \frac{1}{2}O_2\,(g) = O_{(PL)_{2.0}NCG}^{\times} + 2h_{(PL)_{2.0}NCG}^{\cdot} \tag{2}$$

at the (PL)$_{2.0}$NCG/NiO (**A/C**) interface:

$$V_{O_{(PL)_{2.0}NCG}}^{\cdot\cdot} + O_{NiO}^{\times} = O_{(PL)_{2.0}NCG}^{\times} + V_{NiO}^{\cdot\cdot} \tag{3}$$

$$O_{NiO}^{\times} = O_{i_{(PL)_{2.0}NCG}}^{''} + 2h_{(PL)_{2.0}NCG}^{\cdot} \tag{4}$$

where $V_{O}^{\cdot\cdot}$, $O_i^{''}$, $O^{\times}$ and $h^{\cdot}$ are oxygen vacancy, interstitial oxygen, lattice oxygen and electron hole in the respective oxides. (PL)$_{2.0}$NCG consists of alternating rock-salt and perovskite layers along the crystallographic c-axis, and oxygen transport is assumed to occur via an interstitialcy mechanism: an interstitial oxygen in the rock-salt layer displaces an apical oxygen in the perovskite layer, which

in turn processes to an adjacent interstitial oxygen site [13–15]. During the heating process, oxygen is released, which results in a decrease of the interstitial oxygen ($O_i^{''}$) concentration and an increase of the oxygen vacancy ($V_{O}^{\cdot\cdot}$) concentration [22,23]. This is accompanied by a decrease of the valence of the transition metal ions [22,23]. Then, the electron holes ($h_{(PL)_{2.0}NCG}^{\cdot}$) could be supplied by the increase of the valence of metal ions in (PL)$_{2.0}$NCG (**A**) during the cooling process.
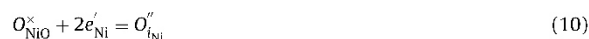
When the NiO (**C**) reaches the stability limit to reduction, the Ni (**B**) interlayer forms between (PL)$_{2.0}$NCG (**A**) and NiO (**C**). Then the bulk (PL)$_{2.0}$NCG (**A**) obtains oxygen from both air and the dissolved oxygen in Ni (**B**) according to the following equations: at the air/(PL)$_{2.0}$NCG (air/**A**) interface:

$$V_{O_{(PL)_{2.0}NCG}}^{\cdot\cdot} + \frac{1}{2}O_2\,(g) = O_{(PL)_{2.0}NCG}^{\times} + 2h_{(PL)_{2.0}NCG}^{\cdot} \tag{5}$$

at the (PL)$_{2.0}$NCG/Ni (**A/B**) interface:

$$V_{O_{(PL)_{2.0}NCG}}^{\cdot\cdot} + O_{i_{Ni}}^{''} = O_{(PL)_{2.0}NCG}^{\times} \tag{6}$$

$$O_{i_{Ni}}^{''} = O_{i_{(PL)_{2.0}NCG}}^{''} \tag{7}$$

$$nil = h_{(PL)_{2.0}NCG}^{\cdot} + e_{Ni}^{'} \tag{8}$$

at the Ni/NiO (**B/C**) interface:

$$NiO = O_{NiO}^{\times} + Ni \tag{9}$$

$$O_{NiO}^{\times} + 2e_{Ni}^{'} = O_{i_{Ni}}^{''} \tag{10}$$

Finally, at all the interfaces (air/**A**, **A/B**, **B/C**), local thermodynamic equilibrium is established as shown in Fig. 7c. And the oxygen chemical potential in these materials does not change at room temperature due to the kinetic limitation [11,28]. Therefore, a Ni (**B**) interlayer between NiO (**C**) and (PL)$_{2.0}$NCG (**A**) is observed.

The partial internal reduction might widespread exist in the ceramic oxide matrices, especially in dual-phase oxide composites. Song et al. observed partial internal reduction in CeO$_2$/YSZ compounds under ambient air [29]. After annealing in 1 bar oxygen atmosphere at 943 K for 30 min and cool down, the CeO$_2$/YSZ interface is nonstoichiometric with high concentration of Ce$^{3+}$ ions close to the interface. The Ce$^{4+}$ ions are dominant in bulk CeO$_2$ regions while those at the interfacial regions tend to be reduced to Ce$^{3+}$ [29]. Recently, Ramasamy et al. discovered a similar partial internal reduction phenomenon in a dual-phase oxygen permeation membrane of Ce$_{0.8}$Gd$_{0.2}$O$_{2-\delta}$ – FeCo$_2$O$_4$ [30]. At the grain boundary between spinel (FeCo$_2$O$_4$) and fluorite (Ce$_{0.8}$Gd$_{0.2}$O$_{2-\delta}$), an oxygen-deficient interphase was observed without any treatment in reducing atmosphere [30]. Similar heterophase grain boundaries are present in dual-phase oxygen permeable membranes, which might be the reason for the increasing oxygen permeation flux with time in the initial period during the permeation test, since the grain boundaries with reduced oxygen content would be reoxidized firstly at high temperature under oxygen-containing atmosphere [31–33].

## 4. Conclusions

The partial internal reduction of NiO precipitate in (PL)$_{2.0}$NCG matrix during the cooling process after sintering has been elucidated. A metallic Ni interlayer between NiO precipitate and mixed ionic-electronic conducting oxide (PL)$_{2.0}$NCG is observed after sintering in ambient atmosphere. The formation mechanism and the diffusion processes during the partial internal reduction have been discussed in detail, which allows a consistent interpretation of the experimental results. The phenomenological description of the diffusion processes that take place during the partial internal reduction process is useful to materials scientists as well as to ceramic

membranes engineers as a model for the interpretation of similar morphologies occurring in metal/oxide or oxides/oxide composite systems.

## Acknowledgements

## References

[1] M. Backhaus-Ricoult, C.B. Carter, Mechanism of the internal reduction of (Mg, Cu)O, J. Am. Ceram. Soc. (1987) C-291–C-294.

[2] K. Ostyn, C.B. Carter, M. Koehne, H. Falke, H. Schmalzried, Internal reactions in oxide solid solutions, J. Am. Ceram. Soc. 67 (1984) 679–685.

[3] H. Schmalzried, M. Backhaus-Ricoult, Internal solid state reactions, Prog. Solid State Chem. 22 (1993) 1–57.

[4] D. Ricoult, H. Schmalzried, Internal reduction of (Mg: Ni)O: effect of a NiO-concentration gradient, Phys. Chem. Miner. 14 (1987) 238–244.

[5] M. Backhaus-Ricoult, S. Hagège, Internal reduction of (Mg Cu)O, Philos. Mag. A 67 (1993) 1471–1493.

[6] U. Brossmann, R. Würschum, U. Södervall, H.E. Schaefer, Oxygen diffusion in ultrafine grained monoclinic $ZrO_2$, J. Appl. Phys. 85 (1999) 7646–7654.

[7] I. Danilenko, F. Glazunov, T. Konstantinova, G. Volkova, V. Burkhovetski, Effect of oxide nanofillers on fabrication structure, and properties of zirconia-based composites, J. Eur. Ceram. Soc. 33 (2013) 2321–2325.

[8] J.T. White, I.E. Reimanis, J. Tong, J.R. O'Brien, A. Morrissey, Internal reduction of $Ni^{2+}$ in $ZrO_2$ stabilized with 10 mol% $Y_2O_3$ examined with VSM and SQUID magnetometry, J. Am. Ceram. Soc. 95 (2012) 4008–4014.

[9] H. Kondo, T. Sekino, N. Tanaka, T. Nakayama, T. Kusunose, K. Niihara, Mechanical and magnetic properties of novel yttria-stabilized tetragonal zirconia/Ni nanocomposite prepared by the modified internal reduction method, J. Am. Ceram. Soc. 88 (2005) 1468–1473.

[10] C.J. Ho, W.H. Tuan, Toughening and strengthening zirconia through the addition of a transient solid solution additive, J. Eur. Ceram. Soc. 32 (2012) 335–341.

[11] H.U. Fuchs, The Dynamics of Heat, Springer, 1996.

[12] A. Feldhoff, M. Arnold, J. Martynczuk, T.M. Gesing, H. Wang, The sol-gel synthesis of perovskites by an EDTA/citrate complexing method involves nanoscale solid state reactions, Solid State Sci. 10 (2008) 689–701.

[13] J. Xue, A. Schulz, H. Wang, A. Feldhoff, The phase stability of the Ruddlesden-Popper type oxide $(Pr_{0.9}La_{0.1})_2Ni_{0.74}Cu_{0.21}Ga_{0.05}O_{4+\delta}$ in an oxidizing environment, J. Membr. Sci. 497 (2016) 357–364.

[14] J. Xue, Q. Liao, W. Chen, H.J.M. Bouwmeester, H. Wang, A. Feldhoff, A new $CO_2$-resistant Ruddlesden-Popper oxide with superior oxygen transport: A-site deficient $(Pr_{0.9}La_{0.1})_{1.9}Ni_{0.74}Cu_{0.21}Ga_{0.05}O_{4+\delta}$, J. Mater. Chem. A 3 (2015) 19107–19114.

[15] M. Yashima, N. Sirikanda, T. Ishihara, Crystal structure diffusion path, and oxygen permeability of a $Pr_2NiO_4$-based mixed conductor $(Pr_{0.9}La_{0.1})_2Ni_{0.74}Cu_{0.21}Ga_{0.05}O_{4+\delta}$, J. Am. Ceram. Soc. 132 (2010) 2385–2392.

[16] A. Golonka, E. Drożdż-Cieśla, N. Moskała, W. Pyda, Effects of the nickel oxalate precursor and SPS consolidation process on properties of $Ni/Al_2O_3$ composites, Materiały Ceramiczne/Ceram. Mater. 65 (2013) 227–234.

[17] E.C. Dickey, V.P. Dravid, P.D. Nellist, D.J. Wallis, S.J. Pennycook, A. Revcolevschi, Structure and bonding at $Ni-ZrO_2$ (cubic) interfaces formed by the reduction of a $NiO-ZrO_2$ (cubic) composite, Microsc. Microanal. 3 (1997) 443–450.

[18] R. Swalin, Thermodynamics of Solids, Wiley-Interscience, 1972.

[19] I. Barin, Thermochemical Data of Pure Substances, Wiley-VCH, 1997.

[20] R.A. Swalin, A.L. King, Thermodynamics of solids, Am. J. Phys. 30 (1962) 778.

[21] V.V. Kharton, A.A. Yaremchenko, A.L. Shaula, M.V. Patrakeev, E.N. Naumovich, D.I. Logvinovich, J.R. Frade, F.M.B. Marques, Transport properties and stability of Ni-containing mixed conductors with perovskite- and $K_2NiF_4$-type structure, J. Solid State Chem. 177 (2004) 26–37.

[22] E. Boehm, J. Bassat, P. Dordor, F. Mauvy, J. Grenier, P. Stevens, Oxygen diffusion and transport properties in non-stoichiometric $LnNiO$ oxides, Solid State Ionics 176 (2005) 2717–2725.

[23] E. Boehm, J.M. Bassat, M.C. Steil, P. Dordor, F. Mauvy, J.C. Grenier, Oxygen transport properties of $La_2Ni_{1-x}Cu_xO_{4+\delta}$ mixed conducting oxides, Solid State Sci. 5 (2003) 973–981.

[24] J.-W. Park, C.J. Altstetter, The diffusion and solubility of oxygen in solid nickel, Metall. Mater. Trans. A 18 (1987) 43–50.

[25] C. Zou, Y.K. Shin, A.C. van Duin, H. Fang, Z.-K. Liu, Molecular dynamics simulations of the effects of vacancies on nickel self-diffusion oxygen diffusion and oxidation initiation in nickel, using the ReaxFF reactive force field, Acta Mater. 83 (2015) 102–112.

[26] B. Bonvalot-Dubois, G. Dhalenne, J. Berthon, A. Revcolevschi, R. Rapp, Reduction of NiO platelets in a $NiO/ZrO_2$ (CaO) directional composite, J. Am. Ceram. Soc. 71 (1988) 296–301.

[27] J. Sunarso, S. Baumann, J.M. Serra, W.A. Meulenberg, S. Liu, Y.S. Lin, J.C. Diniz da Costa, Mixed ionic-electronic conducting (MIEC) ceramic-based membranes for oxygen separation, J. Membr. Sci. 320 (2008) 13–41.

[28] M. Yashima, Diffusion pathway of mobile ions and crystal structure of ionic and mixed conductors – a brief review, J. Ceram. Soc. Jpn. 117 (2009) 1055–1059.

[29] K. Song, H. Schmid, V. Srot, E. Gilardi, G. Gregori, K. Du, J. Maier, P.A. van Aken, Cerium reduction at the interface between ceria and yttria-stabilised zirconia and implications for interfacial oxygen non-stoichiometry, Appl. Mater. 2 (2014) 032104.

[30] M. Ramasamy, S. Baumann, J. Palisaitis, F. Schulze-Küppers, M. Balaguer, D. Kim, W.A. Meulenberg, J. Mayer, R. Bhave, O. Guillon, Influence of microstructure and surface activation of dual-phase membrane $Ce_{0.8}Gd_{0.2}O_{2-\delta}-FeCo_2O_4$ on oxygen permeation, J. Am. Ceram. Soc. 99 (2015) 349–355.

[31] X. Zhu, W. Yang, Composite membrane based on ionic conductor and mixed conductor for oxygen permeation, AIChE J. 54 (2008) 665–672.

[32] H. Luo, K. Efimov, H. Jiang, A. Feldhoff, H. Wang, J. Caro, $CO_2$-stable and cobalt-free dual-phase membrane for oxygen separation, Angew. Chem. Int. Ed. 50 (2011) 759–763.

[33] J. Xue, Q. Zheng, Y. Wei, K. Yuan, Z. Li, H. Wang, Dual phase composite oxide of $Ce_{0.9}Gd_{0.1}O_{2-\delta}-Ba_{0.5}Sr_{0.5}Co_{0.8}Fe_{0.2}O_{3-\delta}$ with excellent oxygen permeation, Ind. Eng. Chem. Res. 51 (2012) 4703–4709.

# Chapter 3
# Dense ceramic hydrogen-separating membranes
## 3.1 Summary

Dense ceramic hydrogen-separating membranes with protonic and electronic conductivity can be applied in some industrial processes such as hydrogen separation and catalytic membrane reactors. For these applications, the ceramic hydrogen-permeable membranes should not only exhibit high hydrogen permeation flux, but also good chemical stability and phase stability under the operational conditions. Among the hydrogen-permeable membranes, $Ni-BaCe_{0.95}Tb_{0.05}O_{3-\delta}$ (Ni-BCT) membrane is outstanding with respect to the hydrogen permeation flux, while it bears a phase segregation, which results in a sharp decline to half the hydrogen permeation flux after a few days of operation. The poor phase stability limits its practical applications.

The zirconate-based oxides exhibit better phase stability than that of cerate-based oxides due to its constant valence state of $Zr^{4+}$. Therefore, to improve the phase stability of Ni-BCT, in section 3.2, Zr was doped into the $BaCe_{0.85}Tb_{0.05}O_{3-\delta}$ (BCT) phase of the Ni-BCT cermet membrane. The Ni-BCTZ membrane shows excellent stability compared to Ni-BCT, and it can be steadily operated in both dry and humid conditions for hydrogen permeation for 5 days at 800 $^{o}$C. Moreover, the hydrogen permeation fluxes of Ni-BCTZ membrane are higher than that of Ni-BCT membrane after two days operation, which promotes the Ni-BCTZ membranes as good candidates for some potential practical applications.

In section 3.3, a novel hydrogen-permeable material $BaCe_{0.85}Tb_{0.05}Zr_{0.1}O_{3-\delta}$ (BCTZ) was developed for the first time with partial substitution of Ce with Zr into the BCT system, which exhibits remarkably enhanced phase stability. The BCTZ asymmetric membranes with 50 μm dense layer have been successfully prepared, and it could be steadily operated for hydrogen separation for over two weeks at 800 $^{o}$C. Moreover, the BCTZ membrane also exhibits good chemical stability under $CO_2$-, $CH_4$-, CO- and $H_2O$-containing atmosphere, so that it can be applied in different industrial applications.

The section 3.4 deals with a catalytic membrane reactor, which combines the methane dehydroaromatization reaction with a hydrogen-permeable ceramic membrane. A high-flux hydrogen-transporting ceramic U-shape hollow-fiber was used and up to 60 % of the produced hydrogen have been *in-situ* extracted. The hydrogen extraction indeed boosts methane conversion and aromatics yield above the reference experiment in a fixed-bed reactor. The yield of aromatics increased in the beginning of the aromatization reaction by about 50% to 75%. The ceramic membrane reactor also shows better long-term stability compared with traditional metal membrane reactors, while abovementioned advantages of the membrane reactor decrease with time, since the removal of hydrogen not only boosts the methane conversion and aromatics yield, but also catalyst deactivation by deposition of carbonaceous deposits. However, the ceramic membrane reactor system (catalyst + membrane) can be easily regenerated by burning the coke away with air. Therefore, this catalytic cense ceramic membrane reactor will contribute to process intensification as a concept in chemical engineering.

## 3.2 Enhanced stability of Zr-doped Ba(CeTb)O$_{3-\delta}$-Ni cermet membrane for hydrogen separation

Yanying Wei, <u>Jian Xue</u>, Wei Fang, Yan Chen, Haihui Wang and Jürgen Caro

# ChemComm

## COMMUNICATION

# Enhanced stability of Zr-doped Ba(CeTb)$O_{3-\delta}$-Ni cermet membrane for hydrogen separation†

Yanying Wei,[*ab] Jian Xue,[a] Wei Fang,[a] Yan Chen,[b] Haihui Wang[*bc] and Jürgen Caro[a]

A mixed protonic and electronic conductor material $BaCe_{0.85}Tb_{0.05}Zr_{0.1}O_{3-\delta}$ (BCTZ) is prepared and a Ni-BCTZ cermet membrane is synthesized for hydrogen separation. Stable hydrogen permeation fluxes can be obtained for over 100 h through the Ni-BCTZ membrane in both dry and humid conditions, which exhibits an excellent stability compared with Ni-$BaCe_{0.95}Tb_{0.05}O_{3-\delta}$ membrane due to the Zr doping.

High-temperature mixed protonic and electronic conductors (HT-MPECs)[1,2] have attracted increasing interest due to their wide potential applications as hydrogen sensors, hydrogen pumps, hydrogen permeable membranes for gas separation,[3–9] catalytic membrane reactors,[10] and solid oxide fuel cells (SOFCs)[11–14] etc. since Iwahara et al.[15] reported that the ceramics based on strontium cerates show relatively high protonic conductivities. For these applications, the HT-MPECs should not only exhibit high protonic and electronic conductivities but also good chemical stability and phase structure stability under the operation conditions. However, for most doped perovskite oxides, such as $BaCeO_3$, $BaZrO_3$, $SrCeO_3$ and $SrZrO_3$ etc., their relatively low electronic conductivity is the bottle neck for hydrogen transportation.[16] Therefore, in order to increase the electronic conductivity, a metal phase (usually nickel) can be added to the perovskite oxide to form a cermet (ceramic–metal) composite, which shows much better hydrogen permeability, such as Ni-$Ba(Zr_{0.8-x}Ce_xY_{0.2})O_{3-\delta}$,[17–19] Ni-$SrCeO_{3-\delta}$,[20] Ni-$Ba(Zr_{0.7}Pr_{0.1}Y_{0.2})O_{3-\delta}$.[21]

*a Institute of Physical Chemistry and Electrochemistry, Leibniz University of Hannover, Callinstrasse 22, 30167 Hannover, Germany. E-mail: yanying.wei@pci.uni-hannover.de*
*b School of Chemistry and Chemical Engineering, South China University of Technology, 510640 Guangzhou, China. E-mail: hhwang@scut.edu.cn*
*c School of Chemical Engineering, The University of Adelaide, Adelaide, SA 5005, Australia*

Till now, the highest hydrogen permeation flux up to $0.914$ ml $min^{-1}$ $cm^{-2}$ was obtained at 850 °C through the Ni-$BaCe_{0.95}Tb_{0.05}O_{3-\delta}$ (Ni-BCT) asymmetric cermet membrane with a 90 μm dense layer on a porous substrate reported by Meng et al.[22] Unfortunately, the hydrogen flux through the Ni-BCT membrane declined by about 50% after 75 h operation at 800 °C due to the phase segregation.[22] Therefore, materials with both high hydrogen permeability and adequate stability are required to be developed. As it is known, the doped $BaZrO_3$ exhibits a much higher stability compared with the doped $BaCeO_3$, and the two oxides can form easily a solid solution.[18,19] It is expected that replacing some Ce with Zr in the Ni-BCT system may enhance its phase structure stability due to the constant valence state of $Zr^{4+}$. Therefore, in the present study, the hydrogen permeability and the phase structure stability of Ni-$BaCe_{0.85}Tb_{0.05}Zr_{0.1}O_{3-\delta}$ (Ni-BCTZ, 50:50 wt%) are investigated. It is found that the Ni-BCTZ cermet membrane can be steadily operated in both dry and humid reducing atmospheres for hydrogen permeation for over 100 h at 800 °C, which demonstrates its excellent stability compared with Ni-BCT.

Firstly, both of the BCT and BCTZ powders were treated in Ar and 50% $H_2$–50% Ar atmospheres for 20 h at 800 °C, respectively. Although no obvious change can be found between the fresh and treated powders, and all the powders exhibit an orthorhombic perovskite structure (Fig. 1a), the lattice parameters ($a$, $b$, $c$) calculated from the Rietveld refinements (Fig. 1d) differ greatly when exposed to different atmospheres which can be mainly attributed to the reduction of $Ce^{4+}$ as well as the formation of oxygen vacancies. The lattice expansion coefficients, $\alpha_i$, which can be described as follows,

$$\alpha_i = (i_{reducing} - i_{inert})/i_{inert} \times 100\%$$

$i$ stands for the lattice parameters of $a$, $b$, $c$ in the three crystallographic directions, the subscript of "reducing" and "inert" stands for the 50% $H_2$–50% Ar and Ar atmospheres, respectively. As shown in Fig. 1c, it is noticed that Zr-doping decreases the lattice expansion coefficient of BCT significantly for all three crystallographic directions. TG and $H_2$-TPR results
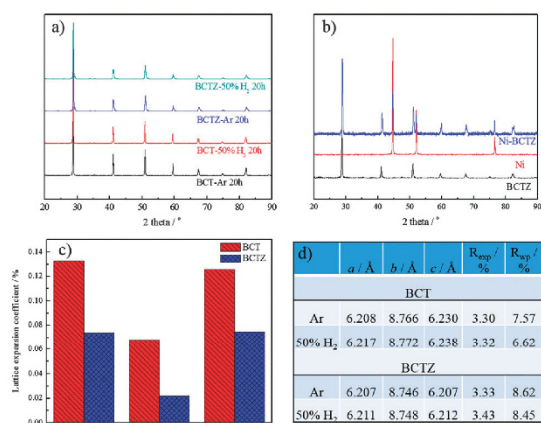
Communication

**Fig. 1** (a) XRD patterns of BCT and BCTZ powder after treatment in Ar and 50% H$_2$–50% Ar atmospheres; (b) XRD patterns of the as-calcined Ni-BCTZ cermet membrane; (c) lattice expansion coefficient of BCT and BCTZ; (d) lattice parameters of BCT and BCTZ after treatment in different atmospheres calculated from Rietveld refinements.
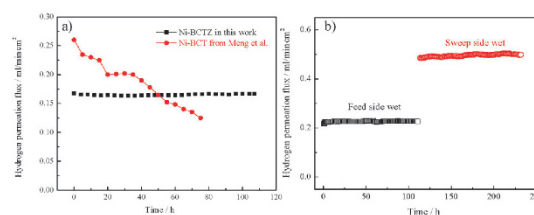


**Fig. 2** (a) Hydrogen permeation flux as a function of time with 50% H$_2$ in feed gas at 800 °C under dry condition. Ni-BCTZ: 0.5 mm symmetric dense membrane, Ni-BCT: asymmetric membrane with 90 μm dense layer, data of Meng *et al.*[22] (reproduction permitted with Elsevier License); (b) long term stability test of Ni-BCTZ membrane under humid reducing atmosphere (containing 0.03 atm water steam in each membrane side) at 800 °C.

(Fig. S1 and S2, ESI†) also prove that Zr-doping has enhanced the phase structure stability. As shown in Fig. 1b for the XRD patterns of the composite Ni-BCTZ membrane, all diffraction peaks can be assigned to either BCTZ or metallic Ni and no new crystalline phases appears, which indicates that no reaction took place between the BCTZ oxide and the metallic nickel during the membrane preparation and the good stability and compatibility between the two phases. BCTZ shows the body-centered orthorhombic phase with space group of *Imma* (74). The lattice parameters of *a*, *b*, *c* were calculated from the Rietveld refinement to be 6.206 Å, 8.747 Å and 6.208 Å, respectively, with the $R_{exp}$ and $R_{wp}$ of 3.32% and 9.26%.

The microstructures of the Ni-BCTZ membrane, as well as the hydrogen permeation test under different conditions, are shown in Fig. S3 to S6 (ESI†). The hydrogen permeation flux increases a little with wet feed gas due to the increase of protonic conductivity. This effect can be ascribed to the hydration of the membrane that allows the formation of two protonated oxygen atoms (lattice or interstitial oxygens), which are the essential charge carriers involved in hydrogen transport.[23,24] The hydrogen flux jumps sharply with wet sweep gas, because in this case some part of the hydrogen comes from the thermal water splitting.[24]

Much attention has been paid in the long term stability of the Ni-BCTZ membrane for hydrogen separation. The measurement was carried out at 800 °C using 50% H$_2$–50% He as the feed gas in both dry and humid conditions. As shown in Fig. 2a under dry condition, the hydrogen permeation flux through the Ni-BCTZ membrane with a thickness of 0.5 mm keeps stable around 0.17 ml min$^{-1}$ cm$^{-2}$ for over 100 h and no decline with time can be found. However, Meng[22] reported that the hydrogen permeation flux through the Ni-BCT membrane decreases from the initial 0.26 ml min$^{-1}$ cm$^{-2}$ to 0.126 ml min$^{-1}$ cm$^{-2}$ after 75 h operation. At the beginning of permeation, the hydrogen

permeation flux through our Ni-BCTZ membrane is lower than that through the Ni-BCT membrane. There are two reasons for this experimental finding. On the one hand, the substitution of Zr for Ce in the BCT material reduces its protonic conductivity to some extent,[25–27] just like doping Zr into BaCe$_{0.9}$Y$_{0.1}$O$_{3-\delta}$ gives lower conductivity, and Zr doping reduces the hydrogen permeation flux.[26] Therefore, we only doped 10 mol% Zr in Ni-BCT aiming to keep its hydrogen permeation flux on a high level. And even so, the hydrogen permeation flux through our Ni-BCTZ membrane is still much higher than that through many other hydrogen permeable cermet membranes, such as Ni-Ba(Zr$_{0.8-x}$Ce$_x$Y$_{0.2}$)O$_{3-\delta}$,[18] Ni-Ba(Zr$_{0.7}$Pr$_{0.1}$Y$_{0.2}$)O$_{3-\delta}$[21] *etc.* On the other hand, the Ni-BCT membrane has an asymmetric structure of 90 μm dense layer supported on a porous substrate which is beneficial for hydrogen transportation while the Ni-BCTZ membrane is a completely dense compact membrane with a thickness of 0.5 mm. On the contrary, our Ni-BCTZ membrane shows excellent stability for the overall process, which is extremely essential for all the applications including hydrogen separation. In the humid reducing atmosphere, Ni-BCTZ membrane also exhibits excellent stability and the hydrogen flux keeps steady for over 100 h.

From the XRD, SEM and EDXS results of the spent Ni-BCTZ membrane shown in Fig. 3 and 4, Fig. S7 and Table S1 (ESI†), no big changes of the microstructure can be found in comparison with the fresh cermet membrane (see Fig. S4, ESI†). The spent Ni-BCTZ membrane still keeps its original structure without impurity phases except some residual ceramic sealant. Combined with more EDXS results and compared with Ni-BCT, (Table S2 and Fig. S8–S11, ESI†), the good phase structure stability of Ni-BCTZ can be evidenced even under reducing atmospheres for a long time. One important thing should be emphasized that among numerous proton conductive oxides for hydrogen separation, there are only a few materials which exhibit both good stability and nice permeation flux (Fig. S12, ESI†). In consideration of both hydrogen permeability and stability, Ni-BCTZ is really a promising material candidate for hydrogen separation.

In summary, after doping Zr into the BCT oxide, the phase structure stability of the Ni-BCTZ cermet membrane has been
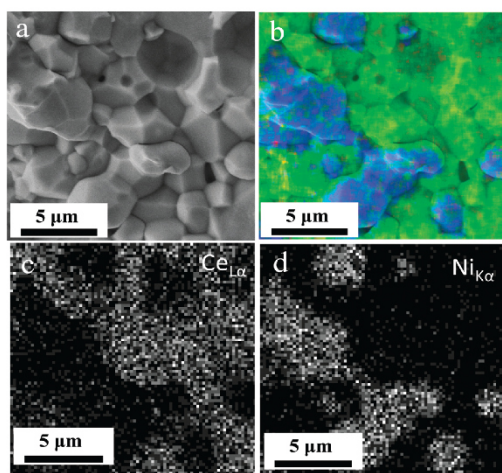
74

**ChemComm**

**Fig. 3** SEM and EDXS elemental distributions of Ce and Ni in the bulk of the spent Ni-BCTZ cermet membrane after 100 h hydrogen permeation. Blue: metallic Ni phase; green: perovskite oxide phase.
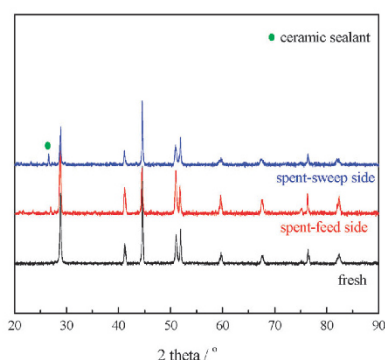


**Fig. 4** X-ray diffraction patterns of the fresh and spent Ni-BCTZ membrane after 100 h hydrogen permeation.

enhanced remarkably. The Ni-BCTZ membrane can be steadily operated under both dry and humid conditions for over 100 h at 800 °C for hydrogen separation, which shows an extremely enhanced stability compared with Ni-BCT. The XRD and SEM results also prove the outstanding phase structure stability, which promotes the Ni-BCTZ material as a proper candidate of an MPEC material for different potential applications.

## Notes and references

1 M. S. Islam, R. A. Daviesa and J. D. Gale, *Chem. Commun.*, 2001, 661–662.
2 S. Li, F. Schönberger and P. Slater, *Chem. Commun.*, 2003, 2694.
3 M. Amsif, A. Magraso, D. Marrero-Lopez, J. C. Ruiz-Morales, J. Canales-Vazquez and P. Nunez, *Chem. Mater.*, 2012, **24**, 3868.
4 S. Escolastico, S. Somacescu and J. M. Serra, *Chem. Mater.*, 2014, **26**, 982.
5 S. Escolastico, V. B. Vert and J. M. Serra, *Chem. Mater.*, 2009, **21**, 3079.
6 S. Escolastico, C. Solis, C. Kjølseth and J. M. Serra, *Energy Environ. Sci.*, 2014, **7**, 3736.
7 S. Escolastico, J. Seeger, S. Roitsch, M. Ivanova, W. A. Meulenberg and J. M. Serra, *ChemSusChem*, 2013, **6**, 1523.
8 J. Seeger, M. E. Ivanova, W. A. Meulenberg, D. Sebold, D. Stover, T. Scherb, G. Schumacher, S. Escolastico, C. Solís and J. M. Serra, *Inorg. Chem.*, 2013, **52**, 10375.
9 D. Holt, E. Forster, M. E. Ivanova, W. A. Meulenberg, M. Müller, S. Baumann and R. J. Vaßen, *J. Eur. Ceram. Soc.*, 2014, **34**, 2381.
10 G. Marnellos and M. Stoukiddes, *Science*, 1998, **282**, 98.
11 D. Pergolesi, E. Fabbri, A. D'Epifanio, E. Di Bartolomeo, A. Tebano, S. Sanna, S. Licoccia, G. Balestrino and E. Traversa, *Nat. Mater.*, 2010, **9**, 846.
12 L. Yang, S. Wang, K. Blinn, M. Liu, Z. Liu, Z. Cheng and M. Liu, *Science*, 2009, **326**, 126.
13 A. Aguadero, D. Perez-Coll, J. A. Alonso, S. J. Skinner and J. Kilner, *Chem. Mater.*, 2012, **24**, 2655.
14 F. Bozza, W. Schafbauer, W. A. Meulenberg and N. Bonanos, *Int. J. Hydrogen Energy*, 2012, **37**, 8027.
15 H. Iwahara, T. Esaka, H. Uchida and N. Maeda, *Solid State Ionics*, 1981, **3/4**, 359.
16 S. J. Song, E. D. Wachsman, J. Rhodes, S. E. Dorris and U. Balachandran, *Solid State Ionics*, 2004, **99**, 167.
17 C. Zuo, T. H. Lee, S. J. Song, L. Chen, S. E. Dorris, U. Balachandran and M. Liu, *Electrochem. Solid-State Lett.*, 2005, **8**, J35.
18 C. Zuo, S. E. Dorris, U. Balachandran and M. Liu, *Chem. Mater.*, 2006, **18**, 4647.
19 C. Zuo, T. H. Lee, S. E. Dorris, U. Balachandran and M. Liu, *J. Power Sources*, 2006, **159**, 1291.
20 S. J. Song, T. H. Lee, E. D. Wachsman, L. Chen, S. E. Dorris and U. Balachandran, *J. Electrochem. Soc.*, 2005, **152**, J125.
21 Z. Zhu, W. Sun, Y. Dong, Z. Wang, Z. Shi, Q. Zhang and W. Liu, *Int. J. Hydrogen Energy*, 2014, **39**, 11683.
22 X. Meng, J. Song, N. Yang, B. Meng, X. Tan, Z. Ma and K. Li, *J. Membr. Sci.*, 2012, **401–402**, 300.
23 R. Haugsrud and C. Kjølseth, *J. Phys. Chem. Solids*, 2008, **69**, 1758.
24 S. Escolastico, C. Solis, T. Scherb, G. Schumacher and J. M. Serra, *J. Membr. Sci.*, 2013, **444**, 276.
25 T. Oh, J. Li, H. Yoon and E. D. Wachsman, *Ionics*, 2009, **15**, 525.
26 Z. Zhong, *Solid State Ionics*, 2007, **178**, 213.
27 K. Katahira, Y. Kohchi, T. Shimura and H. Iwahara, *Solid State Ionics*, 2000, **138**, 91.

75

# Electronic Supplementary Information

# Enhanced stability of Zr-doped Ba(CeTb)O$_{3-\delta}$-Ni cermet membrane for hydrogen separation

Yanying Wei,[a,b,*] Jian Xue,[a] Wei Fang,[a] Yan Chen,[b] Haihui Wang,[b,c,*] Jürgen Caro[a]

[a] Institute of Physical Chemistry and Electrochemistry, Leibniz University of Hannover, Callinstrasse 22, 30167 Hannover, Germany

[b] School of Chemistry and Chemical Engineering, South China University of Technology, 510640 Guangzhou, China

[c] School of Chemical Engineering, The University of Adelaide, Adelaide, SA 5005, Australia

**Experimental section**

The BaCe$_{0.85}$Tb$_{0.05}$Zr$_{0.1}$O$_{3-\delta}$ (BCTZ) perovskite powder was prepared through the glycine-nitrate combustion process. Ba(NO$_3$)$_2$, Ce(NO$_3$)$_3$, Tb(NO$_3$)$_3$, ZrO(NO$_3$)$_2$ and glycine were used as the raw materials to form an aqueous solution in their appropriate stoichiometric ratios. The molar ratio of glycine: total metal ions was 2:1. After evaporation of excess water at 200 °C with stirring, the aqueous solution became a viscous liquid and further heating up to 400 °C caused the auto-combustion process, which produced the BCTZ precursor ash. The BCTZ powder with perovskite structure was obtained after calcining at 1000 °C for 5 h. The as-prepared BCTZ powder was also treated in Ar and 50% H$_2$-50% Ar atmosphere at 800 °C for 20 h. The Ni-BCTZ cermet membrane was synthesized by mixing the BCTZ oxide powder and the commercial metallic nickel powder in a weight ratio of 1:1 followed by sintering at 1400 °C for 10 h in Ar atmosphere.

X-ray diffraction (XRD, D8 Advance, Bruker-AXS, with Cu-Ka radiation) was used to determine the phase structure. Data sets were recorded in a step-scan mode in the 2θ range of 20 - 90° with intervals of 0.02°. The phase analysis was carried out using the database of Powder Diffraction File (PDF) of International Centre of Diffraction Data (ICDD). The lattice parameters were calculated through structure Rietveld refinement by the program TOPAS (Bruker, version of 4.2). The morphology of the fresh and spent Ni-BCTZ cermet membrane were characterized by scanning electron microscopy (SEM) at 2 keV and by energy dispersive X-ray spectroscopy (EDXS) at 15 keV using a Jeol-JSM-6700F. The element distribution in the grains of the cermet membrane was studied on the same electron microscope by EDXS with Oxford Instruments INCA-300 EDX spectrometer at 15 keV.

Thermogravimetric analysis was conducted to study the stability of the BCT and BCTZ powder in $N_2$ atmosphere with NETZSCH-STA449C apparatus. The samples were heated in $N_2$ atmosphere at a rate of 5°C/min before holding at 800°C for 30 min.

Hydrogen temperature-programmed reduction ($H_2$-TPR) was carried out in a U-type quartz tube reactor to identify the chemical reduction properties of all the samples. Sample powder was loaded in a U-type quartz tube and pretreated under a 10% $H_2$-90% Ar atmosphere at a flow rate of 20 ml/min for 30 min at room temperature. The temperature was then increased from room temperature to 800 °C at a ramp rate of 10 °C/min. The consumption of hydrogen was monitored by an in situ thermal conductivity detector (TCD) using a micromeritics-AutoChem II, Chemisorption Analyzer.

For the hydrogen permeation measurement, a disk-shaped dense Ni-BCTZ cermet membrane with 0.5 mm thickness was used. The ceramic sealant was used to seal the membrane with an alumina tube to form the permeation compartment. 30 ml/min of 50% $H_2$ diluted with He were used as feed gas and 60 ml/min of Ar was used as sweep gas. Composition of the permeated effluent gas was measured using an online coupled gas chromatograph (GC, Agilent 6890, Ar as carrier gas) with a thermal conductivity detector (TCD). The concentration of the helium in the sweep side due to the imperfect sealing at high temperatures was less than 0.1% during all the experiments.
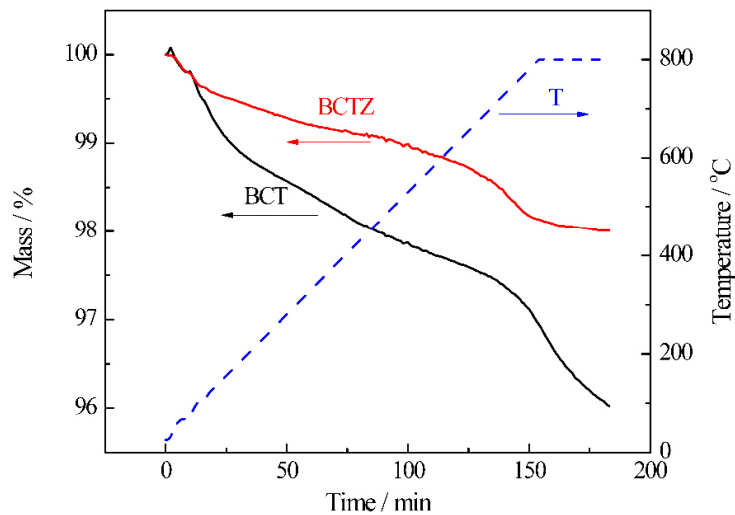
Figure S1. Thermo-gravimetric curves of BCT and BCTZ powder samples in N$_2$ atmosphere.

The mass of both BCT and BCTZ powder slightly decreased in the N$_2$ atmosphere as the temperature increased. The slight weight loss potentially resulted from dehydration and the release of oxygen from the perovskite oxides. It can be found that compared with BCT, the weight loss of BCTZ is more slight which indicates the better stability of the oxide.
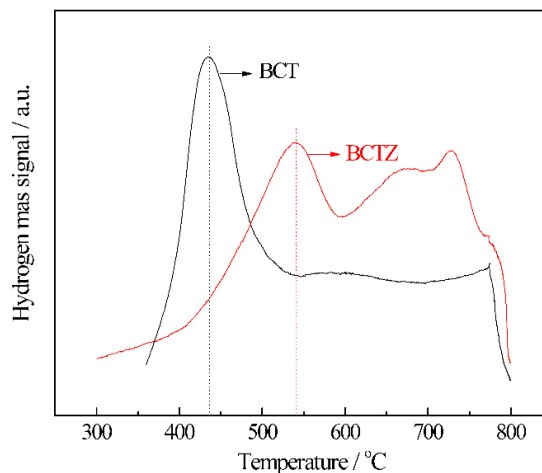
Figure S2. $H_2$-TPR profiles of BCT and BCTZ samples.

As shown in Figure S2, for the BCT sample, a big reduction peak can be observed at approximately 434 °C, which is related to the reduction of $Ce^{4+}$ to $Ce^{3+}$ in the lattice. Compared to BCT, the reduction peak of BCTZ sample has been moved to a higher temperature, the first reduction peak centered at 539 °C can be attributed to the surface $Ce^{4+}$ reduction to $Ce^{3+}$, and the other broad peak located between 658 °C to 729 °C can be attributed to the bulk $Ce^{4+}$ reduction to $Ce^{3+}$.[1,2] It can be found from the $H_2$-TPR results that Zr-doping makes the reduction peak appearing at higher temperature, which indicates that Zr-doping enhances the stability of BCT in the reducing atmosphere.

[1] Y. Liu, R. Ran, S. Li, Y. Jiao, M. O. Tade, Z. Shao. Significant performance enhancement of yttrium-doped barium cerate proton conductor as electrolyte for solid oxide fuel cells through a Pd ingresse-egress approach.    J. Power Sources 257 (2014) 308-318.

[2] C. Decarne, E. Abi-aad, B. G. Kostyuk, V. V. Lunin, A. Aboujais. Characterization of cerium and copper species in Cu-Ce-Al oxide systems by temperature programmed reduction and electron paramagnetic resonance. J. Mater. Sci. 39 (2004) 2349-2356.
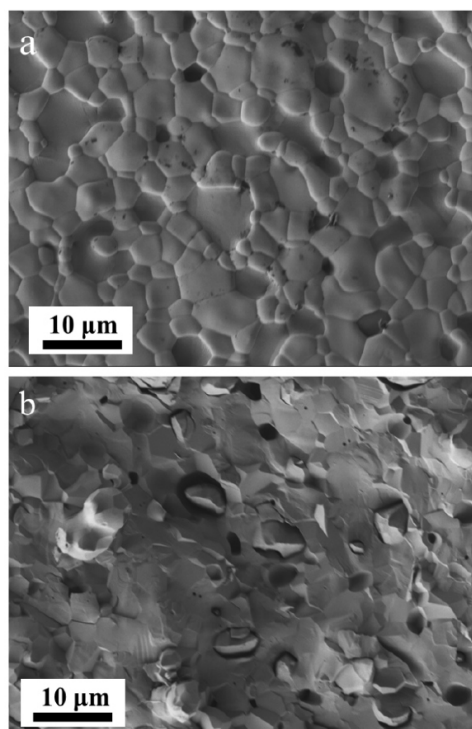
Figure S3. SEM micrographs of (a) the surface and (b) the bulk of the as-calcined Ni-BCTZ cermet membrane.

The SEM images of both the bulk and surface of the Ni-BCTZ cermet membrane (see Figure S3) indicates that it becomes a dense membrane after sintering at 1400 °C for 10 h. It can also be found that the grain size of Ni particles (around 3-7 μm) is a little bigger than that of BCTZ particles (about 2-5 μm). The EDXS elemental distribution (Figure S4c, d and g, h) of both the surface and bulk of the Ni-BCTZ membrane shows the homogeneous distribution of the Ni and the perovskite BCTZ oxide phase, which demonstrates that the metallic nickel and the BCTZ oxide are well mixed. A good homogeneity of the cermet membrane is important for its hydrogen transportation because it guarantees the formation of a percolation network of the two individual phases for both electron and proton transport.
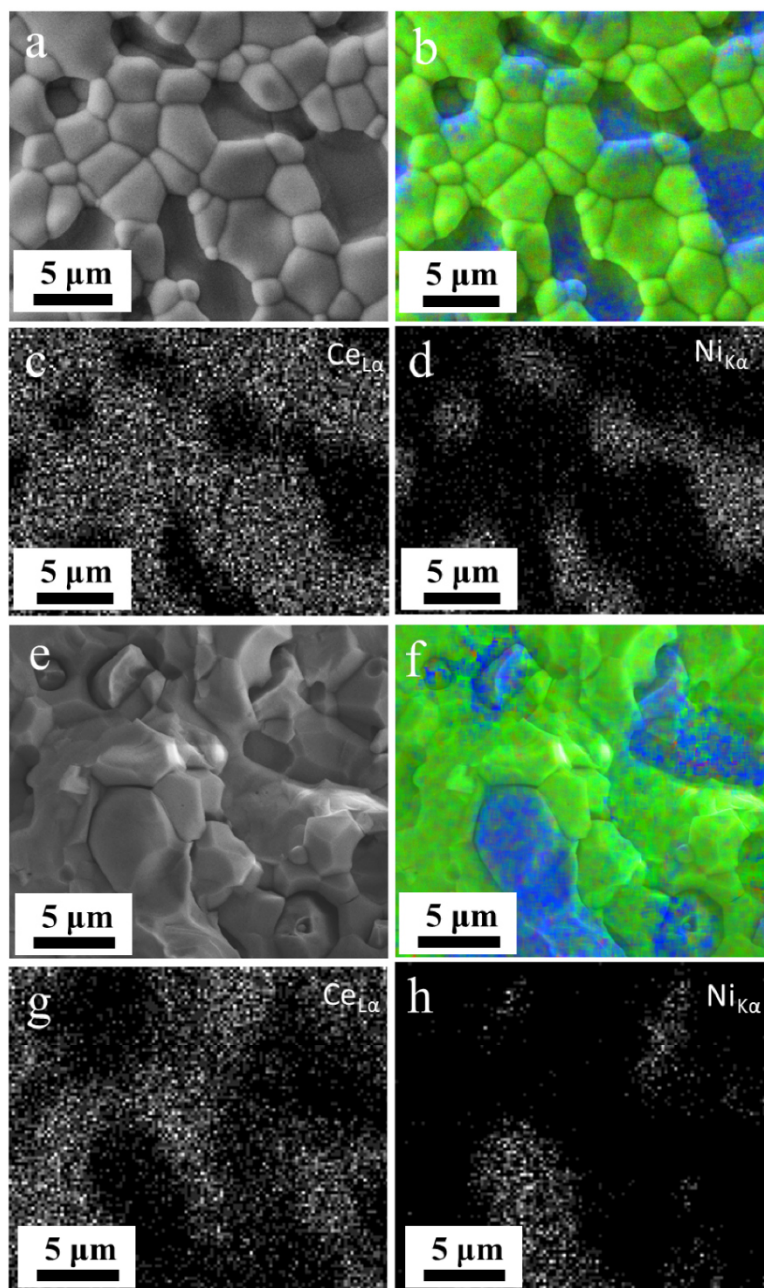
Figure S4. SEM and EDXS elemental distributions of Ce and Ni in (a-d) the surface and (e-h) the bulk of the as-calcined Ni-BCTZ cermet membrane. Blue: metallic Ni phase; green: perovskite oxide phase.
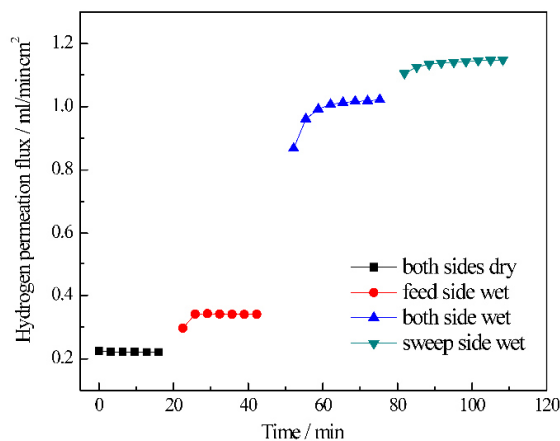
Figure S5. Hydrogen permeation flux variation resulted from the humidity on the feed and sweep sides at 1000 °C. P$_{H2O}$=0.03atm.

The hydrogen permeation flux through the Ni-BCTZ cermet membrane is measured as a function of temperature under four different humid conditions as shown in Figures S5 and S6. The hydrogen permeation flux is only 0.22 ml/min·cm$^2$ when both sides are dry at 1000 °C, while it increases to 0.34 ml/min·cm$^2$ when 0.03 atm steam is added to the feed side, which increases the protonic conductivity. This effect can be ascribed to the hydration of the membrane that allows the formation of two protonated oxygen atoms (lattice or interstitial oxygen), which are the essential charge carriers involved in hydrogen transport. The hydrogen permeation flux can even jump over 1 ml/min·cm$^2$ when 0.03 atm steam is introduced to the sweep side. However, in this case some part of the hydrogen comes from the thermal water splitting.
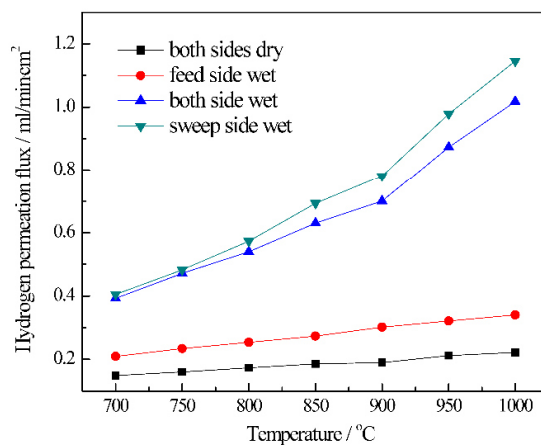
Figure S6. Hydrogen permeation flux as a function of the temperature under four humid conditions. $P_{H2O}$=0.03atm.
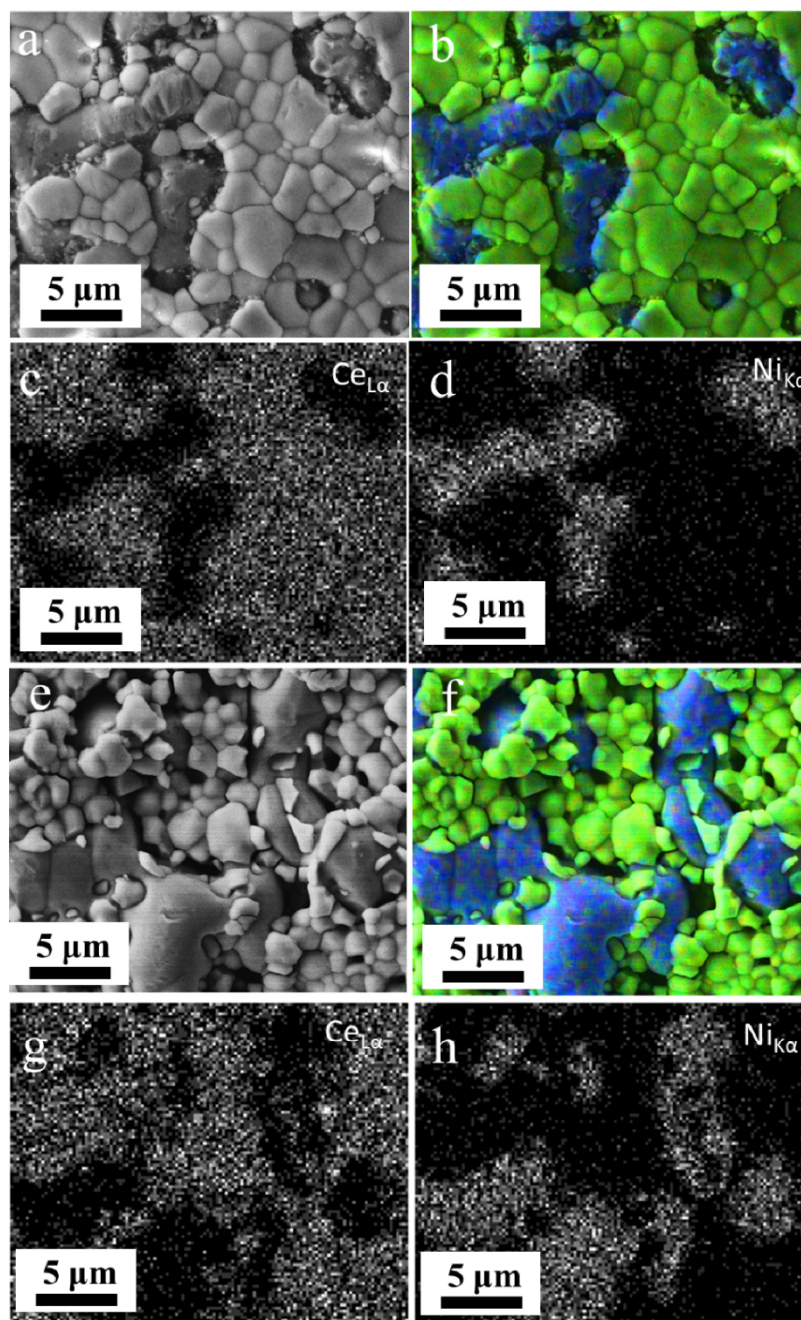
Figure S7. SEM and EDXS elemental distributions of Ce and Ni in the surfaces of the spent Ni-BCTZ cermet membrane after 100 h hydrogen permeation, (a-d) the surface of the feed side; (e-h) the surface of the sweep side. Blue: metallic Ni phase; green: perovskite oxide phase.

| Element | Atomic % | | | |
|---|---|---|---|---|
| | Fresh membrane | Spent membrane | | |
| | | Feed side | Bulk | Sweep side |
| O | 51.43 | 54.31 | 48.97 | 49.18 |
| Ni | 20.93 | 14.95 | 23.08 | 21.87 |
| Zr | 1.41 | 1.17 | 1.06 | 1.5 |
| Ba | 13.89 | 15.74 | 14.03 | 13.87 |
| Ce | 11.64 | 13.06 | 12.33 | 12.64 |
| Tb | 0.71 | 0.77 | 0.54 | 0.94 |
| Ba/Ce | 1.19 | 1.21 | 1.14 | 1.10 |

Table S1. EDXS results on both surfaces and bulk of the spent and fresh Ni-BCTZ membrane.

The EDXS data of the spent Ni-BCTZ membrane after the long term operation is shown in Table S1. For better comparison, the EDXS results for the fresh membrane has also been given. The ratio of Ba/Ce of the fresh membrane is 1.19, which is close to the theoretical value of 1.18. After the long term hydrogen separation, there is only small change on the Ba/Ce ratio in the spent membrane, which illustrates the good stability of Ni-BCTZ membrane.
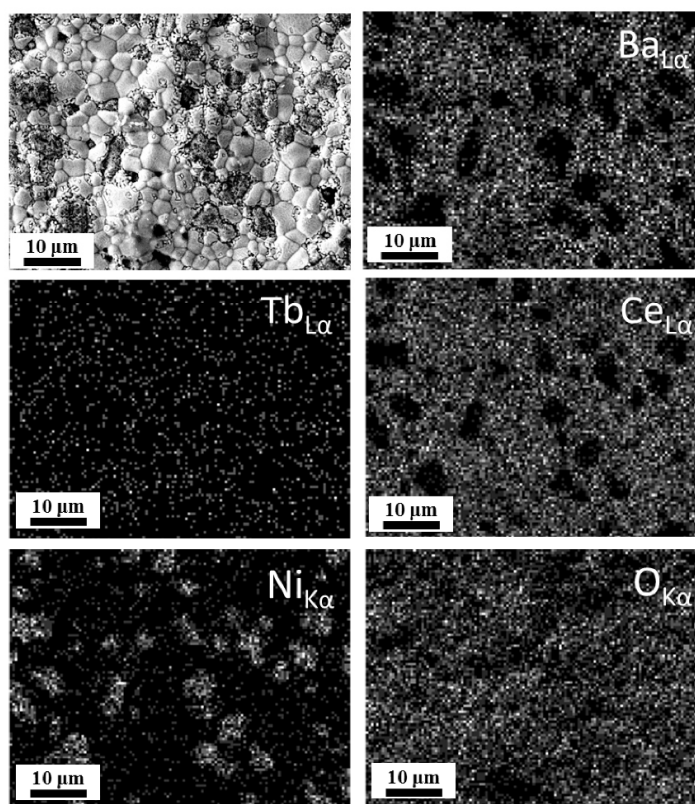
Figure S8. SEM and EDXS elemental distributions on the feed side surface of the spent Ni-BCT cermet membrane.

As shown in Figure S8, although the feed side surface of the spent Ni-BCT membrane still seems to be dense, but there are some coralloid porous structure covered on the surface, especially near the Ni part. On the contrary, it cannot be found on the feed side surface of the spent Ni-BCTZ membrane as shown in Figure S7. For the other side (sweep side) of the spent membrane, it looks like the original intact grain cracked to be many small particles shown in Figure S9, which may attributed to the big change of the lattice cell volume of BCT during the reduction and oxidation processes. Compared with Ni-BCT, the situation of Ni-BCTZ is much better due to the Zr-doping, which restrains the lattice cell expansion in reducing atmosphere and enhanced the phase structure stability.
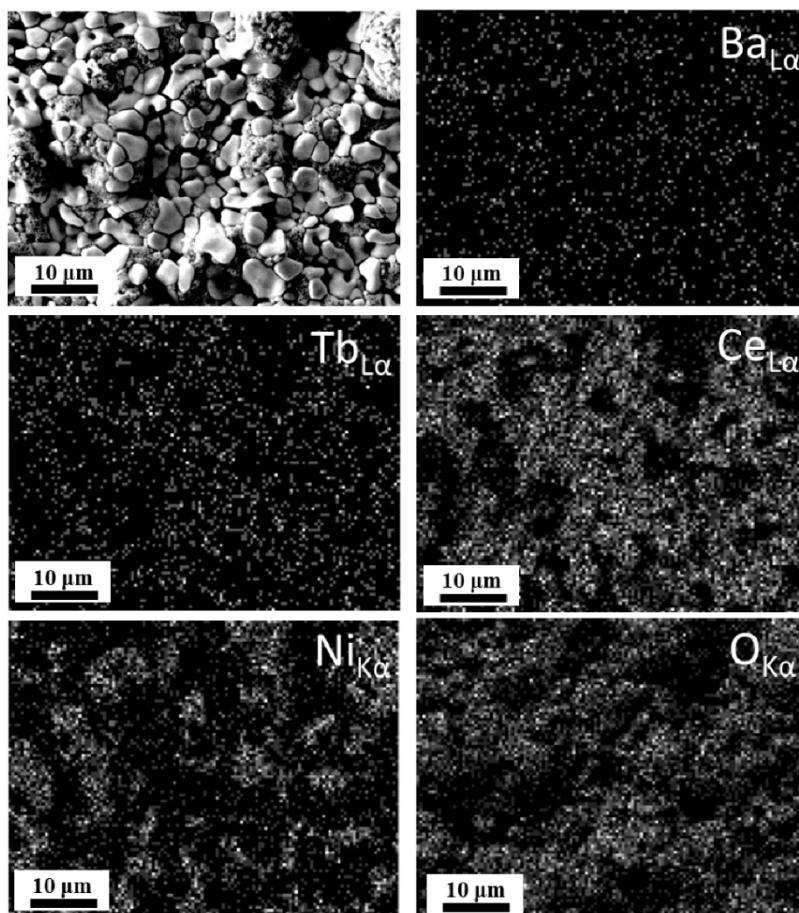
Figure S9. SEM and EDXS elemental distributions on the sweep side surface of the spent Ni-BCT cermet membrane.

| Element | Atomic % | | |
|---------|-----------|------|------------|
|         | Feed side | Bulk | Sweep side |
| O       | 58.27     | 52.27 | 60.09     |
| Ni      | 12.58     | 17.34 | 21.03     |
| Ba      | 13.14     | 15.42 | 0.27      |
| Ce      | 15.17     | 14.35 | 16.74     |
| Tb      | 0.83      | 0.62  | 1.87      |
| Ba/Ce   | 0.87      | 1.07  | 0.02      |

Table S2. EDXS results on both surfaces and bulk of the spent Ni-BCT membrane.

Table S2 shows the EDXS data of the spent Ni-BCT membrane. In the bulk part, the Ba/Ce ratio is 1.07, which is close to the theoretical value of 1.05. But on the feed side surface, Ce content is higher than Ba content. On the sweep side, there is little Ba can be detected unexpectedly. Combined with the XRD result of the spent Ni-BCT shown in Figure S10, it is obvious that the impurity peak of $CeO_2$ appears, which is in accordance with the result of Meng's work.[6] In order to check the Ba-lacked layer on the sweep surface, the SEM image and EDXS elemental distributions on the cross section near the sweep side of the spent Ni-BCT membrane are shown in Figure S11. It can be found that a layer with a thickness of around 13 μm connected to the sweep surface, which is really Ba-lacked compared with that in the membrane bulk. It can be resulted from the elements (such as Ce and Tb) migration from the bulk in the reducing atmosphere.
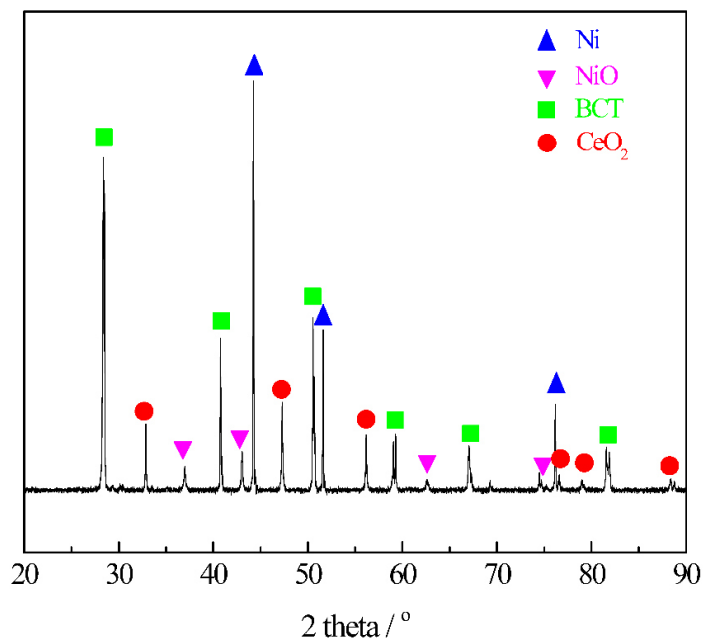
Figure S10. X-ray diffraction pattern of the spent Ni-BCT membrane.
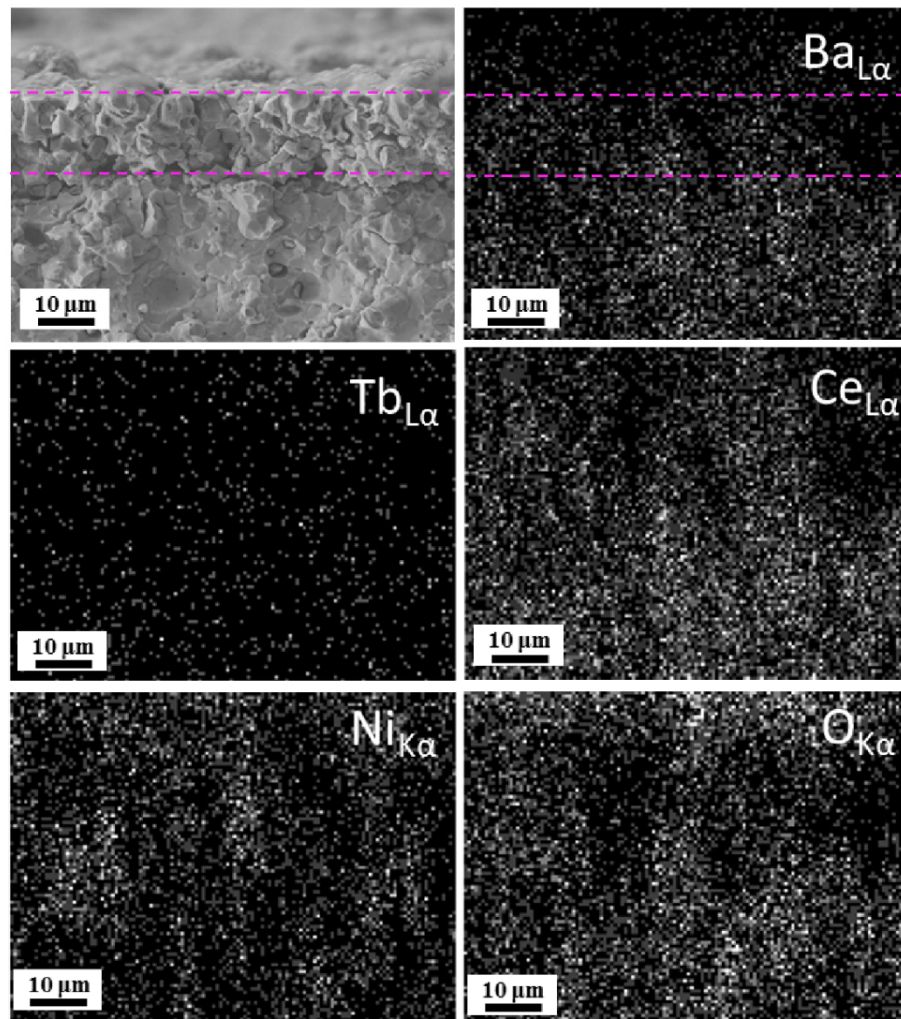
Figure S11. SEM and EDXS elemental distributions on the cross section near the sweep side
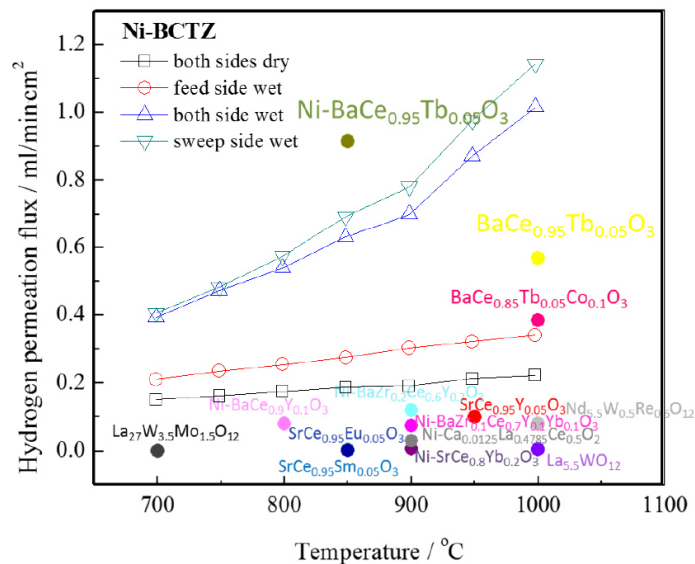
of the spent Ni-BCT cermet membrane.

Figure S12. The hydrogen permeation fluxes through various proton conductive membranes at different temperatures.[3-4]

One important thing should be emphasized that among numerous proton conductive oxides for hydrogen separation, there are only a few materials which exhibit both good stability and nice permeation flux. As shown in Figure S12, for different kind of materials, including the perovskite, tungstate, and cermet dual phase materials, most of the proton conductive membrane exhibit the hydrogen permeation fluxes below 0.1 $ml/min·cm^2$ even at 1000 °C. Compared with these materials, the hydrogen permeation fluxes through the Ni-BCTZ membrane in our work are far above this level, which indicate its attractive hydrogen permeability. On the other hand, from the point of stability, although the fluxes through some

[3] S. Zhan, X. Zhu, B. Ji,W. Wang, X. Zhang, J. Wang, W. Yang, L. Lin. Preparation and hydrogen permeation of SrCe$_{0.95}$Y$_{0.05}$O$_3$ asymmetrical membranes. Journal of Membrane Science 340 (2009) 241–248.
[4] S. Fang, L. Bi, L. Yan, W. Sun, C. Chen, W. Liu. CO$_2$-Resistant Hydrogen Permeation Membranes Based on Doped Ceria and Nickel. J. Phys. Chem. C 2010, 114, 10986–10991.

Tb-containing membrane, such as BaCe$_{0.95}$Tb$_{0.05}$O$_3$, BaCe$_{0.85}$Tb$_{0.05}$Co$_{0.1}$O$_3$, Ni-BaCe$_{0.85}$Tb$_{0.05}$O$_3$, are higher than that through Ni-BCTZ, but their fluxes cannot keep steady for more than several hours.[5,6,10] To the contrary, Ni-BCTZ membrane can be operated steadily for over 100 h in both dry and wet reducing conditions. Therefore, in consideration of both hydrogen permeability and stability, Ni-BCTZ is really a promising material candidate for hydrogen separation.

## 3.3 Hydrogen permeability and stability of BaCe$_{0.85}$Tb$_{0.05}$Zr$_{0.1}$O$_{3-\delta}$ asymmetric membranes

Yanying Wei, Jian Xue, Haihui Wang and Jürgen Caro

Contents lists available at ScienceDirect

# Journal of Membrane Science

journal homepage: www.elsevier.com/locate/memsci

# Hydrogen permeability and stability of BaCe$_{0.85}$Tb$_{0.05}$Zr$_{0.1}$O$_{3-\delta}$ asymmetric membranes

Yanying Wei [a,b,*], Jian Xue [b], Haihui Wang [a,c,**], Jürgen Caro [b]

[a] *School of Chemistry and Chemical Engineering, South China University of Technology, 381 Wushan Road, 510640 Guangzhou, China*
[b] *Institute of Physical Chemistry and Electrochemistry, Leibniz University of Hannover, Callinstrasse 22, 30167 Hannover, Germany*
[c] *School of Chemical Engineering, The University of Adelaide, Adelaide, SA 5005, Australia*

## A R T I C L E   I N F O

## A B S T R A C T

A mixed proton and electron conductor BaCe$_{0.85}$Tb$_{0.05}$Zr$_{0.1}$O$_{3-\delta}$ (BCTZ) has been developed by the partial substitution of Ce with Zr in BaCe$_{0.95}$Tb$_{0.05}$O$_{3-\delta}$ (BCT) to improve the phase structure stability of BCT. The BCTZ membranes with asymmetric structure have been successfully prepared and evaluated for hydrogen separation. A stable hydrogen permeation flux has been found over 370 h operation. The improved stability recommends BCTZ for a potential application in the hydrogen separation.

© 2015 Elsevier B.V. All rights reserved.

## 1. Introduction

The worldwide challenge of the fast depletion of the traditional fossil fuels on the one hand, and the global climate change on the other hand, increasingly forces researchers to search for new technologies for producing clean and renewable energy [1]. As a sustainable and clean energy source, hydrogen is highly attractive due to its high energy capacity, high conversion efficiencies, environmental friendliness and recyclability [2], which will alleviate our dependence on the fossil energy resources [3]. Although hydrogen is still mainly derived from non-renewable natural gas or petroleum [4], in principle it can be generated from renewable resources such as water or biomass [5]. However, hydrogen separation and purification from the gas mixtures are still some key issues.

Hydrogen separation by thin metal films of e.g. Pd and its alloys is a well-known technology for achieving this purification due to their good hydrogen permeability and selectivity [6–9]. But the embrittlement, poor mechanical strength at high operation temperature and poisoning by CO or H$_2$S etc. [10], as well as the high

costs for the noble metal, have become limitations for Pd-based membrane application.

Membranes for hydrogen separation should achieve the following characteristics: i) good selectivity; ii) high flux; iii) low cost and iv) good stability [6]. In this sense, ceramics are the alternative to metals. Since the ceramics based on strontium cerates are reported to exhibit relatively high protonic conductivities [11], high-temperature mixed proton and electron conductors (MPECs) have attracted increasing interest in the past few decades [12–14]. Proton conductive ceramic membranes can be used as hydrogen sensors, hydrogen pumps, hydrogen permeable membranes for gas separation [15–20], and in catalytic membrane reactors [21], solid oxide fuel cells (SOFCs) [22–24]. Among various high-temperature MPECs, the rare earth doped perovskite oxides, such as BaCeO$_3$, SrCeO$_3$, BaZrO$_3$ and SrZrO$_3$, are the state-of-the-art materials. However, the doped BaCeO$_3$ and SrCeO$_3$ have high proton conductivity but poor structure stability; while the doped BaZrO$_3$ and SrZrO$_3$ exhibit good structure stability but low proton conductivity and poor sintering behavior. Fortunately, these two kinds of oxides can easily form solid solution with any composition ratio, and therefore the doped BaCeO$_3$–BaZrO$_3$ solid solutions are widely investigated as good candidates for high temperature MPECs due to their sufficient proton conductivity and good stability [25–27].

As a novel MPEC material, Tb-doped BaCeO$_3$ of the composition BaCe$_{0.95}$Tb$_{0.05}$O$_{3-\delta}$ (BCT) was developed and applied in the SOFC as a proton conducting electrolyte firstly, while its stability needs to be improved [28]. The hydrogen permeation fluxes through the

* Corresponding author at: School of Chemistry and Chemical Engineering, South China University of Technology, 381 Wushan Road, 510640 Guangzhou, China. Tel.: +49 511 7622942.
** Corresponding author at: School of Chemical Engineering, The University of Adelaide, Adelaide, SA 5005, Australia. Tel./fax: +86 20 87110131.
*E-mail addresses:* yanying.wei@pci.uni-hannover.de (Y. Wei), hhwang@scut.edu.cn (H. Wang).

membranes based on BCT were outstanding compared with many other perovskite-type MPEC materials [29,30], but the long-term stability seems to be critical. In order to enhance the phase structure stability of BCT, partial substitution of Ce with Zr in BCT is expected to be positive due to the constant valency state of $Zr^{4+}$, the high stability of $BaZrO_3$ and the good compatibility between $BaCeO_3$ and $BaZrO_3$.

Therefore, in this study, an MPEC material of the composition $BaCe_{0.85}Tb_{0.05}Zr_{0.1}O_{3-\delta}$ (BCTZ) is synthesized through a glycine–nitrate combustion process. Considering that the increase of the Zr content in the solid solution is detrimental to the sintering activity and electrical conductivity. [27,31], 10% Zr-doping is chosen with the aim to make a compromise between the stability and conductivity. Furthermore, the asymmetric BCTZ membranes have been prepared with different thicknesses of the dense layer. The phase structure stability of BCTZ under reducing atmosphere, the hydrogen permeation flux through the asymmetric BCTZ membrane as well as its long term operation stability have been investigated experimentally.

## 2. Experimental

### 2.1. Preparation of BCTZ powder and stability tests

The BCTZ perovskite powder was prepared through glycine–nitrate combustion process. $Ba(NO_3)_2$, $Ce(NO_3)_3$, $Tb(NO_3)_3$, $ZrO(NO_3)_2$ and glycine were used as the raw materials to form an aqueous solution in their appropriate stoichiometric ratios. The molar ratio of glycine:total metal ions was 2:1 [32]. After evaporation of excess water at 200 °C under stirring, the aqueous solution became a viscous liquid and further heating up to 400 °C caused the auto combustion process, which produced the BCTZ precursor ash. The BCTZ powder with perovskite structure was obtained after calcination at 1000 °C for 5 h. The as-prepared BCTZ powder was also treated in Ar and 50% $H_2$–50% Ar at 800 °C for 50 h to examine its phase structure stability.

### 2.2. Preparation of BCTZ asymmetric membrane

Commercial starch was chosen as the pore forming additive for the asymmetric membrane preparation. For the porous substrate, the as-calcined BCTZ powder was mixed with 10% wt starch and pre-pressed at 20 bar for 5 min as a substrate. For the dense layer, a certain amount of BCTZ powder was spread on the substrate followed by uniaxial co-pressing at 100 bar for 15 min. Finally, the dense BCTZ membrane with an asymmetric structure was obtained after co-sintering at 1500 °C for 10 h.

### 2.3. Characterization

X-ray diffraction (XRD, D8 Advance, Bruker-AXS, with Cu-Ka radiation) was used to determine the phase structures of the BCTZ powder and the membrane. Crystal structure of BCTZ powder was also characterized by in situ high-temperature XRD under Ar using D8 Advance. The measurements were conducted in a high-temperature cell HTK 1200N (Anton-Paar) between room temperature and 1000 °C. The heating and cooling rate was 12 °C/min with equilibration time of 30 min for each measurement. Data sets were recorded in a step-scan mode in the $2\theta$ range of 20–90° with intervals of 0.02°.

The morphology of the BCTZ powder precursor after the glycine–nitrate combustion process and calcination as well as the sintered BCTZ membrane with the asymmetric structure were characterized by scanning electron microscopy (SEM) at 2 keV using a Jeol-JSM-6700F.

### 2.4. Hydrogen permeation

The hydrogen permeation has been measured on the disk-shaped BCTZ asymmetric membranes with different thicknesses of the dense layer. The ceramic sealant was used to seal the membrane with an alumina tube to form the permeation compartment, as shown in Fig. 1. 30 ml/min of 50 vol% $H_2$ diluted with He was used as feed gas and 60 ml/min of Ar was used as sweep gas. The influence of the mixed gas feed containing $H_2$, $CO_2$, CO and $H_2O$ on the hydrogen permeation performance and the long-term stability has been also investigated. The composition of the permeated effluent gas was measured using an online coupled gas chromatograph (GC, Agilent 6890, Ar as a carrier gas) with a thermal conductivity detector (TCD). The leakage of helium in the sweep side due to the imperfect sealing at high temperatures was less than 0.1% during all the experiments.
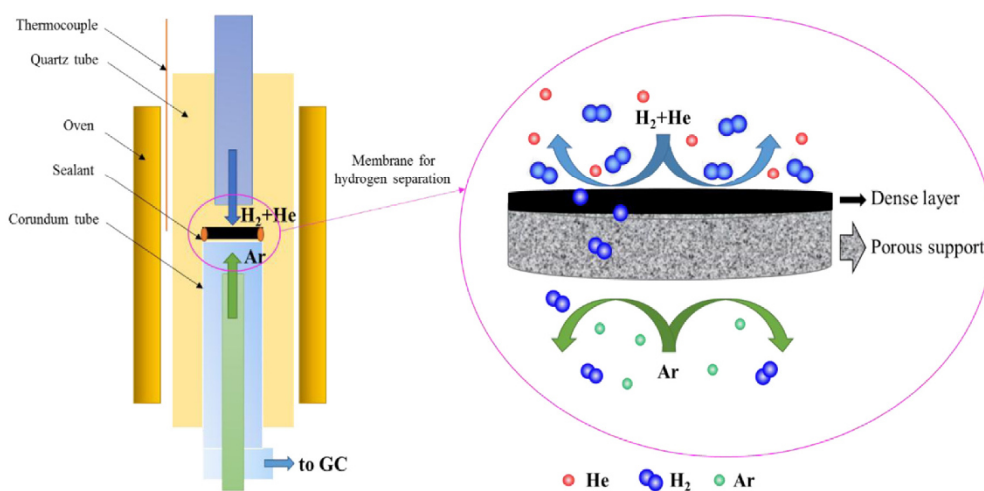


**Fig. 1.** Scheme of the high temperature hydrogen separation cell with planar BCTZ asymmetric membrane.
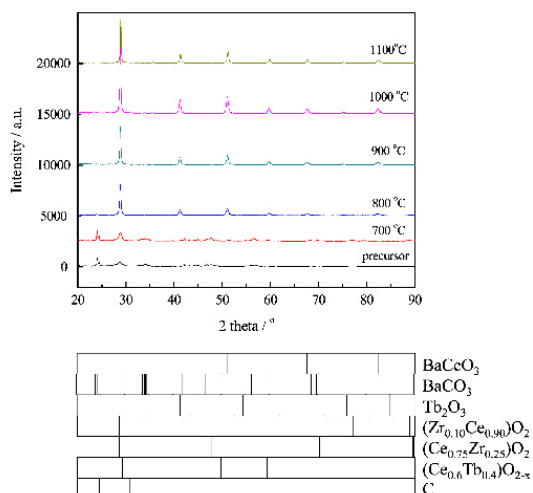
**Fig. 2.** Phase structures of BCTZ powder after calcination in air at different temperatures for 5 h.

## 3. Results and discussion

### 3.1. BCTZ powder

The crystalline phases of the BCTZ powder as a function of calcination temperature are shown in Fig. 2. After the glycine–nitrate combustion process, the powder precursor is a mixture of the metal oxides, carbonates, little carbonaceous residuals and some unknown phases, which is similar like other materials' precursor [28]. A single perovskite phase cannot be obtained until the calcination temperature is higher than 900 °C. With the increase of the calcination temperature, the decreasing peak width also demonstrates that the crystal size of the BCTZ powder increases due to the higher calcination temperature. In order to ensure that the BCTZ powder is well crystallized, the BCTZ powder was calcined at 1000 °C for the following experiments.

Fig. 3 shows the SEM micrographs of the BCTZ powder precursor after glycine–nitrate combustion and the development of the BCTZ powder with perovskite structure by high temperature calcination. It can be seen from Fig. 3a and b that the powder precursor after combustion exhibits a web-like structure with a high porosity. The precursor also looks like a loose sponge with a huge amount of pores with sizes ranging from 1 μm to the nano-scale, which result from the combustion process. After high temperature calcination, the porous structure disappears and the agglomeration of the BCTZ powder particles can be found in Fig. 3c and d. The BCTZ particle size is about 0.1–0.2 μm in diameter and such a fine powder is beneficial for the preparation of the asymmetric membrane with a thin dense layer. Only the oxide powder with small particle size is suitable for the asymmetric membrane preparation.

Fig. 4 shows the XRD of the BCTZ powder before and after treatment in Ar and 50 vol% H$_2$–50 vol% Ar. It can be seen that the as-prepared BCTZ oxide exhibits pure perovskite structure. After heat treatment in Ar and in 50 vol% H$_2$–50 vol% Ar for 50 h at 800 °C, respectively, the powder still maintains their original phase structure, which indicates the good phase structure stability of BCTZ in inert and reducing atmospheres. Furthermore, the in situ high-temperature XRD measurement was performed on BCTZ under N$_2$ atmosphere from room temperature to 1000 °C. As shown in Fig. 5, no other phases can be observed during the heating or cooling process, which demonstrates that BCTZ

possesses good phase structure stability in N$_2$ at high temperatures, as well as in the heating and cooling cycle.

### 3.2. BCTZ asymmetric membrane

Fig. 6a shows the microstructure of the commercial starch powder. The microstructure of the asymmetric BCTZ membrane with a 50 μm dense layer on the membrane top can be seen easily in Fig. 6b. The dense layer and the porous layer are well attached to each other and no interface delamination or crack formation can be found. From the SEM micrographs (Fig. 6c and d) of the membrane surface and the cross section of the dense part, only some small closed pores exist in the membrane dense layer and sufficient gas-tightness can be expected. The porous substrate results from the starch decomposition is shown in Fig. 6e and f, which enables gas transport through the support. It can be also found that most of the pores in the substrate seem like bubbles and the spherical pore shape results from combustion of the spherical commercial starch (see Fig. 6a). In the spherical pore as shown in Fig. 6f, it can be seen the agglomeration of the BCTZ particles with size range of 2–4 μm, which exhibit a different structure compared with the other part, while they show the same composition of BCTZ. This is because when the starch and BCTZ oxide were mixed during the preparation, some of the BCTZ powders were packed inside of the starch ball. The growth of the polycrystalline BCTZ aggregate to a big BCTZ crystalline was limited due to the starch shell until the latter was burnt off. When the temperature increased even higher in the sintering process, the starch was decomposed and disappeared, while the two different structures of the same chemical composition were formed as shown in Fig. 6f.

### 3.3. Hydrogen permeation and stability of the BCTZ asymmetric membrane

Fig. 7 shows the hydrogen permeation fluxes as a function of temperature for different membrane thicknesses (Fig. 7a and b). The black cubes represent the data for the asymmetric BCTZ membrane with a 50 μm thick dense layer, while the red circles stand for the data of a membrane with a 20 μm thick dense layer on the same porous substrate. It can be seen that the hydrogen permeation fluxes increases with increasing temperatures. For instance, the hydrogen permeation flux through the BCTZ asymmetric membrane with the 50 μm dense layer increased from 0.05 to 0.17 ml/min cm$^2$ as the temperature was increased from 700 to 1000 °C at the constant Ar sweep flow rate of 60 ml/min. This finding can be explained by two reasons. On the one hand, the proton bulk diffusion and surface exchange kinetics can be enhanced due to the temperature increase. On the other hand, BCTZ exhibits higher conductivity at higher temperatures, which is similar like BCT [29]. Compared with the 50 μm thick membrane, the hydrogen permeation flux through the 20 μm-dense layer-membrane has increased about twice because of the lower bulk diffusion resistance. Due to the limits of the asymmetric membrane preparation technology of co-pressing followed by co-sintering, it is difficult to prepare an asymmetric membrane with an even thinner dense layer ( < 20 μm). However, the results in Fig. 7 indicate that it is beneficial for hydrogen transport to decrease the thickness of the dense layer of the asymmetric membrane.

For practical applications, the hydrogen separation membranes based on MPECs should not only exhibit high hydrogen permeation fluxes but also good stability under the operation conditions. Fig. 8 shows the long-term stability of the BCTZ asymmetric membrane for hydrogen separation at 800 °C. It can be seen that the hydrogen permeation flux through the BCTZ asymmetric
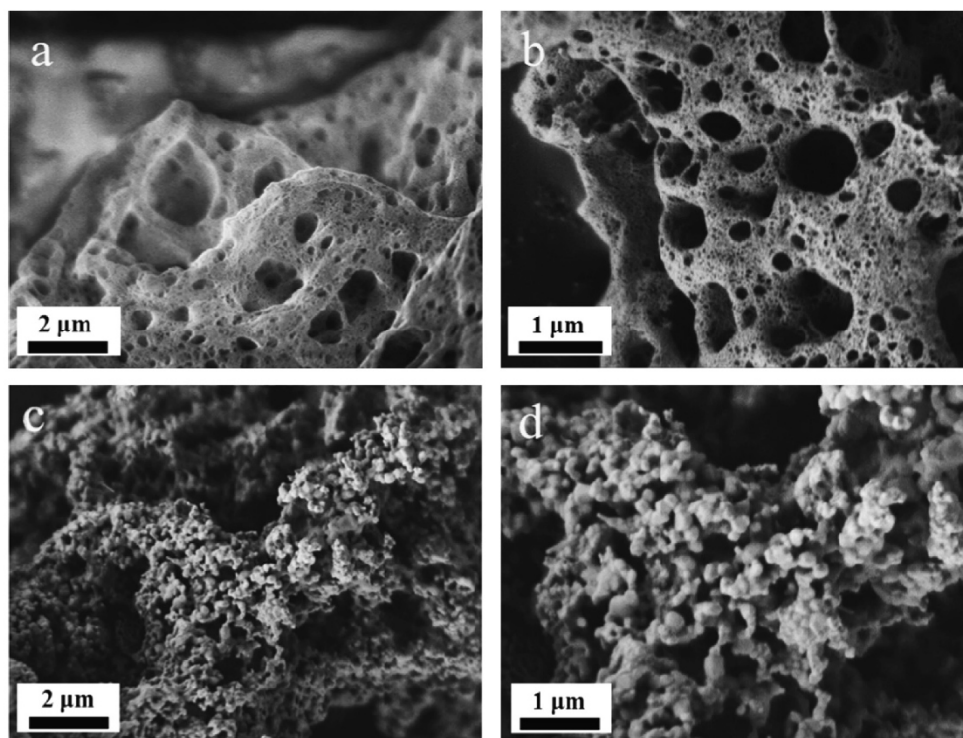
**Fig. 3.** SEM micrographs of (a, b) the precursor after the glycine–nitrate combustion; (c, d) the perovskite BCTZ powder calcined at 1000 °C for 5 h.
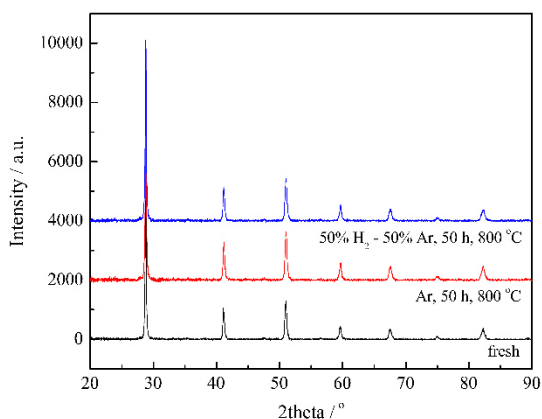


**Fig. 4.** X-ray diffraction patterns of the BCTZ powder before and after treatment in Ar and $H_2$/Ar atmospheres.



**Fig. 5.** In situ high-temperature XRD patterns of the BCTZ powder under $N_2$ atmosphere during the heating and cooling process.

membrane with a 50 µm-thick dense layer keeps stable at around 0.07 ml/min cm$^2$ for over 370 h and no decline with time can be found at 800 °C using 50 vol% $H_2$ diluted with He as feed gas. Compared with the hydrogen flux through the Ni–BCT membrane, which declined by about 50% after 75 h operation at 800 °C due to the phase segregation of BCT [29]. Actually, the long-term stability of BCTZ membrane has been positively tested for more than 370 h. However, testing a membrane for 370 h under lab-scale conditions is still not a final proof for a long-year stability under harsh industrial conditions. Nevertheless, we have to note that we had to stop our test after 370 h and the membrane could have lived much longer.
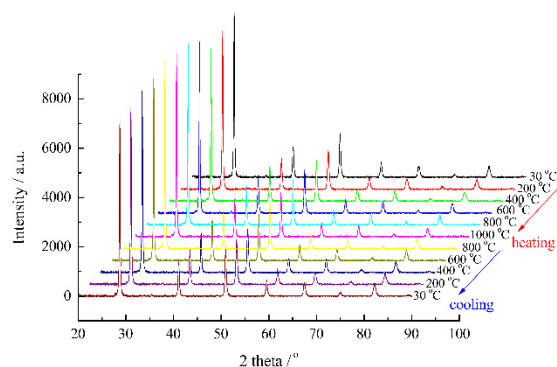
It should be noted that it is not trivial to compare our results with those of others since only the Ni–BCT [29] and our BCTZ membranes synthesized under the same or similar conditions can be compared. Both the BCT [29] and our BCTZ powder were synthesized via the nitrate-complex agent method followed by gel-combustion and high-temperature calcination. Both our BCTZ and the Ni–BCT [29] disk membranes had a similar asymmetric structure of a dense layer supported by a porous substrate. The same pore former starch with the same ratio (10% wt) was used for the substrates preparation, and the asymmetric green membranes were co-pressed with the pre-pressed substrate. All these similar synthesis conditions make our BCTZ and Ni–BCT membranes from the literature comparable.
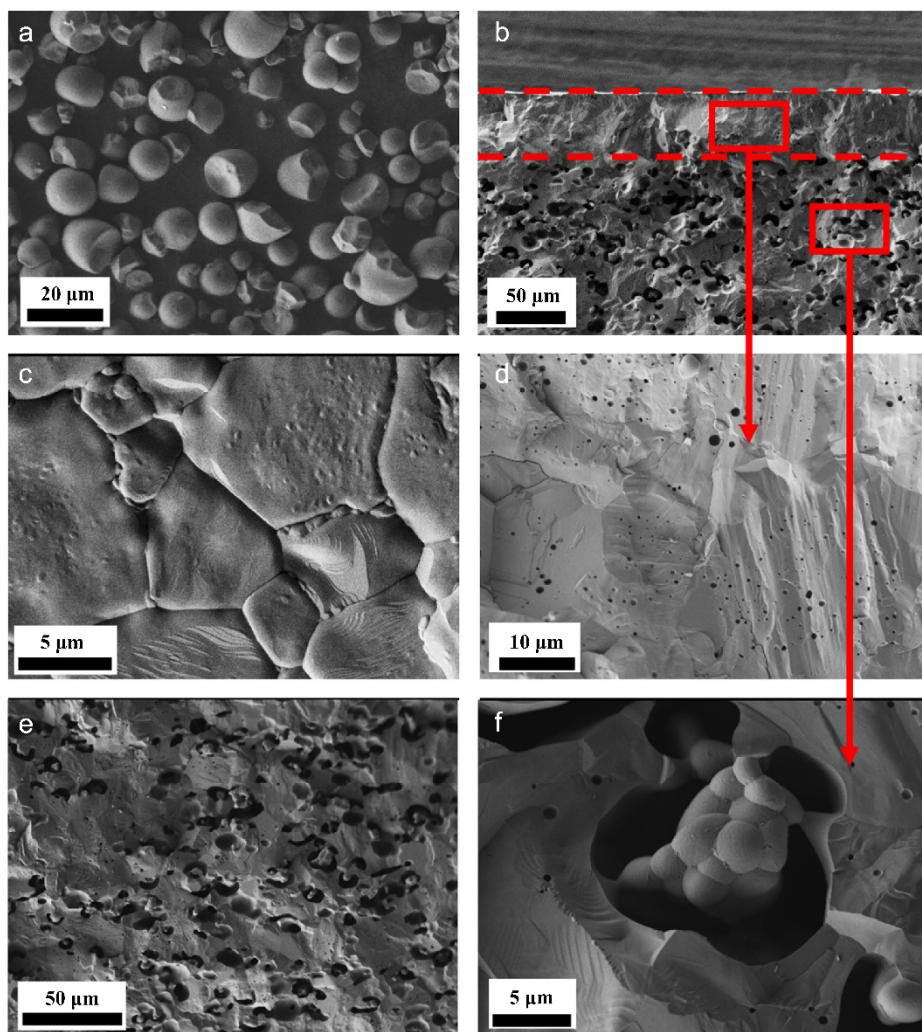
**Fig. 6.** SEM micrographs of the (a) commercial starch powder, (b) cross section of the asymmetric BCTZ disk membrane, (c) surface and (d) bulk of the dense part of the membrane and (e, f) porous part of the membrane with different magnifications.

Meng et al. reported the instability of the Ni–BCT membrane in the long-term hydrogen separation process due to the phase decomposition of the BCT perovskite [29]. Actually, BCT was firstly developed by the same research group and applied in the SOFC as a proton conducting electrolyte, the authors has emphasized that the stability of BCT needs to be improved [28]. Although there are no direct data of BCT membrane for long-term hydrogen permeation, in comparison with Ni–BCT membrane (actually compared with BCT perovskite) [29], BCTZ shows a much better stability after Zr doping. This stabilization can be explained as follows: (i) under the reducing atmosphere, Ce$^{4+}$ (ionic radius=80 pm) [33] is easily reduced to Ce$^{3+}$ (ionic radius=103 pm) [33], which will cause the unit cell volume change due to the different ionic radii [34]. Because of the constant valence state of Zr$^{4+}$, partial substitution of Ce with Zr in BCT enhances the unit cell stability to a certain degree in the reducing atmosphere; (ii) from the point of acid–base property, both of the Ce$^{4+}$ and Ce$^{3+}$ are weakly alkaline, while Zr$^{4+}$ is amphoteric. This is another reason for the better

chemical stability of BCTZ, especially in a CO$_2$ containing atmosphere shown in the following part. Kniep [35] and Ryu [36] et al. also found that introduction of Zr into doped barium cerate greatly enhanced the chemical stability. In summary, after Zr doping, BCTZ exhibits much better stability compared with BCT perovskite.

Compared with the good phase stability of BCTZ in our study, Ni–BCT cermet membrane was not sufficiently stable in hydrogen permeation due to the phase decomposition of the BCT perovskite [29]. Although the hydrogen permeation flux through the Ni–BCT membrane was 0.26 ml/min cm$^2$ at the beginning, which is higher than that through the BCTZ membrane at 800 °C, after 75 h operation, it decreased to 0.126 ml/min cm$^2$, which is similar to that through the BCTZ membrane with 20 μm dense layer.

We studied also the chemical stability of the BCTZ membrane in a reducing atmosphere containing H$_2$, CO$_2$, CH$_4$, CO and H$_2$O. Fig. 9 exhibits the effect of the mixed feed gas on the hydrogen permeation flux through the BCTZ membrane as a function of time. As shown in Fig. 9a, when 10% CO$_2$ is added to the feed gas,
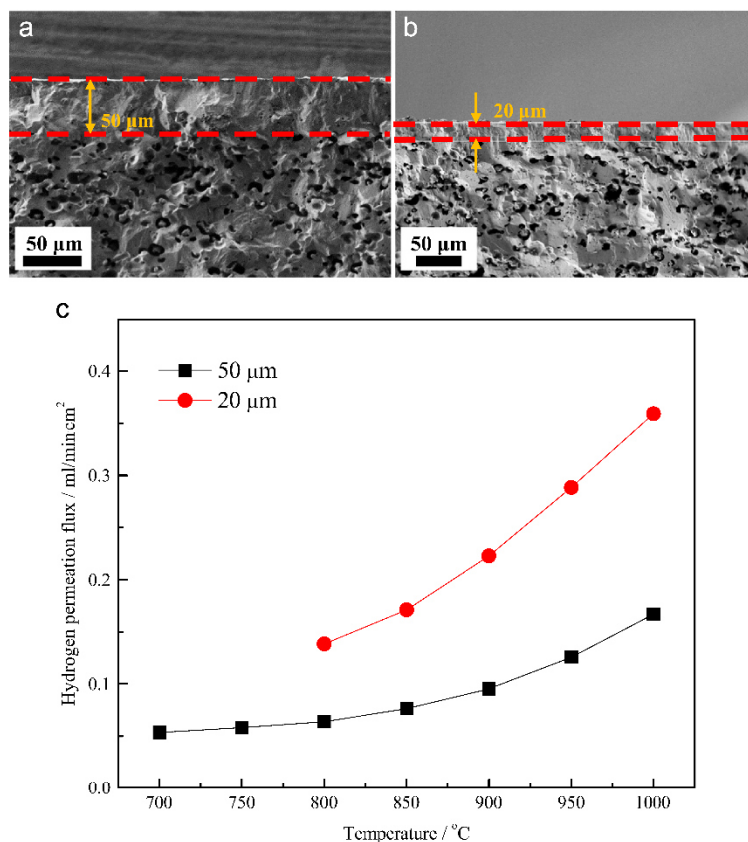
**Fig. 7.** SEM images of the BCTZ asymmetric membranes of different thicknesses of the dense layer, (a) 50 μm thick; (b) 20 μm thick; (c) the hydrogen permeation fluxes as a function of temperature for (a) and (b). For experimental details, see Section 2.4. (For interpretation of the references to color in this figure, the reader is referred to the web version of this article.)
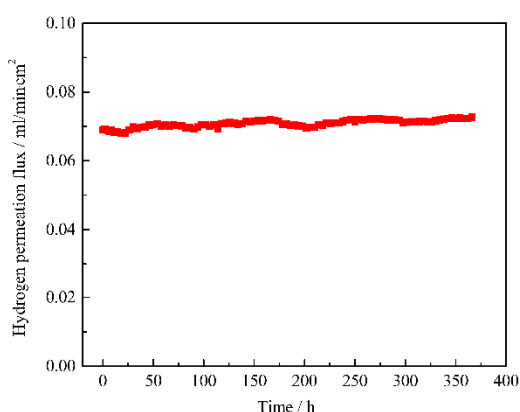


**Fig. 8.** Long-term stability test of the BCTZ asymmetric disk membrane for hydrogen permeation at 800 °C.

the hydrogen permeation flux drops from 0.16 to 0.12 ml/min cm² immediately, but then it keeps constant on this level. Even when higher amounts of $CO_2$ are added to the feed gas, the hydrogen permeation flux drops only a little bit but then it is stable with time. The decrease of the hydrogen permeation flux is due to the $CO_2$ adsorption on the membrane surface and it can be recovered

immediately when $CO_2$ disappears from the feed gas. Fig. 9b shows the hydrogen flux through the BCTZ membrane when $CH_4$ in different concentrations is added to the feed gas. It can be found that the hydrogen permeation flux remains almost unchanged for a 10% $CH_4$-containing feed gas. But it decreases with time when the $CH_4$ concentration in the feed increases to 20 %. This experimental finding is due to the deposition of a carbon layer on the membrane surface by the methane thermal splitting. However, the hydrogen permeation flux can be recovered when $CH_4$ disappears from the feed gas. As shown in Fig. 9c, if CO exists in the feed gas, there is almost no effect on the hydrogen permeation flux. Compared with the reducibility of $H_2$, CO is much milder. So, the effect of CO on the membrane stability and its hydrogen permeation flux can be ignored. Fig. 9d shows the effect of steam in the feed on the hydrogen flux through the BCTZ membrane. When the feed gas is humidified, the hydrogen permeation flux keeps stable with time.

Fig. 10 shows the stability of the hydrogen permeation through the BCTZ asymmetric membrane as a function of time in mixed gas feeds containing $H_2$, $CO_2$, $CH_4$, CO and $H_2O$. It can be found that the hydrogen permeation flux has a sharp decrease once the 50 vol% $H_2$/50 vol% He mixed gas streams is replaced by a feed gas of 50 vol% $H_2$/50 vol% He, $CO_2$, $CH_4$, CO, $H_2O$. This experimental finding is attributed to the gas adsorption on the membrane surface. After a period of decrease, the hydrogen permeation flux starts to increase and finally maintains at 0.14 ml/min cm² steadily
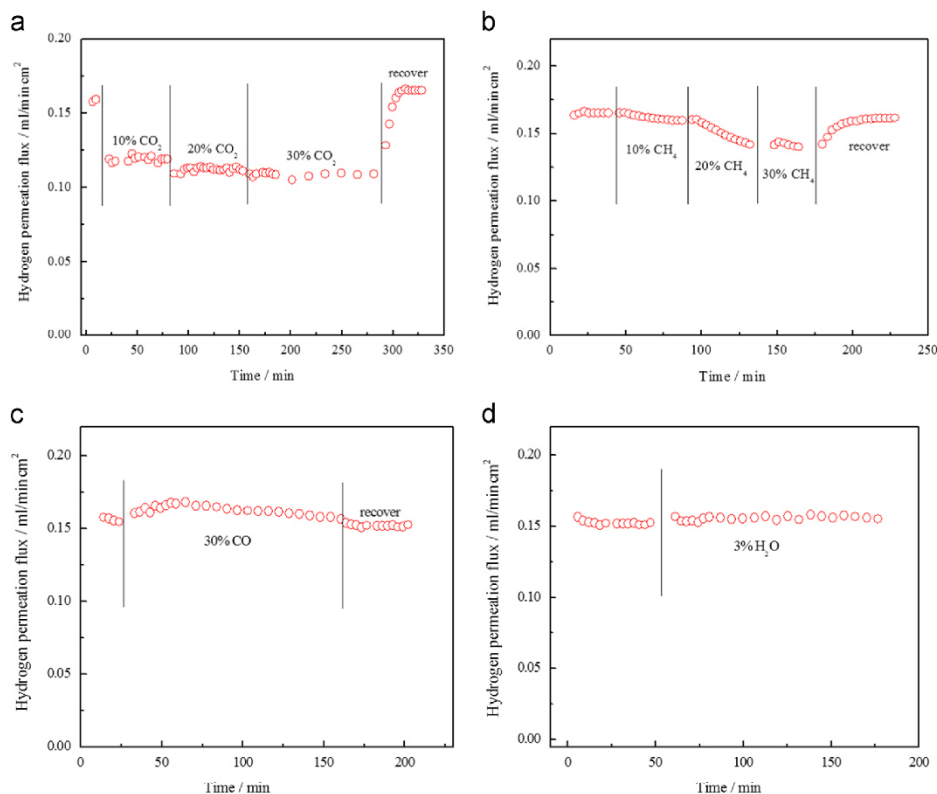
**Fig. 9.** The influence of (a) CO$_2$, (b) CH$_4$, (c) CO, and (d) H$_2$O in the feed gas on the hydrogen permeation flux through the BCTZ membrane as a function of time.
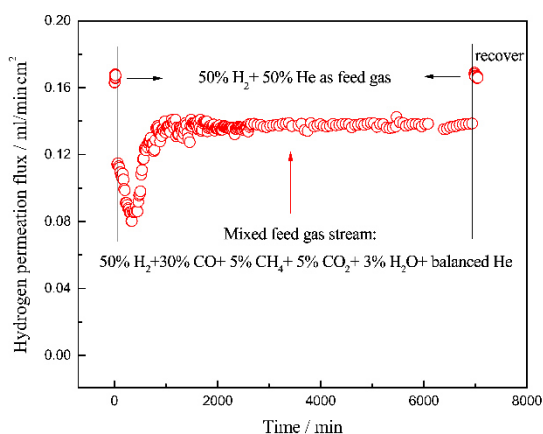


**Fig. 10.** The stability of the BCTZ asymmetric membrane as a function of time with mixed gas feeds for hydrogen separation.

for more than 100 h, which is due to the steady state of several reactions that take place such as methane splitting, reduction of carbon dioxide by H$_2$ etc. When the feed gas is switched back to the 50 vol% H$_2$/50 vol% He feed, the hydrogen permeation flux recovers to about 0.17 ml/min cm$^2$. All these results indicate that the BCTZ membrane can be operated for hydrogen separation in the mixed gas streams steadily.

It has to be pointed out that we did not add trace amount of sulfur impurity to the feed gas to study the stability of the membrane against sulfur species. It is reported that Ba$_{0.5}$Sr$_{0.5}$Co$_{0.8}$Fe$_{0.2}$O$_{3-\delta}$ and Sr$_{0.5}$Ca$_{0.5}$Mn$_{0.8}$Fe$_{0.2}$O$_{3-\delta}$ membranes displayed an instability in oxygen permeation. When the sweep gas contains 360 ppm SO$_2$, sulfur-containing layers were formed on the membrane surface [37]. In our previous work, (Pr$_{0.9}$La$_{0.1}$)$_2$(Ni$_{0.74}$Cu$_{0.21}$Ga$_{0.05}$)O$_{4+\delta}$ was also found to be unstable in SO$_2$-containing atmosphere [38]. It is easy to note that not only the alkaline-earth metal elements (such as Ba, Sr), but also the lanthanides (such as Pr, La) are sensitive to sulfur poisoning due to sulfates formation even with trace amounts of sulfur components. Therefore, from the previous results, we can deduce that BCTZ is also unstable in a sulfur-containing atmosphere, because Ba (alkaline-earth metal element) and Ce, Tb (lanthanide) do not have enough resistance to sulfur poisoning. Development of the sulfur-tolerant membrane materials for both oxygen separation and hydrogen separation is important for their potential applications.

After the long-term hydrogen permeation, the spent BCTZ asymmetric membrane was analyzed by XRD. As shown in Fig. 11, both surfaces of the spent BCTZ asymmetric membrane maintain their perovskite structure after over 370 h hydrogen permeation. No other foreign phases can be found as impurity (except some residual ceramic sealant), which indicates the good phase structure stability of BCTZ even under reducing atmospheres for such a long time.

## 4. Conclusions

The mixed proton and electron conductor material BaCe$_{0.85}$Tb$_{0.05}$Zr$_{0.1}$O$_{3-\delta}$ (BCTZ) was synthesized through a glycine–nitrate
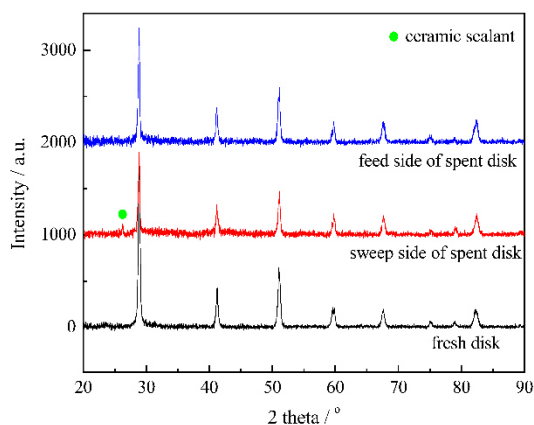
**Fig. 11.** X-ray diffraction patterns of the fresh and the spent BCTZ membrane after 370 h hydrogen permeation (cf. Fig. 8).

combustion process. Asymmetric BCTZ membranes were prepared by using commercial starch as pore forming additive for the porous support. The BCTZ powder sample maintains its original perovskite structure after heat treatment in Ar and 50 vol% $H_2$–50 vol% Ar for 50 h at 800 °C. The in situ high-temperature XRD result shows that BCTZ can even keep the perovskite structure at high temperature up to 1000 °C in $N_2$, as well as in the heating and cooling cycle, which indicates the good phase structure stability of BCTZ in inert and reducing atmospheres. The BCTZ asymmetric membrane with a 50 μm-thick dense top layer can be steadily operated in hydrogen permeation with a stable hydrogen flux of 0.07 ml/min cm² for over 370 h at 800 °C. In the mixed gas feeds including $H_2$, $CO_2$, $CH_4$, CO and $H_2O$, the BCTZ membrane also exhibits good chemical stability for hydrogen separation. The XRD analysis of the spent membrane also demonstrates the good phase structure stability of BCTZ. After doping Zr into $BaCe_{0.95}Tb_{0.05}O_{3-\delta}$, the phase structure stability of the BCTZ membrane has been enhanced remarkably and all results recommend BCTZ as a proper candidate of a MPEC material for various potential applications.

## Acknowledgments

## References

[1] M.I. Hoffert, K. Caldeira, G. Benford, D.R. Criswell, C. Green, H. Herzog, A.K. Jain, H.S. Kheshgi, K.S. Lackner, J.S. Lewis, H.D. Lightfoot, W. Manheimer, J.C. Mankins, M.E. Mauel, L.J. Perkins, M.E. Schlesinger, T. Volk, T.M.L. Wigley, Advanced technology paths to global climate stability: energy for a greenhouse planet, Science 298 (2002) 981–987.

[2] H.G. Park, J.K. Holt, Recent advances in nanoelectrode architecture for photochemical hydrogen production, Energy Environ. Sci. 3 (2010) 1028–1036.

[3] X. Chen, S. Shen, L. Guo, S.S. Mao, Semiconductor-based photocatalytic hydrogen generation, Chem. Rev. 110 (2010) 6503–6570.

[4] J.R. Rostrup-Nielsen, Conversion of hydrocarbons and alcohols for fuel cells, Phys. Chem. Chem. Phys. 3 (2001) 283–288.

[5] R.D. Cortright, R.R. Davda, J.A. Dumesic, Hydrogen from catalytic reforming of biomass-derived hydrocarbons in liquid water, Nature 418 (2002) 964–967.

[6] F. Gallucci, E. Fernandez, P. Corengia, M.S. Annaland, Recent advances on membranes and membrane reactors for hydrogen production, Chem. Eng. Sci. 92 (2013) 40–66.

[7] P.P. Mardilovich, Y. She, Y.H. Ma, M.H. Rei, Defect-free palladium membranes on porous stainless-steel support, AIChE J. 44 (1998) 310–322.

[8] C.Y. Park, T.H. Lee, S.E. Dorris, U. Balachandran, Palladium based film-type cermet membranes for hydrogen separation, J. Mater. Chem. 22 (2012) 4904–4909.

[9] S. Uemiya, State-of-the-art of supported metal membranes for gas separation, Sep. Purif. Methods 28 (1) (1999) 51–85.

[10] P. Kamakoti, B.D. Morreale, M.V. Ciocco, B.H. Howard, R.P. Killmeyer, A. V. Cugini, D.S. Sholl, Prediction of hydrogen flux through sulfur-tolerant binary alloy membranes, Science 307 (2005) 569–573.

[11] H. Iwahara, T. Esaka, H. Uchida, N. Maeda, Proton conduction in sintered oxides and its application to steam electrolysis for hydrogen production, Solid State Ion. 3–4 (1981) 359–363.

[12] C.M. Gore, J.O. White, E.D. Wachsman, V. Thangadurai, Effect of composition and microstructure on electrical properties and $CO_2$ stability of donor-doped, proton conducting $BaCe_{1-(x+y)}Zr_xNb_yO_3$, J. Mater. Chem. A 2 (2014) 2363–2373.

[13] A. Magraso, C.H. Hervoches, I. Ahmed, S. Hull, J. Nordstrom, A.W.B. Skilbred, R. Haugsrud, In situ high temperature powder neutron diffraction study of undoped and Ca-doped $La_{28-x}W_{4+x}O_{54+3x/2}$ ($x$=0.85), J. Mater. Chem. A 1 (2013) 3774–3782.

[14] A. Magraso, R. Haugsrud, Effects of the La/W ratio and doping on the structure, defect structure, stability and functional properties of proton-conducting lanthanum tungstate $La_{28-x}W_{4-x}O_{54+\delta}$: A review, J. Mater. Chem. A 2 (2014) 12630–12641.

[15] M. Amsif, A. Magraso, D. Marrero-Lopez, J.C. Ruiz-Morales, J. Canales-Vazquez, P. Nunez, Mo-substituted lanthanum tungstate $La_{28-y}W_{4-y}O_{54+\delta}$: a competitive mixed electron–proton conductor for gas separation membrane applications, Chem. Mater. 24 (2012) 3868–3877.

[16] S. Escolastico, S. Somacescu, J.M. Serra, Solid state transport and hydrogen permeation in the system $Nd_{5.5}W_{1-x}Re_xO_{11.25-\delta}$, Chem. Mater. 26 (2014) 982–992.

[17] S. Escolastico, C. Solis, C. Kjølseth, J.M. Serra, Outstanding hydrogen permeation through $CO_2$-stable dual-phase ceramic membranes, Energy Environ. Sci. 7 (2014) 3736–3746.

[18] S. Escolastico, J. Seeger, S. Roitsch, M. Ivanova, W.A. Meulenberg, J.M. Serra, Enhanced $H_2$ separation through mixed proton–electron conducting membranes based on $La_{5.5}W_{0.8}Mo_{0.2}O_{11.25-\delta}$, ChemSusChem 6 (2013) 1523–1532.

[19] J. Seeger, M.E. Ivanova, W.A. Meulenberg, D. Sebold, D. Stover, T. Scherb, G. Schumacher, S. Escolastico, C. Solís, J.M. Serra, Synthesis and characterization of nonsubstituted and substituted proton-conducting $La_{6-x}WO_{12-y}$, Inorg. Chem. 52 (2013) 10375–10386.

[20] D. Holt, E. Forster, M.E. Ivanova, W.A. Meulenberg, M. Müller, S. Baumann, R. J. Vaßen, Ceramic materials for $H_2$ transport membranes applicable for gas separation under coal-gasification-related conditions, Eur. Ceram. Soc. 34 (2014) 2381–2389.

[21] G. Marnellos, M. Stoukiddes, Ammonia synthesis at atmospheric pressure, Science 282 (1998) 98–100.

[22] D. Pergolesi, E. Fabbri, A. D'Epifanio, E. Di Bartolomeo, A. Tebano, S. Sanna, S. Licoccia, G. Balestrino, E. Traversa, High proton conduction in grainboundary-free yttrium-doped barium zirconate films grown by pulsed laser deposition, Nat. Mater. 9 (2010) 846–852.

[23] L. Yang, S. Wang, K. Blinn, M. Liu, Z. Liu, Z. Cheng, M. Liu, Enhanced sulfur and coking tolerance of a mixed ion conductor for SOFCs: $BaZr_{0.1}Ce_{0.7}Y_{0.2-x}Yb_xO_{3-\delta}$, Science 326 (2009) 126–129.

[24] F. Bozza, W. Schafbauer, W.A. Meulenberg, N. Bonanos, Characterization of $La_{0.995}Ca_{0.005}NbO_4$/Ni anode functional layer by electrophoretic deposition in a $La_{0.995}Ca_{0.005}NbO_4$ electrolyte based PCFC, Int. J. Hydrog. Energy 37 (2012) 8027–8032.

[25] Z. Shi, W. Sun, W. Liu, Synthesis and characterization of $BaZr_{0.3}Ce_{0.5}Y_{0.2-x}Yb_xO_{3-\delta}$ proton conductor for solid oxide fuel cells, J. Power Sources 245 (2014) 953–957.

[26] S. Barison, M. Battagliarin, T. Cavallin, L. Doubova, M. Fabrizio, C. Mortalo, S. Boldrini, L. Malavasic, R. Gerbasi, High conductivity and chemical stability of $BaCe_{1-x-y}Zr_xY_yO_{3-\delta}$ proton conductors prepared by a sol–gel method, J. Mater. Chem. 18 (2008) 5120–5128.

[27] K. Katahira, Y. Kohchi, T. Shimura, H. Iwahara, Protonic conduction in Zrsubstituted $BaCeO_3$, Solid State Ion. 138 (2000) 91–98.

[28] X. Meng, N. Yang, J. Song, X. Tan, Z. Ma, K. Li, Synthesis and characterization of terbium doped barium cerates as a proton conducting SOFC electrolyte, Int. J. Hydrog. Energy 36 (2011) 13067–13072.

[29] X. Meng, J. Song, N. Yang, B. Meng, X. Tan, Z. Ma, K. Li, Ni–$BaCe_{0.95}Tb_{0.05}O_{3-\delta}$ cermet membranes for hydrogen permeation, J. Membr. Sci. 401–402 (2012) 300–305.

[30] X. Tan, J. Song, X. Meng, B. Meng, Preparation and characterization of $BaCe_{0.95}Tb_{0.05}O_{3-\delta}$ hollow fibre membranes for hydrogen permeation, J. Eur. Ceram. Soc. 32 (2012) 2351–2357.

[31] E. Fabbri, A. D'Epifanio, E. Di Bartolomeo, S. Licoccia, E. Traversa, Tailoring the chemical stability of $Ba(Ce_{0.8-x}Zr_x)Y_{0.2}O_{3-\delta}$ protonic conductors for Intermediate Temperature Solid Oxide Fuel Cells (IT-SOFCs), Solid State Ion. 179 (2008) 558–564.

[32] H. Luo, H. Jiang, T. Klande, F. Liang, Z. Cao, H. Wang, J. Caro, Rapid glycine–nitrate combustion synthesis of the CO$_2$-stable dual phase membrane 40Mn$_{1.5}$Co$_{1.5}$O$_{4\ \delta}$–60Ce$_{0.9}$Pr$_{0.1}$O$_{2\ \delta}$ for CO$_2$ capture via an oxy-fuel process, J. Membr. Sci.423–424 (2012) 450–458.

[33] R.D. Shannon, C.T. Prewitt, Effective ionic radii in oxides and fluorides, Acta Crystallogr. B25 (1969) 925–946.

[34] O. Ravkina, T. Klande, A. Feldhoff, Invetigation of Zr-doped BSCF perovskite membrane for oxygen separation in the intermediate temperature range, J. Soild State Chem. 201 (2013) 101–106.

[35] J. Kniep, Y.S. Lin, Effect of zirconium doping on hydrogen permeation through strontium cerate membranes, Ind. Eng. Chem. Res. 49 (2010) 2768–2774.

[36] K.H. Ryu, S.M. Haile, Chemical stability and proton conductivity of doped BaCeO$_3$–BaZrO$_3$ solid solutions, Solid State Ion. 125 (1999) 355–367.

[37] S. Engels, T. Markus, M. Modigell, L. Singheiser, Oxygen permeation and stability investigations on MIEC membrane materials under operating conditions for power plant processes, J. Membr. Sci. 370 (2011) 58–69.

[38] Y. Wei, O. Ravkina, T. Klande, H. Wang, A. Feldhoff, Effect of CO$_2$ and SO$_2$ on oxygen permeation and microstructure of (Pr$_{0.9}$La$_{0.1}$)$_2$(Ni$_{0.74}$Cu$_{0.21}$Ga$_{0.05}$)O$_{4 \delta}$ membranes, J. Membr. Sci. 429 (2013) 147–154.

## 3.4 Gas to liquids: Natural gas conversion to aromatic fuels and chemicals in a hydrogen-permeable ceramic hollow-fiber membrane reactor

Jian Xue, Yan Chen, Yanying Wei, Armin Feldhoff, Haihui Wang and Juergen Caro

# Gas to Liquids: Natural Gas Conversion to Aromatic Fuels and Chemicals in a Hydrogen-Permeable Ceramic Hollow Fiber Membrane Reactor

Jian Xue,[†] Yan Chen,[‡] Yanying Wei,[*,†,‡] Armin Feldhoff,[†] Haihui Wang,[*,‡,§] and Juergen Caro[*,†]

[†]Institute of Physical Chemistry and Electrochemistry, Leibniz University Hannover, Callinstrasse 3A, D-30167 Hannover, Germany
[‡]School of Chemistry & Chemical Engineering, South China University of Technology, No. 381 Wushan Road, Guangzhou 510640, China
[§]School of Chemical Engineering, The University of Adelaide, Adelaide, SA 5005, Australia

ⓢ Supporting Information

**ABSTRACT:** The performance of a dense ceramic hydrogen-permeable membrane reactor for the nonoxidative methane dehydroaromatization (MDA), according to the equilibrium reaction $6CH_4 \leftrightarrows C_6H_6 + 9H_2$ with a 6 wt % Mo/HZSM-5 bifunctional catalyst was investigated. A U-shaped ceramic hollow fiber membrane of the composition $La_{5.5}W_{0.6}Mo_{0.4}O_{11.25-\delta}$ ($LWM_{0.4}$) has been used for the *in situ* removal of $H_2$ to overcome thermodynamic constraints. The yield of aromatics (benzene, toluene, naphthalene) in the MDA could be increased in the beginning of the aromatization reaction by ~50%−70%, in comparison with the fixed-bed reactor, because 40%−60% of the $H_2$ abstracted have been extracted at 700 °C with a weight hourly space velocity (WHSV) of 840 $cm^3$ $g_{cat}^{-1}$ $h^{-1}$. These advantages of the membrane reactor operation decrease with time on stream, since the removal of $H_2$ boosts not only $CH_4$ conversion and yield of aromatics, but also catalyst deactivation by deposition of carbonaceous deposits. However, the catalyst system could be regenerated by burning the coke away with air.

**KEYWORDS:** *natural gas conversion, nonoxidative methane dehydroaromatization, hydrogen-permeable ceramic membrane, hollow fiber membrane, gas-to-liquids technologies, catalyst regeneration*
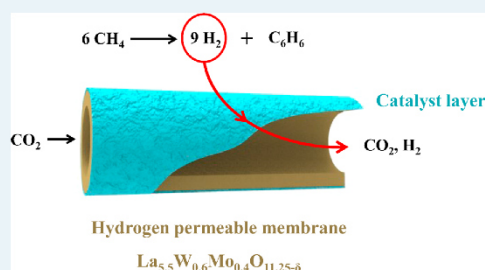
W ith the increasing demands for liquid fuels, gas-to-liquids (GTL) technologies are attracting considerable academ-
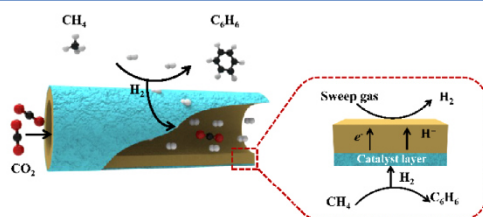


**Figure 1.** Scheme of the LWM0.4 ceramic hollow fiber membrane reactor for nonoxidative methane dehydroaromatization (MDA).

ic and industrial interest. Currently, the research and development on GTL is boosted by the decrease in the price of natural gas. On the other hand, also stranded gas which was flared so far, can be used and converted to saleable products. Among the GTL concepts, methane dehydroaromatization (MDA), according to the reaction

$$6CH_4 \leftrightarrows C_6H_6 + 9H_2 \qquad (1)$$

is promising, because of its potential in the direct conversion of methane to liquid chemicals and fuels.[1] Therefore, intense efforts have been devoted to the development of suitable catalysts for MDA, such as Zn/HZSM-5,[2] Fe/HZSM-5,[3] Ga/HZSM-5,[4] Mo/MCM-22,[5] Mo/HMCM-49,[6] and Mo/HZSM-5,[7] or, just recently, single Fe sites embedded in a silica matrix.[8]

However, limited $CH_4$ conversion is one of the problems of MDA.[9] It follows from thermodynamics, that, for eq 1, an equilibrium-limited $CH_4$ conversion of $X(CH_4) \approx 12\%$, with a benzene yield of $Y(C_6H_6) \approx 4\%$ at 700 °C, can be expected.[10] To overcome this thermodynamic limitation, integration of the MDA reaction with a $H_2$-transporting membrane in a catalytic membrane reactor is an effective approach.

Membrane reactors are one concept for the intensification of chemical processes.[11] A (catalytic) membrane reactor combines a chemical reaction with an *in situ* separation in one unit.[12] Also, MDA was studied in catalytic membrane reactors, for the purpose of increasing $CH_4$ conversion and the yield of aromatics via the continuous removal of $H_2$ to overcome the
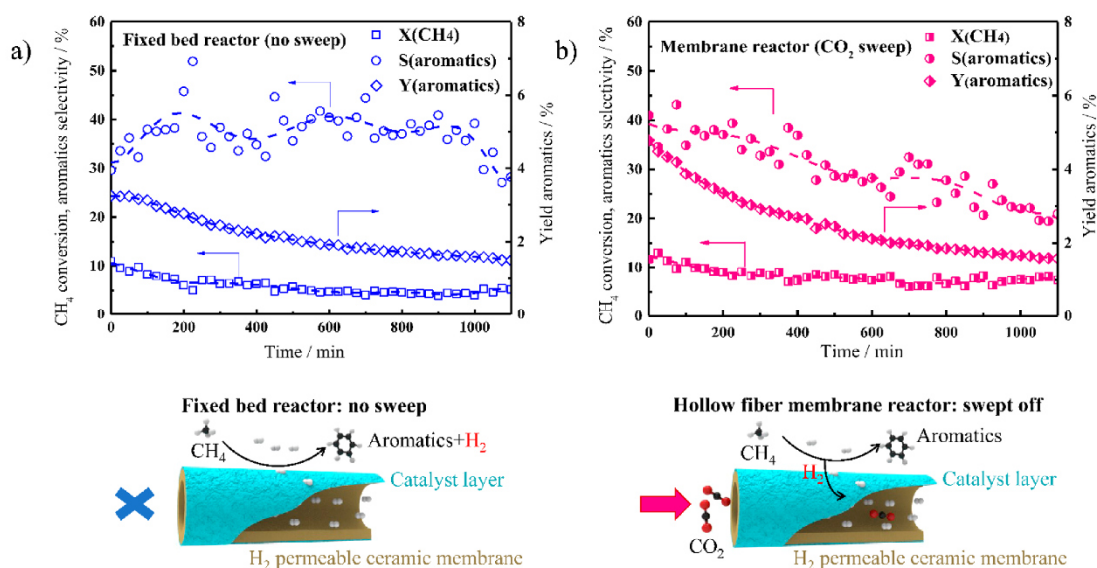
**Figure 2.** Performance of the nonoxidative MDA (a) in the fixed-bed reactor without sweep, and (b) in the LWM0.4 hollow fiber membrane reactors swept with $CO_2$. Conditions: $T$ = 700 °C; feed side, $F_{CH_4}$ = 1.4 cm$^3$ min$^{-1}$, $F_{He}$ = 2.5 cm$^3$ min$^{-1}$, catalyst = 0.1 g 6 wt % Mo/HZSM-5; sweep side, $F_{CO_2}$ = 5 cm$^3$ min$^{-1}$.

equilibrium limitation.[13] Usually, palladium and its alloys are applied as membranes for the *in situ* extraction of $H_2$ during the MDA reaction.[14] However, these Pd alloy membranes were not suitable for MDA, because the endothermic MDA requires high temperatures of at least 700 °C; however, at this temperature— especially in the presence of hydrocarbons—the Pd alloy membranes undergo degradation.[15]

Therefore, ceramic membranes, which can operate at high temperatures and in the presence of hydrocarbons, are needed to support the MDA.[16] In a simulation paper, Iglesia developed a concept for the design and optimization of catalysts and membranes for the nonoxidative conversion of $CH_4$.[16a] It was predicted that a bifunctional catalyst such as Mo/H-ZSM-5, in combination with a continuous removal of $H_2$, should lead to an increased $CH_4$ conversion at practical residence times of ~100 s. In a subsequent pioneering paper, this group used a ceramic membrane (SrCe$_{0.95}$Yb$_{0.05}$O$_{3-\delta}$), but the improvements in the MDA process were very modest (6% improvement of methane conversion, almost no increase in yield of aromatics at 950 K), because of the low $H_2$ permeability of the membrane (only 6.4% $H_2$ removal efficiency).[16b]

Dense ceramic membranes exhibiting mixed proton and electron conductivity, at high temperatures, can selectively permeate $H_2$ rather than other gases from $H_2$-containing mixtures under the driving force of a $H_2$ partial pressure gradient across the membrane. U-shaped hollow fiber membranes with a high area-to-volume ratio can avoid the membrane breakage, because of thermal expansion or shrinkage, and they can be easily assembled to a reactor module.[17] Therefore, in the nonoxidative MDA, we applied a U-shaped high-flux $H_2$-permeable ceramic hollow fiber membrane with a composition of La$_{5.5}$W$_{0.6}$Mo$_{0.4}$O$_{11.25-\delta}$ (LWM0.4).[18] In this paper, we study the increase in the $CH_4$ conversion and the aromatics yield in the classical nonoxidative MDA *in situ*, by removing the $H_2$ from the MDA reactor at the

reaction temperature of 700 °C through a U-shaped $H_2$- selective LWM0.4 hollow fiber.

As illustrated in Figure 1, in the LWM0.4 hollow fiber reactor, helium-diluted $CH_4$ (36 vol % $CH_4$) with a weigth hourly space velocity (WHSV) of 840 cm$^3$ g$_{cat}^{-1}$ h$^{-1}$ is used as feed on the shell side of the hollow fiber membrane to produce aromatics and $H_2$ through MDA on the bifunctional Mo/ HZSM-5 catalyst, which is coated around the fiber. The $H_2$ that is produced is removed to the core side of the fiber with a low $H_2$ partial pressure, where $H_2$ is swept away *in situ*, using $CO_2$ or argon. To assess the impact of the $H_2$ removal, for comparison, fixed-bed reactor experiments were conducted without $H_2$ removal (no sweep gas).
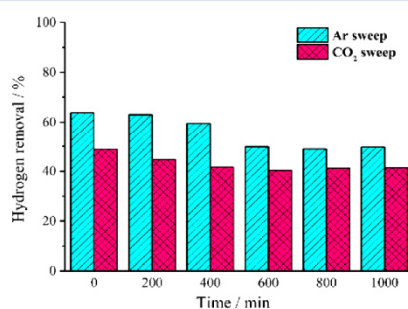
The performances of the MDA reaction in the fixed-bed reactor and the membrane reactor are shown in Figure 2. According to a slightly higher $CH_4$ conversion over the thermodynamic value of 12% at 700 °C and an increased selectivity for aromatics in the membrane reactor, in comparison with the fixed-bed reactor, the starting yield of aromatics in the membrane reactor (Figure 2b) is ~47% higher than that in the fixed-bed reactor (Figure 2a). However, these differences become smaller with increasing time-on-stream. Similar results have been observed when using argon as a sweep gas, as shown in Figure S2 in the Supporting Information. Because of the continuous removal of $H_2$, coking is enhanced in the membrane reactor, which also has been observed for the MDA in Pd alloy membrane reactors.[14b,d,e]

Figure 3 shows the comparison of the yield of aromatics in the fixed-bed reactor and the membrane reactor (Figure 3a). As the accumulated amount of aromatics show, the higher performance of the membrane reactor over the fixed-bed reactor is maintained for a long period (Figure 3b). Figure 3c shows the product distribution as a function of time. For both reactor types, coke is the main product of the MDA reaction. However, ~10% more aromatics are formed in the membrane

a)



b)



c)
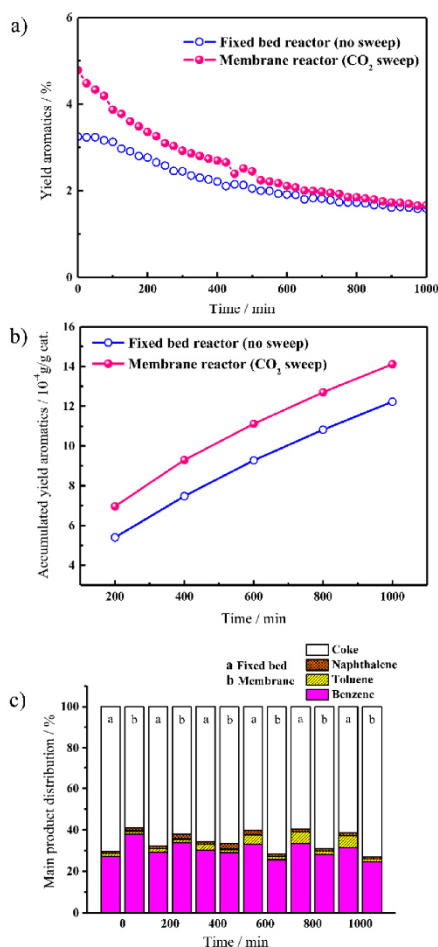


**Figure 3.** (a) Yield of aromatics (benzene, toluene, naphthalene), (b) cumulative yield of aromatics, and (c) main product distribution, as a function of time for the fixed-bed reactor without sweep and the catalytic membrane reactor swept with $CO_2$.



**Figure 4.** Hydrogen removal efficiency (expressed as a percentage) of the abstracted hydrogen through the LWM0.4 membrane in the case of the MDA catalytic membrane reactor.
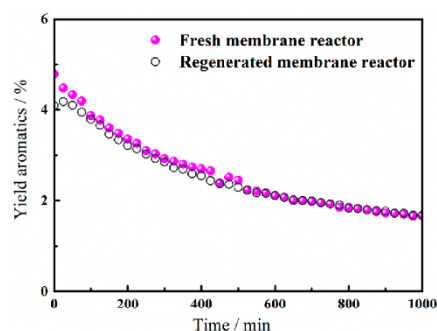


**Figure 5.** Nonoxidative MDA reaction performance of the regenerated LWM0.4 hollow fiber membrane reactors swept with $CO_2$. Regeneration conditions: $T$ = 700 °C; feed side, $F_{air}$ = 30 $cm^3$ $min^{-1}$; sweep side, no gas flow; $t$ = 5 h.

reactor, in comparison with the fixed bed (Figure 3c). The yield of aromatics of the membrane reactor is higher than that of the fixed-bed reactor in the first 300 min, because of the extracted $H_2$. However, because of the enhanced coking due to the $H_2$ removal, after 10 h time-on-stream, the relationship is opposite: now the membrane reactor produces 10% less aromatics but 10% more coke than the fixed-bed reactor. Similar findings have been reported by refs 14b, d, and e. The same results are found with argon as the sweep gas, as shown in Figure S3 in the Supporting Information. However, it follows from Figures 3a and 3b that the instantaneous aromatics formation and the accumulated yield of aromatics, for the membrane reactor, are always higher than for the fixed-bed reactor, within the first 1000 min.

Figure 4 shows that 40%−60% of the $H_2$ generated has been extracted by the LWM0.4 membrane, while only 6% of the produced $H_2$ was removed by the $SrCe_{0.95}Yb_{0.05}O_{3−\delta}$ membrane.[16b] The $H_2$ extraction decreases with time-on-stream, because of the deposition of carbonaceous residues on the membrane and the decreased $H_2$ partial pressure in the feed side, as a result of the reduced $CH_4$ conversion. The $H_2$ fluxes through the LWM0.4 hollow fiber membrane, as a function of time, can be found in Figure S4 in the Supporting Information. The $H_2$ flux is slightly lower for $CO_2$ as the sweep gas than for argon as the sweep gas. This is a common finding for ceramic membranes, because of the stronger adsorptive interaction of $CO_2$ with the perovskite surface, which suppresses the surface exchange reaction more than argon.[18b,19] Compared with the Pd alloy membrane reactor, whose permeability declined to 20% of the initial permeation flux after 60 min and went down after 900 min of operation,[10,15] our ceramic LWM0.4 membrane reactor still exhibits a considerable $H_2$ permeation flux.

The oxidative regeneration of the coked membrane reactor requires both stable membranes and catalysts. Usually, Pd alloy membranes can be only regenerated under reductive conditions in diluted $H_2$; the coke cannot be totally removed, and the MDA performance did not completely recover.[10,14c] Since our ceramic membrane and our catalyst are stable under oxidative conditions, our membrane−catalyst system could be completely regenerated in air. After coke combustion, the MDA reaction was conducted again, as shown in Figure 5, and the regenerated membrane reactor possesses a comparable MDA performance similar to that observed in the first run (Figure

2b), so that the LWM0.4 membrane–Mo/HZSM-5 catalyst system is stable under MDA reaction conditions and can be regenerated.

## ■ CONCLUSION

In summary, this work demonstrates the successful application of a U-shaped hydrogen-permeable hollow fiber ceramic membrane of the composition $La_{5.5}W_{0.6}Mo_{0.4}O_{11.25-\delta}$ (LWM0.4) to support methane dehydrocyclization to aromatic compounds. The LaWM0.4 ceramic membrane is different toward hydrogen-selective palladium membranes, because it is stable over a long period under the reaction conditions of the MDA at 700 °C. If the hydrogen is removed through the LWM0.4 hollow fiber membrane, the yield of aromatics (benzene, toluene, naphthalene) can be increased by 47% (using $CO_2$ as the sweep gas) to 70% (using argon as the sweep gas). Approximately 50% of the abstracted hydrogen has been removed through the hydrogen-permeable ceramic membrane. Because of this hydrogen extraction, the deposition of carbonaceous species is enhanced, and the advantages of the membrane reactor over the fixed-bed reactor become smaller. However, after combustion of the coke with air, the catalyst system could be completely regenerated.

## ■ ASSOCIATED CONTENT

### ⑤ Supporting Information

The Supporting Information is available free of charge on the ACS Publications website at DOI: 10.1021/acscatal.6b00004.

Full experimental details and supporting figures (PDF)

## ■ AUTHOR INFORMATION

**Corresponding Authors**

*E-mail: ceyywei@scut.edu.cn (Y. Wei).
*E-mail: hhwang@scut.edu.cn (H. Wang).
*E-mail: juergen.caro@pci.uni-hannover.de (J. Caro).

**Notes**

The authors declare no competing financial interest.

## ■ ACKNOWLEDGMENTS

## ■ REFERENCES

(1) (a) Choudhary, T. V.; Aksoylu, E.; Wayne Goodman, D. *Catal. Rev.: Sci. Eng.* **2003**, *45*, 151. (b) Choudhary, V. R.; Kinage, A. K.; Choudhary, T. V. *Science* **1997**, *275*, 1286. (c) Lunsford, J. H. *Catal. Today* **2000**, *63*, 165.

(2) Wang, L.; Tao, L.; Xie, M.; Xu, G.; Huang, J.; Xu, Y. *Catal. Lett.* **1993**, *21*, 35.

(3) Weckhuysen, B. M.; Wang, D.; Rosynek, M. P.; Lunsford, J. H. *J. Catal.* **1998**, *175*, 347.

(4) (a) Kwak, B. S.; Sachtler, W. M. H.; Haag, W. O. *J. Catal.* **1994**, *149*, 465. (b) Li, Y. J.; Armor, J. N. *J. Catal.* **1994**, *145*, 1. (c) Wang, D.; Lunsford, J. H.; Rosynek, M. P. *J. Catal.* **1997**, *169*, 347.

(5) Chu, N.; Wang, J.; Zhang, Y.; Yang, J.; Lu, J.; Yin, D. *Chem. Mater.* **2010**, *22*, 2757.

(6) Wang, D. Y.; Kan, Q. B.; Xu, N.; Wu, P.; Wu, T. H. *Catal. Today* **2004**, *93–95*, 75.

(7) (a) Chu, N.; Yang, J.; Wang, J.; Yu, S.; Lu, J.; Zhang, Y.; Yin, D. *Catal. Commun.* **2010**, *11*, 513. (b) Jiang, H.; Wang, L.; Cui, W.; Xu, Y. *Catal. Lett.* **1999**, *57*, 95. (c) Solymosi, F.; Cserényi, J.; Szöke, A.; Bánsági, T.; Oszkó, A. *J. Catal.* **1997**, *165*, 150. (d) Su, L.; Liu, L.; Zhuang, J.; Wang, H.; Li, Y.; Shen, W.; Xu, Y.; Bao, X. *Catal. Lett.* **2003**, *91*, 155. (e) Xu, Y.; Bao, X.; Lin, L. *J. Catal.* **2003**, *216*, 386. (f) Yang, J.; Yu, S.; Hu, H.; Zhang, Y.; Lu, J.; Wang, J.; Yin, D. *Chem. Eng. J.* **2011**, *166*, 1083.

(8) Guo, X.; Fang, G.; Li, G.; Ma, H.; Fan, H.; Yu, L.; Ma, C.; Wu, X.; Deng, D.; Wei, M.; Tan, D.; Si, R.; Zhang, S.; Li, J.; Sun, L.; Tang, Z.; Pan, X.; Bao, X. *Science* **2014**, *344*, 616.

(9) Ma, D.; Wang, D.; Su, L.; Shu, Y.; Xu, Y.; Bao, X. *J. Catal.* **2002**, *208*, 260.

(10) Natesakhawat, S.; Means, N. C.; Howard, B. H.; Smith, M.; Abdelsayed, V.; Baltrus, J.; Cheng, Y.; Lekse, J. W.; Link, D.; Morreale, B. *Catal. Sci. Technol.* **2015**, *5*, 5023.

(11) Sirkar, K. K.; Fane, A. G.; Wang, R.; Wickramasinghe, S. R. *Chem. Eng. Process.* **2015**, *87*, 16.

(12) (a) Dittmeyer, R.; Caro, J. *Handbook of Heterogeneous Catalysis*; Wiley–VCH: Weinheim, Germany, 2008; p 2198. (b) Drioli, E.; Fontananova, E. *Ullmann's Encyclopedia of Industrial Chemistry*; Wiley–VCH: Weinheim, Germany, 2010. (c) Jiang, H.; Cao, Z.; Schirrmeister, S.; Schiestel, T.; Caro, J. *Angew. Chem., Int. Ed.* **2010**, *49*, 5656. (d) Jiang, H.; Wang, H.; Liang, F.; Werth, S.; Schiestel, T.; Caro, J. *Angew. Chem., Int. Ed.* **2009**, *48*, 2983. (e) Jiang, H.; Wang, H.; Liang, F.; Werth, S.; Schirrmeister, S.; Schiestel, T.; Caro, J. *Catal. Today* **2010**, *156*, 187. (f) Jiang, H.; Wang, H.; Werth, S.; Schiestel, T.; Caro, J. *Angew. Chem., Int. Ed.* **2008**, *47*, 9341.

(13) (a) Caro, J. Basic Aspects of Membranes Reactors. In *Comprehensive Membrane Science and Engineering*, Vol. 3; Drioli, E., Giorno, L., Eds.; Elsevier: Amsterdam, 2010; p 1. (b) Spivey, J. J.; Hutchings, G. *Chem. Soc. Rev.* **2014**, *43*, 792. (c) Cao, Z.; Jiang, H.; Luo, H.; Baumann, S.; Meulenberg, W. A.; Assmann, J.; Mleczko, L.; Liu, Y.; Caro, J. *Angew. Chem., Int. Ed.* **2013**, *52*, 13794.

(14) (a) Howard, B.; Killmeyer, R.; Rothenberger, K.; Cugini, A.; Morreale, B.; Enick, R.; Bustamante, F. *J. Membr. Sci.* **2004**, *241*, 207. (b) Iliuta, M. C.; Larachi, F.; Grandjean, B. P.; Iliuta, I.; Sayari, A. *Ind. Eng. Chem. Res.* **2002**, *41*, 2371. (c) Kinage, A. K.; Ohnishi, R.; Ichikawa, M. *Catal. Lett.* **2003**, *88*, 199. (d) Larachi, F.; Oudghiri-Hassani, H.; Iliuta, M.; Grandjean, B.; McBreen, P. *Catal. Lett.* **2002**, *84*, 183. (e) Rival, O.; Grandjean, B. P.; Guy, C.; Sayari, A.; Larachi, F. *Ind. Eng. Chem. Res.* **2001**, *40*, 2212. (f) Skutil, K.; Taniewski, M. *Fuel Process. Technol.* **2006**, *87*, 511.

(15) Jung, S. H.; Kusakabe, K.; Morooka, S.; Kim, S.-D. *J. Membr. Sci.* **2000**, *170*, 53.

(16) (a) Li, L.; Borry, R. W.; Iglesia, E. *Chem. Eng. Sci.* **2002**, *57*, 4595. (b) Liu, Z.; Li, L.; Iglesia, E. *Catal. Lett.* **2002**, *82*, 175.

(17) Wei, Y.; Liu, H.; Xue, J.; Li, Z.; Wang, H. *AIChE J.* **2011**, *57*, 975.

(18) (a) Amsif, M.; Magrasó, A.; Marrero-López, D.; Ruiz-Morales, J.; Canales-Vázquez, J.; Núñez, P. *Chem. Mater.* **2012**, *24*, 3868. (b) Chen, Y.; Liao, Q.; Li, Z.; Wang, H.; Wei, Y.; Feldhoff, A.; Caro, J. *AIChE J.* **2015**, *61*, 1997.

(19) (a) Escolástico, S.; Solís, C.; Scherb, T.; Schumacher, G.; Serra, J. M. *J. Membr. Sci.* **2013**, *444*, 276. (b) Tan, X.; Liu, N.; Meng, B.; Sunarso, J.; Zhang, K.; Liu, S. *J. Membr. Sci.* **2012**, *389*, 216. (c) Xue, J.; Liao, Q.; Chen, W.; Bouwmeester, H. J.; Wang, H.; Feldhoff, A. *J. Mater. Chem. A* **2015**, *3*, 19107.

Supporting Information for

# Gas to Liquids: Natural Gas Conversion to Aromatic Fuels and Chemicals in a Hydrogen-Permeable Ceramic Hollow Fiber Membrane Reactor

Jian Xue,[1] Yan Chen,[2] Yanying Wei, [1,2] Armin Feldhoff,[1] Haihui Wang,[2.3] Juergen

Caro[1]

[1]*Institute of Physical Chemistry and Electrochemistry, Leibniz University Hannover, Callinstrasse*

*3A, D-30167 Hannover, Germany*

[2]*School of Chemistry & Chemical Engineering, South China University of Technology, No. 381*

*Wushan Road, Guangzhou 510640, China.*

[3]*School of Chemical Engineering, The University of Adelaide, Adelaide, SA 5005, Australia*

S1

### Experimental section

The U-shaped LWM0.4 hollow fiber membranes were prepared through the wet-spinning technic followed by high temperature sintering as shown in Figure S1. More details can be found in our previous work.[1] The membrane was sealed onto an alumina tube using ceramic sealant and the effective membrane area was about 1 cm². 0.1 g 6 wt% Mo/HZSM-5 catalyst (Bayer Technology Services, BTS) was mixed with terpilenol then directly coated on the shell side of the hollow fiber. Operation temperature was kept at 700 °C. 1.4 cm³min⁻¹ of $CH_4$ and 2.5 cm³min⁻¹ He was mixed as the feed gas in the shell side for non-oxidative MDA reaction, WHSV is 840 cm³ $g_{cat}^{-1}$ h⁻¹. It can be simulated as a fixed bed reactor when no sweep gas was used in the core side of membrane. 5 cm³ min⁻¹ of Ar or $CO_2$ was also be used as the sweep gas in the case of the catalytic membrane reactor. The concentration of the flue gas was monitored by an on-line gas chromatography (Agilent 7890) and the total gas flow rate at outlet (*F*) was calibrated using a bubble flow meter. The error is below 0.2 %. The $CH_4$ conversion X($CH_4$), aromatics (including benzene, toluene and naphthalene) selectivity S(aromatics) and aromatics yield Y(aromatics) can be calculated as follows:[2]

$$X(CH_4) = \left(1 - \frac{c(CH4,out) \times F}{F(CH4,in)}\right) \times 100\%$$

$$S(aromatics) = \frac{c(aromatics,out) \times F}{F(CH4,in) - c(CH4,out) \times F} \times 100\%$$

$$Y(aromatics) = X(CH_4) \times S(aromatics)$$

$$S(coke) = 1 - S(aromatics)$$
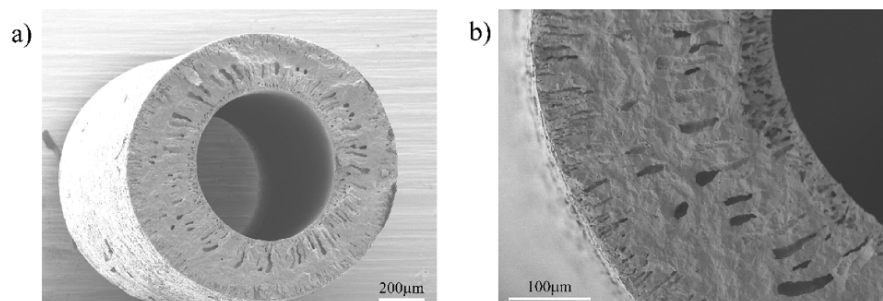
***Supplementary figures***



Figure S1. Micrograph of the cross section of the fresh hydrogen-permeable LWM0.4 ceramic hollow fiber membrane.

The SEM images of the LWM0.4 hollow fiber membrane after sintering is shown in Figure S1a and b. The cross-section (approximately 200 μm thickness) shows two finger-like structures near the inner and outer surfaces and a sponge-like structure in the middle. The cavities are closed, and, therefore, this structure acts as a mechanically stable support for the inner and outer dense surface layers of the hollow fiber membrane.[1]
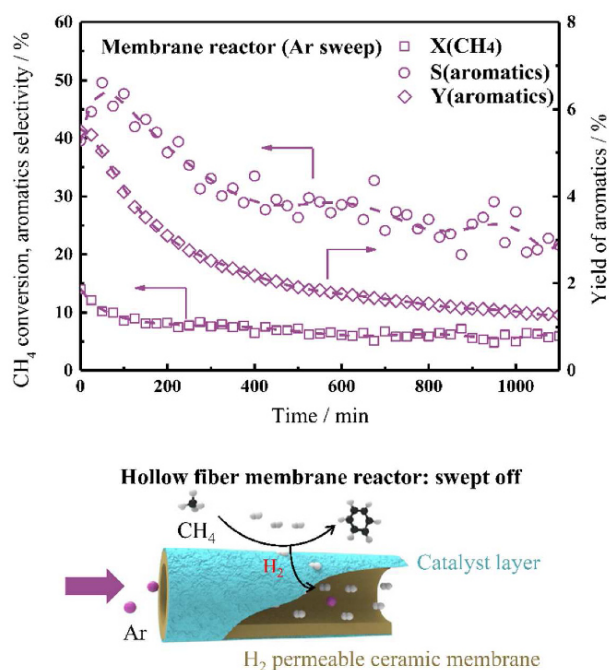
Figure S2. Performance of the non-oxidative MDA reaction in the LWM0.4 hollow fiber membrane reactors swept with Ar.

Conditions: T=700 $^{\circ}$C; feed side: $F_{CH4}$=1.4 cm$^3$min$^{-1}$, $F_{He}$=2.5 cm$^3$min$^{-1}$, cat.: Mo/HZSM-5, 0.1 g, 6 wt% Mo; sweep side: $F_{Ar}$= 5 cm$^3$min$^{-1}$

Higher methane conversion by 26.4 % and aromatics yield by 69.2 % in the membrane reactor was obtained compared with fixed bed reactor as shown in Figure 2a and Figure S2. However, the improvement become smaller with increasing time due to the coke deposition, similar to that when $CO_2$ was used as sweep gas.
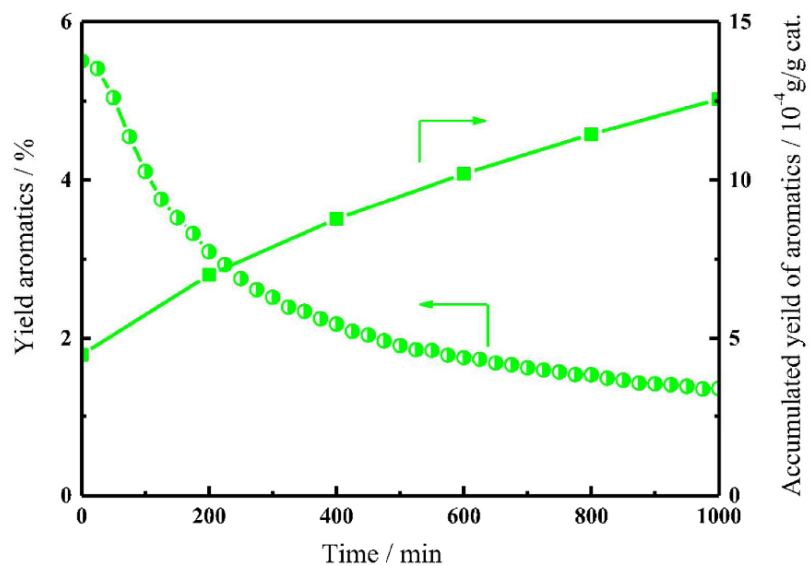
Figure S3. Aromatics yield and cumulative aromatics yield as function of time on stream for the catalytic membrane reactor swept with Ar.

As shown in Figure S3, the instantaneity aromatics yield in the membrane reactor with Ar as sweep gas are decline with time, and the differences of the accumulated yield become smaller with increasing time. The decreasing rate of the aromatics yield with Ar as sweep gas is faster than that with $CO_2$ as sweep gas, due to the higher $H_2$ removing efficiency as shown in Figure 4and S4.
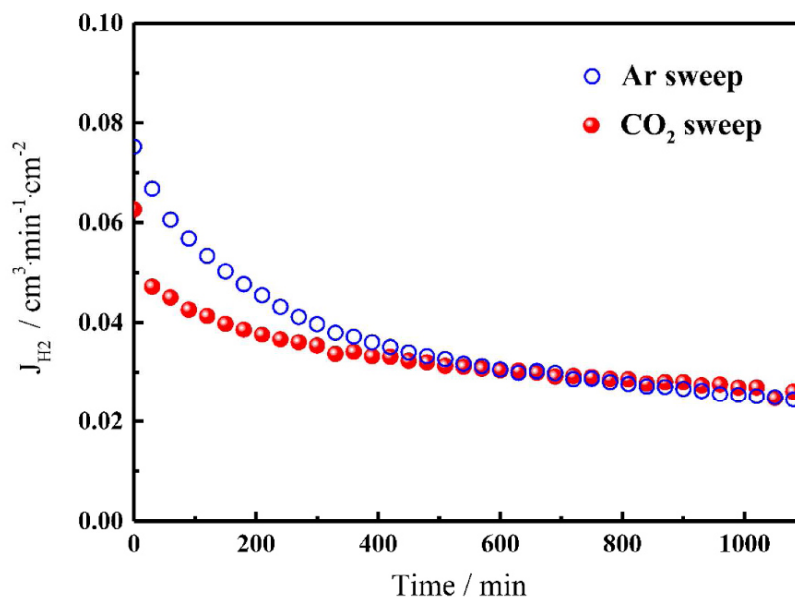
S5

Figure S4. Comparison of hydrogen permeation flux through the LWM0.4 membrane with different sweep gases under the MDA conditions.

The $H_2$ fluxes through the LWM0.4 hollow fiber membrane as a function of time can be found in Figure S4. The $H_2$ flux is slightly lower for $CO_2$ than for Ar as sweep gas. This is a common finding for $O_2$-transporting ceramic membranes because of the stronger adsorptive interaction of $CO_2$ with the perovskite surface which suppresses the surface exchange reaction more than Ar.[1a, 3] Compared with the Pd alloy membrane reactor whose permeability declined to 20% of the initial permeation flux after 60 min and shut down after 900 min of operation,[4] our ceramic LWM0.4 membrane reactor still exhibits a considerable $H_2$ permeation flux.
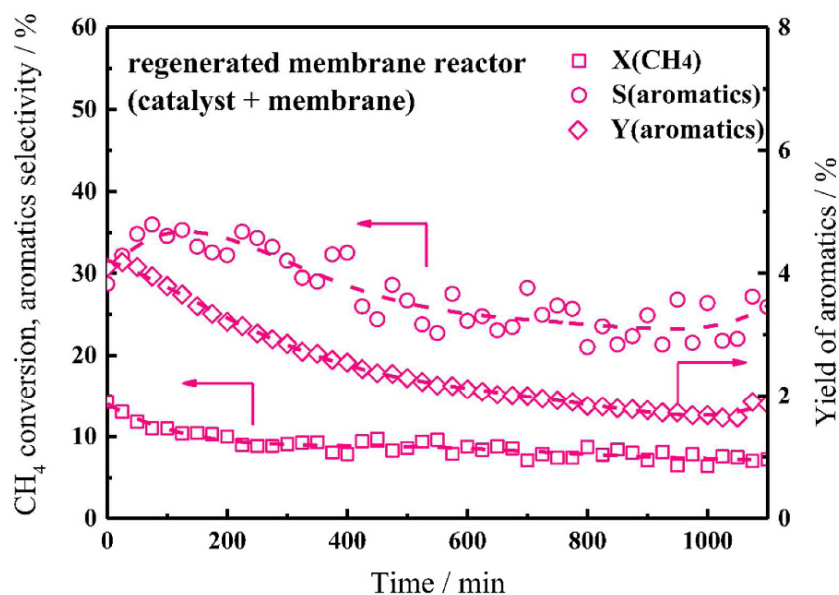
Figure S5. Performance of the non-oxidative MDA reaction in the regenerated LWM0.4 hollow fiber membrane reactors swept with $CO_2$.

Regenerate conditions: T=700 $^oC$; feed side: $F_{air}$=30 $cm^3min^{-1}$, sweep side: no gas; t = 5 h.

Different to the Pd alloy membrane, our ceramic membrane is stable under oxidative conditions. After the MDA operation, therefore, the coke deposition was burnt off with air to refresh the membrane catalyst system, and then MDA reaction was conducted again. As shown in Figure 5 and S5, the regenerated membrane reactor possesses a comparable MDA performance like in the first run (Figure 2b), so that LWM0.4 membrane – Mo/HZSM-5 catalyst system is stable under MDA reaction conditions and can be regenerated.

S7

a) Fresh LWM0.4 membrane
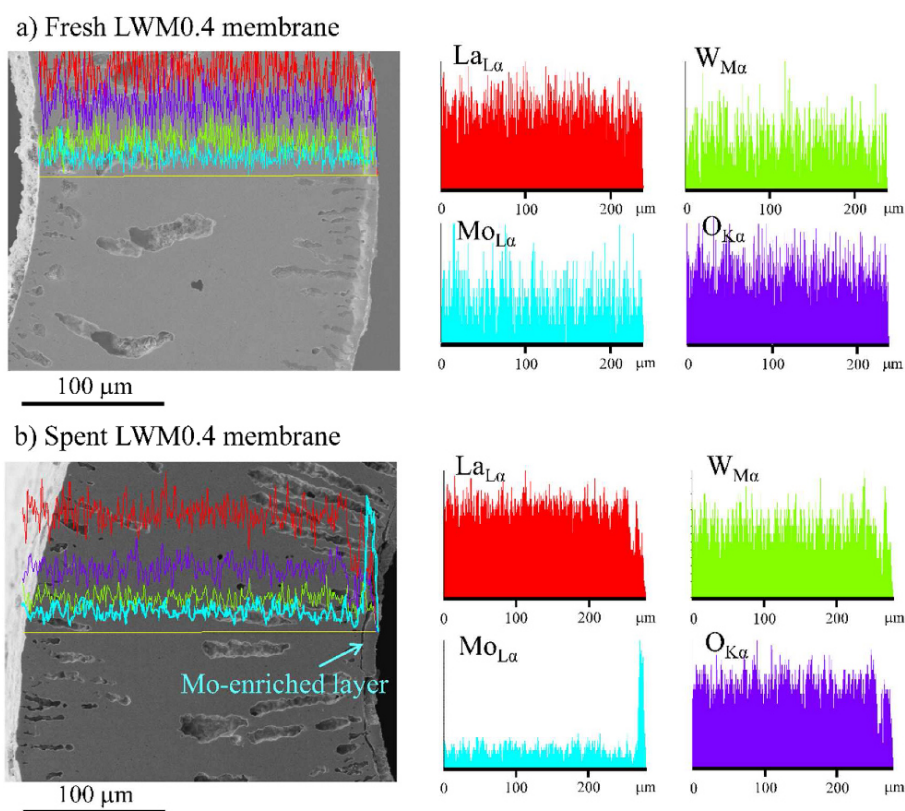
b) Spent LWM0.4 membrane

Figure S6. SEM and EDXS of the cross section of the LWM0.4 hollow fiber before and after the MDA reaction.

The fresh and spent LWM0.4 hollow fiber membranes after the MDA were characterized by SEM and EDXS. As shown in Figure S6, all the metals are distributed homogeneously in the cross section of the fresh membrane, while a Mo-enriched oxide layer can is found near the inner surface (sweep side where the $H_2$ is swept off) of the spent fiber with a thickness of around 10 μm. There is some migration of Mo under reaction conditions forming an oxide layer like found also in ref.[5] Similar findings were observed in other La-W oxides after $H_2$ permeation

S8

116

operation.[5-6] Serra et al. reported that Re oxide precipitates were found on La$_{5.5}$W$_{0.8}$Re$_{0.2}$O$_{11.25-\delta}$ after permeation.[6a] A Mo-rich phase was observed in the La$_{27}$Mo$_{1.5}$W$_{3.5}$O$_{55.5}$ grain boundaries.[6b] However, our spent LWM0.4 hollow fiber membrane was still dense and compact after MDA reaction.
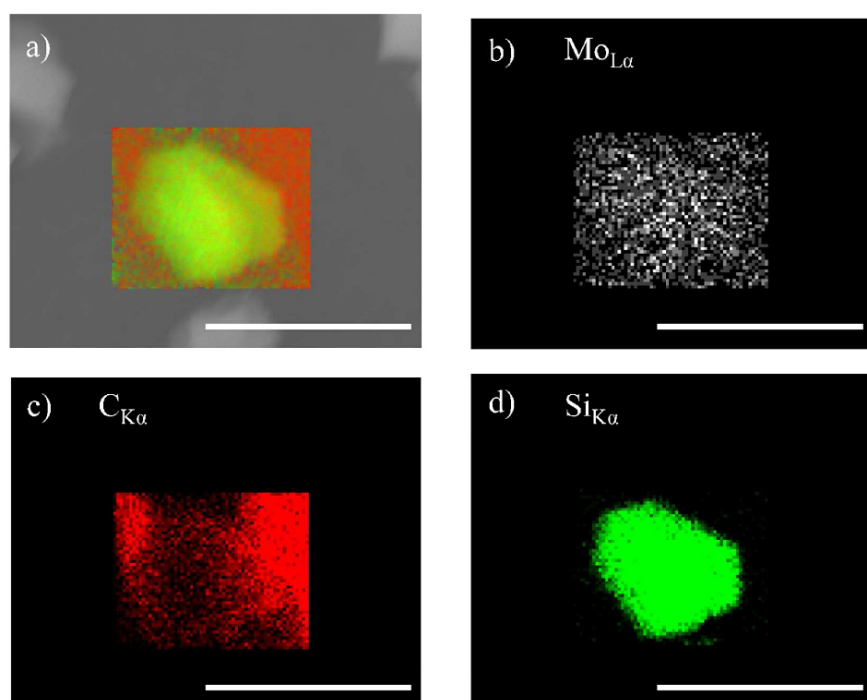


Figure S7. SEM and EDXS of the coke deposition on the Mo/HZSM-5 catalyst after the MDA reaction. Scale bar: 6μm.

Figure S7 shows the coke deposition on the Mo/HZSM-5 catalyst after the MDA reaction. The carbonaceous deposits gradually cover the MoC$_x$ phase and the HZSM-5 and lead to severe deactivation of the catalyst. In the MDA process, two catalytic sites are required for the conversion of CH$_4$ to aromatics: MoCx for C-H

bond activation and initial C-C bond formation, acid site of HZSM-5 for cyclization of $C^{2-}$ hydrocarbons to form aromatics.[7] Whereas the first carbon deposition is useful and necessary to form the catalytically active carbide component MoCx in the initial steps, further carbon deposition goes on and it is difficult to avoid due to the thermodynamics.[7a, 8] Finally, the carbonaceous deposits gradually cover the MoCx phase and the HZSM-5 as shown in Figure S7. The addition of some oxidant to the feed can reduce the carbon formation, while deep oxidization of the starting methane and of the generated hydrocarbons could not be avoided with Mo/HZSM-5 catalyst.[2, 7a] The challenges in MDA reaction is the cleaving of the C-H bond without coke deposition. With Mo/HZSM-5 catalyst, it is hard to obtain simultaneously high aromatics yield and good stability of the catalyst. The development of new type catalyst which could prevent the coke deposition during the non-oxidative MDA reaction is urgent.[9] Then the combination of the new type catalyst with the ceramic $H_2$-transporting membrane is promising to overcome of the thermodynamic limitations and to ensure a good long-term operation stability.

*Reference*

1.    (a) Chen, Y.; Liao, Q.; Li, Z.; Wang, H.; Wei, Y.; Feldhoff, A.; Caro, J., *AIChE J.* **2015**, *61*, 1997; (b) Wei, Y.; Liu, H.; Xue, J.; Li, Z.; Wang, H., *AIChE J.* **2011**, *57*, 975.

2.    Cao, Z.; Jiang, H.; Luo, H.; Baumann, S.; Meulenberg, W. A.; Assmann, J.; Mleczko, L.; Liu, Y.; Caro, J., *Angew. Chem. Int. Ed.* **2013**, *125*, 14039.

3.    (a) Escolástico, S.; Solís, C.; Scherb, T.; Schumacher, G.; Serra, J. M., *J. Membr. Sci.* **2013**, *444*, 276; (b) Tan, X.; Liu, N.; Meng, B.; Sunarso, J.; Zhang, K.; Liu, S., *J. Membr. Sci.* **2012**, *389*, 216; (c) Xue, J.; Liao, Q.; Chen, W.; Bouwmeester, H. J.; Wang, H.; Feldhoff, A., *J. Mater. Chem. A* **2015**, *3*, 19107.

4.    (a) Jung, S. H.; Kusakabe, K.; Morooka, S.; Kim, S.-D., *J. Membr. Sci.* **2000**, *170*, 53; (b) Natesakhawat, S.; Means, N. C.; Howard, B. H.; Smith, M.; Abdelsayed, V.; Baltrus, J.; Cheng, Y.; Lekse, J. W.; Link, D.; Morreale, B., *Catal. Sci. & Techn.* **2015**, *5*, 5023.

5.    Vøllestad, E.; Norby, T.; Haugsrud, R., *Solid State Ionics* **2013**, *244*, 57.

6.    (a) Escolastico, S.; Seeger, J.; Roitsch, S.; Ivanova, M.; Meulenberg, W. A.; Serra, J., *ChemSusChem* **2013,** *6*, 1523; (b) Vøllestad, E.; Vigen, C. K.; Magrasó, A.; Haugsrud, R., *J. Membr. Sci.* **2014,** *461*, 81.

7.    (a) Spivey, J. J.; Hutchings, G., *Chem. Soc. Rev.* **2014,** *43*, 792; (b) Xu, Y.; Bao, X.; Lin, L., *J. Catal.* **2003,** *216*, 386.

8.    Jiang, H.; Wang, L.; Cui, W.; Xu, Y., *Catal. Lett.* **1999,** *57*, 95.

9.    Guo, X.; Fang, G.; Li, G.; Ma, H.; Fan, H.; Yu, L.; Ma, C.; Wu, X.; Deng, D.; Wei, M., *Science* **2014,** *344*, 616.

# Publications and conferences
## Publications included in this thesis

1) The phase stability of the Ruddlesden-Popper type oxide
   $(Pr_{0.9}La_{0.1})_{2.0}Ni_{0.74}Cu_{0.21}Ga_{0.05}O_{4+\delta}$ in an oxidizing environment

   **<u>Jian Xue</u>**, Alexander Schulz, Haihui Wang, Armin Feldhoff
   *Journal of Membrane Science*, 497 (2016) 357-364
   doi: 10.1016/j.memsci.2015.09.026

2) A new $CO_2$-resistant Ruddlesden-Popper oxide with superior oxygen transport: A-site
   deficient $(Pr_{0.9}La_{0.1})_{1.9}(Ni_{0.74}Cu_{0.21}Ga_{0.05})O_{4+\delta}$

   **<u>Jian Xue</u>**, Qing Liao, Wei Chen, Henny J. M. Bouwmeester, Haihui Wang, Armin
   Feldhoff
   *Journal of Materials Chemistry A* 3 (2015) 19107-19114
   doi: 10.1039/c5ta02514a

3) Improvement of the oxygen permeation and stability of Ruddlesden-Popper-type
   membrane by surface modification

   **<u>Jian Xue</u>**, Li Chen, Yanpeng Suo, Yanying Wei, Haihui Wang, Armin Feldhoff
   *Journal of Membrane Science*
   submitted

4) Ambient air partial internal reduction of NiO in a mixed ionic-electronic conducting
   ceramic

   **<u>Jian Xue</u>**, Armin Feldhoff
   *Journal of the European Ceramic Society* 36 (2016) 3451-3456
   doi: 10.1016/j.jeurceramsoc.2016.05.023

5) Enhanced stability of Zr-doped $Ba(CeTb)O_{3-\delta}$-Ni cermet membrane for hydrogen
   separation

   Yanying Wei, **<u>Jian Xue</u>**, Wei Fang, Yan Chen, Haihui Wang, Jürgen Caro
   *Chemical Communications*, 51 (2015) 11619-11621
   doi: 10.1039/c5cc03391h

6) Hydrogen permeability and stability of $BaCe_{0.85}Tb_{0.05}Zr_{0.1}O_{3-\delta}$ asymmetric
   membranes

   Yanying Wei, **<u>Jian Xue</u>**, Haihui Wang, Jürgen Caro
   *Journal of Membrane Science*, 488 (2015) 173-181
   doi:10.1016/j.memsci.2015.04.035

7) Gas to liquids: Natural gas conversion to aromatic fuels and chemicals in a hydrogen-
   permeable ceramic hollow-fiber membrane reactor

   **<u>Jian Xue</u>**, Yan Chen, Yanying Wei, Armin Feldhoff, Haihui Wang, Juergen Caro
   *ACS Catalysis*, 6 (2016) 2448–2451
   doi: 10.1021/acscatal.6b00004

# Contributions to conferences

1) **<u>Jian Xue</u>** and Armin Feldhoff

Effect of cation deficiency on microstructure, electrical conductivity and oxygen transport properties of $(Pr_{0.9}La_{0.1})_2(Ni_{0.74}Cu_{0.21}Ga_{0.05})O_{4+\delta}$

*Electroceramics XIV conference*, 15th - 20th June 2014, Bucharest, Romania

**Oral presentation**.

2) **<u>Jian Xue</u>** and Armin Feldhoff

A-site deficient and $CO_2$-tolerant $(Pr_{0.9}La_{0.1})_2(Ni_{0.74}Cu_{0.21}Ga_{0.05})O_{4+\delta}$ membrane with high oxygen permeability

*12th International Conference on Catalysis in Membrane Reactors*, 22th - 25th June 2015, Szczecin, Poland

**Oral presentation**.

3) Armin Feldhoff and **<u>Jian Xue</u>**

Ambient air internal reduction of nickel oxide in a mixed oxygen-ionic electronic conducting ceramic

91st Deutsche Keramische Gesellschaft (DKG) Annual Meeting & Symposium on High-Performance Ceramics, 07th – 09th March 2016, Freiberg, Germeny

**Oral presentation**.

4) Armin Feldhoff and **<u>Jian Xue</u>**

Ambient air internal reduction of nickel oxide in a mixed oxygen-ionic electronic conductor

Chemiedozententagung 2016, 21st – 23rd March 2016, Heidelberg, Germeny

**Oral presentation**.

# Curriculum Vitae

## Personal data:

| | |
|---|---|
| Name: | Jian Xue |
| Date of birth: | $16^{th}$, July 1988 |
| Place of birth: | Shanxi, China |
| Nationality: | Chinese |
| Marital status: | single |

## Education

10/2013-now    **Ph.D. Candidate**
Institut für Physikalische Chemie und Elektrochemie
Supervisor: Prof. Armin Feldhoff
Gottfried Wilhelm Leibniz Universität Hannover, Hannover
Germany

09/2010-06/2013 **Master degree study:**
Chemical Engineering
South China University of Technology, Guangzhou
China

09/2006-06/2010 **Bachelor degree study:**
Applied Chemistry
South China University of Technology, Guangzhou
China